Global gravity field recovery from satellite-to-satellite tracking data with the acceleration approach

Global gravity field recovery from satellite-to-satellite tracking data with the acceleration approach

Xianglin Liu

Publications on Geodesy 68

NCG Nederlandse Commissie voor Geodesie Netherlands Geodetic Commission

Delft, November 2008

Global gravity field recovery from satellite-to-satellite tracking data with the acceleration approach
Xianglin Liu
Publications on Geodesy 68
ISBN: 978 90 6132 309 6
ISSN 0165 1706

Published by: NCG, Nederlandse Commissie voor Geodesie, Netherlands Geodetic Commission, Delft, The Netherlands
Printed by: Optima Grafische Communicatie, Optima Graphic Communication, Rotterdam, The Netherlands
Cover illustration: Xianglin Liu

NCG, Nederlandse Commissie voor Geodesie, Netherlands Geodetic Commission
P.O. Box 5058, 2600 GB Delft, the Netherlands
T: +31 (0)15 278 28 19
F: +31 (0)15 278 17 75
E: info@ncg.knaw.nl
W: www.ncg.knaw.nl

The NCG, Nederlandse Commissie voor Geodesie, Netherlands Geodetic Commission is part of the Royal Netherlands Academy of Arts and Sciences (KNAW).

To Qin and Sikai

Contents

Abstract

Global gravity field recovery from satellite-to-satellite tracking data with the acceleration approach

This thesis is focused on the development of new techniques for global gravity field recovery from high-low (hl) and low-low (ll) satellite-to-satellite tracking (SST) data. There are a number of approaches to global gravity field recovery known from literature, including the variational equations approach, short arc approach, energy balance approach and acceleration approach. The focus of the thesis is the acceleration approach with an aim to produce high-quality global gravity field models using real data from CHAMP and GRACE satellite missions.

In the first part, the research is devoted to a refinement of CHAMP hl-SST data processing methodology, which was developed at DEOS earlier. The refinement includes two major updates. The first update is usage of smoothed kinematic orbits, instead of reduced-dynamic ones, in data processing. A procedure based on B-splines has been developed for smoothing kinematic orbits by means of a regularised least-squares adjustment. The second update is the implementation of a data noise estimation procedure from the data themselves, with the aim to obtain a statistically optimal gravity field solution. The refined procedure is used to compute both regularised and a non-regularised models from a nearly one-year set of CHAMP accelerations. The regularized model is proved to be better than the regularized ITG-CHAMP01E model, and slightly better than the older DEOS_CHAMP-01C_70 model computed at DEOS. The non-regularized solution is compared to a few non-regularized CHAMP-only models produced by several research groups. The comparison shows that the obtained solution clearly outperforms most of the alternative models.

In the second part of the research, the methodology of processing CHAMP hl-SST data is extended to the case of GRACE hl-SST data, including the GRACE kinematic baselines. The kinematic positions and baselines are processed both individually and jointly. It is found that the kinematic baselines themselves are, in general, not favorable for the derivation of gravity field models. We explain this, first of all, by a poor sensitivity of the baseline data to East-West variations of the gravity field. Nevertheless, kinematic baselines slightly improve the quality

of gravity field modeling if added to a set of kinematic positions.

In the third part of the research, two innovative methodologies of gravity field modeling from GRACE ll-SST data, i.e. so-called 3-point Range Rate Combination (3RRC) approach and 3-point Range Combination (3RC) approach, are developed as extensions of the classic acceleration approach. Corresponding functional models are derived and a comprehensive procedure for processing real GRACE data is developed. The data processing procedure contains two major steps: pre-processing and inversion. The pre-processing includes the computation of purely dynamic orbits as reference ones on the basis of state-of-the-art background models of static and rapidly changing gravity fields. The reference orbits, together with the observed KBR data, are used to form the residual quantities associated with the three functional models. The inversion of these quantities into gravity field parameters is somewhat similar to inversion of kinematic baselines. The developed approaches are compared with each other and with the classic acceleration approach using real GRACE data from both August 2003 and October 2003. The corresponding hydrological models are taken as a reference for the comparison. It is found that the classic acceleration approach produces the worst results, which are not reasonable at all. The 3RC approach gives the best results and, consequently, is chosen as the primary approach to be further refined and used for routine data processing. In the course of the final refinement, an iterative data processing is implemented. It is found that two iterations are sufficient to reach a convergence. Ultimately, the recovered gravity field signals are increased by at least 10%-15% in this way.

Finally, the 3RC approach is applied to process real GRACE data routinely. A 4-year data set, spanning the period from February 2003 to December 2006, is processed on a monthly basis. Each solution represents a set of spherical harmonic coefficients, which describe the average gravity field within the month under consideration. All the solutions are supplied with full variance-covariance matrices. In the course of post-processing, the obtained solutions are subject to de-striping and 400-km Gaussian filtering, resulting in a definitive time series of filtered DEOS solutions. Furthermore, the obtained models are used to estimate secular changes as well as and seasonal and semi-seasonal variations of the Earth's gravity field. For comparison, we compute also the secular, seasonal and semi-seasonal variations from the GLDAS hydrological models. There are many remarkable similarities found in this comparison. A further analysis of the obtained GRACE solutions allowed ice melting in Greenland and Antarctica as well as the Sumatra-Andaman Earthquake to be observed and quantified. Finally, a comprehensive comparison is made of the obtained GRACE solutions with those published by other research centers: CSR, GFZ, JPL and CNES, as well as with the GLDAS hydrological model. The comparison shows that the DEOS solutions are relatively close to the JPL solutions, and less close to the GFZ and CSR solutions, which are, in turn, relatively close to each other. The main differences between the group of DEOS and JPL solutions and the group of GFZ and CSR solutions are concentrated between degree 2 and 5. We also compute

the mean values of water storage changes in sixteen large river basins from all the solutions. The selected basins represent various sizes and climatic environments. The comparison of the results shows that in general the DEOS solutions have a reasonable agreement with other GRACE solutions, and are particularly close to the JPL solutions.

Samenvatting

Mondiale zwaartekrachtveldbepaling uit satelliet-naar-satellietmetingen met de versnellingenmethode

Dit proefschrift richt zich op de ontwikkeling van nieuwe technieken voor de bepaling van het mondiale zwaartekrachtveld met behulp van de hoog-laag (hl) en laag-laag (ll) satelliet-naar-satellietmetingen (SST). Er zijn een aantal benaderingen voor mondiale zwaartekrachtveldbepaling bekend uit de literatuur, zoals de variationele vergelijkingenmethode, korteboogmethode, energiebalansmethode en versnellingenmethode. De focus van dit proefschrift is de versnellingenmethode met als doel de vervaardiging van kwalitatief hoogwaardige mondiale zwaartekrachtveldmodellen met behulp van re ele data van de CHAMP en GRACE satellietmissies.

In het eerste deel is het onderzoek gewijd aan het verbeteren van de methode voor de verwerking van CHAMP hl-SST gegevens, die reeds ontwikkeld was binnen DEOS. Deze verbetering omvat twee belangrijke aanvullingen. De eerste aanvulling is het gebruik van ge effende kinematische banen, in plaats van gereduceerd-dynamische banen, in de gegevensverwerking. Een procedure gebaseerd op B-splines is ontwikkeld voor het effenen van kinematische banen door middel van de geregulariseerde kleinstekwadratenmethode. De tweede aanvulling is de implementatie van de schatting van de meetruis uit de gegevens zelf, met als doel het verkrijgen van een statistisch optimale zwaartekrachtveldoplossing. De verbeterde procedure wordt gebruikt om zowel geregulariseerde en niet-geregulariseerde modellen te berekenen uit een dataset van bijna een jaar aan CHAMP versnellingen. Het geregulariseerde model is bewezen beter te zijn dan het geregulariseerde ITG-CHAMP01E model, en iets beter dan het oudere DEOS_CHAMP-01C_70 model dat is berekend binnen DEOS. De niet-geregulariseerde oplossing is vergeleken met enkele niet-geregulariseerde CHAMP-modellen die door verschillende onderzoeksgroepen vervaardigd zijn. De vergelijking laat zien dat verkregen oplossing duidelijk beter is dan het merendeel van de alternatieve modellen.

In het tweede deel van het onderzoek wordt de methode van de verwerking CHAMP hl-SST gegevens uitgebreid voor het geval van GRACE hl-SST data,

met inbegrip van de GRACE kinematische basislijnen. De kinematische posities en basislijnen zijn zowel individueel als gezamenlijk verwerkt. Het is gebleken dat de kinematische basislijnen zelf over het algemeen niet geschikt zijn voor de bepaling van zwaartekrachtveldmodellen. Wij verklaren dit, in de eerste plaats, door de beperkte gevoeligheid van de basislijngegevens voor oost-westvariaties in het zwaartekrachtveld. Toch kunnen de kinematische basislijnen de kwaliteit van zwaartekrachtmodellering enigzins verbeteren als deze worden toegevoegd aan een reeks van kinematische posities.

In het derde deel van het onderzoek zijn twee innovatieve methoden ontwikkeld voor zwaartekrachtveldmodellering met behulp van GRACE ll-SST gegevens, namelijk de zogenaamde 3-punts Range Rate Combination (3RRC) methode en de 3-punts Range Combination (3RC) methode, als uitbreiding op de klassieke versnellingenmethode. Voor beide methodes is het functionele model afgeleid en is een uitgebreide procedure voor de verwerking van reele GRACE data ontwikkeld. De procedure voor de gegevensverwerking bestaat uit twee grote stappen: voorverwerking en inversie. De voorverwerking omvat de berekening van zuivere dynamische banen als referentiebanen, op basis van de allernieuwste achtergrondmodellen van statische en snel veranderende zwaartekrachtvelden. De referentiebanen worden samen met de gemeten KBR data gebruikt om de residugrootheden, behorende bij de drie functionele modellen, te bepalen. De inversie van deze grootheden in zwaartekrachtveldparameters is enigszins vergelijkbaar met de inversie van kinematische basislijnen. De ontwikkelde methodes worden met elkaar vergeleken en met de klassieke versnellingenmethode, met behulp van echte GRACE gegevens, gemeten van augustus 2003 tot oktober 2003. De overeenkomstige hydrologische modellen worden gebruikt als referentie voor de vergelijking. Het is gebleken dat de klassieke versnellingenmethode resulteert in de slechtste oplossing, die totaal niet reeel is. De 3RC methode geeft de beste resultaten en is zodoende gekozen als de primaire methode die verder wordt uitgewerkt, en wordt gebruikt voor het stelselmatig verwerken van de gegevens. Gedurende de laatste verbetering is een iteratieve verwerking van gegevens geimplementeerd. Het is gebleken dat twee iteraties voldoende zijn om te komen tot een convergentie. Uiteindelijk wordt op deze manier ten minste 10%-15% meer van het zwaartekrachtveldsignaal bepaald.

Ten slotte wordt de 3RC methode toegepast voor het stelselmatig verwerken van reele GRACE gegevens. Een data set van 4 jaar, die de periode van februari 2003 tot en met december 2006 omvat, is verwerkt op een maandelijkse basis. Elke oplossing is een set van sferisch harmonische cofficinten, die een beschrijving geven van het gemiddelde zwaartekrachtveld voor de betreffende maand. Alle oplossingen worden geleverd met volledige variantie-covariantie matrices. Gedurende de naverwerking, worden de verkregen oplossingen ontdaan van strepen en wordt 400-km Gaussische filtering toegepast, wat resulteert in de uiteindelijke tijdreeks van gefilterde DEOS-oplossingen. Bovendien worden de verkregen modellen gebruikt voor de schatting van seculiere veranderingen, alsmede voor seizoens- en halfseizoensgebonden variaties van het zwaartekrachtveld van de aarde. Ter

vergelijking berekenen wij ook de seculiere, seizoens -en halfseizoensgebonden schommelingen van de GLDAS hydrologische modellen. Er zijn veel opmerkelijke gelijkenissen gevonden bij deze vergelijking. Uit een verdere analyse van de verkregen GRACE-oplossingen kon smeltend ijs in Groenland en Antarctica, alsmede de Sumatra-Andaman aardbeving worden waargenomen en gekwantificeerd. Ten slotte is een uitgebreide vergelijking gemaakt van de verkregen GRACE-oplossingen met de oplossingen die zijn gepubliceerd door andere onderzoekscentra: CSR, GFZ, JPL en CNES, alsmede met het GLDAS hydrologische model. De vergelijking laat zien dat de DEOS-oplossingen relatief dicht bij de JPL-oplossingen liggen, en minder dicht bij de GFZ en CSR-oplossingen, die op hun beurt relatief dicht bij elkaar liggen. De belangrijkste verschillen tussen de verzameling van DEOS en JPL-oplossingen en de verzameling van GFZ en CSR-oplossingen bevinden zich voornamelijk tussen graad 2 en 5. We hebben ook voor alle oplossingen de gemiddelde wateropslagveranderingen in zestien grote stroomgebieden berekend. De geselecteerde stroomgebieden hebben verschillende maten en klimatologische omstandigheden. Uit de vergelijking van de resultaten blijkt dat over het algemeen de DEOS-oplossingen redelijk overeenkomen met andere GRACE-oplossingen, en bijzonder dicht bij de JPL-oplossingen liggen.

Curriculum vitae

Xianglin Liu was born in Xinzhou, Hubei Province of P. R. China, on September 3rd 1968. He started his university study in September 1988 at the Department of Engineering Surveying at Wuhan Technical University of Surveying and Mapping (WTUSM), P. R. China, from which he graduated in June 1992. In the same year, he was employed as a junior engineer in the Service Center of Surveying and Mapping Instrument of WUTSM (which later joined Wuhan University) until 2001. During this period, he was awarded a Master of Science degree at the School of Geodesy and Geomatics of WTUSM in 1997 and a commenced studies for a PhD degree at the same School headed by Prof. Jingnan Liu. Both the MSc and PhD projects were carried out part-time whilst he was employed as an engineer. In September 2001, he was awarded a Huygens Scholarship by the Netherlands Organization for International Cooperation in Higher Education (NUFFIC) for a 10-month period. He spent that period as a visiting scientist at the Mathematical Geodesy and Positioning (MGP) section chaired by Prof. Peter Teunissen at Delft University of Technology (DUT). On his return to Wuhan University of P. R. China in July 2002, he continued his studies being finally awarded a Doctor degree entitled "Quality Control and Stochastic Model Refinements for Precise GPS Kinematic Positioning" in December 2002. In January 2003, he worked for a 9-month period as a visiting fellow again at the MGP of DUT, sponsored by a DELTA Scholarship. In October 2003, he became a PhD researcher in the section of Physical Space Geodesy headed by Prof. Roland Klees, Delft Institute of Earth Observation and Space Systems (DEOS), Faculty of Aerospace Engineering of DUT. While writing his PhD thesis, in late 2007 he was working as a Post-doc at the same group. In April 2008, he moved to Fugro Intersite BV as a senior geodesist.

Acknowledgements

First and foremost, I would like to express my deepest gratitude to my supervisor, Dr. Pavel Ditmar, for his remarkable patience and continuous support throughout this study. His support to my research, particularly his inverse engine of gravity field modeling, is essential and proved extremely important. Additionally, his solid theoretical background and rigorous professional attitude are good examples of mine. I also want to thank my promotor, Prof. Roland Klees, for providing me with the opportunity to carry out my PhD research. His critical comments at the periodical assessments guided the research to a right direction.

Many former and current colleagues at Wuhan University and Delft University of Technology have directly or/and indirectly contributed to this thesis. Dr. Q. Zhao and Dr. M. Ge are appreciated for providing the PANDA software (funded by NSFC No:40504002 and No:40874004) and many fruitful discussions, which proved extremely helpful. I am grateful to Dr. P. Visser, Dr. R. Kroes and T. van Helleputte for providing us with GRACE orbits, and Ms. E. Oudman for pre-processing some parts of data. Dr. D. Lavallee and Dr. B. Gunter are appreciated for smoothing English language of the thesis. B. Alberts is acknowledged for translating the abstract into Dutch. Dr. J. Kusche, Dr. E. Schrama and Dr. K. de Jong are thanked for their discussions and interests in my work. Particularly, Dr. Schrama's DINGO software was used for an orbit simulation carried out in the thesis. T. Wittwer, E. Revtova, J. de Teixeira da Encarnacao, J. van Loon, B. Alberts, C. Slobbe and M.-W. Janson and many others (forgive me not mentioning all names) are acknowledged for mutually beneficial collaboration, as well as for computer tricks and funny arguments, which I really enjoyed when working with them. I would like to thank Dr. D. Odijk for providing the layout of the thesis. R. Reudink and R. van Wingaarden are thanked for some ICT and administration stuff.

I aslo appreciate very much all members of the examination committee for their reviews and comments on my thesis.

The National Research Council of the Netherlands is gratefully acknowledged for their financial support to my PhD research. A part of computations have been done on the SGI Altix 3700 super-computer in the framework of the

grant SG-027 provided by Stiching National Computer faciliteiten (NCF). The support of NCF is acknowledged.

I would like to express my thanks to Dr. D. Švehla of Munich University of Technology for providing the CHAMP kinematic and reduced-dynamic orbits. Thanks also go to Dr. J. L. Chen, who provided us with the daily solutions of the GLDAS hydrological models in terms of spherical harmonic coefficients. Additionally, Dr.-ing T. Mayer-Gürr of Bonn University is appreciated for his valuable suggestions during our meetings at conferences. Cooperation with Prof. Ph. Moore and Dr. R. Tenzer of Newcastle University upon Tyne accumulated our experiences on GRACE data processing. Both of them are grateful for their efforts.

Last but not least, I am indebted to my wife, Qin, and my son, Sikai, for their great patience when I stayed in the office at weekends and evenings. Without their quiet support, I could not have this thesis done.

Chapter 1

Introduction

1.1 Background

The Earth's gravity is the sum of gravitational attraction and centrifugal force that the Earth exerts on an object on or near its surface. Its strength is quoted as an object acceleration being approximately $9.8\,\mathrm{m/s^2}$. The precise strength and direction of the Earth's gravity vary from point to point. Thus, the Earth's gravity is a vector function of 3 coordinates or a vector field. The Earth's gravity field is a potential field. It can be represented as the gradient of gravity potential (scalar function), which includes the gravitational and centrifugal potential. Since the centrifugal potential can be precisely determined, the Earth's gravity field is very often linked to only the gravitational potential (e.g. in this thesis). The Earth's gravity field and its spatial and temporal variations reflect the density structure, mass redistribution and dynamics of Earth's surface and interiors.

1.1.1 Applications of precise gravity field models

Determination of the gravity field with the highest possible accuracy is needed in various Earth science related disciplines, such as geodesy, aerospace engineering, oceanography, climatology and solid-Earth physics. In particular, the following applications can be highlighted [Rummel, 2002]:

1) Establishment of a global height reference system for datum connection, which can serve as a fundamental basis for engineering applications, and a reference surface for the study of various topographic processes, including the evolution of ice-sheets and land-surface topography.

2) Precise estimation of the global unified geoid, which is an equipotential surface approximately coinciding with the mean sea level. In particular, the marine geoid is required for the quantitative determination of absolute ocean currents and the associated transport of heat, salt and other substances. This knowledge forms a part of the input for building a global climate change picture.

3) Accurate orbit determination of satellites, particularly low-orbiting ones, which provide high-accurate measurements of Earth's environment and climate change. In addition, the launch, navigation, prediction and tracking of spacecrafts require a precise gravity field model as a constraint condition.

4) Comprehensive description and understanding of the physics of the Earth's interiors, including geodynamics associated with lithosphere, mantle composition and rheology, uplifting and subduction processes. Furthermore, refined local gravity field models can be used in exploration geophysics, e.g. to explore mineral and hydrocarbon deposits.

5) Estimation of thickness of the polar ice sheets through the combination of bedrock topography and ice-sheet surface topography.

6) Investigation and detection of temporal variations of the Earth's gravity field provide unique knowledge on natural mass transportation and re-distribution at the Earth surface and inside the Earth. This includes temporal water storage variations in continents; global re-distribution of water masses between the continents and oceans, and sea level rise; continuous melting of ice at various geographical locations, including mountain glaciers, as well as ice sheets in Greenland and Antarctica; re-distribution of mass in Earth's interiors including the so-called "isostatic adjustment".

1.1.2 Classical observations of the Earth's gravity field

Determination of the Earth's gravity field model can be carried out with a wide variety of different measurement types and solution techniques [Nerem, 1995]. The measurement types can mainly be divided into surface gravity measurements, satellite tracking measurements, and satellite radar altimetry measurements. Surface gravity measurements, including terrestrial absolute (and relative) gravity data as well as airborne gravity data, are the most straight forward information about the Earth's gravity field, but a homogeneous distribution of data over the Earth can not be achieved, even only on land. Satellite altimetry data yield gravity anomalies and geoid over the ocean, provided that the mean dynamic sea surface topography can be adequately modeled. Finally, direct satellite tracking data are used to measure gravitational perturbations affecting satellites. Satellite tracking data from a large number of mostly non-geodetic satellites, including conventional observations acquired by SLR (Satellite Laser Ranging), TRANET (Tracking Station Coordinates for Tracking Network), and DORIS (Doppler Orbitography and Radio positioning Integrated by Satellite) systems, and satellite-to-satellite tracking measurements acquired by TDRSS (Tracking Data and Relay Satellite System) and GPS (Global Positioning System) satellites, were widely used in the 1990's to improve the accuracy and resolution of the gravity field models.

Comprehensive gravity field solutions must incorporate these inhomogeneous data of various types in order to estimate gravity field parameters, e.g. spherical

harmonic coefficients, as well as the errors of estimated parameters. The optimal combination of these data certainly requires the development of complicated computational procedures. One of the most remarkable solutions of this kind is the EGM96 geo-potential model [Lemoine et al., 1998]. The EGM96 model computed up to degree 360 represents a significant improvement over previous models such as JGM-2 [Nerem et al, 1994] and JGM-3 [Tapley et al., 1996] by combining all three above mentioned types of data. Although the EGM96 model had significantly increased our knowledge on the Earth's gravity field, it could not meet the requirements from solid-Earth physics, oceanography and geodesy, not even to a limited extent [Rummel, 2002]. The above three data sources of information about the Earth's gravity field had somewhat reached their intrinsic limits in terms of data distribution and accuracy, particularly for the purpose of mapping the global gravity field model. In particular, there are a number of limitations in the above mentioned types of satellite tracking data. Firstly, most of exploited non-dedicated satellites could be tracked from the ground only over short intervals. Secondly, orbit altitudes were frequently too high to sense sufficient signal at high spherical harmonic degrees. Thirdly, satellite motion is determined not only by gravitational force, but also by surface forces, such as air-drag and solar radiation pressure. These disturbances certainly corrupted the obtained gravity models. These three fundamental limitations motivated the development and launching of low-orbiting dedicated satellite missions, such as CHAMP, GRACE and GOCE [Rummel, 2002].

1.1.3 Dedicated satellite missions: CHAMP, GRACE and GOCE

CHAMP (CHAllenging Minisatellite Payload) is a dedicated low-orbiting gravity field satellite mission, launched in July 2000. The satellite entered into an almost circular, near polar orbit with an initial altitude of 454 km. The purpose of choosing such an orbit is to obtain a homogeneous and complete global orbit coverage, which is important for modeling the global gravitational field with a high spatial resolution [Reigber et al., 2002]. The design lifetime of the satellite system is 5 years. Thanks to excellent executive status, the mission was already extended by a few more years. In order to estimate gravity field parameters, the CHAMP satellite is equipped with a high-end GPS receiver, which acquires high-low Satellite-to-Satellite Tracking (hl-SST) data. The satellite orbit can therefore be derived with high accuracy. The concept of gravity field modeling with the hl-SST observation technique is the following. The LEO is attracted by mass anomalies as it is passing over them, which results in disturbances of the satellite's orbit. The Earth's gravity field can therefore be recovered from the orbit provided that the attitude and the non-gravitational accelerations are measured by a star camera and a three-axis accelerometer respectively. Because the hl-SST data are particularly sensitive to long and medium wavelength (below degree 60-70) gravity field perturbations [Visser and van den IJsel, 2000], the CHAMP mission has dramatically improved the accuracy of the gravity field models at these wavelengths [Reigber et al., 2002, Han et al., 2003, Reigber et al., 2003, Gerlach et al., 2003, Ditmar et al., 2006]. Nevertheless, one of the mission's goals

was not achieved. The CHAMP mission was not able to retrieve time-variable gravity field as was supposed. Therefore, the attention was drawn to another dedicated gravity mission: GRACE.

The Gravity Recovery and Climate Experiment (GRACE) satellites were launched in 2002 also into a near polar orbit, mainly for the purpose of high-precision mapping the Earth's gravity field with an emphasis on its changes with respect to time [Tapley et al., 2004]. The mission consists of two satellites flying at an altitude of about 500 km as a formation at distance of about 200 km apart. The satellites are equipped with a K-band Ranging (KBR) system. Thanks to this low-low Satellite-to-Satellite Tracking technique (ll-SST) changes in the inter-satellite distance are continuously tracked with a precision of a few microns. On-board GPS receivers provide the data to determine satellites' orbits and to synchronize time tags of KBR measurements of the two satellites. In addition, accelerometers measure non-gravitational satellite accelerations, whereas star cameras determine the satellite attitudes. The KBR measurements are provided as biased ranges, derived range-rates, and derived range-accelerations. Thanks to the extremely high ranging accuracy, the ll-SST is more sensitive than hl-SST and can be used to retrieve both the static gravity field and its temporal variations. It should be mentioned that some of GRACE-based solutions were obtained by a combined processing of ll-SST and hl-SST data, see [Tapley et al., 2004, Reigber et al., 2005b, Tapley et al., 2005, Förste et al., 2006, Mayer-Gürr, 2006].

The third satellite gravimetry concept will be realized by the upcoming Gravity Field and steady-state Ocean Circulation Explorer (GOCE) mission, scheduled to be launched on October, 2008. It is dedicated to modeling the Earth's static gravity field and geoid with extremely high accuracy and spatial resolution. The mission has two peculiar features: Satellite Gravity Gradiometry (SGG) as the measurement concept and an extremely low satellite altitude. The SGG system consists of three pairs of highly sensitive accelerometers in a diamond configuration centered at the satellite's center of mass. In other words, two accelerometers are placed on each axis of the instrument triad. Thus, the differences of gravitational accelerations in all three spatial directions are measured, which can be used to derive all the elements of the matrix of second derivatives of the gravitational potential. It should be mentioned that the accelerometers have only two sensitive axes, the third one is less sensitive by a factor of 1000 [Oberndorfer and Mueller, 2002]. The accelerometers are oriented in such a way that the three diagonal components of the matrix of second derivatives are measured with the highest accuracy. The GOCE satellite will fly at an average elevation of 250 km. The purpose is to measure gravity signals at higher spatial frequencies. However, lowering the elevation is limited by the increase in atmospheric drag. To compensate for it as well as for other non-gravitational forces, such as solar radiation pressure, the satellite is equipped with a drag-free control system. The satellite will also carry a high-quality GPS receiver to provide accurate hl-SST data. It should be mentioned that processing SGG data is beyond the scope of the thesis. Mentioning this mission is for

completeness.

1.2 Research objectives

The primary goal of this research is to develop efficient techniques (and procedures) to process the hl- and ll-SST data for the determination of static and/or temporal Earth's gravity field models represented as a series of spherical harmonics. The motivation of the research is to avoid costly computations employed in traditional techniques (e.g. computing the partial derivatives which requires a numerical integration of variation equations). Additionally, the techniques to be developed are to make use of in-situ observations (e.g. accelerations), which provide directly the information of gravity field at the vicinity of observation points.

The primary research related to processing hl-SST data starts from a so-called average acceleration approach developed earlier by Ditmar and van Eck van der Sluijs [2004]. The approach has been successfully used to produce the DEOS_CHAMP-01C_70 model of the Earth's static gravity field [Ditmar et al., 2006]. One of goals in the thesis is to refine the pre-processing of CHAMP data, in order to compute a gravity field model as independently as possible from a priori CHAMP-based information, and meanwhile to improve the model. Another goal is to develop a procedure for an accurate estimation of the stochastic model of data noise needed for improving the accuracy of the gravity field model. The third goal is to extend the data processing methodology to make it applicable to the GRACE hl-SST data. The new procedure is more than a simple joint estimation by combining two satellite data sets, because processing kinematic baselines of two GRACE satellites also has to be considered. The reason is that the kinematic baselines directly estimated from GPS data are more accurate than the ones derived from individual kinematic orbits.

The primary research goal related to processing GRACE ll-SST data is to identify a linear functional model that could be used to treat GRACE data as in-situ observations. The research is to focus on the so-called classic acceleration approach [Rummel, 1979] and two innovative ones proposed in the thesis, i.e. the so-called 3-point Range Rate Combination (3RRC) and 3-point Range Combination (3RC) approach. The investigation is to not only derive the mathematical models, and has to also include real data processing. A comprehensive data processing methodology is to be developed for producing high-quality GRACE gravity models, and for identifying the optimal approach. Necessary refinements of the selected approach may also be needed for routine production of monthly GRACE models.

The secondary goal of the research is to analyze the produced time series of GRACE solutions. The parameters of the global inter-annual water changes and hydrological cycle should be derived. Some important geophysical phe-

nomena, e.g. the ice melting rate in Greenland and Antarctica, should be analyzed. Additionally, the produced solutions should be used to investigate mass re-distribution associated with the co-seismic and post-seismic deformation due to the Sumatra-Andaman earthquake. Furthermore, a comprehensive comparison of the solutions with those produced by other processing centers, such as CSR, GFZ, JPL and CNES is to be conducted with an emphasis on water storage variations in several selected large river basins.

1.3 Outline of the thesis

This thesis comprises seven chapters. Chapter 2 gives a brief overview of techniques for gravity field modeling from SST data. The spherical harmonic representation of the gravity field and the transformation of the gradient of gravitational potential from one frame to another are presented. Next, the precise orbit determination is discussed, since high-precision orbits play a central role in gravity field modeling from CHAMP and GRACE data. A few different methodologies of gravity field modeling, i.e. variational equations, short-arc, energy balance and acceleration approaches, are introduced in order to provide a basis for the further discussion. The emphasis is on the average acceleration approach, since it is extensively used in the further chapters.

Chapter 3 is devoted to gravity field modeling on the basis of CHAMP data. Two refinements on the average acceleration approach are presented. The first one is the development of a new algorithm for computing a smooth and accurate satellite orbit. Such an orbit is an important ingredient for computing a CHAMP model without any CHAMP-based prior information involved. The algorithm is based on B-splines and regularization in the form of acceleration constraints. Simulations and real data processing are carried out. The other refinement is the estimation of noise model from *a posterior* residuals in order to obtain an optimal gravity field solution. The noise model is represented in terms of power spectral density. The simulation and real data processing prove that the noise estimation procedure is a key ingredient of the accurate gravity field modeling. These two refinements are used to compute a regularized CHAMP model and a non-regularized one. A comparison of the computed models with those produced by other research groups confirms a high quality of our models.

Gravity field modeling methodology is extended in chapter 4 to the case of GRACE hl-SST data. In particular, processing the kinematic baselines is discussed. The kinematic positions and baselines of GRACE satellites are processed, both individually and jointly. The obtained results are inter-compared and analyzed.

Chapter 5 focuses on novel methodologies for processing GRACE ll-SST data. The chapter starts from the classical acceleration approach proposed by Rummel [1979], which makes use of range acceleration data and inter-satellite

velocity vectors. Since radial components of inter-satellite velocities in the approach are not accurate enough, no reasonable results can be obtained. After that, a novel approach, namely, the 3RRC approach, is proposed, which explicitly connects a linear combination of gravitational potential gradients with a linear combination of range-rate measurements at three successive epochs. The idea behind this approach is that the radial component of inter-satellite velocities is derived from KBR data themselves. In addition, we propose a new variant of average acceleration approach, i.e. the 3RC approach, in which the functional model connects gravity field parameters with a linear combination of bias-corrected range measurements at three successive epochs without an explicit involvement of inter-satellite velocity vectors at all. The details of data processing are given, and results produced by these three approaches are analyzed. The conclusion is that the 3RC approach produces the best solution compared to the other two approaches. On the basis of the conclusion, a further refinement of the 3RC processing procedure is made. Finally, almost 4 years of GRACE ll-SST data are processed on the monthly basis with the 3RC approach.

A post-processing and analysis of the produced GRACE monthly model is the subject of chapter 6. In particular, the seasonal variations and global inter-annual changes in the Earth's gravity field are derived. The secular mass changes in Greenland and Antarctic are considered in detail. The effects of co-seismic and post-seismic deformation due to the rupture caused by the Sumatra-Andaman earthquake are also discussed in the chapter. Finally, the chapter contains a comparison of our solutions with GRACE solutions produced by some other research institutes as well as with the GLDAS hydrological model. The comparison is focused on the spectral assessment and the differences of water storage changes in large river basins.

Finally, the major findings of the thesis are summarized and recommendations for further researches are given in chapter 7.

Chapter 2

Gravity field modeling from SST data: an overview

2.1 Introduction

This chapter gives an overview of techniques for gravity field modeling from Satellite-to-Satellite Tracking (SST) data with emphasis on the average acceleration approach. The conceptional background and the latest development of methodologies applied in the global gravity field analysis are briefly presented, in order to provide a basis for the research conducted in the thesis.

Section 2.2 gives the mathematical expressions for gravitational potential and geoid as a series of spherical harmonics. The coefficients of the basis functions are the principle parameters to solve for in the thesis. As will be intensively used in the thesis, the expression for mass change, power spectrum and potential gradient are also given in this section. A brief description of related coordinate frames and the rotations among them are given in section 2.3. A high-precision orbit plays a central role in gravity field modeling through being the input data or/and providing precise locations for measurements of other types. Therefore, it is necessary to describe some relevant aspects of precise orbit determination. This is done in section 2.4, which includes three different approaches widely used for determining CHAMP, GRACE and future GOCE satellite orbits, i.e. kinematic, dynamic and reduced-dynamic orbit determination. Moreover, some properties of these types of orbits are analyzed. In section 2.5, we briefly discuss the current strategies of global gravity recovery from the SST data. A few different approaches, i.e. variational equations, short-arc, energy balance and acceleration approaches, are discussed. The basic functional models of these approaches are presented, and the relevant gravity field models produced with these approaches are listed. The advantages and disadvantages of these methodologies are analyzed as well. Section 2.6 describes the inversion of observations into gravity field parameters with a focus on the average acceleration approach. The adopted strategy to obtain the least-squares solution is to perform the inversion iteratively using the preconditioned conjugate gradient method. Besides this, fast synthesis

and co-synthesis as well as the data weighting are briefly explained in the section. The procedure of computing CHAMP acceleration residuals is also described as a platform for further development in the next chapters.

2.2 Gravity field and its functionals

2.2.1 Gravitational potential

The static part of the Earth's *gravitational potential* V at any point P at the Earth's surface is commonly expressed as a series of spherical harmonics (see, e.g. [Heiskanen and Moritz, 1984]):

$$V(r,\vartheta,\lambda) = \frac{GM}{R}\left\{\sum_{l=0}^{\infty}\left(\frac{R}{r}\right)^{l+1}\sum_{m=0}^{l}\left(C_{lm}\cos m\lambda + S_{lm}\sin m\lambda\right)\bar{P}_{lm}(\cos\vartheta)\right\}, \tag{2.1}$$

where r,ϑ,λ are the spherical geocentric coordinates of the computation point: radius, co-latitude and longitude, respectively; GM is the geocentric gravitational constant; R is the semi-major axis of a reference ellipsoid; C_{lm}, S_{lm} are the spherical harmonic (or Stokes') coefficients with l,m being degree and order, respectively; and $\bar{P}_{lm}(\cos\vartheta)$ are the fully normalized associated Legendre functions.

The estimation of degree 0 coefficient is beyond this thesis, since it can not be estimated accurately from the data acquired by the LEO satellites. The degree 1 spherical harmonic coefficients (i.e. C_{10}, C_{11}, S_{11}) are related to the geocenter coordinates and defined in this thesis as 0, due to the assumption that the coordinate system's origin always coincides with the geocenter. These coefficients are not possible to be estimated accurately, even without the assumption. Therefore, the minimum degree $L_{\min}$ is usually set equal to 2 in this thesis.

The spherical harmonic coefficients represent the global structure and irregularities of the Earth's gravity field. Higher degrees correspond to a higher spatial resolution. In reality, the gravity field can not be estimated with unlimited spatial resolution. Therefore, a certain truncation degree needs to be set in the expression equation (2.1). The maximum degree $L_{\max}$ relates to the spatial resolution at the Earth surface as

$$\lambda_{\min} \approx 40000\,\mathrm{km}/(L_{\max}+0.5), \tag{2.2}$$

where $\lambda_{\min}$ is the minimum wavelength of the gravity field features. The $\left(\frac{R}{r}\right)^{l+1}$ term of equation (2.1) reflects the attenuation of the signal with altitude. According to the precision of the available data, the measurement altitude and the aim of gravity field modeling, a reasonable maximum degree can be chosen somewhere between 50 and 70 for the CHAMP hl-SST data, and between 70 and 150 for the GRACE KBR measurements.

It should be mentioned that spherical harmonics are functions with a global support. Therefore, the local signal and erroneous information could be spread over the entire globe. Spherical harmonics may not be a very efficient tool to localize the regional signals. Alternative representations of gravitational potential, which are more suitable for regional signals are spherical radial basis function [Klees et al., 2008] or spherical wavelets [Fengler et al, 2007]. However, this is beyond the scope of this thesis, which is devoted to modeling the gravity field globally.

The goal of the SST data processing is either to improve the estimates of the mean spherical harmonic coefficients, or to compute the time variations of them. It is common practice to subtract the contribution of an *a-priori* mean gravity field model from the observations. The residual observations then reflect the deviations of the true gravity field from the *a-priori* reference model. Inversion of these residuals will result in coefficients of the residual gravity field model, which has to be added to the reference model. Let us introduce the *residual potential* $\Delta V(r, \vartheta, \lambda)$, the spherical harmonic expansion of which then reads

$$\Delta V(r,\vartheta,\lambda) = \frac{GM}{R} \sum_{l=L_{\min}}^{L_{\max}} \left(\frac{R}{r}\right)^{l+1} \sum_{m=0}^{l} \left(\Delta C_{lm} \cos m\lambda + \Delta S_{lm} \sin m\lambda\right) \bar{P}_{lm}(\cos\vartheta) \tag{2.3}$$

with $\Delta C_{lm}, \Delta S_{lm}$ are the corrections (or changes) of individual spherical harmonic coefficients. The number of coefficients N_{coef} in this series expansion is given by

$$N_{\text{coef}} \quad = \quad L_{\max}^2 - L_{\min}^2 + 2L_{\max} + 1. \tag{2.4}$$

By definition, the $S_{l,0}$ terms are zero and therefore are not counted in equation (2.4).

2.2.2 Geoid

The geoid is defined as an equipotential sureface that coincides with the mean sea level. An Earth's gravity field variation can be quantified in terms of geoid height $N(\vartheta, \lambda)$, which is the distance between the geoid and the respective reference ellipsoid. According to the Bruns formula [Heiskanen and Moritz, 1984], the geoid height can be derived from the disturbing potential, which is the difference between the real gravitational potential $V(R, \vartheta, \lambda)$ and the normal gravitational potential $U(R, \vartheta)$:

$$N(\vartheta,\lambda) = \frac{V(R,\vartheta,\lambda) - U(R,\vartheta)}{\gamma(\vartheta,\lambda)}, \tag{2.5}$$

where $\gamma(\vartheta, \lambda)$ denotes the normal gravity at the geoid, which can be approximated by GM/R^2 with a relative accuracy of 0.3%. Let us consider residual geoid heights. The normal gravitational potential $U(R, \vartheta)$, by definition, does not change, and

therefore, the differences in the *geoid heights* are completely determined by the residuals or changes of the gravitational potential, i.e. $\Delta V(R, \vartheta, \lambda)$. Hence, the residuals or changes in geoid heights can also be represented as a series of spherical harmonics:

$$\Delta N(\vartheta, \lambda) = R \sum_{l=L_{\min}}^{L_{\max}} \sum_{m=0}^{l} (\Delta C_{lm} \cos m\lambda + \Delta S_{lm} \sin m\lambda)\, \bar{P}_{lm}(\cos \vartheta). \tag{2.6}$$

This expression is frequently employed in the thesis to compare different models and to analyze the noise or signal behavior of estimated corrections or time-varying models.

2.2.3 Mass change

When working with a time series of spherical harmonic coefficients, for example, monthly solutions from GRACE data, the term *surface mass density* is often used. The variation of surface mass density can also be expanded as a sum of residual spherical harmonics under the assumption that the variation can be attributed to a thin water layer at the Earth's surface (see e.g. [Wahr et al., 1998]):

$$\Delta\sigma(\vartheta, \lambda) = R\rho_w \sum_{l=L_{\min}}^{L_{\max}} \sum_{m=0}^{l} \left(\Delta\check{C}_{lm} \cos m\lambda + \Delta\check{S}_{lm} \sin m\lambda\right) \bar{P}_{lm}(\cos \vartheta), \tag{2.7}$$

where ρ_w is the density of water to make the surface density coefficients $\Delta\check{C}_{lm}$, $\Delta\check{S}_{lm}$ dimensionless. It is assumed to be $1000\,\mathrm{kg/m^3}$. The ratio $\Delta\sigma/\rho_w$ yields the variation in *equivalent water thickness*, which will be often used for the analysis of the solved-for monthly solutions in this thesis. The relation between the surface density coefficients and the gravitational potential ones is given by:

$$\left\{ \begin{array}{c} \Delta\check{C}_{lm} \\ \Delta\check{S}_{lm} \end{array} \right\} = \frac{\rho_{\mathrm{ave}}(2l+1)}{3\rho_w(1+k_l)} \left\{ \begin{array}{c} \Delta C_{lm} \\ \Delta S_{lm} \end{array} \right\}, \tag{2.8}$$

with ρ_{ave} being the average density of the Earth ($5517\,\mathrm{kg/m^3}$) and k_l the degree dependent load Love numbers [Farrell, 1972, Wahr et al., 1998]. The factor $(1+k_l)$ in equation (2.8) takes both the direct mass potential and solid Earth loading deformation potential into account. With equation (2.8), it is easy to derive the variations in surface density $\Delta\sigma(R, \vartheta, \lambda)$ from changes in the potential coefficients

$$\Delta\sigma(\vartheta, \lambda) = \sum_{l=L_{\min}}^{L_{\max}} \sum_{m=0}^{l} (\Delta C_{lm} \cos m\lambda + \Delta S_{lm} \sin m\lambda)\, K_l \bar{P}_{lm}(\cos \vartheta), \tag{2.9}$$

with

$$K_l = \frac{R\rho_{\mathrm{ave}}(2l+1)}{3(1+k_l)}. \tag{2.10}$$

Vice versa, the geoid height changes $\Delta N(\vartheta, \lambda)$ can be determined from the surface density coefficients as

$$\Delta N(\vartheta, \lambda) = R^2 \rho_w \sum_{l=L_{\min}}^{L_{\max}} \sum_{m=0}^{l} \left(\Delta \check{C}_{lm} \cos m\lambda + \Delta \check{S}_{lm} \sin m\lambda \right) \frac{1}{K_l} \bar{P}_{lm}(\cos \vartheta). \quad (2.11)$$

2.2.4 Power spectrum

It is common that a new gravity field solution in terms of potential coefficients (S_{lm} and C_{lm}) is accompanied with their respective standard deviations $\sigma_{C_{lm}}$ and $\sigma_{S_{lm}}$, which are obtained via an error propagation process. The signal degree amplitudes σ_l, i.e. square root of power per degree, can be defined as follows in terms of unitless coefficients as follows:

$$\sigma_l = \sqrt{\sum_{m=0}^{l} (C_{lm}^2 + S_{lm}^2)}, \quad (2.12)$$

and the error degree amplitudes can be similarly defined as:

$$\widehat{\sigma}_l = \sqrt{\sum_{m=0}^{l} (\sigma_{C_{lm}}^2 + \sigma_{S_{lm}}^2)}. \quad (2.13)$$

The signal degree amplitudes can be also computed in terms of geoid heights:

$$\sigma_l(N) = R \cdot \sigma_l, \quad (2.14)$$

and in terms of equivalent water heights:

$$\sigma_l(W) = \frac{R \rho_{\text{ave}} (2l+1)}{3 \rho_w (1 + k_l)} \cdot \sigma_l. \quad (2.15)$$

The corresponding error degree amplitudes can be expressed similarly by replacing σ_l with $\widehat{\sigma}_l$. In some cases, when two different gravity field models are compared, we need to compute the *difference signal degree amplitudes*, in order to see the agreement of two models. In this case, the coefficients of equation (2.12) should be replaced by the differences of coefficients between the two models.

The cumulative amplitudes as a function from minimum to maximum degree represent the power (signal, error, difference) spectrum accumulated over a spectral band from $l_{\min}$ to $l_{\max}$:

$$\sigma_{l_{\min}, l_{\max}} = \sqrt{\sum_{l=l_{\min}}^{l_{\max}} \sigma_l^2}. \quad (2.16)$$

2.2.5 Potential gradient

The focus of the thesis is to connect the satellite acceleration vectors to the gravitational potential gradient. The partial derivatives of the gravitational potential $V(r,\vartheta,\lambda)$ with respect to ϑ,λ,r can be given as:

$$\begin{cases} \dfrac{\partial V}{\partial \vartheta} = & -\dfrac{GM}{R}\displaystyle\sum_{l=L_{\min}}^{L_{\max}}\left(\dfrac{R}{r}\right)^{l+1}\sum_{m=0}^{l}\left\{C_{lm}\cos m\lambda + S_{lm}\sin m\lambda\right\}\bar{P}'_{lm}(\cos\vartheta)\sin\vartheta \\ \dfrac{\partial V}{\partial \lambda} = & \dfrac{GM}{R}\displaystyle\sum_{l=L_{\min}}^{L_{\max}}\left(\dfrac{R}{r}\right)^{l+1}\sum_{m=0}^{l} m\left\{-C_{lm}\sin m\lambda + S_{lm}\cos m\lambda\right\}\bar{P}_{lm}(\cos\vartheta) \\ \dfrac{\partial V}{\partial r} = & -\dfrac{GM}{R^2}\displaystyle\sum_{l=L_{\min}}^{L_{\max}}(l+1)\left(\dfrac{R}{r}\right)^{l+2}\sum_{m=0}^{l}\left\{C_{lm}\cos m\lambda + S_{lm}\sin m\lambda\right\}\bar{P}_{lm}(\cos\vartheta). \end{cases} \tag{2.17}$$

Here, the derivative of $V(r,\vartheta,\lambda)$ with respect to ϑ is a function of the partial derivative of the associated Legendre functions, i.e. P'_{lm}, which can obtained with a recursive formula, see also [Heiskanen and Moritz, 1984],

$$P'_{lm}(\cos\vartheta) = \frac{-l\cos\vartheta P_{lm}(\cos\vartheta) + (l+m)P_{l-1,m}(\cos\vartheta)}{\sin^2\vartheta}. \tag{2.18}$$

It should be mentioned that C_{lm} and S_{lm} in equation (2.17) can be treated as coefficients of either full signal or residual. We do not specifically distinguish them later in the thesis. For example, they are understood as residual ones in the case of building an explicit relationship with the residual satellite accelerations.

2.3 Reference frames and rotation of vectors

The potential gradients, as well as satellite positions and velocities, are computed as vectors in a certain reference frame. Therefore, rotations between different frames are necessary. It is useful to introduce an intermediate coordinate system, i.e. the so-called Geographical Reference Frame (GRF), which is a local right-handed Cartesian frame with the origin at the satellite location. The **x**-axis of the frame is oriented towards the North, the **z**-axis points radially outward, and the **y**-axis to the West, see figure 2.1. The potential gradient vector $\mathbf{a}^{(\mathbf{G})}$ in this frame can be represented in terms of the spherical coordinates:

$$a_x^{(G)} = -\frac{1}{r}\frac{\partial V}{\partial \vartheta}, \qquad a_y^{(G)} = -\frac{1}{r\sin\vartheta}\frac{\partial V}{\partial \lambda}, \qquad a_z^{(G)} = \frac{\partial V}{\partial r}. \tag{2.19}$$

Transformation of the potential gradient vector from GRF into the Terrestrial Reference Frame (TRF), i.e. Earth-Center Earth-Fixed coordinate system, can be performed by a standard rotation

$$\mathbf{a}^{(\mathbf{T})} = \mathbf{R}_{\mathbf{z}}(\pi-\lambda)\,\mathbf{R}_{\mathbf{y}}(\vartheta)\,\mathbf{a}^{(\mathbf{G})}, \tag{2.20}$$

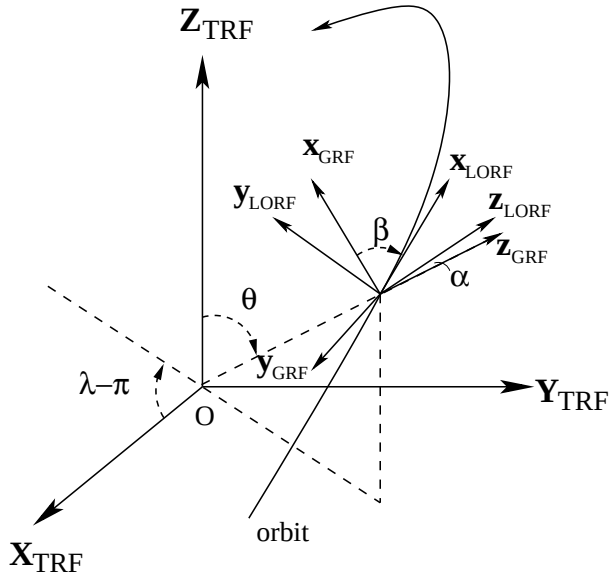

Fig. 2.1. Relations among TRF and GRF, LORF

where $\mathbf{R_y}(\vartheta)$ and $\mathbf{R_z}(\pi - \lambda)$ are 3×3 matrices of elementary rotation through a given angle around the **y**-axis and **z**-axis respectively. The rotation matrix $\mathbf{R}$ represents a relative orientation between two frames when they have a common axis. The new frame can be obtained from the old one by means of an elementary rotation around the common axis [Seeber, 2003]. Furthermore, any rotation matrix has the following property.

$$[\mathbf{R}^{\mathbf{A}\rightarrow\mathbf{B}}]^T = [\mathbf{R}^{\mathbf{A}\rightarrow\mathbf{B}}]^{-1} = [\mathbf{R}^{\mathbf{B}\rightarrow\mathbf{A}}], \tag{2.21}$$

where $\mathbf{A}$ and $\mathbf{B}$ present two coordinate systems, respectively. It is worth mentioning that for any elementary rotation matrix it holds:

$$\mathbf{R}(x)^{-1} = \mathbf{R}(-x), \tag{2.22}$$

with x being the rotation angle.

It may be needed to transform the potential gradient vector from GRF into the so-called Local Orbital Reference Frame (LORF). The frame is defined as follows: the **x**-axis is directed along the track, the **y**-axis coincides with the direction of the orbital angular momentum and the **z**-axis completes the frame to a right-handed one, see figure 2.1. The frame is very often used in this thesis since it offers at least two advantages. It is nearly consistent with the orientation of the on-board accelerometer (CHAMP and GRACE missions). Additionally, a nearly block-diagonal normal matrix can be built up on its basis [Ditmar and van Eck van der Sluijs, 2004]. The transformation is also

implemented by a standard rotation:

$$\mathbf{a}^{(\mathbf{L})} = \mathbf{R}_{\mathbf{y}}(-\alpha)\,\mathbf{R}_{\mathbf{z}}(-\beta)\,\mathbf{a}^{(\mathbf{G})}, \tag{2.23}$$

where β is the azimuth of satellite velocity vector (measured from the North clockwise), and α is the angle between the velocity vector in case of a circular orbit and the actual instantaneous velocity vector of the satellite (measured upwards). Therefore, it is rather simple to convert the gradient of potential from the TRF frame into LORF frame via the intermediate GRF frame:

$$\mathbf{a}^{(\mathbf{L})} = \mathbf{R}_{\mathbf{y}}(-\alpha)\,\mathbf{R}_{\mathbf{z}}(-\beta)\,\mathbf{R}_{\mathbf{y}}(-\vartheta)\mathbf{R}_{\mathbf{z}}(\lambda-\pi)\,\mathbf{a}^{(\mathbf{T})}. \tag{2.24}$$

The transformation between the TRF frame and the Celestial Reference Frame (CRF), i.e. the so-called (quasi-)inertial frame, is also necessary for some computations, e.g. when the input acceleration vectors are derived with numerical differentiation. The transformation matrix at epoch t can be written as (see e.g. [Montenbruck and Gill, 2000] or [McCarthy and Petit, 2003])

$$\mathbf{R}^{(\mathbf{C}\to\mathbf{T})}(t) = \Pi(t)\Theta(t)\mathbf{N}(t)\mathbf{P}(t), \tag{2.25}$$

where $\mathbf{C}$ presents CRF and $\mathbf{T}$ TRF frame, respectively; the rotation matrices $\Pi, \Theta, \mathbf{N}$ and $\mathbf{P}$ describe the coordinate changes due to polar motion, Earth rotation, nutation and precession, respectively. The International Astronomical Union (IAU) conventions adopted some resolutions at the 24th General Assembly to compute each of these matrices with an accuracy of microarcsecond level. The required input for the computation of these matrices, such as polar motion parameters and the UT1-UTC time offsets, can be obtained from the International Earth Rotation Service (IERS).

The non-gravitational measurements are very often provided in a so-called Satellite Body Frame (SBF). To transform the SBF into the CRF, the data from the attitude control system (e.g. a star camera) are used . The rotation angles are expressed in terms of quaternions, which contain a scalar part q_0 and a vectorial part $\mathbf{q}$:

$$q = (q_0, \mathbf{q}) = (q_0, q_1, q_2, q_3). \tag{2.26}$$

The attitude data provided are not as complete as the accelerometer data, since the Sun and the Moon blind the star camera regularly depending on the satellite orbit. Quaternions are very well suited in this case for the description of rotations as they can be interpolated. Other alternative representations of rotations, such as rotation matrices and Euler angles, are not suitable for that purpose. As soon as the quaternions q are known, the corresponding rotation matrix $\mathbf{R}^{(\mathbf{S}\to\mathbf{C})}$ can be easily assembled [Schwintzer et al., 2002] as follows:

$$\mathbf{R}^{(\mathbf{S}\to\mathbf{C})} = \begin{pmatrix} q_0^2+q_1^2-q_2^2-q_3^2 & 2q_1q_2-2q_0q_3 & 2q_1q_3+2q_0q_2 \\ 2q_1q_2+2q_0q_3 & q_0^2-q_1^2+q_2^2-q_3^2 & 2q_2q_3-2q_0q_1 \\ 2q_1q_3-2q_0q_2 & 2q_2q_3-2q_0q_1 & q_0^2-q_1^2-q_2^2+q_3^2 \end{pmatrix}. \tag{2.27}$$

2.4 Precise orbit determination

2.4.1 Relation with gravity field modeling

Precise orbit determination (POD) plays a central role in the context of the dedicated gravity field missions due to at least two reasons. First of all, POD is needed to locate the data, e.g. the KBR observations of the GRACE mission or SGG measurements of the GOCE mission in three-dimension space. Secondly, the orbit is mainly a result of the Earth's gravitation. The combined analysis of orbit data with non-gravitational accelerations, measured by an on-board accelerometer, can be used to model the gravity field.

POD has entered a new era with space geodetic techniques. One of examples is the Satellite Laser Ranging (SLR). The ground-based tracking SLR systems accurately measure distance by determining the two-way travel time of laser pulses transmitted to a satellite and returned by a retro-reflector. An accuracy of several centimeters can be achieved in this way depending on the distance to the satellite and the strength of the returned signal, which therefore allows the orbit of target satellites to be determined. Being applied to dedicated satellites like Starlette and Lagoes, the SLR technique has contributed to the study of geocenter variations and extraction of gravity field coefficients. However, for low-orbiting satellites, a purely ground-based tracking system suffers from a limited number of stations, so that the available tracking measurements cover only a small fraction of the orbit. An alternative positioning concept is offered by the GPS system. Usage of a space-borne GPS receiver allows the data to be collected continuously. Moreover, the GPS measurements can provide a precise time transfer to synchronize time tags of other in-situ measurements, e.g. KBR measurements.

In principle, the POD and gravity field modeling can be done simultaneously using all available measurements collected by dedicated gravity missions, such as (LEO-based and/or ground-based) GPS code and carrier phase data, accelerometer data, KBR range and range-rate data and even ground-based satellite laser ranging data. In Zhu et al. [2004], an integrated adjustment procedure, which is called 'one-step' approach, was proposed to make use of all these data for simultaneous determination of the orbits of GPS and LEO satellites, geocenter variations and gravity field parameters. The criterion for distinguishing one-step and two-step approaches in Zhu et al. [2004] is whether the high attitude GPS orbits are updated altogether with the coefficients of the Earth's gravity field. Although there is a potential to improve the accuracy of the gravity field parameters by using such an integrated adjustment method, the computation burden is high, which makes the approach unpractical. In this thesis, we assume that precise GPS satellite ephemerides and clock products are sufficiently accurate, so that it is not needed to update them in the course of gravity field modeling. Therefore, the one-step method in our definition is an approach when the LEO-based GPS raw measurements are directly used to simultaneously determine the orbit of the LEO satellite and the parameters of

gravity field with GPS satellite positions and clocks being fixed. On the other hand, a two-step approach implies that the orbit of the LEO satellite is firstly determined by using GPS raw observations and is then employed in the second step to form pseudo-observations for gravity field recovery. A similar definition of one-step and two-step methods can be seen in Reubelt et al. [2006] as well.

The LEO satellite orbit can be determined using un-differenced GPS measurements kinematically (not using force models) and dynamically (using force models). In order to compute as accurate as possible the satellite orbit, the determination is very often a compromise between a kinematic approach and a dynamic approach, resulting in a so-called reduced-dynamic orbit determination. It should be mentioned that the LEO orbit of one satellite can be determined with respect to the other one. In this case, differentiated GPS measurements can be used in order to eliminate or reduce common data errors. In relative orbit determination, the absolute orbit of one satellite, serving as the reference, has to be known to the best possible extent. The procedure of relative orbit determination is basically identical to that of the normal POD, with the main difference that the 'relative' parameters are used instead of the 'absolute' ones. For example, the initial state vector is replaced by the initial relative state vector (i.e. baseline and velocity difference).

In section 2.4, the focus is on the (absolute) orbit determination without considering the improvement of gravity field model. However, we will show a hint for further discussion of the one-step approach which is given in section 2.5. The remaining part of section 2.4 describes different orbit determination approaches, including their principles, computation procedures and some analysis of results.

2.4.2 Kinematic orbit determination

The kinematic orbit determination is a straightforward point-wise calculation of the satellite positions from the available GPS observations without an involvement of any force model. The determination is usually done by using the un-differenced ionosphere-free GPS measurements combined with precise orbits of GPS satellites and GPS clock products provided by the International GPS Service (IGS), (see e.g. [Zhao, 2004] and [Kroes, 2006]). At any given epoch t_i, the set of unknown parameters is defined as the phase center position of the GPS receiver antenna and the GPS receiver clock offset, $\mathbf{x_i} = (x_i, y_i, z_i, c\delta t_i)$, with c being the velocity of light. These parameters must be estimated at every epoch since the satellite is continually moving. The total number of these parameters in a single day is 11520 if the sampling rate is 30 seconds. Additionally, the carrier phase measurements contain the term of the ionosphere free ambiguity, such as $b_j = (\lambda_{IF} A_{IF})_j$, with A_{IF} being the ambiguity and λ_{IF} being the wavelength of ionosphere-free carrier phase. The ambiguity remains unchanged over an interval of continuous tracking unless a cycle slip or phase break occurs. The interval is usually not longer than about 40 minutes due to rapid change of relative geometry between LEO and GPS satellites, Therefore, there are about 15 continuous passes with constant ambiguities per day for a

single GPS satellite [Kroes, 2006]. In most cases, the total number of ambiguity parameters over 24 hours is approximately 500. Therefore, the total number of parameters that need to be estimated for a single day is about 12000. The estimation problem is in principle over-determined because an average number of 6 good quality observations (code and carrier phase) are available for each epoch, resulting in 35000 measurements in total. Nevertheless, it is sometimes impossible to avoid large errors in determining high-precision kinematic positions, particularly in the case when measurements contain outliers or cycle slips. Therefore, the data cleaning is a crucial step in the kinematic orbit determination [Zhao et al., 2007]. Nowadays, the accuracy of kinematic orbit determination may reach a few mm [Švehla and Rothacher, 2002, Kroes, 2006, Zhao et al., 2007].

The kinematic POD is preferable for gravity field modeling, because it results in a series of satellite positions that is nearly free from force model assumptions. Evidence is that the noise is almost uncorrelated in time though the variances may vary considerably according to our analysis, see figure 2.2. As far as relatively large noise is concerned, it can be taken into account by a proper stochastic model. However, a kinematic orbit can still contain outliers not removed at the orbit determination phase. The usual way of final cleaning a kinematic orbit from outliers is to compare the kinematically determined position differences between two successive epochs with their counterparts obtained from a dynamic or reduced dynamic orbit. Positions for which the differences exceed a certain threshold are then rejected [Ditmar et al., 2006].

2.4.3 Dynamic orbit determination

Dynamic orbit determination implies that satellite positions are computed arc-by-arc rather than point-by-point. The initial state vector of each arc (together with a few empirical dynamic parameters) has to be estimated as a part of the orbit determination process. The dynamic force models are therefore used to accurately transit the initial state vector in the inertial frame [Montenbruck and Gill, 2000]. The resulting orbit should fit the input data best according to the chosen minimum criterion. In this way, the number of solved-for parameters is dramatically reduced.

Following [Montenbruck and Gill, 2000, Zhao, 2004, Kroes, 2006, Beutler, 2006], the equation of motion of an Earth-orbiting satellite can be described in an inertial frame as:

$$\ddot{\mathbf{r}} := \mathbf{a} = \mathbf{a}_g + \mathbf{a}_t + \mathbf{a}_{ng} + \mathbf{a}_p, \tag{2.28}$$

where $\mathbf{r}$ is the position of the satellite, $\mathbf{a}$ is the total accelerations of the satellite, of which $\mathbf{a}_g$ is the gravitational acceleration on the basis of a static gravity field model, $\mathbf{a}_t$ is the known temporal gravitational acceleration caused by tides, loading effects and atmospherical and oceanic mass variations, $\mathbf{a}_{ng}$ is the non-gravitational accelerations measured by the accelerometers or computed on the basis of non-conservative model, and $\mathbf{a}_p$ is the unmodeled accelerations.

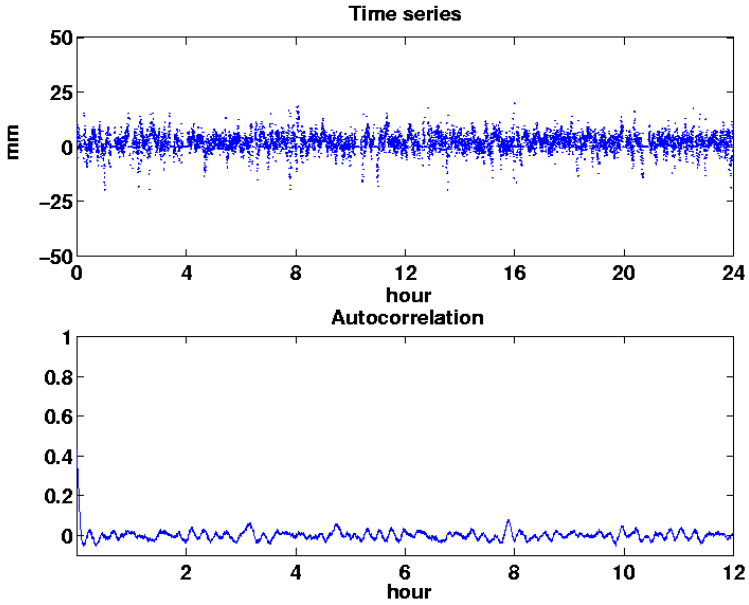

Fig. 2.2. Autocorrelation analysis of noise of kinematic orbit. Time series of differences between the GRACE KBR ranges and the ranges computed from two individual kinematic orbits (top). The noise of KBR ranges is much smaller than orbits, therefore they are ignored. The time series can be thought as noise of kinematic orbits (as a whole, notice of two satellites and three components). The RMS of the time series is less than 4 mm. Autocorrelation coefficients of the time series (bottom), which shows that the positions of kinematic orbits are almost uncorrelated. The computation of auto-correlation coefficients will be described in appendix A. The kinematic orbits used are August 1, 2003 with a sampling of 30 sec. The orbits are provided by [Kroes, 2006]

Let the satellite dynamic parameter vector in the inertial frame be written as

$$\mathbf{x}(t) = \begin{pmatrix} \mathbf{y}(t) \\ \mathbf{p} \end{pmatrix}, \tag{2.29}$$

where $\mathbf{y}(t)$ is the state vector, including the position $\mathbf{r}(t)$ and the velocity $\dot{\mathbf{r}}(t)$ vectors within an arc. Vector $\mathbf{p}$ is the so-called additional dynamic parameter vector in the context of dynamic orbit determination. It includes typically only biases or scaling factors of non-gravitational accelerations. However, the additional dynamic parameter vector may be extended by some other parameters, which will be described in the next sections devoted to reduced-dynamic orbit determination or gravity field modeling with the one-step approach. The initial value at epoch t_0 is expressed as $\mathbf{x}(t_0)$, which is to be estimated. In other words, the first group of parameters to be estimated includes the initial state vector and the additional

dynamic parameters. The first order differential equations of the state vector can be written as:

$$\mathbf{F}(t, \mathbf{y}(t), \mathbf{p}) := \frac{d}{dt}\mathbf{y}(t) = \begin{pmatrix} \dot{\mathbf{r}}(t) \\ \ddot{\mathbf{r}}(t) \end{pmatrix}. \tag{2.30}$$

Furthermore, let us consider another group of parameters to be estimated. Write the measurement vector as $\mathbf{d} = (\mathbf{d}_1, \mathbf{d}_2, \cdots, \mathbf{d}_n)^T$, assuming that the measurements are taken within the arc at times $t_1, t_2, \cdots, t_n$, and that s measurements are collected at each epoch. The observation equation can be written as

$$d_i^s(t_i) = g_i^s(t_i, \mathbf{x}(t_i), \mathbf{z}(t_i)) + \epsilon = h_i^s(t_i, \mathbf{x}(t_0), \mathbf{z}(t_i)) + \epsilon, \tag{2.31}$$

where g_i^s denotes the physical or geometrical relationship at the epoch t_i between the measurements and the parameters. The latter ones include dynamic parameters $\mathbf{x}(t_i)$ and measurement-related parameters $\mathbf{z}(t_i)$ (e.g. GPS receiver clock biases $\mathbf{T}$ and carrier phase ambiguities $\mathbf{B}$). Symbol h_i^s denotes the model value as a function of the state $\mathbf{x}(t_0)$ at the reference epoch t_0. The quantity ϵ accounts for the difference between actual and modeled measurements due to the measurement and modeling errors. The partial of the modeled measurement h_i^s with respect to the clock bias vector can be expressed as:

$$\frac{\partial h_i^s}{\partial \mathbf{T}} = (0, ..., 0, 1_{(i)}, 0, ..., 0). \tag{2.32}$$

The non-zero element is only set for the epoch t_i, and the length of this vector equals the number of epochs n. Similarly, the partial of the carrier phase ambiguities is

$$\frac{\partial h_i^s}{\partial \mathbf{B}} = (0, ..., 0, 1_{(k)}, 0, ..., 0). \tag{2.33}$$

The only non-zero element is for the kth ambiguity relating to the carrier phase measurement from satellite s at epoch t_i. The length of partial vector is the number of ambiguities. For the code measurements, the elements of the partial are not set at all.

A priori LEO positions $\mathbf{x}_0(t)$ are obtained, preliminarily from a GPS code solution or from a rapid orbit provided by other resources. An *a priori* initial state vector $\mathbf{x}(t_0)$ may be computed from this position of data, and the additional dynamic parameters may be set as 0 at the beginning. Dynamic orbit determination can therefore be considered as a procedure to estimate corrections of the dynamic parameters. Apart from the evaluation of the partials with respect to the measurement-related parameters, we have to compute the partials with respect to the initial dynamic parameter vector, i.e.

$$\frac{\partial h_i^s}{\partial \mathbf{x}(t_0)} = \left(\frac{\partial h_i^s}{\partial \mathbf{y}(t_0)} \quad \frac{\partial h_i^s}{\partial \mathbf{p}} \right) = \left(\frac{\partial h_i^s}{\partial \mathbf{y}(t_i)} \frac{\partial \mathbf{y}(t_i)}{\partial \mathbf{y}(t_0)} \quad \frac{\partial h_i^s}{\partial \mathbf{y}(t_i)} \frac{\partial \mathbf{y}(t_i)}{\partial \mathbf{p}} \right). \tag{2.34}$$

Equation (2.34) can be re-arranged as:

$$\frac{\partial h_i^s}{\partial \mathbf{x}(t_0)} = \left(\frac{\partial h_i^s}{\partial \mathbf{y}(t_i)} \Phi(t_i, t_0) \quad \frac{\partial h_i^s}{\partial \mathbf{y}(t_i)} \mathbf{S}(t_i) \right), \tag{2.35}$$

where

$$\Phi(t_i, t_0) = \frac{\partial \mathbf{y}(t_i)}{\partial \mathbf{y}(t_0)}, \tag{2.36}$$

which is the so-called state transition matrix, and

$$\mathbf{S}(t_i) = \frac{\partial \mathbf{y}(t_i)}{\partial \mathbf{p}}, \tag{2.37}$$

which is the so-called sensitivity matrix. The first element on the right-hand side of equation (2.35) presents the measurement-related partials with respect to the current satellite state vector, which differs according to the types of measurements. For example, the partials of the GPS measurements with respect to the current satellite state vector are given as:

$$\frac{\partial h_i^s}{\partial \mathbf{y}(t_i)} = \left(\frac{\partial h_i^s}{\partial \mathbf{r}(t_i)} \quad \frac{\partial h_i^s}{\partial \dot{\mathbf{r}}(t_i)} \right) = \left(-(\mathbf{e}^s(t_i))^T \quad \mathbf{0}_{1\times 3} \right), \tag{2.38}$$

where $\mathbf{e}^s(t_i)$ is the unit vector of the line of sight between the LEO satellite and the individual GPS satellite s in the inertial frame.

The state transition matrix can be obtained by differentiating equation (2.30) with respect to the initial state:

$$\frac{\partial}{\partial \mathbf{y}(t_0)} \frac{d}{dt} \mathbf{y}(t) = \frac{\partial \mathbf{F}(t, \mathbf{y}(t), \mathbf{p})}{\partial \mathbf{y}(t_0)} = \frac{\partial \mathbf{F}(t, \mathbf{y}(t), \mathbf{p})}{\partial \mathbf{y}(t)} \cdot \frac{\partial \mathbf{y}(t)}{\partial \mathbf{y}(t_0)}. \tag{2.39}$$

The order of the partial derivatives in the left-hand side can be inter-changed, so that we have

$$\frac{d}{dt} \frac{\partial \mathbf{y}(t)}{\partial \mathbf{y}(t_0)} = \frac{d}{dt} \Phi(t, t_0) = \frac{\partial \mathbf{F}(t, \mathbf{y}(t), \mathbf{p})}{\partial \mathbf{y}(t)} \cdot \Phi(t, t_0), \tag{2.40}$$

with

$$\frac{\partial \mathbf{F}(t, \mathbf{y}(t), \mathbf{p})}{\partial \mathbf{y}(t)} = \begin{pmatrix} \mathbf{0}_{3\times 3} & \mathbf{I}_{3\times 3} \\ \dfrac{\partial \ddot{\mathbf{r}}(t)}{\partial \mathbf{r}(t)} & \dfrac{\partial \ddot{\mathbf{r}}(t)}{\partial \dot{\mathbf{r}}(t)} \end{pmatrix}_{6\times 6}. \tag{2.41}$$

Equation (2.40) is a first order differential equation with the identity matrix as the initial value, $\Phi(t_0, t_0) = \mathbf{I}_{6\times 6}$. In a similar way the sensitivity matrix can be obtained by differentiation equation (2.30) with respect to the additional dynamic parameters:

$$\frac{\partial}{\partial \mathbf{p}} \frac{d}{dt} \mathbf{y}(t) = \frac{\partial \mathbf{F}(t, \mathbf{y}(t), \mathbf{p})}{\partial \mathbf{y}(t)} \cdot \frac{\partial \mathbf{y}(t)}{\partial \mathbf{p}} + \frac{\partial \mathbf{F}(t, \mathbf{y}(t), \mathbf{p})}{\partial \mathbf{p}}. \tag{2.42}$$

Therefore, the first order differential equations of equation (2.37) can be specifically written as

$$\frac{d}{dt}\mathbf{S}(t) = \begin{pmatrix} \mathbf{0}_{3\times3} & \mathbf{I}_{3\times3} \\ \dfrac{\partial\ddot{\mathbf{r}}(t)}{\partial\mathbf{r}(t)} & \dfrac{\partial\ddot{\mathbf{r}}(t)}{\partial\dot{\mathbf{r}}(t)} \end{pmatrix}_{6\times6} \cdot \mathbf{S}(t) + \begin{pmatrix} \mathbf{0}_{3\times n_p} \\ \dfrac{\partial\ddot{\mathbf{r}}(t)}{\partial\mathbf{p}} \end{pmatrix}_{6\times(6+n_p)}, \tag{2.43}$$

where the initial values of the elements of the sensitivity matrix are zero since the initial state vector does not depend on the additional dynamic parameters. Equations (2.40) and (2.43) can be combined as the so-called variational equations:

$$\frac{d}{dt}(\Phi,\mathbf{S}) = \begin{pmatrix} \mathbf{0}_{3\times3} & \mathbf{I}_{3\times3} \\ \dfrac{\partial\ddot{\mathbf{r}}(t)}{\partial\mathbf{r}(t)} & \dfrac{\partial\ddot{\mathbf{r}}(t)}{\partial\dot{\mathbf{r}}(t)} \end{pmatrix}_{6\times6} \cdot(\Phi,\mathbf{S}) + \begin{pmatrix} \mathbf{0}_{3\times6} & \mathbf{0}_{3\times n_p} \\ \mathbf{0}_{3\times6} & \dfrac{\partial\ddot{\mathbf{r}}(t)}{\partial\mathbf{p}} \end{pmatrix}_{6\times(6+n_p)}, \tag{2.44}$$

which is suitable and adequate for use with numerical integration methods to evaluate the solution of the first order initial value problem. Within the orbit determination process the variational equations are integrated simultaneously with satellite trajectory. As far as the latter procedure is concerned, accurate force models including known temporal gravity field variations are needed to compute the satellite accelerations, see e.g. chapter 3 of [Montenbruck and Gill, 2000]. Furthermore, the variational equations depend on the partial derivatives of the acceleration with respect to the state vector and the dynamic parameters. How to compute these elements can be found in detail in chapter 7 of [Montenbruck and Gill, 2000].

From the estimated initial dynamic parameters and the accurate background force models, position at any given epoch along the orbit can be computed. The dynamic orbit is relatively smooth, therefore positioning errors are highly time-correlated compared with the kinematic orbit, see figures (2.2) and (2.3). The dynamic orbit depends on the background force models and positions are strongly correlated in time. Therefore, an orbit of this type can not be taken as a set of observations for later gravity field recovery. However, it can be used to compute reference values that are subtracted from the observations (e.g. KBR measurements or kinematic positions). It should be noticed that there are homogeneous solution and resonance effects in the the dynamic orbit caused by errors in the estimated initial state vector and in the zonal coefficients of the background gravity field. As can be seen from figure 2.3, these effects mostly map into a one-cycle-per-revolution (cpr) pattern. These effects should be carefully considered when the orbit is taken as the reference value [Visser, 2005].

2.4.4 Reduced-dynamic orbit determination

As we discussed in the previous sections, a purely kinematic orbit is sensitive to erroneous measurements and data gaps, while the purely dynamic POD results

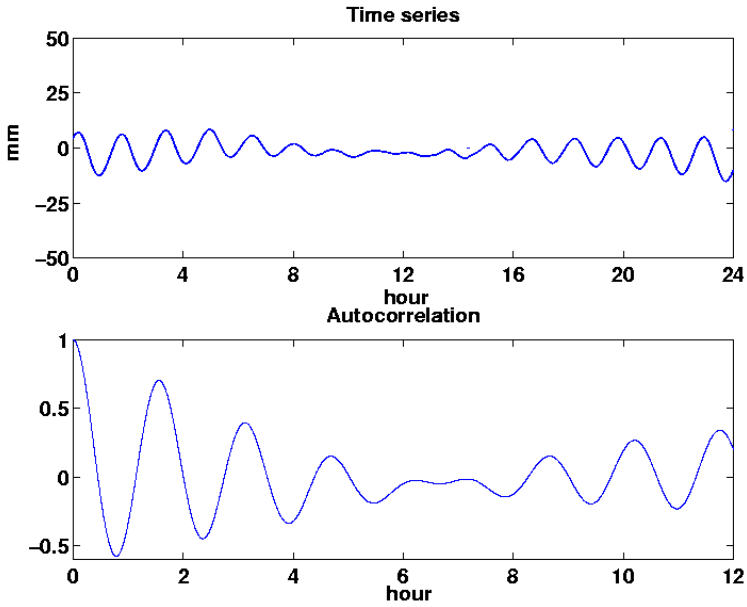

Fig. 2.3. Autocorrelation analysis of the noise (or error) of a purely dynamic orbit. Time series of differences between the GRACE KBR ranges and the ranges computed from two individual dynamic orbits (top). The RMS of the time series is 5 mm. Autocorrelation coefficients of the time series (bottom). The dynamic orbits used are August 1, 2003 with a sampling of 30 sec. The orbits are computed by the PANDA software for August 1, 2003 [Zhao et al., 2007].

in robust continuous positions even within data gaps, but depends on the force models. However, the forces acting on a LEO satellite are hardly known *a priori* with the accuracy matching the accuracy level of GPS measurements. Due to these drawbacks of both kinematic and dynamic orbits, the POD is very often performed with the reduced-dynamic approach. In this approach, the additional dynamic parameters $\mathbf{p}$ in equation (2.29) are extended in order to absorb a priori model errors or any other model deficiency. There are, in general, two ways to take additional empirical parameters into account: instantaneous velocity changes and empirical accelerations.

2.4.4.1 Instantaneous velocity changes

The concept of instantaneous velocity changes, or pulses, was introduced as empirical parameters by [Beutler et al, 1994] to improve the orbit quality of the GPS satellites. Such a concept is also useful for reduced-dynamic POD of LEO satellites since the parameters can be set up efficiently [Jäggi et al., 2006]. Assume that a vector of pulses $\mathbf{p}_v$ in three components is taken as a part of dynamic parameters

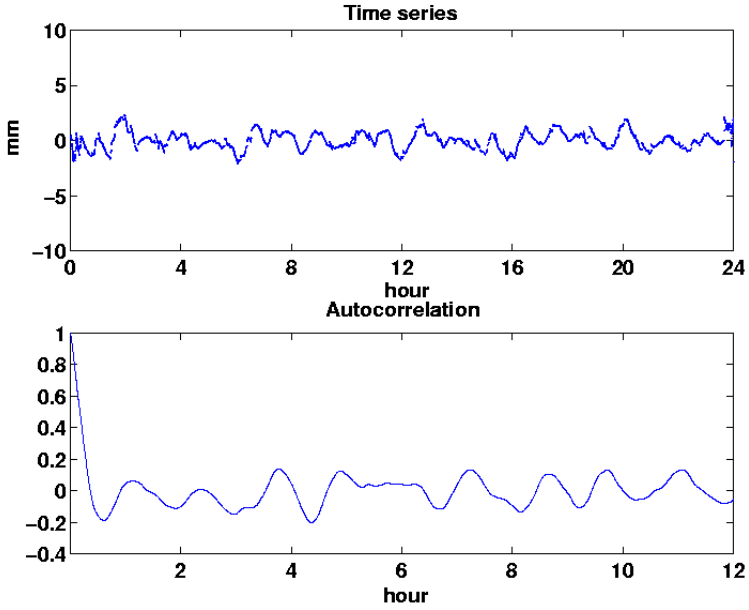

Fig. 2.4. Autocorrelation analysis of noise of reduced-dynamic orbit. Time series of differences between the GRACE KBR ranges and the ranges computed from reduced-dynamic baselines (top). The RMS of the time series is 0.7 mm. Autocorrelation coefficients of the time series (bottom). The reduced-dynamic baselines used are August 1, 2003 with a sampling of 10 sec. The baselines are provided by [Kroes, 2006]

$\mathbf{p}$ for a pre-defined sub-interval $[t_j, t_{j+n_v})$, with n_v being the number of epochs of the sub-interval. The pulses at three directions are characterized by velocities $\mathbf{v}_j$ introduced at time t_j with the pre-determined matrix $\mathbf{E}(t_j)$ (formed by unit vectors of radial, along-track and cross-track directions). The contribution of $\mathbf{p}_v$ in $\ddot{\mathbf{r}}(t)$ may formally be written as $\delta(t-t_j)\cdot\mathbf{v}_j^T\cdot\mathbf{E}(t)$, where $\delta(\cdot)$ denotes Dirac's delta distribution and $\mathbf{E}(t)$ is the rotation matrix (from Earth centered frame to local reference frame) at the epoch t [Jäggi et al., 2006]. The corresponding element of variational equations in equation (2.44) reads:

$$\frac{\partial\ddot{\mathbf{r}}(t)}{\partial\mathbf{p}_v} = \delta(t-t_j)\cdot\mathbf{E}(t). \tag{2.45}$$

A reasonable choice of interval length of pulses is $6-15$ minutes. The approach using instantaneous velocity changes, resulting in precise reduced-dynamic orbits, are widely used by the gravity field community [Švehla and Rothacher, 2002], [Beutler, 2005] and [Jäggi et al., 2006]. A drawback is that the resulting orbit $\mathbf{r}(t)$ is continuous in the entire interval, but the velocities $\dot{\mathbf{r}}(t)$ are discontinuous at the epochs of introduced changes.

2.4.4.2 Empirical accelerations

In order to overcome the disadvantages of instantaneous velocity changes, empirical accelerations are usually introduced as piecewise constants $\mathbf{a}$ with the predetermined directions $\mathbf{E}(t_j)$ in a pre-defined sub-interval $[t_j, t_{j+n_a})$, with n_a being the number of epochs of the sub-interval. The contribution of the vector of empirical acceleration $\mathbf{p}_a$ in $\ddot{\mathbf{r}}(t)$ can be written as $\mathbf{a}^T \cdot \mathbf{E}(t)$ in the designated time interval. The corresponding element of variational equations in equation (2.44) reads:

$$\frac{\partial \ddot{\mathbf{r}}(t)}{\partial \mathbf{p}_a} = \begin{cases} \mathbf{E}(t); & t \in [t_j \quad t_{j+n_a}) \\ \mathbf{0}; & \text{otherwise} \end{cases} \tag{2.46}$$

Experiments show that empirical accelerations can absorb the unmodeled signal efficiently, see [Zhao, 2004] and [Kroes, 2006]. A reasonable choice of interval length is roughly 10 minutes, which compromises the computation efficiency and the capability of absorbing unmodeled errors. A drawback of this type of orbit is that the accelerations $\ddot{\mathbf{r}}(t)$ is not differentiable at the epoch t_j. There are a few extended researches to handle the drawback by using piecewise linear accelerations, refer to [Jäggi et al., 2006] and [Kroes, 2006] for details.

The accuracy of a reduced-dynamic orbit (or relative orbit) is higher than that of a purely dynamic orbit and the auto-correlation errors are reduced, see figure 2.4. The price to be paid is a reduction of the smoothness. The orbit is not advisable as a set of data for gravity field recovery, because one cannot expect that these empirical parameters preserve all characteristics of the gravity field, i.e. loss of information, is practically inevitable.

2.5 Approaches to gravity field modeling

As we discussed before, raw GPS measurements can be directly employed to recover the gravity field model by using the one-step approach, see section 2.4.1. In the approach, the coefficients of gravity field are included into the parameters of dynamic POD. This will be further discussed in this section on the basis of equation (2.44). On the other hand, we prefer the two-step approach in the thesis, i.e. taking the POD results as input data, for gravity field modeling. The main reason is that the number of GPS measurements is an order of magnitude larger than the number of LEO positions. Therefore, the computation of partials of those GPS measurements with respect to gravity field parameters is relatively time-consuming. In addition, GPS measurements, besides unavoidable observation noise, may contain errors due to unresolved ambiguities, multipath effects or temporary malfunction of the receiver. These errors could influence the results of gravity field modeling considerably. It is therefore necessary that these influences are removed as much as possible before inversion of the data is carried out.

If the techniques of recovery of gravity field parameters from satellite tracking data are classified according to the physical or geometrical relations between

the parameters and measurements, two physical laws are of importance: (1) the energy conservation law and (2) Newton's second law of motion. Based on these laws, there are roughly four different approaches to link precise satellite data to the Earth's gravity field. The variational equation approach, being one of them, can be one-step or two-step. Other approaches make use of orbits of the satellites rather than GPS raw measurements directly, therefore they are classified as two-step approaches. In the following, the corresponding functional models and latest results are described as well as the advantages and disadvantages of different approaches.

2.5.1 Variational equations approach

2.5.1.1 One-step

The traditional approach to determine gravity field parameters from satellite-to-satellite tracking data can be combined with the dynamic orbit determination discussed in section 2.4.3. In this case, the dynamic parameters $\mathbf{p}$ are extended to the Stokes coefficients C_{lm} and S_{lm}, rather than empirical accelerations or velocity pulses, for absorbing the unmodeled signals. The relation between these coefficients and hl-SST and/or ll-SST measurements is not linear. Therefore, linearization and iterations are necessary steps. The partials of measurements to the Stokes coefficients must be integrated via the variational equations. With the chain rule of differentiation, the term $\frac{\partial \ddot{\mathbf{r}}(t)}{\partial \mathbf{p}_0}$ in equation (2.44) turns into :

$$\frac{\partial \ddot{\mathbf{r}}(t)}{\partial \mathbf{p}} = \begin{pmatrix} \frac{\partial}{\partial C_{lm}}(\frac{\partial V}{\partial \mathbf{r}(\mathbf{t})}) \\ \\ \frac{\partial}{\partial S_{lm}}(\frac{\partial V}{\partial \mathbf{r}(\mathbf{t})}) \end{pmatrix} = \begin{pmatrix} \frac{\partial}{\partial \mathbf{r}(\mathbf{t})}(\frac{\partial V}{\partial C_{lm}}) \\ \\ \frac{\partial}{\partial \mathbf{r}(\mathbf{t})}(\frac{\partial V}{\partial S_{lm}}) \end{pmatrix} \tag{2.47}$$

where

$$\frac{\partial V}{\partial C_{lm}} = \frac{GM}{R}\left(\frac{R}{r}\right)^{l+1} \bar{P}_{lm}(\cos\vartheta)\cos m\lambda, \tag{2.48}$$

and

$$\frac{\partial V}{\partial S_{lm}} = \frac{GM}{R}\left(\frac{R}{r}\right)^{l+1} \bar{P}_{lm}(\cos\vartheta)\sin m\lambda. \tag{2.49}$$

In this way, the partials of the orbit to Stokes coefficients can be numerically integrated altogether with the partials to the initial state vector. However, this dramatically increases the computation burden and memory with the increase of maximum degree of the coefficients under consideration, in particular when incorporating different types of measurements.

In addition, the measurement-related partials, i.e. $\frac{\partial h_i^s}{\partial \mathbf{y}(t)}$, should be considered. In the one-step approach, the elements of $\frac{\partial h_i^s}{\partial \mathbf{y}(t)}$ for GPS measurements has

been given in equation (2.38). If there are KBR measurements available, e.g. the ranges ρ and range-rates $\dot{\rho}$, we have to consider the measurement partials with respect to the state vectors of two satellites. These partials of the leading satellite can be written for range measurements as:

$$\frac{\partial \rho_i}{\partial \mathbf{y}(t)} = \left(\frac{\partial \rho_i}{\partial \mathbf{r}(t)} \quad \frac{\partial \rho_i}{\partial \dot{\mathbf{r}}(t)} \right) = \left(-(\mathbf{e}_{AB}(t))^T \quad \mathbf{0}_{1\times 3} \right), \tag{2.50}$$

where $\mathbf{e}_{AB}(t)$ is the LOS unit vector of two GRACE satellites. The partials of the trailing satellite is the same as ones of the leading satellite, but with opposite sign. For the case of range-rates, these partials for the leading satellite can be written as:

$$\frac{\partial \dot{\rho}_i}{\partial \mathbf{y}(t)} = \left(\frac{\partial \dot{\rho}_i}{\partial \mathbf{r}(t)} \quad \frac{\partial \dot{\rho}_i}{\partial \dot{\mathbf{r}}(t)} \right) = \left(-\frac{1}{\rho} \left(\dot{\mathbf{r}}_{AB}(t) - \dot{\rho}\mathbf{e}_{AB}(t) \right)^T \quad - (\mathbf{e}_{AB}(t))^T \right) \tag{2.51}$$

where $\dot{\mathbf{r}}_{AB}(t)$ is relative velocity vector. Again, the partials for the trailing satellite are identical up to the sign.

In the one-step approach, a nominal orbit has to be computed firstly on the basis of a suite of background mean and time-variable Earth gravity field models. No attempt is made to reduce the effect of unmodeled signals and model error. Therefore, the total effect of these signals and errors will be included in the dynamic orbit. The nominal orbit is then used to compute the nominal hl-SST and/or ll-SST measurements. The resulting differences between the real measurements and the nominal ones can then be used to estimate the corrections to the background gravity field model. This procedure is repeated until the corrections to the gravity field parameters are negligible. In practice, the satellite orbit is normally split into arcs. One initial state vector has to be estimated for each arc. The length of a nominal arc is selected as a compromise between the need for a short arc in order to prevent an increase of the unmodelled errors (e.g. linearization error), and a longer arc to reduce the number of unknowns. The admissible length of the orbital arc is mostly determined by the quality of the background gravity field model, e.g. $6-24$ hours.

A number of gravity field models were directly computed from CHAMP GPS measurements by the one-step approach [Reigber et al., 2002, Reigber et al., 2003]. The last model in this series is called EIGEN-CHAMP03S [Reigber et al., 2005a]. The GGM and EIGEN series of static models based on GRACE KBR data as well as the corresponding monthly models are also computed by this method [Tapley et al., 2004], [Reigber et al., 2005b], [Förste et al., 2006] and [Biancale et al., 2005]. The most recent and widely used are GGM02 [Tapley et al., 2005] and EIGEN-GL04C [Förste et al., 2007].

2.5.1.2 Two-step

The two-step variational equations approach defined here is similar to the traditional one-step approach. The main difference is that the approach determines

gravity field parameters from high precision satellite orbits (plus KBR measurements in GRACE case) rather than from raw GPS measurements. High-precision (preferably kinematic) orbits should be computed beforehand. In this approach, the partials of orbit to the Stokes coefficients are computed exactly in the same as in equation (2.47), but the measurement-related partials, i.e. $\frac{\partial h_i^s}{\partial \mathbf{r}(t)}$, are different. Taking the existing orbit as input data, $\mathbf{e}^s(t)$ in equation (2.38) is replaced by a unit matrix, since the measurement h_i^s taken here is position itself (three components).

A drawback of the variational equation approach is high computation costs even if the input is defined as a kinematic orbit. This is because for every iteration, orbit integration and integration of the variational equations have to be performed and the least-squares solution for the variational parameter corrections needs to be calculated. Furthermore, an additional initial state vector has to be estimated for every arc.

2.5.2 Short arc approach

The short-arc approach is similar to the variational equations approach in the sense that the positions (or range measurements) are defined as observations directly. The approach is based on Newton's equation of motion formulated as a boundary value problem in the form of a Fredholm-type integral equation. Consider an orbit arc that spans the time interval $[t_P, t_Q], t_P < t_Q$. Let the satellite positions at two boundaries of the arc be $\mathbf{r}(t_P)$ and $\mathbf{r}(t_Q)$, respectively. According to [Mayer-Gürr et al., 2005, Mayer-Gürr, 2006], it can be shown that the position at any time $t \in [t_P; t_Q]$ is equal to:

$$\mathbf{r}(\tau) = (1-\tau)\mathbf{r}(t_P) + \tau\mathbf{r}(t_Q) - (t_Q - t_P)^2 \int_{\tau'=0}^{1} K(\tau,\tau')\ddot{\mathbf{r}}(\tau')d\tau', \tag{2.52}$$

where τ is the normalized time: $\tau := \frac{t-t_P}{t_Q-t_P}$, and the kernel function $K(\tau,\tau')$ is:

$$K(\tau,\tau') := \begin{cases} \tau'(1-\tau) & \text{if} \quad \tau' \leq \tau \\ \tau(1-\tau') & \text{if} \quad \tau' > \tau'. \end{cases} \tag{2.53}$$

In the short arc approach, equation (2.52) is used for the processing of precise kinematic orbit. The positions $\mathbf{r}(\tau)$ are the observed quantities.

For the GRACE mission, the precise inter-satellite range and range-rate measurements are available. The functional model, e.g. for range observations, can be derived by projecting the baseline vector onto the LOS direction:

$$\rho(\tau) = \mathbf{e}_{AB} \cdot (\mathbf{r}_B(\tau) - \mathbf{r}_A(\tau)). \tag{2.54}$$

Again, the subscripts "A" and "B" correspond to the two satellites, respectively. Similar to the variational equations approach, the partials of the range measure-

ment with respect to the Stokes coefficients can be written as:

$$\frac{\partial \rho(\tau)}{\partial \mathbf{p}} = \frac{\partial \rho(\tau)}{\partial \mathbf{r}(\tau)} \cdot \frac{\partial \mathbf{r}(\tau)}{\partial \ddot{\mathbf{r}}(\tau)} \cdot \frac{\partial \ddot{\mathbf{r}}(\tau)}{\partial \mathbf{p}}. \tag{2.55}$$

The first term at the right hand side can be referred to equation (2.50), and the second term can be derived from equation (2.52). Equation (2.47) can be used for the third term. These terms are individually computed for the two satellites. To compute the elements of the second term, a procedure of the so-called numerical quadrature is used, instead of integration of variation equations [Mayer-Gürr et al., 2005]. Another feature of the approach is that the length of an individual satellite arc is usually chosen to be not very long, e.g. 30 minutes [Mayer-Gürr et al., 2005]. In this way, the accumulation of model errors (e.g. linearization error and resonance effects) can be controlled. However, the positions at two boundaries of the arc $\mathbf{r}_A$ and $\mathbf{r}_B$ should be adjusted together with gravity field parameters, which may increase the computation costs.

The short-arc approach has been used successfully to derive the series of ITG-CHAMP01 models from CHAMP kinematic orbit [Mayer-Gürr et al., 2005] and the high-precision ITG-GRACE series of models from GRACE KBR data [Mayer-Gürr, 2006, Mayer-Gürr et al., 2006].

2.5.3 Energy balance approach

The energy balance approach is based on the energy conservation law. According to the law, the sum of kinetic and potential energy of a satellite (or a satellite constellation) must be constant, if it is only subject to conservative static forces. In reality, non-conservative forces like atmospheric drag, solar radiation pressure, etc. also influence the motion of the satellites whereas the gravitational field experiences temporal variations. The energy subsequently accumulated or dissipated needs to be accounted for in order to conserve total energy. Hence, the conservation of energy of one satellite can be written in an inertial frame as:

$$E_{\text{kin}} + E_{\text{pot}} - \Delta E_{\text{rot}} - E_{\text{ng}} = \text{C}, \tag{2.56}$$

where all the quantities are given per unit mass; E_{kin} and E_{pot} represent the kinetic and potential energy, respectively; E_{ng} is the energy accumulated or dissipated due to the non-conservative forces (i.e. non-gravitational accelerations), which are measured by on-board accelerometers; ΔE_{rot} is the so-called 'potential rotation', accounting for temporal variations of the gravitational potential at a given point in the inertial frame; C is an unknown constant value.

In an inertial reference system, the kinetic energy of the satellite is defined by

$$E_{\text{kin}} = \frac{\| \dot{\mathbf{r}}(t) \|^2}{2}, \tag{2.57}$$

where $\dot{\mathbf{r}}(t)$ is the velocity vector, and $\| \cdot \|$ the norm operator. The potential energy in the Earth's gravitational field is equal to:

$$E_{\text{pot}} = -V(\mathbf{r}(t), t). \tag{2.58}$$

The temporal variations of the gravitational potential at the satellite locations, i.e. ΔE_{rot}, can be written as:

$$E_{\text{rot}} = -\int_{t_0}^{t} \frac{\partial V(\mathbf{r}(t), t)}{\partial t} dt, \tag{2.59}$$

where t_0 is the reference epoch, usually the beginning of the orbital arc. According to [Jekeli, 1999], this term is primarily caused by the rotation of the Earth, and can be approximately given by:

$$\int_{t_0}^{t} \frac{\partial V(\mathbf{r}(t), t)}{\partial t} dt \approx \omega_e (r_x(t)\dot{r}_y(t) - r_y(t)\dot{r}_x(t)), \tag{2.60}$$

where ω_e is the Earth's rotation rate, which is assumed constant to be 7.292115×10^{-5} rad/s; $\mathbf{r}(t) = (r_x(t), r_y(t), r_z(t))$ and $\dot{\mathbf{r}}(t) = (\dot{r}_x(t), \dot{r}_y(t), \dot{r}_z(t))$. Strictly speaking, the temporal variations of the gravitational potential due to tides, loading effects and other geodynamic phenomena should be included here for the computation of the term of E_{rot}. However, in practice, their effects are largely absorbed by bias or low-order polynomial parameters used to remove an along-track instrumental bias of accelerometer in real data processing [Kusche and Ditmar, personal communication, September 25, 2008]. It should be mentioned that all time variations of the gravitational potential must also be taken into account in the term E_{pot} [Han, 2003].

Considering the non-gravitational forces, their work at an elementary path $d\mathbf{s} = \dot{\mathbf{r}}(t)dt$ is

$$dE_{\text{ng}} = \mathbf{a}_{\text{ng}}(t) \cdot \dot{\mathbf{r}}(t) dt. \tag{2.61}$$

Hence, the work at the time interval $[t_0, t]$ is

$$E_{\text{ng}} = \int_{t_0}^{t} \mathbf{a}_{\text{ng}}(t) \cdot \dot{\mathbf{r}}(t) dt. \tag{2.62}$$

Obviously, this term depends on non-gravitational forces at all epochs since the epoch t_0.

On the basis of equations (2.56)-(2.62), the gravitational potential in the inertial frame can be finally computed as follows:

$$V(\mathbf{r}(t), t) = \frac{\| \dot{\mathbf{r}}(t) \|^2}{2} + \omega_e (r_x(t)\dot{r}_y(t) - r_y(t)\dot{r}_x(t)) - \int_{t_0}^{t} \mathbf{a}_{\text{ng}}(t) \cdot \dot{\mathbf{r}}(t) dt - C \tag{2.63}$$

Thus, the energy balance approach results in a functional model that virtually connects the squared magnitude of the satellite's velocity linearly to the gravitational potential. The satellite velocities, thought as pseudo-observations, are usually obtained by numerical differentiation of the precise orbit positions (we leave numerical differentiation to be discussed in next section). The unknown constant C can be absorbed as an empirical parameter accounting for the bias, which may be estimated once per an orbital arc or within a successive measuring period of non-gravitational accelerations.

In the GRACE case, it is possible to link the observed range-rates to the inter-satellite gravitational potential differences. Let us write the functional model of the energy conservation law for satellites A and B:

$$\begin{cases} V_A = E_{\mathrm{kin},A} - E_{\mathrm{rot},A} - E_{\mathrm{ng},A} - C_A \\ V_B = E_{\mathrm{kin},B} - E_{\mathrm{rot},B} - E_{\mathrm{ng},B} - C_B \end{cases} \tag{2.64}$$

where (t) is not shown for the brevity. By subtracting the first equation from the second one, we obtain:

$$V_{AB} := V_B - V_A = E_{\mathrm{kin},AB} - E_{\mathrm{rot},AB} - E_{\mathrm{ng},AB} - C_{AB} \tag{2.65}$$

where the subscript "AB" denotes the difference between the corresponding quantities with subscripts "B" and "A". The kinetic energy difference can be written as:

$$E_{\mathrm{kin},AB} = \frac{1}{2}\left(\parallel \dot{\mathbf{r}}_B \parallel^2 - \parallel \dot{\mathbf{r}}_A \parallel^2\right) = \frac{1}{2}\left(\dot{\mathbf{r}}_B + \dot{\mathbf{r}}_A\right)^T \dot{\mathbf{r}}_{AB}, \tag{2.66}$$

where $\dot{\mathbf{r}}_{AB}$ is the relative velocity of two satellites. The relative position of two GRACE satellites $\mathbf{r}_{AB}$ can be connected with the range measurement ρ as:

$$\mathbf{r}_{AB} = \rho \mathbf{e}_{AB}, \tag{2.67}$$

where $\mathbf{e}_{AB}$ is the LOS unit vector pointing from satellite A to satellite B. Taking the derivative, we split the relative velocity vector into the along-track part and the orthogonal part:

$$\dot{\mathbf{r}}_{AB} = \dot{\rho}\mathbf{e}_{AB} + \rho\dot{\mathbf{e}}_{AB}, \tag{2.68}$$

where $\dot{\rho}$ is the so-called range-rate and $\dot{\mathbf{e}}_{AB}$ is the time derivative of unit vector of LOS. Inserting equation (2.68) into equation (2.66) results in:

$$E_{\mathrm{kin,AB}} = \frac{1}{2}\left(\dot{\rho}\left(\dot{\mathbf{r}}_B + \dot{\mathbf{r}}_A\right)^T \mathbf{e}_{AB} + \rho\left(\dot{\mathbf{r}}_B + \dot{\mathbf{r}}_A\right)^T \dot{\mathbf{e}}_{AB}\right). \tag{2.69}$$

Therefore, the kinetic energy difference can be linked with the KBR measurements. In principle, this relationship allows the observed range-rates to be converted into inter-satellite potential differences, with a subsequent determination of gravity field parameters by means of a least-squares adjustment.

The energy balance approach is more numerically efficient than the variational equations approach. The costly integration of the variational equations is not necessary any more. In addition, the observation model is linear, so that no iterations are needed if the orbits provided are sufficiently accurate. Furthermore, the estimation of the initial state vectors is not necessary in case of the energy balance approach. On the other hand, it is important to notice that velocities need to be derived as pseudo-observations by numerical differentiation. Consequently, noise in these observations will be correlated, since differentiation causes noise amplification proportional to the frequency in spectral representation. A frequency-dependent weighting may be helpful in this case. Another disadvantage of the energy balance approach is that it does not exploit fully the information presented in the precise orbit in the case of hl-SST data processing [Ditmar and van Eck van der Sluijs, 2004]. The functional model only links velocity magnitudes to the gravity potential. As the velocities are vector quantities, the direction information is lost in the inversion process. For GRACE, the functional model still contains the velocity vectors $\dot{\mathbf{r}}_A$ and $\dot{\mathbf{r}}_B$, which can not be directly derived from the high-precise KBR range-rate measurements. Therefore, a complicated pre-processing procedure may be needed to adjust the velocities by using the range-rate measurements, in order to improve the accuracy of velocities, at least in the along-track direction, see e.g. [Han et al., 2006a].

Nevertheless, the energy balance approach can lead to satisfying results provided that the noise of the pseudo-observations is properly handled in the inversion process. The energy balance approach was used, in particular, to compute TUM-1S and TUM-2S gravity field models from the CHAMP data, see [Gerlach et al., 2003]. The intensive research on the approach was carried out at the Ohio State University. The CHAMP case can be referred to [Han et al., 2003] and [Han, 2003], and for the GRACE case, see [Han, 2003], [Han et al., 2005] and [Han et al., 2006a]. A remarkable achievement made by the energy balance approach is that [Han et al., 2006b] successfully observed effects of co-seismic and post-seismic deformation due to the rapture from the great Sumatra-Andaman earthquake on December 26, 2004 by using GRACE range-rate measurements.

2.5.4 Acceleration approach

The acceleration approach is based on the Newton's second law of motion, which links the acceleration vector to the gradient of the gravitational potential. The acceleration vector is derived by double numerical differentiation of the satellite positions along the precise orbit. The basic functional model reads:

$$\mathbf{a}_g = \nabla V(r(t)), \tag{2.70}$$

with $\mathbf{a}_g$ representing as before the gravitational acceleration vector, which means that other forces are corrected beforehand. As the gradient ∇ is a linear operator, (see e.g. equation (2.17)), equation (2.70) represents a linear functional model with respect to the unknown potential coefficients.

The advantage of the acceleration approach, just as is the case for the energy balance approach, is that no linearization errors are introduced and no iterations are needed. The computation can be done very efficiently. An additional advantage, compared to the functional model derived from the energy conservative law, is that equation (2.70) represents a vector observation equation in the case of hl-SST case. Therefore the three-direction information presented in the derived accelerations can be exploited in the inversion. Note also that there are no nuisance parameters inherently related to the inversion process, like the initial state vector in the orbit integration approach.

The price to be paid is that the noise propagation of this approach can be considered as the worst case scenario compared to the other two. The double numerical differentiation results in a noise amplification proportional to the squared frequency. Thus, the noise at high frequencies can be amplified very significantly. In the time domain, the noise level can be even higher than the level of signal to be solved for. Therefore, a frequency-dependent data weighting should be incorporated into the inversion procedure.

There are at least two different variants of the acceleration approach depending on how to derive observed accelerations $\ddot{\mathbf{r}}(t)$: the one based on point-wise accelerations and the other based on average accelerations.

2.5.4.1 Point-wise acceleration approach

The point-wise acceleration approach is very straightforward. The functional model represented by equation (2.70) can be directly used without any modification. However, the point-wise accelerations must be derived from the kinematic orbit since the accelerations themselves are generally not provided as output of the orbit determination. If the positions are given in the terrestrial frame, they must be firstly transformed into the inertial frame in order to result in accelerations that are free from frame accelerations (centrifugal, Coriolis and others). Numerical differentiation is used to derive point-wise accelerations from satellite positions just as in the energy balance approach. The goal of numerical differentiation is to calculate the (first or second) derivative of a polynomial function defined at a set of epochs, for example, in the time interval $[t - n\Delta t, t + n\Delta t]$ with Δt being the sampling rate and n being an integer number. Assume that the kinematic positions can be approximated in the time interval with a polynomial of degree $2n$:

$$r(t+s) = \sum_{j=0}^{2n} c_j s^j, \quad s \in [-n\Delta t, n\Delta t], \tag{2.71}$$

where $r(t+s)$ is one component of positions and c_j represents the unknown coefficients. Equation (2.71) can be written in matrix notation:

$$\mathbf{r} = \mathbf{V}\mathbf{c}, \tag{2.72}$$

where $\mathbf{r}$ is the vector composed of kinematic positions in the given time interval, $\mathbf{c} = (c_0, c_1, c_2, ..., c_{2n})^T$, and $\mathbf{V}$ is a square matrix defined as follows:

$$\mathbf{V} = \begin{pmatrix} 1 & -n\Delta t & \cdots & (-n\Delta t)^k & \cdots & (-n\Delta t)^{2n} \\ 1 & (-n+1)\Delta t & \cdots & ((-n+1)\Delta t)^k & \cdots & ((-n+1)\Delta t)^{2n} \\ \vdots & \vdots & \ddots & \vdots & \ddots & \vdots \\ 1 & (-n+k)\Delta t & \cdots & ((-n+k)\Delta t)^k & \cdots & ((-n+k)\Delta t)^{2n} \\ \vdots & \vdots & \ddots & \vdots & \ddots & \vdots \\ 1 & n\Delta t & \cdots & (n\Delta t)^k & \cdots & (n\Delta t)^{2n} \end{pmatrix} \tag{2.73}$$

Therefore, the coefficients $\mathbf{c}$ can be found as a solution of a Vandermonde-type system of linear equations:

$$\mathbf{c} = \mathbf{V}^{-1}\mathbf{r}. \tag{2.74}$$

Remarkably, it is not necessary to find the polynomial function itself. In other words, the coefficients $\mathbf{c}$ may not be explicitly estimated. The double differentiation of equation (2.71) yields:

$$\ddot{r}(t+s) = \frac{\partial^2}{\partial s^2} \sum_{j=0}^{2n} c_j s^j = \sum_{j=2}^{2n} j(j-1) c_j s^{j-2} := \mathbf{w}^T \cdot \mathbf{c}, \tag{2.75}$$

where $\mathbf{w} = (0, 0, 2, 3! \cdot s, 4! \cdot s^2, ..., (2n)! \cdot s^{2n-2})^T$. Let us consider a special case when we compute the derivative at the middle point of the time interval, i.e. $s = 0$. Then $\mathbf{w} = (0, 0, 2, 0, ..., 0)^T$. Inserting the equation (2.74) into equation (2.75) results in

$$\ddot{r}(t) = \mathbf{w}^T \cdot \mathbf{V}^{-1}\mathbf{r} := \mathbf{e}^T\mathbf{r}, \tag{2.76}$$

where

$$\mathbf{e} = (\mathbf{w}^T \cdot \mathbf{V}^{-1})^T = (\mathbf{V}^T)^{-1}\mathbf{w}. \tag{2.77}$$

Here, the vector $\mathbf{e}$ is considered as a differentiation operator, and the elements of the vector are constant, therefore they can be computed just once for the whole data set. A similar procedure can be used to derive the satellite velocity. The only difference is that the vector $\mathbf{w}$ must be obtained by using the single differentiation of equation (2.71), so that $\mathbf{w} = (0, 1, 0, 0, ..., 0)^T$.

In order to obtain a good approximation of point-wise accelerations, relatively high degree polynominals should be used, which requires a sufficient number of epochs to be involved into the differentiation. At least, n should be larger than 4 [Reubelt et al., 2006]. However, the Vandermonde system rapidly becomes ill-conditioned as the degree of the polynomial increases, therefore it must be solved with a tailored algorithm [Press et al., 1992]. Furthermore, the propagation of orbit noise increases with a high degree scheme. According to [Reubelt et al., 2006], the 9-point scheme offers a good compromise between

approximation errors and errors propagated from kinematic positions, which are apparently not smooth, see figure 2.2. In the case of smooth orbits (such as dynamic ones), a higher-order scheme (e.g. a 13-point scheme or a 15-point one) can be used.

It is natural to use the point-wise accelerations to connect the satellite positions with gravity field parameters [Reubelt et al., 2003]. However, in practice such a functional model has its disadvantages. Firstly, derivation of point-wise accelerations requires a multi-point scheme, therefore, even one missing observation in terms of orbit data causes a relatively broad gap in terms of accelerations. Secondly, designing an accurate and efficient data weighting procedure would be not trivial in case of the multi-point differentiation. It should be mentioned that the point-wise acceleration approach was used in [Götzelmann et al., 2006] to derive a gravity field model from CHAMP kinematic orbit. Importantly, it is possible to connect the GRACE KBR (point-wise) range-accelerations with gravity field parameters. To make this connection, however, the inter-satellite velocities have to be involved. The approach was firstly proposed by [Rummel, 1979]. This approach will be presented in detail in chapter 5 in the context of the real GRACE data processing.

2.5.4.2 Average acceleration approach

If we consider a 3-point differentiation scheme, $\mathbf{V}$ in equation (2.73) should be written as:

$$\mathbf{V} = \begin{pmatrix} 1 & -\Delta t & (-\Delta t)^2 \\ 1 & 0 & 0 \\ 1 & \Delta t & (\Delta t)^2 \end{pmatrix}, \tag{2.78}$$

and $\mathbf{w} = (0, 0, 2)^T$. Computation of the differentiation operator using equation (2.77) results in $(\frac{1}{(\Delta t)^2}, \frac{-2}{(\Delta t)^2}, \frac{1}{(\Delta t)^2})^T$. The differentiation operator can be used to derive satellite accelerations from a precise orbit as follows:

$$\bar{\ddot{\mathbf{r}}}(t) = \frac{\mathbf{r}(t-\Delta t) - 2\mathbf{r}(t) + \mathbf{r}(t+\Delta t)}{(\Delta t)^2}. \tag{2.79}$$

It is obvious that satellite accelerations derived in this way cannot be treated as point-wise ones.

As a matter of fact, the single numerical differentiation of positions results exactly in the average velocity within the differentiation interval according to the definition of the average velocity. A similar statement holds also for accelerations. The acceleration $\bar{\ddot{\mathbf{r}}}(t)$ obtained with equation (2.79) can be interpreted as the *exact average acceleration*.

$$\bar{\ddot{\mathbf{r}}}(t) = \int_{-\Delta t}^{\Delta t} w(s)\, \ddot{\mathbf{r}}(t+s)\, ds, \tag{2.80}$$

with a weight function

$$w(s) = \frac{\Delta t - |s|}{(\Delta t)^2}. \tag{2.81}$$

It has been proved by [Ditmar and van Eck van der Sluijs, 2004] that:

$$\int_{-\Delta t}^{\Delta t} w(s)\, \ddot{\mathbf{r}}(t+s)\, ds = \frac{\mathbf{r}(t-\Delta t) - 2\mathbf{r}(t) + \mathbf{r}(t+\Delta t)}{(\Delta t)^2}. \tag{2.82}$$

The next question is how to link the gravity field parameters to average accelerations defined by equation (2.80). As we know that the accelerations $\mathbf{a}_g$ are point-wise values, it is, however, possible to apply an averaging filtering to both sides of equation (2.70) [Ditmar and van Eck van der Sluijs, 2004]. In this way, one can transform point-wise accelerations (i.e. gradient of potential in the right-hand side of equation (2.70) computed along the orbit) into average ones. Let us consider this idea in more detail. Similar to the case of numerical differentiation, we can represent the accelerations (rather than positions in the differentiation case) in a given time interval $[t - n\Delta t, t + n\Delta t]$ as a high-degree polynomial:

$$a(t+s) = \sum_{j=0}^{2n} c_j s^j, \quad s \in [-n\Delta t, n\Delta t], \tag{2.83}$$

where the scalar function $a(t+s)$ represents one component of the accelerations $\mathbf{a}_g$ in an inertial frame, n is an even number, and c_j are the coefficients of the polynomial. Similar to equation (2.74), the coefficients $\mathbf{c} = (c_0, c_1, \ldots, c_{2n})^T$ can be written as:

$$\mathbf{c} = \mathbf{V}^{-1}\mathbf{a}, \tag{2.84}$$

where $\mathbf{a}$ is the vector composed of point-wise accelerations at times $(t-n\Delta t, \ldots, t+n\Delta t)$ by inserting equation (2.83) into equation (2.80) and taking into account the weighting function expressed with equation (2.81), we obtain:

$$\bar{a}(t) = \int_{-\Delta t}^{\Delta t} w(t) a(t+s) ds =$$

$$= \int_{-\Delta t}^{0} \frac{\Delta t + s}{(\Delta t)^2} \sum_{j=0}^{2n} c_j s^j \mathrm{d}s + \int_{0}^{\Delta t} \frac{\Delta t - s}{(\Delta t)^2} \sum_{j=0}^{2n} c_j s^j \mathrm{d}s$$

$$= \frac{1}{\Delta t} \sum_{j=0}^{2n} c_j \int_{-\Delta t}^{\Delta t} s^j \mathrm{d}s + \frac{1}{(\Delta t)^2} \sum_{j=0}^{2n} c_j \int_{-\Delta t}^{0} s^{j+1} \mathrm{d}s - \frac{1}{(\Delta t)^2} \sum_{j=0}^{2n} c_j \int_{0}^{\Delta t} s^{j+1} \mathrm{d}s$$

$$= \frac{1}{\Delta t} \sum_{j=0}^{2n} \frac{c_j}{j+1} s^{j+1} \Bigg|_{-\Delta t}^{\Delta t} + \frac{1}{(\Delta t)^2} \sum_{j=0}^{2n} c_j \frac{s^{j+2}}{j+2} \Bigg|_{-\Delta t}^{0} - \frac{1}{(\Delta t)^2} \sum_{j=0}^{2n} c_j \frac{s^{j+2}}{j+2} \Bigg|_{0}^{\Delta t}$$

$$= \sum_{j=0}^{2n} c_j \left\{ \frac{(\Delta t)^j + (-\Delta t)^j}{j+1} - \frac{(-\Delta t)^j + (\Delta t)^j}{j+2} \right\} := \mathbf{w}_a^T \mathbf{c}, \tag{2.85}$$

where elements of the vector $\mathbf{w}_a$ are defined as:

$$\{\mathbf{w}_a\}_j = \begin{cases} \dfrac{2(\Delta t)^j}{(j+1)(j+2)} & \text{for even} \quad j \\ 0 & \text{for odd} \quad j \end{cases} \qquad (j = 0, 1, ..., 2n) \tag{2.86}$$

Inserting the equation (2.84) into equation (2.85) results in:

$$\bar{a}(t) = \mathbf{w}_a^T \cdot \mathbf{V}^{-1}\mathbf{a} := \mathbf{e}^T \mathbf{a}, \tag{2.87}$$

where

$$\mathbf{e} = (\mathbf{V}^T)^{-1}\mathbf{w}_a. \tag{2.88}$$

Thus the coefficients $\mathbf{e}$ can be obtained similarly to the case of numerical differentiation. Again, elements of the vector $\mathbf{e}$ are constant and play a role of filter coefficients. The difference between the averaging filter used in average acceleration approach and the numerical differentiation used in point-wise acceleration approach is that the input vector $\mathbf{w}$ of the Vandermonde-type system is different. Furthermore, the average filter is applied to reference quantities, not observed ones. Reference quantities are usually computed on the basis of force models and therefore smoother than the observed ones, see an example in section 2.6.4.3. Therefore, the order of the averaging filter can be chosen to be relatively high: somewhere between 12 to 16 (n = 6 to 8). Choosing a higher order does not make any practical difference according to the simulation in [Ditmar and van Eck van der Sluijs, 2004].

The technique based on average accelerations has been used to compute the DEOS_CHAMP-01C_70 gravity field model, for which purpose a one-year set of CHAMP data was utilized [Ditmar et al., 2006]. It should be mentioned that the approach will be the focus of this thesis. The details of processing of (real) average accelerations for the CHAMP case will be further discussed below. In addition, the extension of this approach to GRACE data processing and its results will be presented in chapter 5.

2.6 Data processing strategy: average acceleration approach

This section will describe the data processing strategy in a general sense with an emphasis on the average acceleration approach for processing CHAMP satellite data. We refer the section mostly to [Ditmar and van Eck van der Sluijs, 2004] and [Ditmar et al., 2006]. The section provides a basis for further developments in the thesis.

2.6.1 Solution of Gauss-Markov model

2.6.1.1 Functional model

As we discussed above, the goal of gravity field modeling is to determine a set of spherical harmonic coefficients. These unknowns are arranged as a parameter vector $\mathbf{m}$. Furthermore, additional unknowns can be included in the vector $\mathbf{m}$, e.g. empirical biases and scale factors of non-gravitational accelerations. The available satellite measurements can be represented as a data vector $\mathbf{y}$. In general, the number of measurements is much larger than the number of parameters. A certain physical or geometrical relation, i.e. functional model, has to be established to connect these two vectors to each other:

$$\mathbf{y} = \mathbf{\Phi}(\mathbf{m}). \tag{2.89}$$

Depending on the actual definition of the vector $\mathbf{y}$, the relationship of equation (2.89) can be either linear or non-linear. For example, satellite accelerations can be related to the vector $\mathbf{m}$ linearly, see section 2.5.4, whereas for an observed satellite orbit this relation is non-linear, see section 2.5.1.2. In any case, equation (2.89) allows a set of data to be simulated on the basis of a given set of spherical harmonic coefficients. It is important to notice that in practice the functional model of equation (2.89) may suggest rather advanced computations.

In a non-linear functional model, the determination of the unknown vector $\mathbf{m}$ should start from a linearization. A certain realistic reference model $\mathbf{m_0}$ should be specified and used to compute the corresponding model response $\mathbf{y_0}$:

$$\mathbf{y_0} = \mathbf{\Phi}(\mathbf{m_0}). \tag{2.90}$$

The required accuracy of such a computation depends on how accurate the data are. For example, in CHAMP data processing, temporal gravity field variations caused by mass transport in the oceans and atmosphere are typically ignored; in GRACE data processing, taking them into account is a must.

As long as the reference model is sufficiently close to the true one, equation (2.89) can be approximated by the Taylor expansion where only the zero- and first-order terms are retained:

$$\mathbf{y} = \mathbf{y_0} + \mathbf{A}(\mathbf{m} - \mathbf{m_0}), \tag{2.91}$$

with $\mathbf{A}$ the matrix of partial derivatives (or the design matrix):

$$A_{ij} = \left. \frac{\partial \Phi_i(\mathbf{m})}{\partial m_j} \right| \mathbf{m} = \mathbf{m}_0 \quad . \tag{2.92}$$

The relationship of equation (2.91) yields a linear functional model:

$$\mathbf{d_1} = \mathbf{A}\mathbf{x}, \tag{2.93}$$

with $\mathbf{x}$ the model correction to be found: $\mathbf{x} = \mathbf{m} - \mathbf{m_0}$, and $\mathbf{d_1}$ the residual observations: $\mathbf{d_1} = \mathbf{y} - \mathbf{y_0}$. Correspondingly, the final model can be computed at

the last stage of data processing as $\mathbf{m} = \mathbf{m_0} + \mathbf{x}$. In fact, it is advisable to operate with residual observations even if the functional model is linear. This is because the accuracy and resolution of any satellite data set is limited. For example, it will be always impossible to recover high-frequency components of the gravity field (say, above degree 300 or slightly higher). Splitting observations into the reference model response and the residual part allows one to circumvent this problem. In this way, the final model is assembled of two ingredients: $\mathbf{m_0}$, which may contain all the knowledge about the gravity field collected prior to the satellite mission, and $\mathbf{x}$, which contains only such corrections that are needed to make the final gravity field model fitting to the newly acquired satellite data. How to derive the quantities, such as $\mathbf{y}$, $\mathbf{y_0}$ and then $\mathbf{d_1}$ for the average acceleration approach in the case of processing CHAMP data will be described in section 2.6.4.

2.6.1.2 Least-squares solution

In general, the set of residuals $\mathbf{d}_1$ contains measurement noise. Suppose firstly that noise is random and Gaussian. Therefore, one can introduce a standard Gauss-Markov (G-M) model

$$\mathcal{E}\{\mathbf{d_1}\} = \mathbf{A}\mathbf{x}, \qquad \mathcal{D}\{\mathbf{d_1}\} = \mathbf{C}_{\mathbf{d_1}}, \tag{2.94}$$

where $\mathcal{E}$ and $\mathcal{D}$ denote the expectation and dispersion operators, respectively; $\mathbf{C}_{\mathbf{d_1}}$ is the noise variance-covariance matrix. Without regularization, the optimal solution $\hat{\mathbf{x}}$ (2.94) can be obtained by least-squares:

$$\hat{\mathbf{x}} = \mathbf{N}^{-1}\left(\mathbf{A}^T\mathbf{C}_{\mathbf{d_1}}^{-\mathbf{1}}\mathbf{d_1}\right), \tag{2.95}$$

where $\mathbf{N}$ is the normal matrix:

$$\mathbf{N} = \mathbf{A}^T\mathbf{C}_{\mathbf{d_1}}^{-\mathbf{1}}\mathbf{A}. \tag{2.96}$$

The variance-covariance of the solution can be presented by the inverse of the normal matrix.

The normal matrix $\mathbf{N}$ may be ill-conditioned (e.g. in the presence of downward continuation and/or data gaps), so that physically meaningful solution may not be obtained. Then, additional constraints have to be included into the least-squares procedure. The constraints can be another group of real or fictitious measurements. Let us introduce such constraints as a set of additional (pseudo-)observation without losing generality:

$$\mathcal{E}\{\mathbf{d_2}\} = \mathbf{B}\mathbf{x}, \qquad \mathcal{D}\{\mathbf{d_2}\} = \mathbf{C}_{\mathbf{d_2}}, \tag{2.97}$$

where $\mathbf{d_2}$ is a given vector of (fictitious) measurements, which could be, for example, a priori values of the unknown parameters, or the derivatives of the unknown parameters or even another type (group) of real measurements. $\mathbf{C}_{\mathbf{d_2}}$ is the noise variance-covariance matrix of data set $\mathbf{d_2}$. In a majority of practical applications we assume that $\mathbf{C}_{\mathbf{d_2}} = \mathbf{I}$, but it also can be chosen arbitrarily. $\mathbf{B}$ is a transport matrix that relates the unknown parameters to the (fictitious) measurements.

2.6.1.3 General regularized solution

In order to balance the contributions of two data sets, a regularization parameter $\alpha \geq 0$ can be introduced. It is easy to obtain the regularized solution for the given regularization parameter:

$$\hat{\mathbf{x}}_\alpha = \mathbf{N}_\alpha^{-1}(\mathbf{A}^T\mathbf{C}_{\mathbf{d_1}}^{-\mathbf{1}}\mathbf{d_1} + \alpha\mathbf{B}^T\mathbf{C}_{\mathbf{d_2}}^{-\mathbf{1}}\mathbf{d_2}), \tag{2.98}$$

where $\mathbf{N}_\alpha$ is the regularized normal matrix

$$\mathbf{N}_\alpha = \mathbf{A}^T\mathbf{C}_{\mathbf{d_1}}^{-\mathbf{1}}\mathbf{A} + \alpha\mathbf{B}^T\mathbf{C}_{\mathbf{d_2}}^{-\mathbf{1}}\mathbf{B}. \tag{2.99}$$

This is the general Tikhonov regularized solution for constrained least-squares. From equation (2.98), we can consider the following cases:

Case 1: $\alpha = 1$. $\hat{\mathbf{x}} = (\mathbf{A}^T\mathbf{C}_{\mathbf{d_1}}^{-\mathbf{1}}\mathbf{A} + \mathbf{B}^T\mathbf{C}_{\mathbf{d_2}}^{-\mathbf{1}}\mathbf{B})^{-1}(\mathbf{A}^T\mathbf{C}_{\mathbf{d_1}}^{-\mathbf{1}}\mathbf{d_1} + \mathbf{B}^T\mathbf{C}_{\mathbf{d_2}}^{-\mathbf{1}}\mathbf{d_2})$. This is actually a joint estimation of two types of observations in the case when their covariance matrices are sufficiently accurate, which is widely employed in geodesy for processing angle and distance observations jointly, and in orbit determination for processing code and phase GPS observations simultaneously.

Case 2: $\alpha \neq 1$. This case corresponds to the situation when the noise covariances $\mathbf{C}_{\mathbf{d_1}}$ and $\mathbf{C}_{\mathbf{d_2}}$ are not properly scaled. The optimal solution can be obtained by choosing an optimal regularization parameter, i.e. the relative weighting [Koch and Kusche, 2002] and [Ditmar et al., 2003]. We leave this to be further discussed in section 3.3.2 when dealing with a particular case.

Case 3: $\mathbf{d_2} = \mathbf{x_0}$. The prior knowledge of unknowns is taken as the fictitious observation. In this case, $\mathbf{B} = \mathbf{I}$. Hence, the solution is:

$$\hat{\mathbf{x}} = (\mathbf{A}^T\mathbf{C}_{\mathbf{d_1}}^{-\mathbf{1}}\mathbf{A} + \alpha\mathbf{C}_{\mathbf{x_0}}^{-\mathbf{1}})^{-1}(\mathbf{A}^T{\mathbf{C}_{\mathbf{d_1}}}^{-1}\mathbf{d_1} + \alpha\mathbf{C}_{\mathbf{x_0}}^{-\mathbf{1}}\mathbf{x_0}), \tag{2.100}$$

which can be interpreted as the Bayesian maximum *a posteriori* estimate of the unknown parameters, assuming a Gaussian distribution of *a priori* model with mean $\mathbf{x_0}$ and *a priori* covariance matrix $\mathbf{C}_{\mathbf{x_0}}$ [Koch, 1999].

Case 4: $\mathbf{d_2} = \mathbf{0}$. The prior model is usually mapped and then subtracted from observations of the first-type, as is the case when corrections of the geopotential coefficients are estimated. In this case, the prior estimate $\mathbf{x_0}$ can be set equal to zero. So that, the solution is

$$\hat{\mathbf{x}} = (\mathbf{A}^T\mathbf{C}_{\mathbf{d_1}}^{-\mathbf{1}}\mathbf{A} + \alpha\mathbf{C}_{\mathbf{x_0}}^{-\mathbf{1}})^{-1}\mathbf{A}^T\mathbf{C}_{\mathbf{d_1}}^{-\mathbf{1}}\mathbf{d_1}. \tag{2.101}$$

It can be understood as a solution subject to the Kaula regularization provided that the covariance matrix $\mathbf{C}_{\mathbf{x_0}}$ is a diagonal matrix with the elements given by Kaula's rule of thumb [Kaula, 1966]. $\mathbf{C}_{\mathbf{x_0}}$ can be also *a priori* covariance matrix as in Case 3. If the covariance $\mathbf{C}_{\mathbf{x_0}}$ matrix is set as unit matrix $\mathbf{I}$, the solution is

$$\hat{\mathbf{x}} = (\mathbf{A}^T\mathbf{C}_{\mathbf{d_1}}^{-\mathbf{1}}\mathbf{A} + \alpha\mathbf{I})^{-1}\mathbf{A}^T\mathbf{C}_{\mathbf{d_1}}^{-\mathbf{1}}\mathbf{d_1}, \tag{2.102}$$

which can be then regarded as the general ridge regression [Xu and Rummel, 1994]. In the case, the solution may be biased.

The dimension of the normal matrix $\mathbf{N}$ (or $\mathbf{N}_\alpha$) is equal to the number of unknowns. Even for a modest size model complete up to degree and order 120, more than 14400 coefficients have to be found. Together with a much larger number of observations (in GRACE data processing about half million per month) it makes direct computation of design and normal matrix very time consuming. Furthermore, the storage of these huge matrices may cause a problem. To avoid these problems, the normal equations can be solved iteratively. The preconditioned conjugate gradient method is frequently used for that purpose. The method has already been applied successfully in producing the DEOS_CHAMP-01C_70 gravity field model [Ditmar et al., 2006] and in the inversion of simulated SGG data [Schuh, 2003], [Ditmar et al., 2003].

2.6.1.4 Preconditioned conjugate gradient method

The conjugate gradient (CG) iteration is an effective method to solve symmetric positive (semi-)definite systems of equations. The convergence rate of the CG method can be improved if a so-called pre-conditioner is introduced, which is an approximation of the normal matrix. This results in the so-called preconditioned conjugate gradient (PCCG) method. The better the approximation, the faster the iterations will converge. Importantly, the preconditioner should be chosen in such a way that the approximate system of normal equations can be solved much faster than the exact one. In satellite gravimetry, a block-diagonal preconditioner $\mathbf{N_{bd}}$ is frequently used. Considering the regularization of Case 4, the PCCG iterations are carried out according to the following scheme, see also [Ditmar et al., 2003] and [van Eck van der Sluijs, 2003]:

1. $\mathbf{x}_0 = \tilde{\mathbf{x}}_0 = 0$, $\mathbf{r}_0 = \tilde{\mathbf{r}}_0 = \mathbf{A}^T\mathbf{C}_{\mathbf{d_1}}^{-1}\mathbf{d_1}$, $\mathbf{p}_0 = \tilde{\mathbf{p}}_0 = {\mathbf{N_{bd}}}^{-1}\mathbf{r}_0$, $k = 0$
2. $\mathbf{a_k} = \mathbf{N}\mathbf{p_k}$
3. $\alpha_k = \frac{{\mathbf{r_k}}^T\mathbf{p_k}}{{\mathbf{a_k}}^T\mathbf{p_k}}$
4. $\mathbf{x_{k+1}} = \mathbf{x_k} + \alpha_k\mathbf{p_k}$
5. $\mathbf{r_{k+1}} = \mathbf{r_k} - \alpha_k\mathbf{a_k}$
6. $\mathbf{e_k} = \tilde{\mathbf{r}}_\mathbf{k} - \mathbf{r_{k+1}}$
7. $\gamma_k = -\frac{{\mathbf{r_{k+1}}}^T\mathbf{e_k}}{\tilde{\mathbf{r}}_\mathbf{k}{\mathbf{r_{k+1}}}^T\mathbf{e_k}}$
8. $\tilde{\mathbf{x}}_\mathbf{k+1} = \mathbf{x_{k+1}} + \gamma_k\left(\tilde{\mathbf{x}}_\mathbf{k} - \mathbf{x_{k+1}}\right)$
9. $\tilde{\mathbf{r}}_\mathbf{k+1} = \mathbf{r_{k+1}} + \gamma_k\left(\tilde{\mathbf{r}}_\mathbf{k} - \mathbf{r_{k+1}}\right)$
10. If $\frac{||\tilde{\mathbf{r}}_\mathbf{k+1}||}{||\mathbf{r_o}||} < \epsilon$, set $\mathbf{x} = \tilde{\mathbf{x}}_\mathbf{k+1}$ and stop

11. $\tilde{\mathbf{p}}_{\mathbf{k+1}} = {\mathbf{N}_{\mathbf{bd}}}^{-1}\mathbf{r}_{\mathbf{k+1}}$

12. $\beta_{k+1} = \frac{{\mathbf{r}_{\mathbf{k+1}}}^T \tilde{\mathbf{p}}_{\mathbf{k+1}}}{{\mathbf{r}_{\mathbf{k}}}^T \tilde{\mathbf{p}}_{\mathbf{k}}}$

13. $\mathbf{p}_{\mathbf{k+1}} = \tilde{\mathbf{p}}_{\mathbf{k+1}} + \beta_{k+1}\mathbf{p}_{\mathbf{k}}$

14. $k = k + 1$, go to item (2)

A major advantage of the PCCG method is that there is no need to build up the normal matrix explicitly. Applying the normal matrix to a vector $\mathbf{p_k}$ (step 2) can be represented by a series of matrix-vector multiplications:

$$\mathbf{N}\mathbf{p}_{\mathbf{k}} = \mathbf{A}^T(\mathbf{C}_{\mathbf{d_1}}^{-\mathbf{1}}(\mathbf{A}\mathbf{p}_{\mathbf{k}})) + \alpha\mathbf{C}_{\mathbf{x_0}}^{-\mathbf{1}}\mathbf{p}_{\mathbf{k}}. \tag{2.103}$$

This considerably reduces the required computer memory, as now only vectors need to be stored. The second term on the right-hand side of equation (2.103) is not present if no a-priori information is used. The operation $\mathbf{A}\mathbf{p}_{\mathbf{k}}$ is nothing but spherical harmonic synthesis. The multiplication of the matrix $\mathbf{C}_{\mathbf{d_1}}^{-\mathbf{1}}$ with the resulting vector is called thereafter data weighting. Applying the vector $\mathbf{A}^T$ to the vector that results from data weighting will be referred to as co-synthesis, see also [Ditmar et al., 2003].

2.6.2 Synthesis and co-synthesis

2.6.2.1 Steps of synthesis and co-synthesis

In this section, we take the average acceleration approach as an example to discuss the steps of synthesis and co-synthesis. The synthesis is basically implemented in two steps: (1) point-wise synthesis and (2) averaging. Besides the basic steps, necessary rotations have to be taken into account since the averaging filter has to be applied in an inertial frame for all point-wise accelerations, while the data are defined in the LORF frame. All synthesis operations are linear, therefore the synthesis can be represented as:

$$\mathbf{y} = \mathbf{A}\mathbf{p} = \mathbf{R}^{(\mathbf{C}\rightarrow\mathbf{L})}\mathbf{E}\mathbf{R}^{(\mathbf{L}\rightarrow\mathbf{C})}\mathbf{A}_{\mathbf{pw}}\mathbf{p}, \tag{2.104}$$

where $\mathbf{p}$ is the synthesis input (e.g. the Stokes' coefficients) and the vector $\mathbf{y}$ is the synthesis output (e.g. acceleration vector); Matrix $\mathbf{E}$ is the averaging matrix. It consists of three groups of elements for three components of data, respectively. The elements of each group are comprised of coefficients obtained from equation (2.88). $\mathbf{R}^{(\mathbf{L}\rightarrow\mathbf{C})}$ is the matrix for rotation of the data set from the LORF into an inertial frame; $\mathbf{R}^{(\mathbf{C}\rightarrow\mathbf{L})}$ is the matrix for rotation in the opposite direction. $\mathbf{R}^{(\mathbf{C}\rightarrow\mathbf{L})}$ can be obtained by combining equation (2.25) and (2.24), given a point with coordinates $\{r, \vartheta, \lambda\}_j$ and the additional angles $\{\alpha, \beta\}_j$ at the time t_j

$$\mathbf{R}^{(\mathbf{C}\rightarrow\mathbf{L})}(t_j) = \mathbf{R}_{\mathbf{y}}(-\alpha_j)\,\mathbf{R}_{\mathbf{z}}(-\beta_j)\,\mathbf{R}_{\mathbf{y}}(-\vartheta_j)\mathbf{R}_{\mathbf{z}}(\lambda_j - \pi)\,\mathbf{R}^{(\mathbf{C}\rightarrow\mathbf{T})}(t_j). \tag{2.105}$$

Matrix $\mathbf{A_{pw}}$ in equation (2.104) is the point-wise design matrix, which can be symbolically represented at epoch j as

$$(\mathbf{A_{pw}})_j = \mathbf{R_y}(-\alpha_j)\mathbf{R_z}(-\beta_j) \begin{pmatrix} \mathbf{A}_j^{(\mathbf{x})} \\ \mathbf{A}_j^{(\mathbf{y})} \\ \mathbf{A}_j^{(\mathbf{z})} \end{pmatrix}_{\mathrm{GRF}}, \tag{2.106}$$

with $\mathbf{A}_j^{(\mathbf{x})}$, $\mathbf{A}_j^{(\mathbf{y})}$ and $\mathbf{A}_j^{(\mathbf{z})}$ being the transposed matrices, formed by expressions in equations (2.17) and (2.19). Multiplication of these matrices with geo-potential coefficients results respectively in the synthesized **x**-, **y**-, and **z**-component of the acceleration vector in the GRF.

The co-synthesis is applied to an arbitrary input vector $\mathbf{z}$ and results in an output vector $\mathbf{q}$ This can be implemented in a similar way as the synthesis, provided that all the operations are understood in the transposed sense:

$$\mathbf{q} = \mathbf{A}^T\mathbf{z} = \mathbf{A_{pw}}^T\mathbf{R}^{(\mathbf{C}\rightarrow\mathbf{L})}\mathbf{E}^T\mathbf{R}^{(\mathbf{L}\rightarrow\mathbf{C})}\mathbf{z}, \tag{2.107}$$

with

$$(\mathbf{A_{pw}})_j^T = \Big(\begin{array}{ccc} (\mathbf{A}_j^{(\mathbf{x})})^T & (\mathbf{A}_j^{(\mathbf{y})})^T & (\mathbf{A}_j^{(\mathbf{z})})^T \end{array} \Big)_{\mathrm{GRF}} \mathbf{R_z}(\beta_j)\mathbf{R_y}(\alpha_j). \tag{2.108}$$

Here we make use of the fact that rotation matrices are orthogonal.

2.6.2.2 Fast synthesis and co-synthesis

The point-wise synthesis and co-synthesis can be simply carried out as described in the previous section by the standard matrix-to-vector multiplication. However, this way is relatively time-consuming. The most computation costs come from the computation of the elements of $\mathbf{A_{pw}}$, which includes, in particular, the computation of the Legendre functions at each orbit point since the co-latitude ϑ_j changes. The number of operations required by the straightforward matrix-to-vector multiplication would be of the order of $L_{\max}^2$ per observation point. An alternative approach was developed earlier in [Sneeuw, 1994], [Ditmar et al., 2003] and [Ditmar and van Eck van der Sluijs, 2004], which is the so-called fast synthesis and co-synthesis. The fast synthesis is basically composed of three steps. In the first step, the accelerations are computed at the nodes of a regular 3-D spherical grid in the local geographical frame. This step can be efficiently carried out thanks to the Fast Fourier Transformation (FFT) as well as to the fact that the Legendre functions are only needed to be computed once per latitude. Important is that the computation costs required by this step are independent of the number of observation points. In the second step, the computed values are interpolated onto the observation points with the 3-D Overhauser splines. In the third step, the computed values are rotated from the local geographical frame into the LORF. The total computation cost mostly depends on the density of the chosen grid nodes. It is much more efficient than the straightforward one, especially if the maximum degree $L_{\max}$ and the number of measurement points are large. Furthermore, each

of the three fast synthesis steps can be represented as a matrix-to-vector multiplication. Therefore, the fast co-synthesis can be implemented by applying them in the transposed sense and in the reverse order.

2.6.3 Data weighting

The data weighting in the acceleration approach is the application of the inverse covariance matrix $\mathbf{C}_{\mathbf{d_1}}^{-\mathbf{1}}$ to the vector $\mathbf{y}$, i.e. to the output vector of the spherical harmonics synthesis, at each iteration of the PCCG procedure:

$$\mathbf{z} = \mathbf{C}_{\mathbf{d_1}}^{-\mathbf{1}}\mathbf{y}. \tag{2.109}$$

Data-weighting is non-trivial if the covariance matrix is fully populated. Fortunately, it is not necessary to compute its inverse explicitly. Ditmar and van Eck van der Sluijs [2004] have already presented a frequency-dependent data weighting algorithm based on the assumption that noise in the orbit data is stationary. A more general algorithm developed later by Ditmar et al. [2007] does not require such an assumption. The section only summarizes the frequency-dependent data weighting algorithm without a detailed derivation.

Let us firstly assume that the kinematic orbit is given in the terrestrial frame (TRF), so that the accelerations $\mathbf{d_1}$ are derived from the vector of orbit data $\mathbf{r}$ according to the following expression:

$$\mathbf{d_1} = \mathbf{R}^{(\mathbf{C}\rightarrow\mathbf{L})}\mathbf{D}\mathbf{R}^{(\mathbf{T}\rightarrow\mathbf{C})}\mathbf{r}, \tag{2.110}$$

where D is the matrix of the double numerical differentiation. For each observational component, a fragment of matrix D related to an uninterrupted series of observations is

$$\mathbf{D} = \frac{1}{\Delta t^2}\begin{pmatrix} 1 & -2 & 1 & & \\ & \ddots & \ddots & \ddots & \\ & & 1 & -2 & 1 \end{pmatrix} \tag{2.111}$$

According to the law of variance-covariance propagation, the covariance matrix $\mathbf{C}_{\mathbf{d_1}}$ can be explicitly represented as

$$\mathbf{C}_{\mathbf{d_1}} = \mathbf{R}^{(\mathbf{C}\rightarrow\mathbf{L})}\mathbf{D}\mathbf{R}^{(\mathbf{T}\rightarrow\mathbf{C})}\mathbf{C}_{\mathbf{r}}{}^{(T)}\mathbf{R}^{(\mathbf{C}\rightarrow\mathbf{T})}\mathbf{D}^T\mathbf{R}^{(\mathbf{L}\rightarrow\mathbf{C})}, \tag{2.112}$$

where $\mathbf{C}_{\mathbf{r}}{}^{(T)}$ is the covariance matrix of noise in positions in the TRF frame. Let $\mathbf{C}_{\mathbf{d_1}}{}^{(C)} = \mathbf{D}\mathbf{R}^{(\mathbf{T}\rightarrow\mathbf{C})}\mathbf{C}_{\mathbf{r}}{}^{(T)}\mathbf{R}^{(\mathbf{C}\rightarrow\mathbf{T})}\mathbf{D}^T$. Then, the inverse covariance matrix can be expressed as:

$$\mathbf{C}_{\mathbf{d_1}}^{-\mathbf{1}} = \mathbf{R}^{(\mathbf{L}\rightarrow\mathbf{C})}\left(\mathbf{C}_{\mathbf{d_1}}{}^{(C)}\right)^{-1}\mathbf{R}^{(\mathbf{C}\rightarrow\mathbf{L})}. \tag{2.113}$$

Therefore, applying the matrix $\mathbf{C}_{\mathbf{d_1}}^{-\mathbf{1}}$ to a vector mainly depends on the computation of the matrix $\left(\mathbf{C}_{\mathbf{d_1}}{}^{(C)}\right)^{-1}$. This could be easily done if the double differentiation operator $\mathbf{D}$ were invertible. However, this is not the case since the

number of columns in this matrix exceeds the number of rows. To solve the problem, the matrix can be approximately written as a circular one by the following manipulations: (1) remove the first and last column in order to make the number of columns equal the number of rows; (2) fill the top-right and the bottom-left corners with value 1; (3) change the sign of all the elements in order to make the matrix positive semi-definite (the sign can be defined arbitrarily since $\mathbf{D}$ will be operated twice in the covariance matrix ${\mathbf{C_{d_1}}}^{(C)}$); (4) regularize the matrix by adding a small number ϵ^2 to its diagonal elements. The new matrix looks like:

$$\tilde{\mathbf{D}} = \frac{1}{\Delta t^2}\begin{pmatrix} 2+\epsilon^2 & -1 & & & -1 \\ -1 & 2+\epsilon^2 & -1 & & \\ & \ddots & \ddots & \ddots & \\ & & -1 & 2+\epsilon^2 & -1 \\ -1 & & & -1 & 2+\epsilon^2 \end{pmatrix} \tag{2.114}$$

The inverse of a circular matrix can be found with ease by means of the discrete Fourier transform [Davis, 1979]. Let us introduce the matrix of discrete Fourier transform $\mathbf{F}$:

$$\{\mathbf{F}\}_{j,k} = e^{i\frac{2\pi(j-1)(k-1)}{N}}; \quad j,k = 1,\dots N, \tag{2.115}$$

where N is the number of rows/columns in the circular matrix $\tilde{\mathbf{D}}$ defined above. It is easy to see that $\mathbf{F}\mathbf{F}^* = \mathbf{F}^*\mathbf{F} = N\mathbf{I}$, where $\mathbf{F}^*$ is the Hermitian conjugate (transposed complex-conjugate) of $\mathbf{F}$. Next, it is necessary to introduce a diagonal matrix $\mathbf{S_D}$ obtained by distributing the discrete Fourier spectrum of the first row of the matrix $\tilde{\mathbf{D}}$ along the main diagonal:

$$\mathbf{S_D} = \mathrm{diag}\left(\frac{1}{N}\mathbf{F}\left\{\tilde{\mathbf{D}}\right\}_1\right) \tag{2.116}$$

Then, the matrix $\tilde{\mathbf{D}}$ can be restored from the matrix $\mathbf{S_D}$ as follows [Davis, 1979]:

$$\tilde{\mathbf{D}} = \mathbf{F}^*\mathbf{S_D}\mathbf{F}. \tag{2.117}$$

Importantly, the inverse of a circular matrix is also circular [Davis, 1979]. The inverse of the matrix $\tilde{\mathbf{D}}$ can be found as

$$\tilde{\mathbf{D}}^{-\mathbf{1}} = \frac{1}{N^2}\mathbf{F}^*\left(\mathbf{S_D}\right)^{-1}\mathbf{F}. \tag{2.118}$$

The elements of the diagonal matrix $\mathbf{S_D}$ can be computed analytically from equations (2.114), (2.115) and (2.116) [Ditmar and van Eck van der Sluijs, 2004]:

$$\{\mathbf{S_D}\}_{kk} = \frac{1}{N(\Delta t)^2}\left[2(1-\cos(\omega_k\Delta t)) + \left(\frac{\Delta t}{\tau}\right)^2\right], \tag{2.119}$$

where ω_k is the angular frequency corresponding to the k-th spectral line: $\omega_k = 2\pi k/(N\Delta t)$; and $\tau \equiv \Delta t/\epsilon$ is the filter halfwidth. Consider the spectrum of equation (2.119) at low frequencies: $\omega_k\Delta t \ll 1$. Under this condition, the function

$\cos(\omega_k \Delta t)$ can be approximated as $1 - (\omega_k \Delta t)^2/2$, hence equation (2.119) transforms into:

$$\{\mathbf{S_D}\}_{kk} \approx \frac{1}{N}\left(\omega_k^2 + \frac{1}{\tau^2}\right). \tag{2.120}$$

This expression helps to justify the introduction of parameter τ by adding the term $1/\tau^2$. We assume that noise in accelerations is not infinitely small at any frequency, so that the weights assigned to different frequencies cannot be infinitely large.

For practical reasons, the inverse filtering is implemented in the time domain rather than in the Fourier domain. The explicit expression for the inverse filter, which approximates the application of the matrix $\tilde{\mathbf{D}}^{-1}$ to a vector, is as follows:

$$\left\{\tilde{\mathbf{D}}\right\}_{ij} \approx \frac{\Delta t \tau}{2} e^{-\frac{|i-j|\Delta t}{\tau}}. \tag{2.121}$$

The inverse of ${\mathbf{C_{d_1}}}^{(C)}$ involves also another inverse matrix $\left({\mathbf{C_r}}^{(T)}\right)^{-1}$. The inversion ${\mathbf{C_r}}^{(T)}$ can be done easily since noise in satellite positions is assumed to be non-correlated in time (though correlations between the components are not excluded). Therefore, this matrix is block-diagonal with the size of blocks being 3×3. To implement the data weighting, the analytical noise representation (i.e. parameter τ and relative weighting of the components) has to be determined. In the previous studies, these values were determined on basis of comparing the obtained models with the ground truth [Ditmar et al., 2006]. In chapter 3, we will discuss how to determine them from the data themselves. It should be mentioned that introduction of a circular structure can cause strong edge effects, particularly if data gaps are present. To solve this, the low-level PCCG scheme is used.

2.6.4 Computation of residual accelerations

2.6.4.1 Steps of computation

In order to provide a basis for the further discussion in the thesis, the procedure of computing the residuals in the average acceleration approach has to be explained, see figure 2.5. It should be stressed that the residual accelerations refer to the LORF frame defined in section 2.3. The computation of residual accelerations mainly includes (1) the derivation of the observed satellite accelerations, (2) the computation of reference accelerations, and (3) the preprocessing of the non-gravitational satellite accelerations. The residual averaged accelerations are therefore obtained as follows:

$$\mathbf{d_1}_j = \bar{\ddot{\mathbf{r}}}_j^{(\mathrm{obs})} - \bar{\ddot{\mathbf{r}}}_j^{(\mathrm{ref})} - \bar{\ddot{\mathbf{r}}}_j^{(\mathrm{ng})} \tag{2.122}$$

There is an alternative way to directly compute the residual accelerations by using a residual orbit in the inertial frame via the three-point differentiation scheme. The

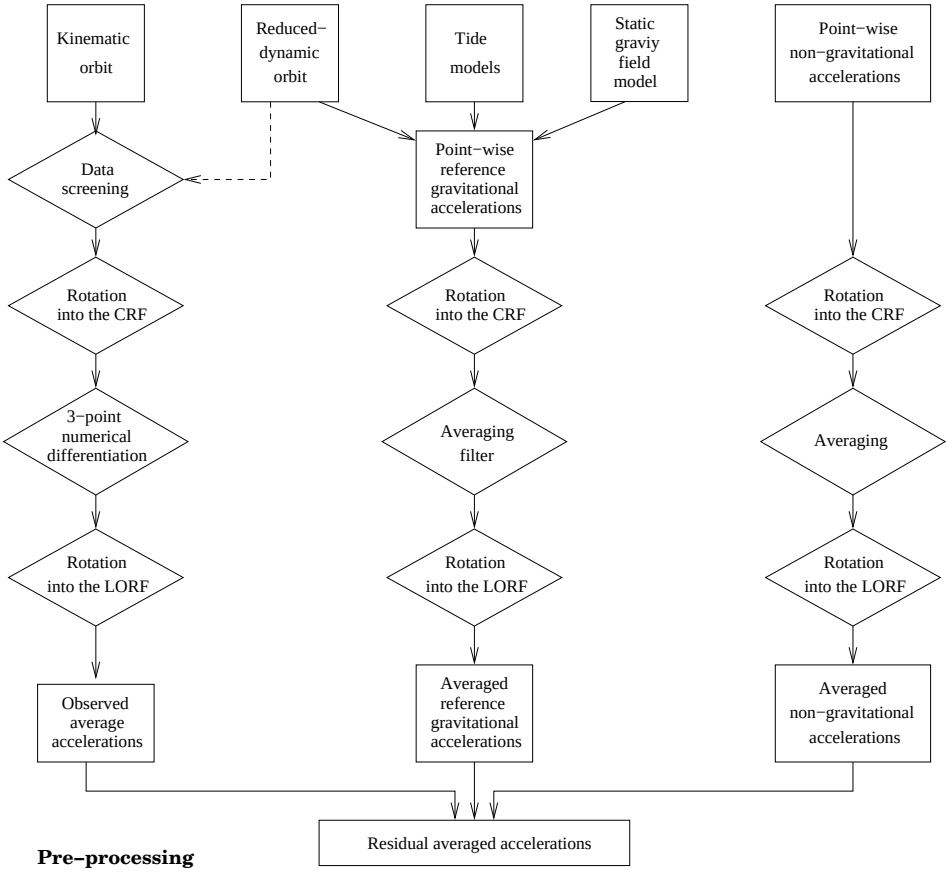

Fig. 2.5. Flow chart of CHAMP data pre-processing from [Ditmar et al., 2006]

residual orbit is obtained by subtracting a purely dynamic orbit from a kinematic orbit. The purely dynamic orbit is integrated according to the procedure described in section 2.4.3 on the basis of the reference gravity field model and the temporal force models. In this way, the reference force models should be as accurate as possible. Otherwise, the error of the background force models will increase the orbit error in the integrated dynamic orbit, which may be finally mapped into the residual accelerations. This idea is not applied to actual CHAMP data processing but serves a basis for developing a procedure of processing GRACE ll-SST data (see chapter 5).

2.6.4.2 Deriving observed accelerations: outlier detection

Before deriving observed accelerations, a comprehensive outlier detection is implemented to screen the kinematic orbit on the basis of the discrepancies of kinematic

and reduced-dynamic orbits. The outlier detection step includes four steps:

1) If there are epochs not supplied with covariance matrices at all, such epochs are discarded, since those data are not considered reliable.

2) If the position formal error exceeds a given threshold (e.g. 5 cm) for any of the components, the epoch is discarded. Those data are considered as of low quality.

3) If the distances between the kinematic and reduced-dynamic positions are larger than a given threshold (e.g. 50cm), these epochs are discarded. Those kinematic positions may have large error.

4) The neighboring time-differences of the orbit discrepancies altogether with the noise descriptions are used to execute a generalized likelihood ratio test. If the statistics of the test is larger than a certain threshold, the corresponding epochs are also excluded from the further data processing, see [Ditmar et al., 2006].

After the outlier detection, the cleaned kinematic positions are used to derive the observed accelerations $\bar{\ddot{\mathbf{r}}}_j^{(\mathrm{obs})}$ by means of the three-point differentiation scheme, see equation (2.79). The obtained series of satellite accelerations are then rotated into the LORF frame using equations (2.25) and (2.24).

2.6.4.3 Computation of reference accelerations

The computation of the reference accelerations $\bar{\ddot{\mathbf{r}}}_j^{(\mathrm{ref})}$ is performed in four steps:

1) The static point-wise reference accelerations are computed using equation (2.19) at the points of the reduced-dynamic orbit with the same sampling intervals as that of the observed accelerations. A static Earth's gravity field (e.g. the EGM96 model in this thesis) is used in the step. Besides, the temporal point-wise accelerations caused by astronomic, solid Earth and ocean tides are computed. Both static and temporal accelerations are summed as the reference accelerations. The GRACE de-aliasing products, like atmospheric and oceanic effects are not considered in the CHAMP data processing.

2) To be consistent with the functional model, the point-wise accelerations have to be transformed into averaged ones. In order to implement the average filter, it is necessary to rotate the reference accelerations into the inertial frame using equation (2.25).

3) The point-wise accelerations are transformed into averaged ones using the averaging filter of equation (2.80).

4) The computed averaged accelerations are rotated into the LORF.

2.6.4.4 Processing of non-gravitational accelerations

The point-wise non-gravitational accelerations provided by the accelerometer on board are transformed into the inertial frame by using the quaternions measured by the star camera. After that, averaging of the point-wise non-gravitational accelerations is required. One way to do that is to apply the averaging filter as used for reference accelerations. Importantly, the order of the filter in this case should be lower since a series of real non-gravitational accelerations cannot be considered as a very smooth function. This approach requires that the sampling rate of the accelerometer data is equal to that of the total satellite accelerations obtained by the double differentiation of the satellite orbit. An alternative approach can be used if the accelerometer data are sampled denser. Consider, for example, a situation when the sampling rate of non-gravitational accelerations is 10 sec (in the CHAMP case), and the sampling rate of the orbit is 30 sec. In this case, equation (2.80) is directly applicable for a numerical integration, e.g. with a simple trapezium rule [Ditmar et al., 2006]. Then, the averaged non-gravitational accelerations can be obtained as:

$$\bar{\mathbf{a}}(t_j) = \frac{1}{9}\Big(\mathbf{a}(t_j-20)+2\mathbf{a}(t_j-10)+3\mathbf{a}(t_j)+2\mathbf{a}(t_j+10)+\mathbf{a}(t_j+20)\Big). \quad (2.123)$$

If the camera data or accelerometer data are absent at one or more of the five epochs in equation (2.123), $\bar{\mathbf{a}}(t_j)$ is not computed, and the epoch t_j is excluded from the further data processing. The averaged non-gravitational accelerations are then rotated into the LORF frame, forming the vector $\bar{\ddot{\mathbf{r}}}_j^{(\mathrm{ng})}$.

The measured non-gravitational accelerations should be calibrated. The bias and scaling factor per accelerometer axis are to be estimated. The distributed accelerometer data are typically supplied with an initial estimation of the calibration parameters. However, they are usually adjusted further in the course of the gravity field modeling. This means that the true non-gravitational accelerations $\mathbf{a}(t_j)$ to be used in the data processing are related to the corresponding observed non-gravitational measurements $\tilde{\mathbf{a}}(t_j)$ as

$$\mathbf{a}(t_j) = \mathbf{B}_k + (\mathbf{S}_k + \mathbf{I})\tilde{\mathbf{a}}(t_j), \quad (2.124)$$

where $\mathbf{B}_k$ is a 3×1 bias vector, $\mathbf{S}_k$ is a 3×3 diagonal matrix containing the residual scaling factors, and $\mathbf{I}$ is the 3×3 unit matrix. The subscript k has been introduced because biases and scale factors are defined not for the whole data set but once per estimation interval. The length of the estimation interval is somewhere between several hours and several days (e.g. 10 days for CHAMP data processing). The unknown parameters comprising the vectors $\mathbf{B}_k$ and matrices $\mathbf{S}_k$ are determined together with the gravity field parameters in the course of the least-squares adjustment.

2.7 Summary and remarks

This chapter focused on the description of the theoretic background and previous developments in gravity field modeling related to the research conducted in this

thesis. The solved-for parameters are the spherical harmonic coefficients, which are used to represent the Earth's gravity field. Some of basic functionals of the gravity field model were given. The related coordinate frames and the rotations among them were described as well. The orbit determination is closely related to the gravity field modeling using the SST data. Therefore, various aspects of precise orbit determination were discussed in the chapter. The statistical properties of three types of orbits, i.e. kinematic, reduced-dynamic and purely dynamic one, were analyzed. The relation between the orbit determination and gravity field modeling was explained. Several linear and nonlinear functional models connecting the gravity field parameters and the SST data had been set up. The gravity field modeling approaches corresponding to these functional models are such as variation equation approach, short arc approach, energy balance approach and acceleration approach. The advantages and disadvantages of these approaches were discussed. The thesis is focused on a linear functional models, in particular on the acceleration approach, which makes use of Newton's second law of motion that links the acceleration vectors to the Earth's gravitational field vector. Therefore, a relatively comprehensive description had been given of how the inversion of the acceleration residuals into gravity field parameters is carried out. The practical procedure of computing the acceleration residuals in the case of CHAMP data processing was also described to provide a basis for the next chapters.

Chapter 3
Gravity field modeling from CHAMP data

3.1 Introduction

This chapter is devoted to gravity field modeling on the basis of CHAMP data. We exploit the acceleration approach to compute parameters of the Earth's gravity field. The orbit-derived accelerations are directly related to the Earth's gravity field according to Newton second law. Two refinements of the acceleration approach will be discussed in this chapter: 1) a new algorithm to compute a smooth and accurate satellite orbit, which can be used for calculating reference accelerations and the entries of the design matrix. 2) a better stochastic modeling of data noise. The aims of these two refinements are: 1) to optimize the resulting gravity field model; 2) to make it as independent as possible from any other CHAMP-based *a priori* information about the Earth gravity field.

The chapter starts from section 3.2, where we motivate these two refinements, and then re-arrange the computation procedure of gravity field modeling. Section 3.3 presents the algorithm, which is used to compute a smoothed kinematic orbit. In section 3.4, the estimation of the noise model from *posterior* least-squares residuals is described, and the results of a simulation case study are presented. Section 3.5 presents the results of real data processing and a comparison of them with other CHAMP- or GRACE-based solutions.

3.2 Motivations to refine the data processing strategy

In the acceleration approach, both the observed and the reference accelerations have to be computed, see section 2.6.4. To do that, the orbit of a particular type (e.g. kinematic, reduced-dynamic or dynamic) has to be used. The kinematic orbit is calculated entirely from GPS measurements. It suffers from interruptions and relatively strong noise, see [Visser and van den IJsel, 2000] and [Švehla and Rothacher, 2002]. An important property of an orbit of this type, however, is that it is not biased towards any *a priori* gravity field model as was discussed in the previous chapter. Therefore, the kinematic orbit is

preferable for calculating the observed accelerations. The situation is different for the computation of reference gravitational accelerations. It is more physical to take a smooth orbit to define a set of points where reference accelerations are calculated. Furthermore, gaps in such an orbit are undesirable: the reference accelerations can not be computed within gaps and neither at a few observation points before and after a gap, as an operation of averaging filtering has to be performed [Ditmar and van Eck van der Sluijs, 2004]. Then, an unnecessary loss of data may occur. The loss of data may be significant if the number of data gaps is large (e.g. due to outliers). Thus, a smoothed orbit with a minimum number of interruptions is needed for the computation of reference accelerations. One example of such an orbit is a reduced-dynamic orbit, which is smooth and accurate. However, the reduced-dynamic orbit is produced by integration of the equations of motion on the basis of a force model and probably contains artificial velocity jumps. On the one hand, discontinuities in terms of satellite velocities is non-physical and therefore an undesirable feature of such an orbit. On the other hand, a high-quality gravity field model may be used in computing the reduced-dynamic orbit. For example, a CHAMP-based or even a GRACE-based gravity model is used to determine the orbit of the CHAMP satellite. Although this orbit is only used to compute reference accelerations, it may have an indirect influence on the estimated gravity model. Does it contribute somehow to high quality of the obtained results? If so, it is not fair to compare the model obtained by one research group with those published by others. Additionally, the resulting models cannot be called CHAMP-only model anymore. This was the motivation to investigate an alternative way to obtain a smooth satellite orbit, which should be free from CHAMP-based or GRACE-based *a priori* information. By comparing the results with those produced with the reduced-dynamic orbit, we may estimate the indirect influence of an *a priori* gravity field model, i.e. the influence on quality of the estimated model via the orbit used to compute the reference accelerations. Another motivation was to see if such a smoothed orbit can improve the quality of the obtained gravity field model.

In addition, a crucial aspect of accurate gravity field modeling is a proper data weighting, which requires an adequate noise model. In particular, it is important to take into account that data noise is time-correlated. Even if correlations are absent in raw measurements, they may be introduced in the course of data pre-processing. For example, noise in observed satellite accelerations becomes correlated (frequency-dependent) due to the operation of numerical differentiation. In order to obtain the optimal model of the Earth's gravity field, one has to use a proper stochastic model, which takes such a noise behavior into account. If the dependency of noise on frequency is not known a priori, it is necessary to implement a procedure to estimate it from the data themselves.

When adding a noise estimation procedure, the entire hl-SST data processing can be organized as shown in figure 3.1, which includes three parts: data pre-processing, data processing and post-processing. In the flow chart, we also include the procedure of computing a smooth and accurate satellite orbit.

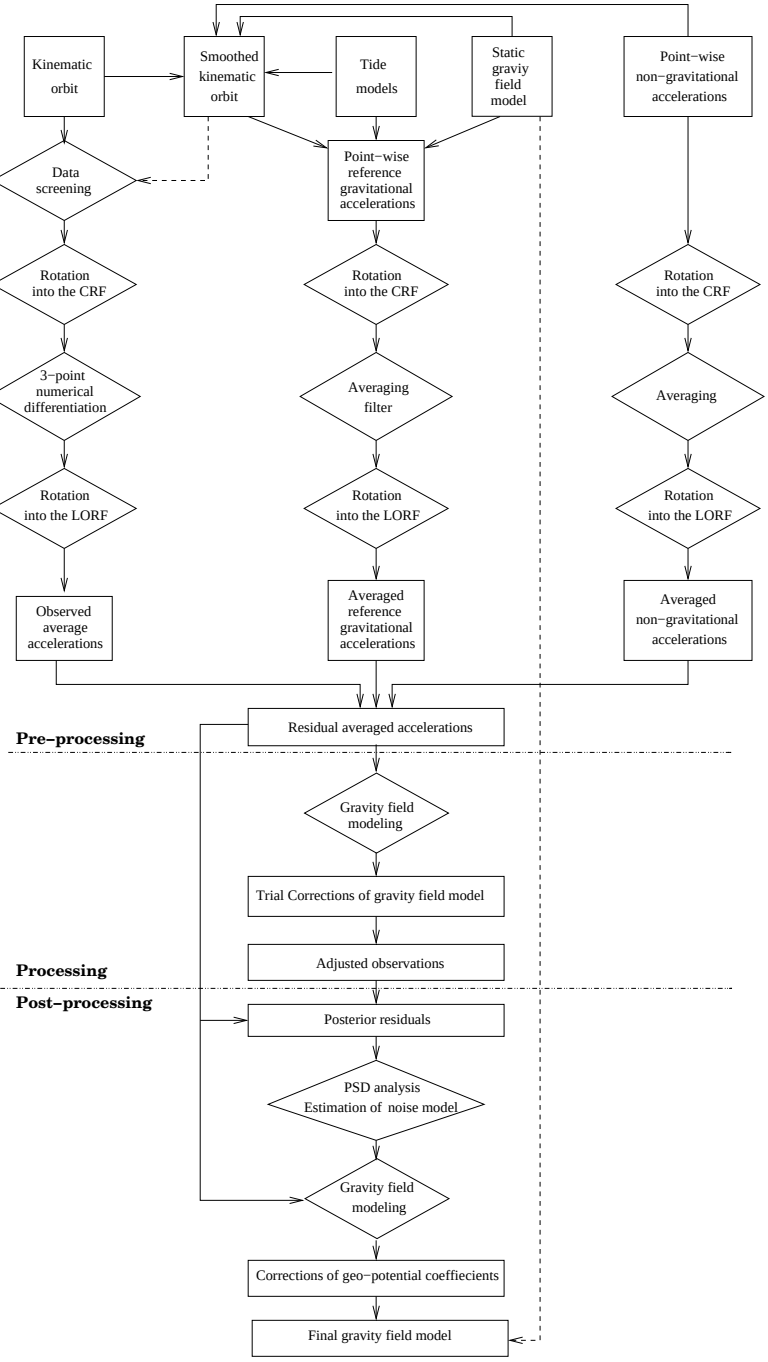

Fig. 3.1. Flow-chart of improved hl-SST data processing

3.3 Orbit smoothing for computing reference accelerations

The proposed orbit smoothing procedure uses a kinematic satellite orbit as input, and is based on a regularized estimation of B-spline coefficients. Section 3.3.1 describes a least-squares procedure for orbit smoothing on the basis of B-splines; Section 3.3.2 is devoted to regularization issues, in particular, to the optimal choice of the regularization parameter. In section 3.3.3 and 3.3.4 a simulation study and real CHAMP orbit smoothing for gravity field modeling are tackled, respectively. The contents of this section has been partly published in the paper [Liu and Ditmar, 2006].

3.3.1 Orbit smoothing on the basis of B-splines

Given a set of data values $\{y_r, r = 1, \ldots, m\}$, which are one component of a kinematic orbit (i.e. X-, or Y- or Z-coordinate) in an inertial frame, and a set of corresponding time variables t_r within a time interval $a \leq t_r < t_{r+1} \leq b$, a polynomial representation of the orbit, $y(t)$, $t \in [a, b]$, is determined to fit the y_r according to the least squares criterion, so that $y(t_r) \simeq y_r$. If the kinematic orbit were accurate enough, it would be sufficient to determine $y(t)$ by an interpolation, i.e. such that $y(t_r) = y_r$. However, the values y_r contain measurement noise, e.g. due to GPS carrier phase measurement noise. Furthermore, y_r may also contain errors due to unfixed ambiguities, multi-path effects or temporary malfunction of the GPS receiver. Therefore, a least-square adjustment procedure has to be preferred. In this procedure, a noise variance-covariance matrix may be taken into account. The developed adjustment procedure is based on a B-spline parameterization [de Boor, 2001, Dierckx, 1993].

B-splines are frequently used to represent a function, since it preserves the function smoothness up to an arbitrarily chosen order k. With the given set of knots $\{\lambda_i : i = -k, -k+1, ..., 0, 1, ..., n, n+1, ..., n+k+1\}$, one can construct $n+k+1$ linearly independent B-splines of degree k, i.e. $N_{i,k+1}(t)$ for $i = -k, ..., n$, with knots λ_i satisfying:

$$\begin{aligned} \lambda_{-k} \leq \lambda_{-k+1} \leq \quad \ldots \quad \leq \lambda_{-1} \leq \lambda_0 = a, \\ a \leq \lambda_1 \leq \lambda_2 \leq \quad \ldots \quad \leq \lambda_{n-1} \leq \lambda_n \leq b, \\ b = \lambda_{n+1} \leq \lambda_{n+2} \leq \ldots \leq \lambda_{n+k} \leq \lambda_{n+k+1}. \end{aligned}$$

$N_{i,k+1}(t)$ has the following *basic properties:*

1. *Local support:* $N_{i,k+1}(t) = 0 \quad \text{if} \quad t \notin (\lambda_i, \lambda_{i+k+1})$;
2. *Positivity:* $N_{i,k}(t) \geq 0 \quad \text{for all} \quad t$;
3. *Normalization:* $\sum_{i=-k}^{n} N_{i,k+1}(t) = 1 \quad \text{for all} \quad t \in [a, b]$;

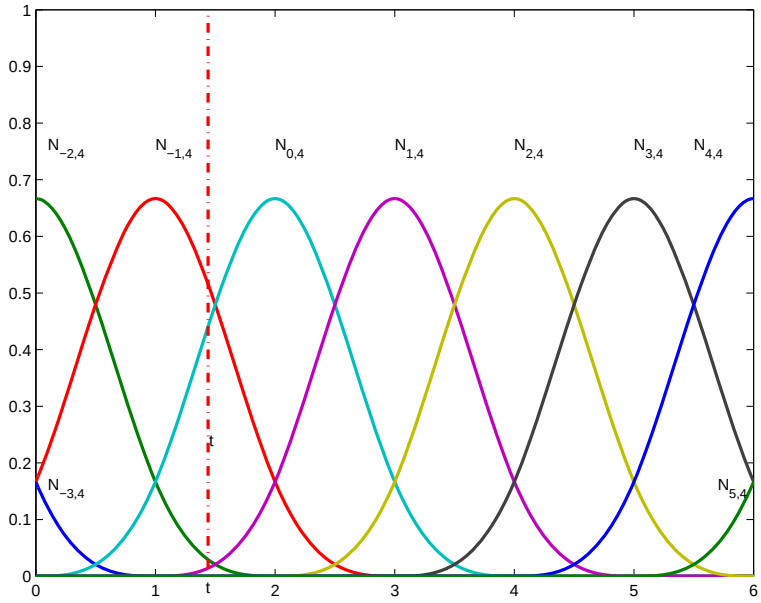

Fig. 3.2. An example of B-spline basis functions with knots [-3 -2 -1 0 1 2 3 4 5 6 7 8 9]. Four basis functions of B-spline, namely $N_{-2,4}$, $N_{-1,4}$, $N_{0,4}$ and $N_{1,4}$, pass through the area [1, 2]. Therefore, a spline to be evaluated in this interval can be formulated as: $y(t) = \sum_{i=-2}^{1} c_i N_{i,4}(t)$.

4. *Recursion:* $N_{i,l+1}(t) = \frac{t-\lambda_i}{\lambda_{i+l}-\lambda_i} N_{i,l}(t) + \frac{\lambda_{i+l+1}-t}{\lambda_{i+l+1}-\lambda_{i+1}} N_{i+1,l}(t)$;
   with: $N_{i,1}(t) = \begin{cases} 1, & \text{if } t \in [\lambda_i, \lambda_{i+1}), \\ 0, & \text{if } t \notin [\lambda_i, \lambda_{i+1}). \end{cases}$

5. *Derivative of a B-spline:* $N'_{i,k+1}(t) = k\{\frac{N_{i,k}(t)}{\lambda_{i+k}-\lambda_i} - \frac{N_{i+1,k}(t)}{\lambda_{i+k+1}-\lambda_{i+1}}\}$.

Figure 3.2 shows some B-splines for a given set of knots. A function $y(t)$ can be represented as a weighted sum of B-splines:

$$y(t) = \sum_{i=-k}^{n} c_i N_{i,k+1}(t), \tag{3.1}$$

where c_i are called the B-spline coefficients of $y(t)$.

To find coefficient estimates from the given data set $\{(t_r, y_r) : r = 1, ..., m\}, (m \geq n + k + 1)$, one has to solve a system of linear equations:

$$y_r = \sum_{i=-k}^{n} c_i N_{i,k+1}(t_r), \quad r = 1, ..., m. \tag{3.2}$$

Let the kinematic orbit errors be described by a zero-mean, Gaussian noise with covariance matrix $\mathbf{Q_y} = \sigma^2\mathbf{W}^{-1}$ with the standard deviation σ not necessarily known, and weight matrix $\mathbf{W}$. Then, the relationship between the observations and the unknown parameters can be expressed as the Gauss-Markov model similar as equation (2.94):

$$\mathcal{E}\{\mathbf{y}\} = \mathbf{Ac}, \qquad \mathcal{D}\{\mathbf{y}\} = \mathbf{Q_y}, \tag{3.3}$$

where $\mathbf{y}$ is the vector of given values y_r of one component of the kinematic orbit; $\mathbf{c}$ is the vector of unknown B-spline coefficients; and $\mathbf{A}$ is the design matrix, which is built from $N_{i,k+1}(t_r)$. The optimal set of coefficients $\hat{\mathbf{c}}$ can be obtained as the least-square solution, i.e.

$$\hat{\mathbf{c}}_{ls} = \left(\mathbf{A}^T{\mathbf{Q_y}}^{-1}\mathbf{A}\right)^{-1}\left(\mathbf{A}^T{\mathbf{Q_y}}^{-1}\mathbf{y}\right). \tag{3.4}$$

Because $N_{i,k+1}$ is nonzero only within the interval $(\lambda_i, \lambda_{i+k+1})$, the design matrix is sparse, and the normal matrix $\mathbf{N}_{ls}$, i.e. $\mathbf{A}^T{\mathbf{Q_y}}^{-1}\mathbf{A}$, is a banded matrix with $2k+1$ bandwidth, which makes solving of the linear system particularly easy. The smoothed orbit can be therefore obtained as

$$\hat{\mathbf{y}}_{ls} = \widetilde{\mathbf{A}}\hat{\mathbf{c}}_{ls}, \tag{3.5}$$

where $\widetilde{\mathbf{A}}$ is built from $N_{i,k+1}(t)$ at any time within $[a, b]$. With regard to a stable evaluation of B-splines and computational schemes for a banded matrix, we refer to [de Boor, 2001, Dierckx, 1993]. Depending on the sampling rate and the order of splines, the presented procedure can also handle data with gaps provided that they are not too long, e.g. less than 5 minutes for the CHAMP orbit. Longer data gaps may cause the matrix $\mathbf{A}$ to be rank defect in our case.

3.3.2 Regularization in the form of acceleration constraints

Accuracy of estimations can be improved if *a priori* information is taken into account. An orbiting satellite experiences an influence of forces. As soon as a force model is known, satellite accelerations can be computed at any point along the kinematic orbit. Although the accelerations from a force model might not be very accurate, they can be considered as *a priori* information regarding the second derivative of the orbit.

3.3.2.1 Acceleration constraints

An advantage of B-splines is that *a priori* information in the form of acceleration constraints can be easily included. The second derivative of equation (3.2) can be expressed as:

$$y_r^a = \sum_{i=-k}^{n} c_i N_{i,k+1}^{''}(t_r), \quad r = 1, ..., m, \tag{3.6}$$

where y_r^a is one acceleration component (e.g. the X-component) calculated from a force model along the kinematic orbit. $N_{i,k+1}^{''}(t_r)$ is the second derivative of the

B-spline, and it can be calculated as:

$$N''_{i,k+1}(t_r) = k\left\{\frac{N'_{i,k}(t_r)}{\lambda_{i+k} - \lambda_i} - \frac{N'_{i+1,k}(t_r)}{\lambda_{i+k+1} - \lambda_{i+1}}\right\}, \tag{3.7}$$

with $N'_{i,k}(t_r)$ given by

$$N'_{i,k}(t_r) = (k-1)\left\{\frac{N_{i,k-1}(t_r)}{\lambda_{i+k-1} - \lambda_i} - \frac{N_{i+1,k-1}(t_r)}{\lambda_{i+k} - \lambda_{i+1}}\right\}. \tag{3.8}$$

Thus, the second derivative of a spline function of degree k is a spline of degree $k-2$ having the same knots.

Equation (3.6) can be used as the basis for the following Gauss-Markov model similar to that of equation (2.97):

$$\mathcal{E}\{\mathbf{y_a}\} = \mathbf{Bc}, \qquad \mathcal{D}\{\mathbf{y_a}\} = \mathbf{Q_{y_a}}, \tag{3.9}$$

where $\mathbf{y_a}$ is the vector of accelerations y_r^a; $\mathbf{c}$ is the same vector of unknown coefficients as before; $\mathbf{B}$ is the design matrix formed by the B-spline second derivatives, and $\mathbf{Q_{y_a}}$ is the covariance matrix of noise in accelerations. Notice that in practice it is not easy to estimate the stochastic properties of acceleration noise. For this reason, we have just set $\mathbf{Q_{y_a}}$ equal to a scaled unit matrix.

With the acceleration constraints, the optimal solution can be obtained by minimizing the objective function

$$\tilde{\eta} := (\mathbf{Ac} - \mathbf{y})^T \mathbf{Q_y}^{-1}(\mathbf{Ac} - \mathbf{y}) + \alpha(\mathbf{Bc} - \mathbf{y_a})^T(\mathbf{Bc} - \mathbf{y_a}), \tag{3.10}$$

where α is a regularization parameter. The objective function is somewhat similar to the criterion function for a cubic natural spline in Voltring [1986]. The first term of both functions force the spline to fit the data. The meaning of the second term is, however, different. The second term of equation (3.10) makes the second derivatives of the spline match the force model, whereas the second term in the criterion function [Voltring, 1986] only makes the spline as smooth as possible without a specific physical sense. The purpose of α is to balance the first and the second term. In other words, it has to balance errors of the kinematic orbit and inaccuracies of accelerations computed on the basis of a force model. If α tends to zero, the least-squares solution is obtained. If α tends to infinity, a spline which exactly fits the force model in the least-squares sense is obtained. Hereafter, we call the minimum of the objective function equation (3.10) the *regularized solution*. The regularized solution for a given regularization parameter α has already been given by equation (2.98). For this particular case, the solution is written as:

$$\hat{\mathbf{c}}_\alpha = \mathbf{N}_\alpha^{-1}(\mathbf{A}^T \mathbf{Q_y}^{-1}\mathbf{y} + \alpha \mathbf{B}^T \mathbf{y_a}), \tag{3.11}$$

where $\mathbf{N}_\alpha$ is the regularized normal matrix:

$$\mathbf{N}_\alpha = \mathbf{A}^T \mathbf{Q_y}^{-1}\mathbf{A} + \alpha \mathbf{B}^T \mathbf{B}. \tag{3.12}$$

Similarly to the least-squares solution, the smoothed force model-based orbit can be obtained from the regularized solution as:

$$\hat{\mathbf{y}}_\alpha = \widetilde{\mathbf{A}}\hat{\mathbf{c}}_\alpha. \tag{3.13}$$

The problem of finding the optimal regularization parameter will be discussed in the next section.

The regularization procedure can deal with longer data gaps in the kinematic orbit than the original least-square procedure. In the presence of gaps, the smoothed orbit is computed iteratively in the regularization procedure. First of all, the gaps are filled in by approximately determined satellite positions, for which purpose a numerical integration with a Runge-Kutta scheme is applied [Montenbruck and Gill, 2000]. Accelerations computed at those positions are used as constraints in computing a smoothed orbit. Then, positions from the smoothed orbit are utilized to compute an improved set of accelerations, and the smooth orbit is obtained again. The iterations are stopped when the recovered positions within gaps differ in average at two successive iterations less than a threshold.

3.3.2.2 Parameter choice by generalized cross-validation

For regularization solution, the proper selection of α is rather crucial. There are a few methods to find the optimal regularization parameter, of which the L-curve and generalized cross-validation (GCV) attracted a lot of attention [Voltring, 1986, Hansen, 1992]. As far as the geodetic community concerns, Kusche and Klees [2002] compared the two methods in the context gravity recovery from satellite gravity gradients, and stated that the L-curve method might give over-smooth solution, whereas, the GCV method demonstrates relatively good performance. An alternative way could be the variance-covariance component estimation, see [Koch and Kusche, 2002]. We will only consider the GCV method to choose the regularization parameter in this research.

The principle of the GCV method is based on the leave-out-one or 'jackknife' idea. Traditionally, it is applied when only one data set is under consideration. In other words, vector $\mathbf{y_a}$ has to be equal to zero. A careful analysis of this method has shown, however, that it can also be used in the context of two data sets as in our case. In this situation, the 'leave-out-one' idea has to be applied only to the data set $\mathbf{y}$. Then, the problem reduces to minimization of the GCV function, which looks as follows:

$$f_\alpha^{gcv} = \frac{m(\mathbf{A}\hat{\mathbf{c}}_\alpha - \mathbf{y})^T \mathbf{Q}_\mathbf{y}^{-\mathbf{1}}(\mathbf{A}\hat{\mathbf{c}}_\alpha - \mathbf{y})}{(m - \mathcal{T}_\alpha)^2}, \tag{3.14}$$

where m is the number of data in the set $\mathbf{y}$, $\mathcal{T}_\alpha = \mathrm{trace}(\mathbf{F}_\alpha)$, and $\mathbf{F}_\alpha$ is the influence matrix related to the data set $\mathbf{y}$:

$$\mathbf{F}_\alpha = \mathbf{A}(\mathbf{A}^T\mathbf{Q}_\mathbf{y}^{-\mathbf{1}}\mathbf{A} + \alpha\mathbf{B}^T\mathbf{B})^{-1}\mathbf{A}^T\mathbf{Q}_\mathbf{y}^{-\mathbf{1}}. \tag{3.15}$$

The regularization parameter α for which the GCV function reaches the minimum is considered as the optimal one. To use GCV in large-scale problems, a fast algorithm for the computation of the trace of the influence matrix is needed [Uteras, 1981]. Girard [1989] proposed a fast Monte-Carlo method for this purpose. The method introduces a random vector $\mathbf{z}$ of length m with $\mathcal{E}\{\mathbf{z}\} = 0$ and $\mathcal{D}\{\mathbf{z}\} = \mathbf{I}$. Then, an unbiased trace estimation is given by

$$\mathcal{T}_\alpha = \mathcal{E}\{\mathbf{z}^T \mathbf{F}_\alpha \mathbf{z}\}. \tag{3.16}$$

Application of the expectation operator suggests that a number of random vectors $\mathbf{z}$ have to be used with a subsequent averaging of trace estimations [Kusche and Klees, 2002, Ditmar et al., 2003]. However, just one realization of $\mathbf{z}$ may be sufficient if the number of data is sufficiently large [Kusche and Klees, 2002]. In satellite gravity modeling, this condition is always met. Thus, an unbiased trace estimation can be obtained as:

$$\mathcal{T}_\alpha = \mathbf{z}^T \mathbf{A}(\mathbf{A}^T \mathbf{Q}_\mathbf{y}^{-\mathbf{1}} \mathbf{A} + \alpha \mathbf{B}^T \mathbf{B})^{-1} \mathbf{A}^T \mathbf{Q}_\mathbf{y}^{-\mathbf{1}} \mathbf{z}. \tag{3.17}$$

In practice, the computation of $\mathcal{T}_\alpha$ is divided into the following steps:

1. Generate a random vector $\mathbf{z}$.
2. Calculate two auxiliary vectors: $\mathbf{y}_1 = \mathbf{A}^T \mathbf{Q}_\mathbf{y}^{-\mathbf{1}} \mathbf{z}$ and $\mathbf{y}_2 = \mathbf{A}^T \mathbf{z}$.
3. Choose the regularization parameter,
   - For each admissible regularization parameter α in a given range, solve the system of linear equation $(\mathbf{A}^T {\mathbf{Q}_\mathbf{y}}^{-1} \mathbf{A} + \alpha \mathbf{B}^T \mathbf{B})\mathbf{q}_\alpha = \mathbf{y}_1$ and the system of equation (3.11). It makes sense to solve both systems simultaneously because they share the same normal matrix.
   - Compute the trace estimator $\mathcal{T}_\alpha = \mathbf{y}_2^T \mathbf{q}_\alpha$ and the GCV function itself [equation (3.14)].
   - Choose the regularization parameter α, which makes f_α^{gcv} minimum.

Thus, each computation of the GCV function reduces to only two inversions: one is to obtain the estimates $\hat{\mathbf{c}}_\alpha$, and the other to compute $\mathbf{q}_\alpha$.

3.3.3 Simulation study

In order to demonstrate the performance of the method proposed, we have simulated a CHAMP-like kinematic orbit (sampling: 30 seconds, and the time interval: 00:00:00 - 24:00:00 of 2000-01-01) by means of a numerical integration technique [Schrama, 2001]. In doing so, we made use of the EGM96 gravity field model [Lemoine et al., 1998]. This orbit was considered as the true one. At the next stage, three realizations of Gaussian white noise with a standard deviation of 5 cm were generated and added to all three components of the true orbit. The resulting noisy orbit has played a role of the kinematic orbit that can be obtained from GPS data. Furthermore, this noisy orbit was used to compute the force acting

on the satellite at each orbit point. This information is needed for the purpose of regularization. Considering that the precise force model is not known in practice, two force data sets were generated by using the EGM96 model truncated at degree 10 and 50, respectively. A smoothed orbit was obtained with three processing schemes:

- Scheme A: Least-square smoothing without acceleration constraints.
- Scheme B: Forces generated from the degree 10 gravity field model are used as acceleration constraints. The GCV procedure is employed to find the optimal regularization parameter.
- Scheme C: The same as Scheme B, but the forces are computed from the degree 50 gravity field model.

The degree of B-splines used in computations was set equal to 5 (degrees larger than 5 could be also chosen, but it has no significant effect on the final solutions). The knots were defined at every second epoch. No iteration is needed in this simulation since no data gaps are simulated in the case. Figure 3.3 shows differences between the smoothed orbits recovered by the three processing schemes and the true orbit. The RMS statistics of the discrepancies between the smoothed orbits and the true orbit is displayed in table 3.1. It can be seen that the Scheme C leads to the best result. This confirms that the estimation procedure can benefit from an *a priori* force model and that the more precise the force model is, the higher the accuracy of the smoothed orbit. On the other hand, even a relatively simple force model (e.g. up to degree 10) significantly reduces noise in positions.

Figure 3.4 shows the GCV values against regularization parameters for Scheme B and C. The optimal regularization parameters chosen for Scheme B and C were found to be 10^6 and 10^{10}, respectively. This indicates that the more precise the acceleration constraints, the larger they contribute to the solution. Notice that the solution obtained with the Scheme A is free from regularization.

3.3.4 Smoothing a real CHAMP orbit for gravity field modeling

In order to further demonstrate the performance of the proposed procedure for kinematic orbit smoothing, we consider a 322-day set of CHAMP data (March

Table 3.1. The RMS statistics of the smoothed orbits and the true orbit

difference RMS	noise (cm)	Scheme A (cm)	Scheme B (cm)	Scheme C (cm)
along-track	5.03	3.53	2.54	0.87
cross-track	5.13	3.57	2.25	1.21
radial	5.11	3.68	2.61	1.17

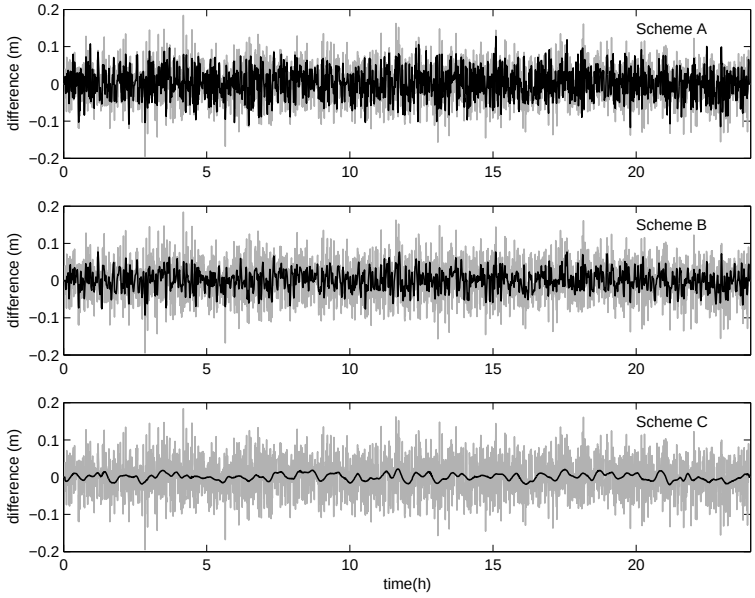

Fig. 3.3. The difference between the smoothed orbits and the true orbit of along-track component in black; the grey line depicts the simulated noise. The force models make the orbit smoother

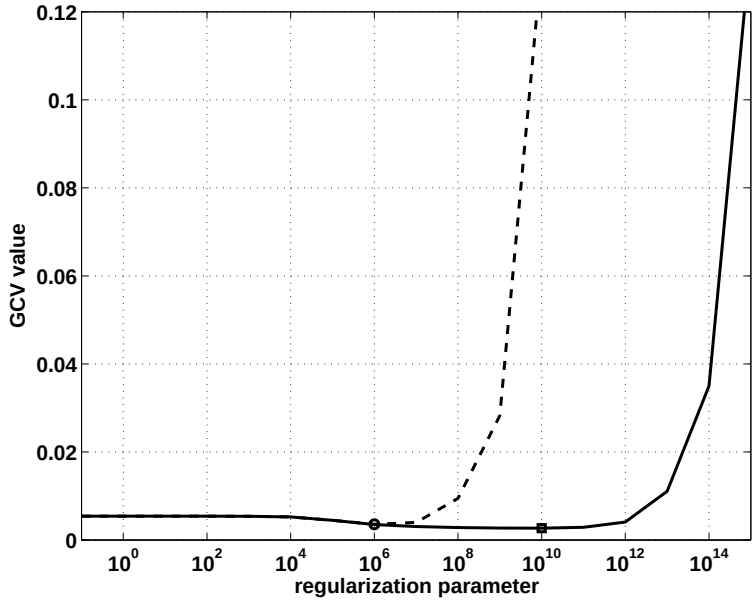

Fig. 3.4. GCV functions depending on the regularization parameters (dashed line for Scheme B and solid line for Scheme C). The optimal parameters are indicated by circle for the Scheme B, and with the square for the Scheme C

2002 to January 2003) in the context of gravity field modeling. The data sets consist of: (i) a kinematic orbit; (ii) description of the kinematic orbit noise in the form of a 3×3 position error covariance matrix per epoch (taken as *a prior* noise model of the input data); (iii) a reduced-dynamic orbit computed on the basis of the EIGEN-2 gravity field model [Reigber et al., 2002]; (iv) a set of accelerometer data supplied with star camera data and other supporting information. The first 3 data sets were kindly provided by D. Švehla and M. Rothacher, Technical University Munich [Švehla and Rothacher, 2002]. The accelerometer data are distributed by CHAMP's Information System and Data Center (ISDC) at GeoForschungsZentrum Potsdam (GFZ).

The first step of the study is to smooth the real CHAMP kinematic orbit. Three versions of a smoothed orbit are calculated:

(1) A smoothed kinematic orbit computed without a force model, i.e. no acceleration constraint. A least-squares solution is obtained in this case.

(2) A smoothed kinematic orbit with the acceleration constraint, the force model is based on the EGM96 gravity field model complete to degree/order 360.

(3) The same as (2), but the force model is based on the EIGEN-CG03C gravity field model also complete to degree/order 360. This model is much accurate than EGM360 since it was compiled from GRACE data.

Both (2) and (3) are regularized solutions. The purpose of using a GRACE-based model is to see how important the accuracy of a force model in orbit smoothing is. During the orbit smoothing, X-,Y- and Z- components of the orbit are processed separately, and the formal standard deviations of three components at each epoch are used to form the covariance matrix $\mathbf{Q_y}$. Correlations between components and between epochs are not considered, i.e. the matrix $\mathbf{Q_y}$ is diagonal. For the least-squares solution (strategy 1), the smoothed orbit is split into independent fragments if a gap in the kinematic orbit exceeds 5 minutes, in order to avoid a rank deficiency of the normal matrix. Due to the presence of gaps in the kinematic orbit, the regularized solutions (strategy 2 and 3) are computed iteratively, the threshold of the stopping criterion is 1 mm. If, however, a gap is sufficiently long ($>$ 15 minutes), the orbit is simply split into independent fragments to be processed separately. The optimal regularization parameter is chosen for each fragment, individually.

After that, we have used the procedure discussed in section 3.2 to recover gravity field models up to degree/order 70 (the post-processing was not applied in this case). All three smoothed orbits are used to compute the reference accelerations. In order to complete the comparison, the original reduced-dynamic orbit and kinematic orbit are also considered. The data screening is implemented on the basis of the discrepancies between a smoothed and the kinematic orbit. In the case of the kinematic orbit, when no smoothed orbit is involved in computing the reference accelerations, the data screening is based on the

smoothed kinematic orbit computed with the EGM96 model. The reference model for computing the reference accelerations is the EGM96 model. The reason for this is that the model was until recently one of the most accurate models of the Earth's gravity field computed without CHAMP and GRACE data. It should be mentioned that the observed accelerations are always derived from the kinematic orbit. The covariance matrix of data noise of the kinematic orbit is used. However, the *a prior* covariance matrix of the EGM96 model is not used for this computation, therefore, no regularization is implemented in the course of the inversion. Furthermore, we do not consider the frequency-dependent data weighting discussed in section 2.6.3. It means that the noise in accelerations is considered as non-correlated. The reason for this is that we intend to minimize the influence of other operations, in order to find out only how large the indirect influence of a gravity field model is through the orbit used to compute the reference accelerations. Five models are obtained and compared in terms of geoid height with the EIGEN-GL04C model, which is one of the state-of-the-art models computed on the basis of GRACE and LAGEOS as well as surface gravity field data [Förste et al., 2006, Förste et al., 2007]. The dominating contributor to the EIGEN-GL04C model at degrees below 70 is a two-year set of GRACE data. Since these data are significantly more accurate than CHAMP data, discrepancies between a CHAMP-based model and the EIGEN-GL04C model can be safely interpreted as errors in a CHAMP-based model.

Table 3.2. The cumulative geoid height differences between the produced models and the EIGEN-GL04C model at degree 2, 5, 10, 30, 50 and 70, respectively. 'ko', 'sko_ls', 'sko_EGM96', 'sko_CG03C' and 'rdo' stand for reference accelerations computed along 'the kinematic orbit', 'the kinematic orbit smoothed without constraint', 'the kinematic orbit smoothed with EGM96', 'the kinematic orbit smoothed with EIGEN-CG03C', and 'the reduced-dynamic orbit', respectively

Geoid height difference	$l = 2$ (mm)	$l = 5$ (mm)	$l = 10$ (mm)	$l = 30$ (mm)	$l = 50$ (mm)	$l = 70$ (mm)
ko	2.8	6.3	9.6	24.2	87.8	358.5
sko_ls	2.1	4.8	8.2	21.0	75.3	312.5
sko_EGM96	2.3	4.9	7.8	20.6	71.7	301.8
sko_CG03C	2.3	4.8	7.7	20.5	70.7	299.2
rdo	4.7	5.9	7.9	19.4	67.9	288.4

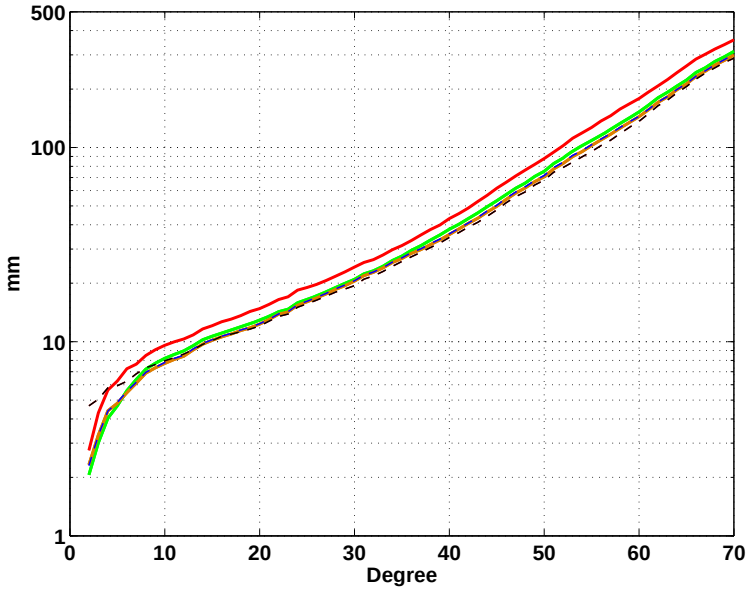

Fig. 3.5. The cumulative geoid height differences between the produced models and the EIGEN-GL04C model. In producing these models, the corresponding reference accelerations are computed along the kinematic orbit (red solid line), the kinematic orbit smoothed without constraint (green solid line), the kinematic orbit smoothed with the EGM96 model (orange solid line), the kinematic orbit smoothed with the CG03C model (blue dashed line), and the reduced-dynamic orbit (black dashed line)

From figure 3.5 and table 3.2, we can see the following features: (1) Usage of smoothed orbits to compute the reference accelerations produce better models than usage of the kinematic orbit. At least 10% improvement can be observed. (2) The smoothed orbits on the basis of regularization are slightly superior to the least-squares one. (3) As far as the smoothed orbits with force models are concerned, the choice of the gravity field model in the force model shows a very minor influence on the quality of the final product. (4) The reduced-dynamic orbit results in a slightly worse model than smoothed orbits up to degree 10. Above that degree, it produces slightly better model, though the difference is very limited.

Through this case study of real data processing, one can see, on the one hand, that the smoothed kinematic orbit can replace the reduced-dynamic orbit in the procedure of data processing since it can produce a model of almost the same accuracy as the reduced-dynamic orbit. On the other hand, we found the orbit used to compute the reference accelerations has relatively small influence on the accuracy of the gravity field, provided that the orbit is sufficiently smooth and accurate. Therefore, the answer to the question raised in section 3.2 is the following. The reduced-dynamic orbit does not cause significantly higher quality of the gravity models via the orbit used to compute the reference accelerations. However, a smoothed orbit is worthy to be computed since this guarantees that our CHAMP model is fully independent from any other CHAMP- or GRACE-

based *a priori* information. Therefore, we will use the smoothed kinematic orbit in further experiments on gravity field modeling in this chapter.

3.4 Noise estimation from posterior residuals

The section will describe the theory and the procedure of noise estimation. A numerical simulation of data processing is carried out, and its results are demonstrated. The section is partly based on our papers [Liu et al., 2005, Ditmar et al., 2007].

3.4.1 Theory

A data processing strategy results in a statistically optimal model only, if it fully benefits from the acquired information. From this point of view, the full covariance matrix of observation noise has to be exploited. If the *a priori* covariance matrix of observation noise is not accurate, or missing, one of the possible ways to estimate the noise properties is to derive them from the data themselves. Followed the average acceleration approach discussed in the previous sections, the estimation of a gravity field model is given as:

$$\hat{\mathbf{x}} = \left(\mathbf{A}^T\mathbf{C}_{\mathbf{d}}^{-1}\mathbf{A} + \mathbf{C}_{\mathbf{x_o}}^{-1}\right)^{-1}\mathbf{A}^T\mathbf{C}_{\mathbf{d}}^{-1}\mathbf{d}, \tag{3.18}$$

where $\mathbf{A}$ is the design matrix, $\mathbf{d}$ is the set of computed residual accelerations (here only one input data set is considered), and $\mathbf{C}_{\mathbf{x_o}}$ is the covariance matrix of the reference gravity model; its inverse plays the role of the regularization matrix. It is expected that the matrix $\mathbf{C}_{\mathbf{x_o}}$ is provided *a priori*. In the previous section, we did not use this matrix in gravity field modeling. The matrix $\mathbf{C}_{\mathbf{d}}$ may be an *a priori* covariance matrix of the data noise. However, this prior stochastic model may not be accurate enough to reflect the real noise characteristics. In order to obtain the optimal solution, it can be advisable to (re-)estimate the noise covariance matrix. This section focuses on an estimation procedure.

It is assumed [Ditmar et al., 2007] that the noise covariance matrix can be represented as:

$$\mathbf{C}_{\mathbf{d}} = \mathbf{P}\mathbf{C}^{(\mathbf{nst})}\mathbf{P}^T, \tag{3.19}$$

where $\mathbf{C}^{(\mathbf{nst})}$ is a diagonal matrix of size $N' \times N'$; $\mathbf{P}$ is a rectangular matrix of size $N \times N'$ obtained from a band-limited Toeplitz matrix by a corresponding 'horizontal extension'. N is the number of a data in a segment without gaps, and $N' = N + N_p - 1$, where N_p is the number of non-zero diagonals in $\mathbf{P}$. The matrix $\mathbf{C}^{(\mathbf{nst})}$ is responsible for the non-stationarity of the noise model, whereas the matrix $\mathbf{P}$ introduces correlations. The definition of equation (3.19) resembles the noise propagation formula. It can be interpreted as the assumption that actual noise is produced from non-stationary and non-correlated noise, i.e. the covariance matrix $\mathbf{C}^{(\mathbf{nst})}$, through the linear transformation given by the matrix $\mathbf{P}$. The matrix $\mathbf{P}$ is introduced purely on a formal basis. We do not introduce a

physical meaning for the matrix. In this section, we will discuss how entries of the matrix $\mathbf{P}$ can be estimated.

The matrix $\mathbf{C}^{(\mathbf{nst})}$ is assumed to be given *a priori*. We believe that this assumption is reasonable, because in most cases the measurements are supplied with error estimates, which give an idea of how the measurement accuracy changes in time. The only elements of the matrix $\mathbf{C}^{(\mathbf{nst})}$ that are not available in this way are the elements at the edges, which have to be included as the result of the extension of the matrix $\mathbf{P}$ and, consequently, of the matrix $\mathbf{C}^{(\mathbf{nst})}$. We propose to set these elements equal to σ^2, the average value of the available diagonal elements of the matrix $\mathbf{C}^{(\mathbf{nst})}$. Furthermore, the matrix $\mathbf{P}$ still has to be defined. Therefore, we can assume without loss of generality that $\sigma^2 = 1$: the necessary scaling can be assigned to the matrix $\mathbf{P}$. This means that the unavailable diagonal elements of the matrix $\mathbf{C}^{(\mathbf{nst})}$ can simply be set equal to 1.

If the data set contains gaps, the matrix $\mathbf{C_d}$ has to be modified by a mask matrix $\mathbf{M}$ obtained from the unit matrix by removing the rows that correspond to the missing data [Klees and Ditmar, 2003, Ditmar and van Eck van der Sluijs, 2004]. Notice that a gap in the data series is, most probably, accompanied by a gap in the time-series of primary formal measurement errors, i.e. more elements of the matrix $\mathbf{C}^{(\mathbf{nst})}$ might not be available *a priori* than in the case of an uninterrupted data set. These elements can be filled in the same way as the unavailable elements at the edges.

To estimate the covariance matrix of a stationary noise, we need to know a noise realization $\mathbf{n}$. Since $\mathbf{n}$ is by definition the difference between the data $\mathbf{d}$ and the response of the true model $\mathbf{Ax}$, the best possible gravity field model is needed at this stage. Usage of such a model, however, would make the results of data processing dependent on that model. Therefore, it is more appropriate for the noise estimation to use the model produced solely from the data set under consideration. Then, the noise realization $\mathbf{n}$ is approximated by the set of posterior residuals. This approach suggests that the gravity field modeling consists of a few iterations. In the course of the iterations, the gravity field model and the stochastic model of data noise (expressed by the covariance matrix $\mathbf{C_d}$) are successively improved. In practice, two iterations are sufficient; further update of the gravity field model is not necessary provided that the number of data substantially exceeds the number of unknown parameters, which is indeed the case of static gravity field modeling from SST data. The practical objective of the estimation is to define the matrix $\mathbf{P}$ of equation (3.19), which is the only ingredient of the noise model that is not given *a priori*. According to [Ditmar et al., 2007], the whole procedure is as follows:

Step 1 Posteriori residuals $\hat{\mathbf{n}}$ are computed as the differences between the original and adjusted observations $\hat{\mathbf{n}} := \mathbf{d} - \mathbf{A}\hat{\mathbf{x}}$. The residuals are considered as an approximation of data noise.

Step 2 The noise auto-covariance are estimated from the posteriori residuals (see

also Appendix A).

$$c_k = \frac{1}{N_k} \sum_j n_j n_{j\pm k} \quad (0 \le k \le N_a), \tag{3.20}$$

where n_j and $n_{j\pm k}$ are posteriori residuals at two epochs separated by lag k; N_a is the maximum lag for which the auto-covariance is estimated. In practice, $N_a = N/10$ is appropriate [Klees and Broersen, 2002]. and N_k is the number of pairs of elements that are used in the estimation of the k-th auto-covariance element. Notice that both elements of each pair should have indices in the interval $(1, N)$, where N is the number of posteriori residuals. Furthermore, some pairs with proper indices may be discarded if a noise realization is replaced by a posteriori residuals, because such a series may contain interruptions related to gaps in the original data.

Step 3 The auto-covariance elements such that the element with index zero becomes the first one, as $\mathbf{c} := (c_0, c_1, c_2, ..., c_{N_a-1}, c_{N_a}, c_{N_a-1}, ..., c_1)$.

Step 4 The noise PSD is smoothed to ensure that it is positive at all frequencies and, consequently, that the noise covariance matrix $\mathbf{C_d}$ is positive-definite. The smoothing is implemented by multiplying the original auto-covariance with a function that rapidly decreases in time:

$$\tilde{c}_k := c_k w_k \qquad (0 \le k \le N_a). \tag{3.21}$$

with the truncation function w_k being

$$w_k = e^{-\frac{(k\Delta t)^2}{2Q^2}}. \tag{3.22}$$

The maximum possible half-width Q of the truncation function can be defined by means of the trial-and-error method. The procedure starts from a very large Q and gradually decreases until the PSD becomes positive at all the frequencies.

Step 5 The step is to estimate the noise Power Spectral Density (PSD) $u(f)$, where f is the frequency. The noise PSD can be obtained from the auto-covariance sequence through a discrete Fourier transformation,

$$\mathbf{u} \approx \Delta t \mathbf{F}^* \mathbf{c}, \tag{3.23}$$

where $\mathbf{F}$ is the matrix of discrete Fourier transform, $\left\{\mathbf{F}\right\}_{jk} = e^{ijk\frac{2\pi}{N_a}}$, $\mathbf{F}^*$ the transposed complex conjugate of $\mathbf{F}$, and Δt the sampling interval.

Step 6 The matrix $\mathbf{P}$ is computed by applying the inverse Fourier transformation to the square root of the smoothed PSD as:

$$\mathbf{P} = \mathbf{M}\sqrt{\frac{\Delta f'}{N'}}\mathbf{F}\mathbf{U}^{\frac{1}{2}}\mathbf{F}^*, \tag{3.24}$$

with $\mathbf{M}$ being the mask matrix, and the diagonal matrix $\mathbf{U}$ being composed of the elements of vector $\mathbf{u}$, and $\Delta f' = 1/(N'\Delta t)$, which is the sampling interval in the frequency domain.

In the context of our research, Step 6 is extended by computing an analytical function (i.e. derived from equations (2.116), (2.119) and (3.23) with considering *a priori* accuracy and necessary scaling) that approximates the noise PSD $u(f)$, or to be more precise, the square root of it:

$$\sqrt{u(f)} = \frac{\beta \cdot \sigma}{(\Delta t)^{\frac{3}{2}}} \left[2\left(1 - \cos(2\pi f \Delta t)\right) + \left(\frac{\Delta t}{\tau}\right)^2 \right], \tag{3.25}$$

where $f = k\Delta f'$, β is the scaling factor that plays a role of a relative weighting factor applied to given component, σ is the *a priori* average positioning accuracy of the component and τ is a parameter that controls the behavior of the PSD at low frequencies as discussed in chapter 2. The advantage of this approximation is that the corresponding noise covariance matrix can be built analytically. In the absence of data gaps, the noise covariance matrix per component can be represented as $\mathbf{C_d} = \mathbf{P}\mathbf{C}^{(\mathbf{nst})}\mathbf{P}^T$, where

$$\mathbf{P} = \frac{\beta \cdot \sigma}{(\Delta t)^2} \begin{pmatrix} -1 & 2+\left(\frac{\Delta t}{\tau}\right)^2 & -1 & & \\ & \ddots & \ddots & \ddots & \\ & & -1 & 2+\left(\frac{\Delta t}{\tau}\right)^2 & -1 \end{pmatrix}. \tag{3.26}$$

The optimal estimation of the parameters β and τ is found by means of a non-linear least-squares adjustment to the square root of the smoothed PSD obtained in Step 5. Let the parameters β and τ form the vector of unknowns $\mathbf{b}$. Then, the estimation procedure is as follows:

(1) Set the initial guess $\mathbf{b_0} := (\beta_0, \tau_0)^T$ (e.g. $\beta_0 = 1$, $\tau_0 = 180$ s, which are the settings for the trial gravity field modeling).

(2) Compute vector $\Delta\mathbf{y} := \sqrt{u(\mathbf{f})} - \sqrt{u(\mathbf{f})}\Big|_{\mathbf{b=b_0}}$.

(3) Compute the partial derivatives,

$$\begin{aligned} \frac{\partial\left(\sqrt{u(\mathbf{f})}\right)}{\partial\beta}\Big|_{\mathbf{b=b_0}} &= \frac{\sigma_0}{(\Delta t)^{3/2}}\left(2(1-\cos(2\pi\cdot\mathbf{f}\cdot\Delta t)) + (\Delta t/\tau_0)^2\right) \\ \frac{\partial\left(\sqrt{u(\mathbf{f})}\right)}{\partial\tau}\Big|_{\mathbf{b=b_0}} &= \frac{-2\sigma_0\cdot\beta_0}{(\Delta t)^{3/2}}\left((\Delta t)^2/{\tau_0}^3\right), \end{aligned}$$

and form the design matrix

$$\mathbf{H} := \begin{pmatrix} \frac{\partial\left(\sqrt{u(\mathbf{f})}\right)}{\partial\beta}\Big|_{\mathbf{b=b_0}} & \frac{\partial\left(\sqrt{u(\mathbf{f})}\right)}{\partial\tau}\Big|_{\mathbf{b=b_0}} \end{pmatrix}. \tag{3.27}$$

(4) Compute the corrections: $\Delta\mathbf{b} = (\mathbf{H^T H})^{-1}(\mathbf{H^T \Delta y})$.

(5) Set $\mathbf{b_0} = \mathbf{b_0} + \Delta\mathbf{b}$, if $\|\Delta\mathbf{b}\| > \epsilon$ go to (2), otherwise go to (6).

(6) $(\hat{\beta}, \hat{\tau})^T = \mathbf{b_0}$.

Finally, the matrix $\mathbf{C_d}$ can be obtained according to equation (3.19). It can be then used for another estimation of the Earth's gravity field.

3.4.2 Simulation case

The purpose of our simulation is to evaluate how accurately the noise stochastic properties can be assessed from data posteriori residuals and how an inaccuracy of the used stochastic model can influence the gravity field model. We recall that the data are defined as residual satellite accelerations averaged over sampling intervals. In order to simulate the reality as close as possible, some real CHAMP data sets are used.

3.4.2.1 Setup of the simulation

In the numerical study, we consider stationary and non-stationary colored noise added to a series of simulated residual accelerations. In the simulation case, the true noise is known, and consequently, the truly optimal estimation of the gravity field can be obtained. Therefore, the study provides an opportunity to validate our estimation methodology. The following data sets are used:

1) Satellite orbit: a 322-day reduced-dynamic CHAMP orbit from March 10, 2002 to January 25, 2003; 30-s sampling.

2) Error bars: the formal errors of a 322-day kinematic orbit of the CHAMP satellite. Only variances of three components are considered.

3) Simulated accelerations $\mathbf{d_{obs}}$: this data set is computed from EIGEN-CG01C model of the Earth's gravity field [Förste et al., 2005] along the satellite orbit. The data gaps from the real CHAMP kinematic orbit are included, because the kinematic orbit is used to derive the "observed" accelerations in real CHAMP data processing [Ditmar et al., 2006]. The EIGEN-CG01C model is taken as the true model later for the purpose of comparison.

4) The reference model: EGM96 model is used to compute the reference satellite accelerations, $\mathbf{d_{ref}}$. Then, the residual (noise-free) accelerations are obtained as $\mathbf{d} := \mathbf{d_{obs}} - \mathbf{d_{ref}}$.

5) Covariance matrix $\mathbf{C_{x_0}}$ of the reference model up to degree and order 70. It means that we consider a regularized solution in this simulation.

6) Simulated noise: for each component, a realization of stationary colored noise $\mathbf{n^{sc}}$ is generated. Each realization is obtained as:

$$n_i^{sc} = \frac{\sigma}{(\Delta t)^2}\Big(- n_{i-1} + \Big(2 + (\Delta t/\tau)^2\Big)n_i - n_{i+1}\Big), \tag{3.28}$$

where $\Delta t = 30s$ (the sampling rate of the data set); τ is the parameter that controls the behavior at low frequencies (we set $\tau = 40\,\text{sec}$ according to our experiences with real CHAMP data); σ is the standard deviation of position errors (we set $\sigma_X = 1.9\,\text{mm}$, $\sigma_Y = 1.4\,\text{mm}$ and $\sigma_Z = 4.4\,\text{mm}$ for three components, respectively, according to our experiences with real CHAMP data) and $n_i \quad (i = 1, 2, ..., nr$ with $nr = 927360)$ is a white noise realization with a unit standard deviation and zero mean. These noise realizations are used to generate a noisy data set $\mathbf{d_1} := \mathbf{d} + \mathbf{n^{sc}}$. The noise behavior in the frequency domain is shown in figure 3.6.

7) Three realizations of non-stationary noise $\mathbf{n^{ns}}$ are obtained as:

$$n_i^{ns} = \frac{1}{(\Delta t)^2}\Big(- \sqrt{a_{i-1}}n_{i-1} + \Big(2 + (\Delta t/\tau)^2\Big)\sqrt{a_i}n_i - \sqrt{a_{i+1}}n_{i+1}\Big), \quad (3.29)$$

where a_i are the scaled variances of the kinematic orbit (data set 2). The scaling was applied in such a way that the average of the square root of these variances is 1.9 mm, 1.4 mm and 4.4 mm for **x**-, **y**-, **z**-component, respectively. Notice that the obtained noise realizations are not only non-stationary, but also time-correlated. These noise realizations are used to generate another noisy data set $\mathbf{d_2} := \mathbf{d} + \mathbf{n^{ns}}$.

8) An inaccurate *a priori* stochastic model with diagonal covariance matrix $diag\{\Sigma_X^2, \Sigma_Y^2, \Sigma_Z^2\}$ is considered for data set $\mathbf{d_1}$: $\Sigma_X = 11.2\,\text{mm}$, $\Sigma_Y = 9.8\,\text{mm}$ and $\Sigma_Z = 15.8\,\text{mm}$. These values are actually obtained by averaging the square root of formal variances (data set 2). The unscaled formal variances of the CHAMP kinematic positions are taken as the *a priori* stochastic model for the data set $\mathbf{d_2}$.

3.4.2.2 Results of simulation

According to figure 3.1, we implemented in the first step a trial gravity field estimation on the basis of the two generated data sets containing stationary and non-stationary noise, respectively. The inaccurate *a priori* stochastic models (data set 8) are used at this step. τ is set to 180 s and β is set to 1. This results in trial gravity field models, see the processing step in figure 3.1. On the basis of the trial gravity field models, the posterior residuals for two cases are computed. After that, we follow the procedure described in section 3.4.1 to estimate the noise model by using the analytical expression of equation (3.25). The noise model is then used in the final data processing. Consequently, the final gravity field model is obtained. For comparison, we also use the true *a priori* stochastic model to process the data which results in the optimal gravity field model. The final gravity field model in each case is obtained by the summation of the result of the least-squares adjustment and the reference model (EGM96). All the gravity field models are computed up to degree and order 70.

Results in the case of stationary noise are displayed in figures 3.6 and 3.7. Figure 3.6 shows the square root of PSDs used to derive the trial and final gravity

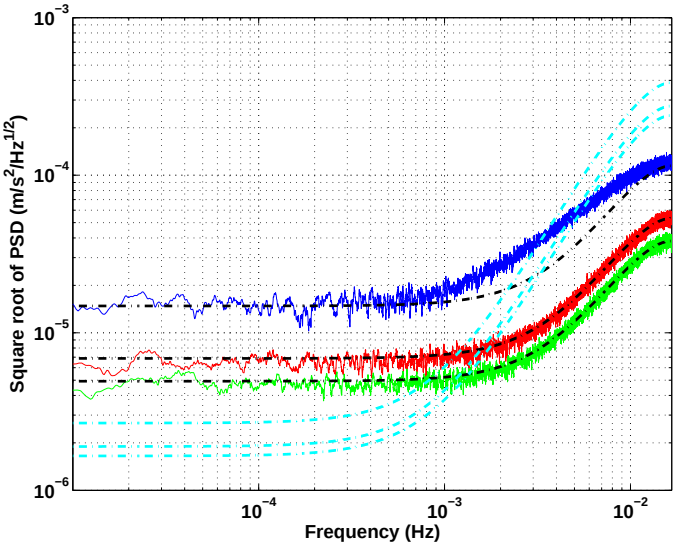

Fig. 3.6. Estimation of noise PSD in the case of stationary noise for radial component (blue line), along-track component (red line) and cross-track component (green line), respectively. Black dashed curves depict the true square-root PSD of noise. Light blue dashed lines correspond to the *a priori* stochastic model

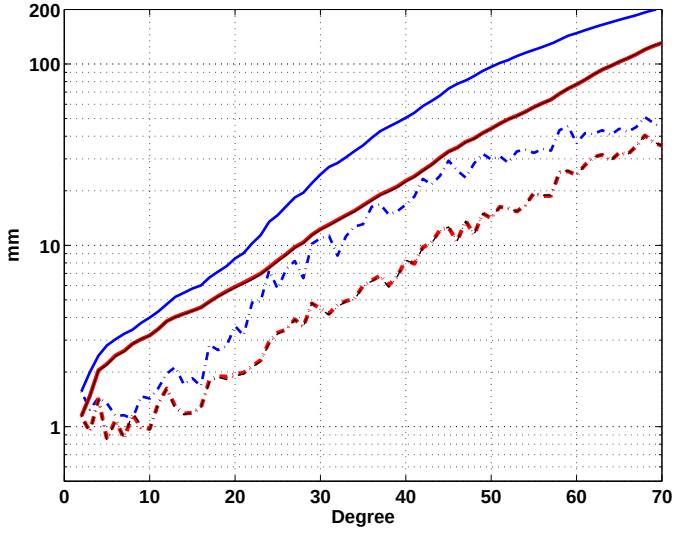

Fig. 3.7. Accuracy of gravity field models obtained in the case of the simulated stationary noise data: cumulative geoid height differences (solid lines) and geoid height differences per degree (dashed lines) with respect to the "ground-truth". The models are obtained using the trial noise model (blue), the estimated final noise model (red) and the true noise model (black)

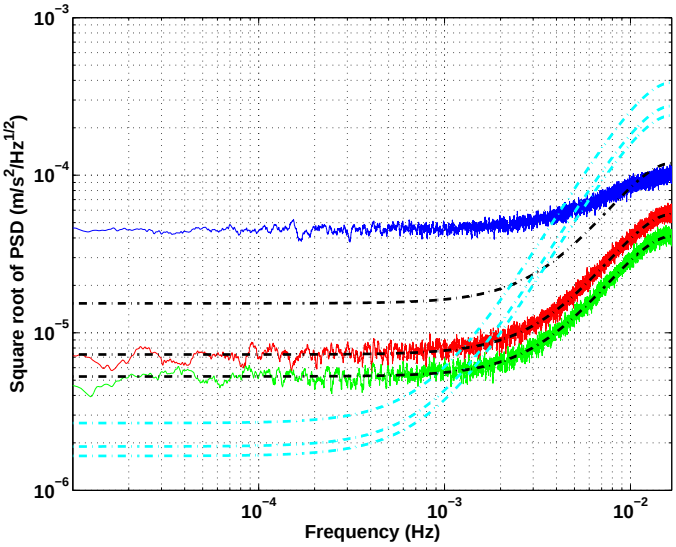

Fig. 3.8. Estimation of noise PSD in the case of non-stationary noise for radial component (dark blue line), along-track component (red line) and cross-track component (green line), respectively. Black dashed curves depict the true square-root PSD of noise. Light blue dashed lines correspond to the *a priori* stochastic model

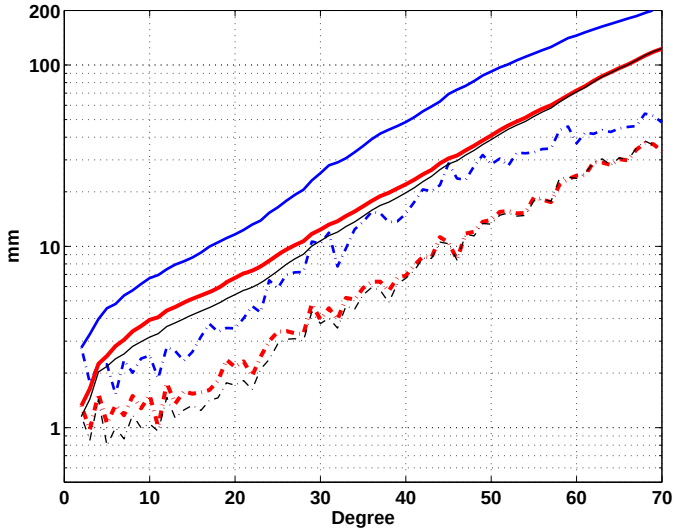

Fig. 3.9. Accuracy of gravity field models obtained in the case of the simulated non-stationary noise data: cumulative geoid height differences (solid lines) and geoid height differences per degree (dashed lines) with respect to the "ground-truth". The models are obtained using the trial noise model (blue), the estimated final noise model (red) and the true noise model (black)

field models as well as the true one. It is obvious that the dependence of noise on frequency is determined rather accurately: the estimations of posterior residual PSDs are much closer to the true noise PSDs than the *a priori* PSDs. Figure 3.7 compares the obtained gravity field models with the true model (EIGEN CG01C) in terms of geoid heights. We can see clearly that the final gravity field model is very close to the optimal one obtained with the true stochastic model of simulated noise.

Figures 3.8 and 3.9 show results in the case of non-stationary noise, similar to figure 3.6 and 3.7. The conclusion can be drawn that certain differences between the true and the estimated noise square-root PSD is noticeable in the radial component. The probable reason is that the non-stationarity of noise manifest itself as a strong noise at low frequencies if the spectral representation is used. Additionally, it is found that the accuracy of the final gravity field model is close to that of the optimal model, even though the exploited stochastic model somewhat deviates from the true one. This can be explained by the fact that the error in the variance-covariance matrix has a second-order order influence on the estimated parameters. It is important to add that we have made an effort of a third iteration, but no obvious improvement has been obtained in both stationary and non-stationary noise cases.

In addition, it can be noticed that knowledge of data noise may noticeably improve the quality of gravity field modeling, and that the procedure of noise estimation allows one to avoid tuning of some processing parameters by comparing the results with a state-of-the-art model as it was proposed by [Ditmar et al., 2006]. This is rather important when there is no suitable state-of-the-art model available, e.g. in the context of GRACE data processing.

3.5 Results of real CHAMP data processing

The simulations conducted prove that the process of noise estimation can improve the quality of the resulting gravity field model. Therefore, we have applied it also to real data processing. We have processed the same real data set: a 322-day set of CHAMP data as described in section 3.3.4. The differences with the previous data processing strategy different are as follows:

(1) The smoothed kinematic orbit based on the EGM96 model (one of the smoothing outputs of section 3.3.4) is taken as a set of observation locations to compute the reference accelerations. The EGM96 model up to degree and order 360 is again used for this purpose. Thus, a reduced-dynamic orbit is not used at all.

(2) As in the simulation case, the full covariance matrix of the EGM96 model up to degree and order 70 is used as the regularization matrix during the inversion in order to obtain the optimal solution.

(3) The full 3×3 covariance matrix at each epoch, instead of only the variance

matrix, is used to construct the matrix $\mathbf{C}^{(\mathbf{nst})}$. This covariance matrix is scaled so that the average variance per component (along track, cross-track and radial) is equal to one.

(4) As before, the inversion is performed twice; the first time to compute the preliminary trial gravity field modeling, and the second time to obtain the final gravity field model.

The lag number (k in equation 3.20) in the computation of the auto-covariance is set equal to $2^{15}+1$, which corresponds to the time interval of $32,769 \times 30\,\text{sec} \approx 273\,\text{hr}$. To ensure the positiveness of the computed PSD, it is smoothed with $Q \approx 23\,\text{hr}$ for the along-track and cross-track components and with $Q \approx 29\,\text{hr}$ for the radial component. The smoothed square-root PSDs for the three components shown in figure (3.10) are used to compute the matrix $\mathbf{P}$ using the analytic expression described with equation (3.25). It is observed that the square-root PSDs of the real data case are closer to the stationary noise case (see figure (3.6)) than to the non stationary noise case (see figure (3.8)). The parameters chosen for the analytic approximation are: $\beta = 0.17,\ 0.14,\ 0.28$ for the along-track, cross-track and radial component, respectively; $\tau = 35\,\text{sec}$ for all three components. The obtained noise model is exploited to produce the final model, see figure 3.11 and table 3.3. The final model is named as DEOS_CHAMP-02C_70. Other gravity field models, such as EGM96, ITG-CHAMP01E, the trial field, and DEOS_CHAMP-01C_70 model, are also shown for comparison. The ITG-CHAMP01E model was produced from the same data set (the kinematic orbits used in the thesis) using the short-arc approach [Mayer-Gürr et al., 2005]. The model was also regularized using the EGM96 model. The DEOS_CHAMP-01C_70 model was produced by a stochastic model obtained with validating gravity field modeling results with a GRACE-based model [Ditmar et al., 2006]. In the comparison, the gravity field model EIGEN-GL04C, truncated at degree 70, is exploited as the ground truth. Both our trial and final models demonstrate a significant improvement with respect to the EGM96 model at all degrees. In addition, our final model outperforms the ITG-CHAMP01E model, likely due to more accurate modeling of the stochastic properties of the data noise. It is also worthwhile to note that the total RMS of the geoid height error for the final model is better than that for the DEOS_CHAMP-01C_70 model. More importantly, the empirical procedure to choose the optimal noise model used in computing the DEOS_CHAMP-01C_70 model is replaced by the one based on *a posteriori* residuals, so that the use of a state-of-the-art model is no longer required.

There are more CHAMP gravity field solutions computed by other research institutes; however, these models are generally not regularized. In order to make a comparison with those solutions, we have also computed CHAMP-only gravity field model without a regularization (the model is named as DEOS_CHAMP-02S_70). Figure 3.12 shows the comparison of our CHAMP-only solution with others, including the TUM-2S, EIGEN-CHAMP03S, ITG-CHAMP01S and AIUB-CHAMP01S models, in terms of geoid height differences per degree with respect to the EIGEN-GL04C model. In addition, Table 3.4 offers the cumulative geoid height differences

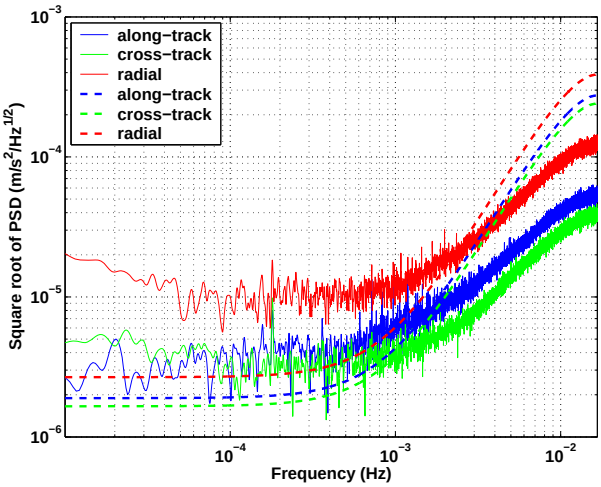

Fig. 3.10. The square-root PSD of the noise model for the three components. The dashed lines depict the prior stochastic model used for the trial gravity field modeling. The solid lines denote the estimated square-root PSD of the noise. The corresponding stochastic model is used to re-process the data

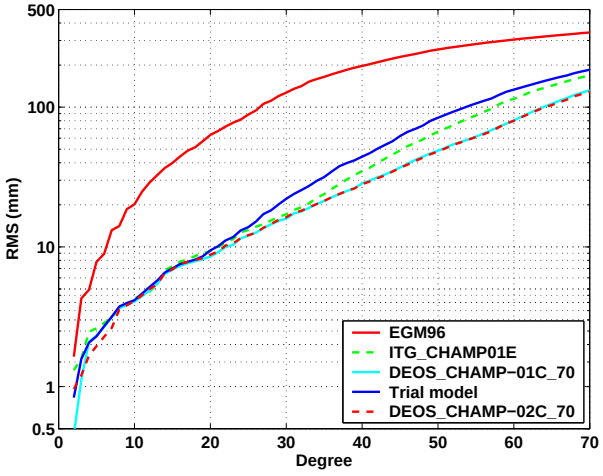

Fig. 3.11. The cumulative geoid height differences with respect to the EIGEN-GL04C model for the following models: (i) EGM96 (red solid), (ii) ITG-CHAMP01E (green dashed), (iii) the trial model without the noise estimation of residuals (blue), (iv) the final model after noise was estimated (red dashed) and (v) the DEOS_CHAMP-01C_70 model (light blue)

Table 3.3. The cumulative geoid height differences, with respect to the EIGEN-GL04C model, computed for various gravity field models

Geoid height difference	$l = 2$ (mm)	$l = 5$ (mm)	$l = 10$ (mm)	$l = 30$ (mm)	$l = 50$ (mm)	$l = 70$ (mm)
EGM96	1.6	7.8	20.2	126.9	258.8	342.0
ITG-CHAMP01E	1.3	2.6	4.3	17.1	66.6	168.7
DEOS_CHAMP-01C_70	0.5	2.3	4.1	15.9	48.9	132.2
the trial model	0.8	2.3	4.2	22.1	83.9	185.2
DEOS_CHAMP-02C_70	0.9	1.9	4.1	16.3	48.3	128.3

for these models. The TUM-2S model was computed up to degree and order 60 using the energy balance approach by the Institute for Astronomical and Physical Geodesy of Technical University Munich (TUM) [Wermuth et al., 2004]. The model is based on two years of CHAMP data spanning the interval from March, 2002 to March 2004. The EIGEN-CHAMP03S model produced by GFZ is a CHAMP-only gravity field model derived for the period from October 2000 to June 2003 (totally 33 months) [Reigber et al., 2004]. The model was computed using the variational equations approach (one step). The model contains spherical harmonic coefficients complete to degree and order 120 plus selected terms up to degree 140. In the comparisons shown, this model was truncated to degree and order 70. Since other three remaining solutions were produced from approximately one year of data, the degree errors of the TUM and GFZ solutions were scaled by the factor of $\sqrt{2}$ and $\sqrt{3}$, respectively, to make the comparison more fair. The ITG-CHAMP01S model [Mayer-Gürr et al., 2005] was again derived from the same kinematic orbit as was used to produce the DEOS solutions. The AIUB-CHAMP01S model was recently computed at the Astronomical Institute of University of Bern (AIUB) by using the orbit integration approach (two-step) [Prange et al. 2007]. The ITG and AIUB models were computed up to degree and order 70 as our CHAMP models.

From the comparison, one can see that the TUM-2S performs the worst at all degrees, particularly at the low ones, and it shows errors several times larger than the others. Even if the model is not multiplied by a factor of $\sqrt{2}$, the result is still much worse than for the other models tested. This is not very surprising because the energy balance approach only makes use of the velocity magnitude, leading to a situation when only the along-track information is exploited [Ditmar and van Eck van der Sluijs, 2004]. The EIGEN-CHAMP03S model (multiplied with $\sqrt{3}$) demonstrates less accuracy than the other three. The probable explanation here is that the model was produced using a sub-optimal stochastic model of the data noise. The same explanation can probably be given to the differences between our solution and the ITG-CHAMP01S model, particularly for the mid-degrees (i.e., starting from degree 31). Compared with the AIUB-CHAMP01S

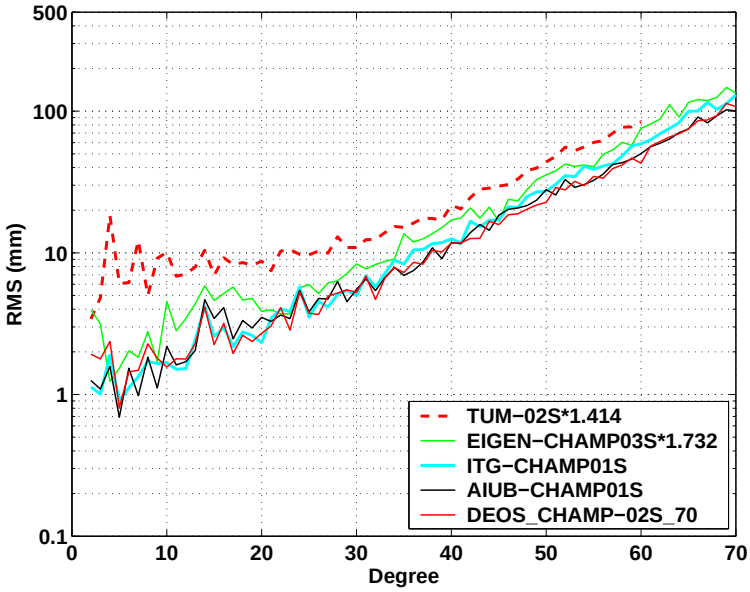

Fig. 3.12. The geoid height differences per degree with respect to the EIGEN-GL04C model computed for the models: (i) TUM-2S (red dashed line), (ii) EIGEN-CHAMP03S (green line), (iii) ITG-CHAMP01S (cyan line), (iv) AIUB-CHAMP01S (blue line) and (v) DEOS_CHAMP-02S_70 (red line). The values of TUM-02S and EIGEN-CHAMP03S are multiplied by a factor of $\sqrt{2}$ and $\sqrt{3}$, respectively.

Table 3.4. The cumulative geoid height differences with respect to the EIGEN-GL04C model computed for the models obtained at degree 10, 20, 40, 50, 60, 70, respectively. The values of TUM-02S and EIGEN-CHAMP03S models are multiplied with $\sqrt{2}$ and $\sqrt{3}$, respectively

Geoid height difference	$l = 10$ (mm)	$l = 20$ (mm)	$l = 40$ (mm)	$l = 50$ (mm)	$l = 60$ (mm)	$l = 70$ (mm)
TUM-2S	28.5	38.7	71.9	125.1	241.4	--
EIGEN-CHAMP03S	8.2	16.8	45.8	90.1	185.2	408.2
ITG-CHAMP01S	4.3	9.3	35.0	73.7	156.3	345.8
AIUB-CHAMP01S	4.3	10.8	32.1	69.3	137.4	290.5
DEOS_CHAMP-02S_70	5.3	9.8	31.8	64.1	131.3	294.7

model, our solution displays a remarkable similarity. The AIUB-CHAMP01S has slightly better accuracy at the two extremes, i.e. below degree 10 and above degree 60, while our solution shows better performance at the mid-degrees (from degree 10 to degree 60). This is likely an indication that both solutions are close to the statistically optimal one.

3.6 Summary and remarks

In this chapter, two refinements of the CHAMP data processing were discussed. The major objective of both refinements was to compute an optimal model that is independent of any reference gravity field model. The first refinement was the development of a procedure for smoothing a kinematic orbit by means of a regularized least-squares adjustment. The smoothed orbit is represented by B-splines. Processing was carried out using real data, in which the smoothed kinematic orbit produced a model of nearly the same level of accuracy as the reduced-dynamic orbit. In this way, dependence on a CHAMP-based model was avoided. In addition, we found that the orbit used to compute the reference accelerations has a relatively small influence on the accuracy of the gravity field. The second refinement was the implementation of a procedure for noise estimation from *a posteriori* residuals in order to obtain an optimal solution. The simulation and real data processing proved that the procedure is a key ingredient for accurate modeling the gravity field. These two refinements were used to compute both a regularized and non-regularized gravity field model from CHAMP data. The regularized CHAMP model was shown to perform better than alternative regularized models, such as the ITG-CHAMP01E and DEOS_CHAMP-01C_70. More importantly, the optimal noise model was determined from the *a posteriori* residuals as opposed to a GRACE-based model. The non-regularized solution was compared with other non-regularized CHAMP-only models. Our solution was shown to perform better than the TUM-2S model, as well as the EIGEN-CHAMP03S model if the difference in the length of the considered data sets is taken into account. Furthermore, our model shows improved accuracy over the ITG-CHAMP01S model, particularly at the high degrees. Compared with the AIUB-CHAMP01S model, our solution demonstrates remarkably small differences in quality, which can be interpreted as an indication that both solutions are close to the statistically optimal one.

Chapter 4

Gravity field modeling from GRACE hl-SST data

4.1 Introduction

In the previous chapter, we developed a CHAMP data processing strategy and processed a set of real CHAMP data. The GRACE satellites are each equipped with a high-end GPS receiver, so that the kinematic orbits of the two satellites can be obtained. Each of these two GRACE satellites can be considered as a single satellite mission of the CHAMP-type. Therefore, the CHAMP data processing, in the first instance, is applicable to processing of GRACE hl-SST data as well. This idea was investigated, in particular, by [Weigelt, 2007], who used the energy balance approach. The goal of our study is to develop this idea further by also taking into account the kinematic baselines of the two satellites as well. The kinematic baselines used in this chapter are not a simple difference of the kinematic orbits of the two GRACE satellites. Instead, they are determined directly from the GPS measurements by way of relative positioning. In this way, one satellite is taken as a reference, and the relative position of the other satellite, i.e. the baseline, is estimated from differenced GPS measurements, where the double-difference ambiguities are fixed at a relatively high success-rate (see [Kroes, 2006]). To derive the gravity field model from these kinematic baselines, we extend our data processing of kinematic positions. There are many differences between processing positions and baselines. This will be described in section 4.2. Section 4.3 will present the results of the baseline processing, as well as results obtained from kinematic orbits of the individual GRACE satellites.

4.2 Peculiar features of processing kinematic baselines

The flow chart of processing kinematic baselines is, in general, the same as that of processing kinematic positions, see figure 2.5 and figure 3.1. However, some steps need to be altered due to the change of the functional model and the available data.

This section will discuss the peculiar features of processing kinematic baselines.

4.2.1 Functional model

The functional model used to process the baselines of the two satellites involves Inter-Satellite Accelerations (ISA) rather than acceleration vectors of a single satellite.

$$\ddot{\mathbf{r}}_{AB}(t) = \nabla V(\mathbf{r}_B(t)) - \nabla V(\mathbf{r}_A(t)), \tag{4.1}$$

where $\ddot{\mathbf{r}}_{AB}(t)$ is the point-wise ISA at the epoch t, and the right-hand side is the difference of the potential gradients between two satellites.

4.2.2 Derivation of inter-satellite accelerations

The ISA vectors are derived from the precise kinematic baselines:

$$\bar{\ddot{\mathbf{r}}}_{AB}(t) = \frac{\mathbf{r}_{AB}(t-\Delta t) - 2 \cdot \mathbf{r}_{AB}(t) + \mathbf{r}_{AB}(t+\Delta t)}{(\Delta t)^2}, \tag{4.2}$$

where $\mathbf{r}_{AB}(t)$ is the kinematic baseline at epoch t in the CRF frame, and $\bar{\ddot{\mathbf{r}}}_{AB}(t)$ is the average ISA at time t. Notice that the left-hand side of equation (4.1) represents a point-wise value, while the left-hand side of equation (4.2) is an average value. As a result, an averaging filter has to be applied in order to relate them together. This can be done in the same way as in processing kinematic orbits. The ISAs derived from the satellite baselines are used as input to produce residual ISAs by deducing the reference ISAs and non-gravitational ISAs. We will discuss this further after introducing a new reference frame.

4.2.3 Line-Of-Sight related Reference Frame

The residual ISAs used in processing kinematic baselines are transformed into a so-called Line-Of-Sight Reference Frame (LOSRF) rather than into the LORF frame used previously. In the LOSRF frame, the **x**-axis is directed along the LOS, from the trailing satellite to the leading one; the **z**-axis points upwards (nearly radial), and is orthogonal to the **x**-axis in the plane formed by the two satellites and the center of the Earth. The **y**-axis is orthogonal to the **x**- and **z**-axis forming a right-hand frame, as shown in figure (4.1). The LOSRF frame is very similar to the LORF frame since the two GRACE satellites follow each other in nearly the same orbit. The computation of the unit vectors that define the LOSRF in the Earth-centered inertial reference frame is important for transforming vectors from one frame to the other. The unit vector of LOS can be easily computed as:

$$\mathbf{e}_{\mathbf{x}} = \frac{\mathbf{r}_{AB}}{\rho}, \tag{4.3}$$

where ρ is the distance between the two satellites, and $\mathbf{r}_{AB}$ is the position difference of the two satellites. In order to compute the unit vector defining the **z**-axis, we

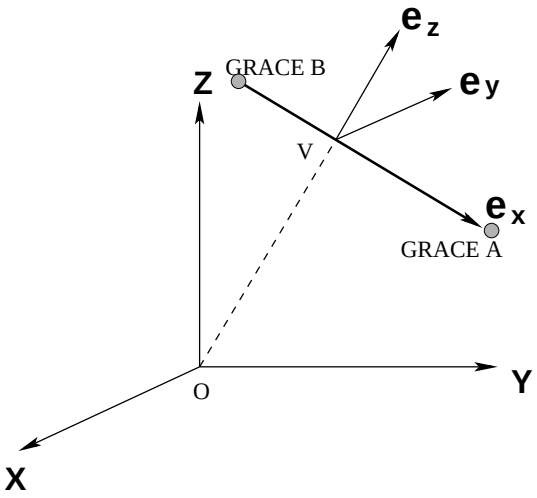

Fig. 4.1. Definition of the LOSRF and computation of unit vectors in the inertial frame. $\mathbf{X}$,$\mathbf{Y}$,$\mathbf{Z}$ represent the three axes of the inertial frame, while $\mathbf{x}$, $\mathbf{y}$, $\mathbf{z}$ represent the three axes of the LOSRF

should find the point V in the LOS which minimizes the distance from the Earth's center to the LOS. The position vector of this point can be represented as a linear combination of the vectors $\mathbf{r}_A$ and $\mathbf{r}_B$:

$$\mathbf{r}_V = \mathbf{r}_A + (\mathbf{r}_B - \mathbf{r}_A)\beta, \tag{4.4}$$

where β is an unknown variable. The squared distance between the point V and the Earth's center is therefore

$$s^2 = \| \mathbf{r}_A + (\mathbf{r}_B - \mathbf{r}_A)\beta \|^2 . \tag{4.5}$$

To minimize this distance, we must set $d(s^2)/d\beta = 0$ and solve for β, which yields

$$\beta = -\frac{\mathbf{r}_A \cdot (\mathbf{r}_B - \mathbf{r}_A)}{\rho^2}. \tag{4.6}$$

The vector $\mathbf{r}_V$ is then easily obtained by substituting equation (4.6) into equation (4.4). The $\mathbf{z}$-axis unit vector can then be computed as:

$$\mathbf{e_z} = \frac{\mathbf{r}_V}{\| \mathbf{r}_V \|}, \tag{4.7}$$

where $\| \cdot \|$ is the norm operator. The $\mathbf{y}$-axis unit vector is obtained by the cross-product of the unit vectors of the $\mathbf{x}$- and $\mathbf{z}$- axis. The $\mathbf{x}$-, $\mathbf{y}$-, and $\mathbf{z}$-axis can be interpreted as the along-track, cross-track, and radial axis, respectively. The matrix of rotation from the inertial frame to the LOSRF frame can therefore be written as:

$$\mathbf{R}^{(\mathbf{C}\rightarrow\mathbf{LF})} = (\mathbf{e_x}, \mathbf{e_y}, \mathbf{e_z})^T, \tag{4.8}$$

where **LF** stands for the LOSRF frame. It should be mentioned that for computing these unit vectors, smoothed (or reference) satellite orbits are used. By using the transformation matrix $\mathbf{R}^{(\mathbf{C}\rightarrow\mathbf{LF})}$, the observed inter-satellite accelerations can be transformed into the LOSRF as follows:

$$\ddot{\mathbf{r}}^{\mathbf{LF}}_{AB}(t) = \mathbf{R}^{(\mathbf{C}\rightarrow\mathbf{LF})}\ddot{\mathbf{r}}_{AB}(t) \tag{4.9}$$

4.2.4 Synthesis and co-synthesis

The synthesis and co-synthesis can be generally carried out in the same way as was done for processing the kinematic orbits; however, the design matrix $\mathbf{A}$ presented in equations (2.104) and (2.107) should be replaced by the following expression.

$$\mathbf{A_{bsl}} = \mathbf{R}^{(\mathbf{C}\rightarrow\mathbf{LF})}\mathbf{E}\mathbf{R}^{(\mathbf{T}\rightarrow\mathbf{C})}(\mathbf{A_{pw,B}} - \mathbf{A_{pw,A}}), \tag{4.10}$$

where $\mathbf{A_{bsl}}$ is the new design matrix, $\mathbf{E}$ is the averaging matrix as used in equation (2.104), and $\mathbf{R}^{(\mathbf{T}\rightarrow\mathbf{C})}$ is the transformation matrix from TRF to CRF. $\mathbf{A_{pw,A}}$ and $\mathbf{A_{pw,B}}$ are the satellite A and B related point-wise design matrices in the TRF, respectively. For example, $\mathbf{A_{pw,A}}$ can be represented as:

$$(\mathbf{A_{pw,A}})_j = \mathbf{R_z}(\pi - \lambda_j)\mathbf{R_y}(\theta_j)\begin{pmatrix}\mathbf{A}_j^{(\mathbf{x})}\\ \mathbf{A}_j^{(\mathbf{y})}\\ \mathbf{A}_j^{(\mathbf{z})}\end{pmatrix}_{\mathrm{GRF}} \tag{4.11}$$

where $\mathbf{A}_j^{(\mathbf{x})}$, $\mathbf{A}_j^{(\mathbf{y})}$ and $\mathbf{A}_j^{(\mathbf{z})}$ are the same matrices as the ones presented in equation (2.106). It should be emphasized that the $\mathbf{x}$, $\mathbf{y}$ and $\mathbf{z}$ axes in equation (4.11) are defined in the GRF at a given epoch t_j for a given satellite.

4.2.5 Computation of the reference inter-satellite accelerations

Calculation of the reference ISAs is carried out in four steps: (1) The point-wise accelerations are computed in the TRF for both satellites using the reference gravity field and tide models. This is the same procedure as was used in processing the kinematic positions. (2) The point-wise accelerations of satellite A are subtracted from those of satellite B, and then rotated into the CRF frame. (3) The ISAs are averaged. (4) The averaged ISAs are then rotated into the LOSRF.

4.2.6 Processing of non-gravitational inter-satellite accelerations

Processing of the non-gravitational ISAs is done in the same way as described in section 2.6.4.4 except that (1) we have to process the non-gravitational accelerations of both satellites and then subtract one from the other; (2) the non-gravitational ISAs have to be rotated into the LOSRF rather than into the LORF.

4.3 Results of data processing

We consider a data period of 101 days (July 9, 2003 to October 17, 2003) since all of the necessary data sets are available for this period. For comparison, the CHAMP hl-SST data for the same period are also processed. The data sets are as follows:

- Kinematic and reduced-dynamic positions of GRACE A/B and CHAMP from the Institute for Astronomical and Physical Geodesy (IAPG), TU Munich [Švehla and Rothacher, 2002]. The kinematic positions are supplied with the variance-covariance matrices.
- Kinematic and reduced-dynamic baselines of GRACE A/B from the Astrodynamics and Satellite Systems group of the Delft Institute of Earth observation and Space System (DEOS), TU Delft [Kroes et al., 2005]. The baselines are supplied with variances.
- The accelerometer and quaternion data from CHAMP provided again by GeoForschungsZentrum Potsdam, and the corresponding non-gravitational data from GRACE provided by the Physical Oceanography Distributed Active Archive Center (PO.DAAC) of NASA's Jet Propulsion Laboratory (JPL).

On the basis of the above-mentioned data sets, we computed the following solutions:

- Solution A: estimated from the kinematic orbits of the GRACE A satellite only
- Solution B: estimated from the kinematic orbits of the GRACE B satellite only
- Solution C: jointly estimated from the kinematic orbits of the GRACE A and B satellites
- Solution D: estimated from the kinematic orbits of the CHAMP satellite
- Solution E: estimated from kinematic baselines of the two GRACE satellites
- Solution F: jointly estimated from the kinematic orbits of GRACE A and the kinematic baselines of the two satellites
- Solution G: jointly estimated from the kinematic orbits of GRACE A and B, as well as kinematic baselines of two satellites

The data processing procedure for solution A, B, C and D is the same as that described in section 3.2, including the estimation of the stochastic properties of the data noise. The purpose of computing a CHAMP-based model (solution D) is to make a comparison with the results obtained from the GRACE hl-SST data. The processing of the kinematic baselines is discussed in the previous section.

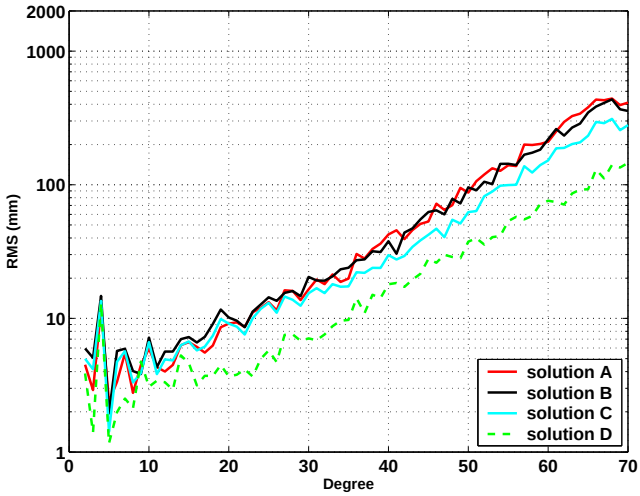

Fig. 4.2. Degree geoid height differences with respect to the EIGEN-GL04C model computed for (i) solution A (red), (ii) solution B (black), (iii) solution C (light blue) and (iv) solution D (dashed green). Regularization is not applied

It should be mentioned that the reduced-dynamic orbits are used for computing the reference accelerations in this case study, not kinematic orbits. In fact, the type of exploited orbits is not so important because our primary goal is to compare our solutions produced from kinematic baselines with those produced from kinematic orbits. We are not aiming at comparing our results with ones obtained at other research institutes: no results based on the kinematic baselines have been published so far.

The outlier detection algorithm used for the calculation of the kinematic baselines is adapted to this data type. A given epoch is discarded if: (1) the kinematic baseline is supplied with zero elements of variances; (2) any component of the baseline formal error exceeded a given threshold (10 cm); (3) the discrepancy between the lengths of the kinematic baseline and the reduced-dynamic baseline is larger than a given threshold (5 times the RMS of discrepancies).

Figures 4.2 and 4.3 display the RMS of the geoid height differences with respect to the EIGEN-GL04C model for solutions A, B, C and D. No regularization is applied when computing these solutions. From these two figures, it is easy to observe:

1) The GRACE A-only and GRACE B-only solutions show similar accuracy as a whole, though the GRACE A-only solution demonstrates slightly better results at the low degrees, and slightly worse results at the high degrees,

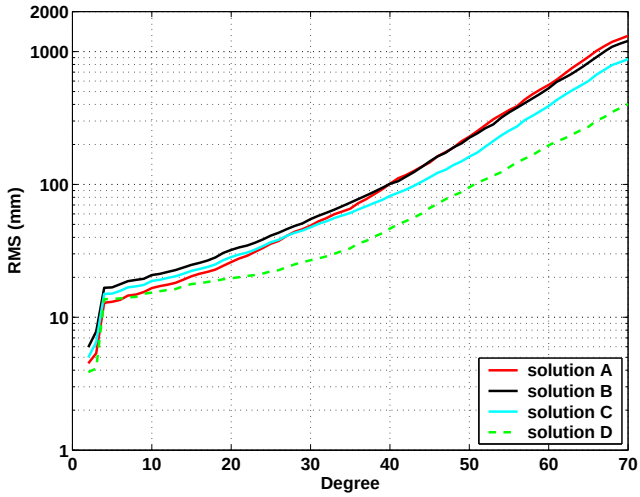

Fig. 4.3. Cumulative geoid height differences with respect to the EIGEN-GL04C model computed for: (i) solution A (red), (ii) solution B (black), (iii) solution C (light blue) and (iv) solution D (dashed green). Regularization is not applied

with the crossing point at approximately degree 40.

2) For all of the solutions, there is a peak of roughly one centimeter at degree 4. Similar error peaks were also found by other research groups that employed the same version of Munich orbits, see, [Götzelmann et al., 2006] and [Weigelt, 2007]. While the reason for this error is currently unknown, it may have been caused by a systematic error in the orbit determination process.

3) The joint solution estimated from the data of GRACE A and B improves accuracy by about a factor of $\sqrt{2}$, which is the expected result. The cumulative error of solutions obtained from the individual satellites 1.31 m and 1.20 m, for GRACE A and B respectively, while that of the joint solution is 0.88 m. However, the joint solution has lower accuracy compared to the GRACE A-only solution at the low degrees (i.e., below degree 20). This is likely due to the contamination of GRACE B data. To deal with this properly, a more accurate stochastic model of the data noise should be developed. We did not make further efforts on this issue.

4) The CHAMP solution is the best solution among the four, particularly at the high degrees, due to the lower orbit of the CHAMP satellite and, hence, its increased sensitivity to the gravity signal.

Figures 4.4 and 4.5 show the RMS of the geoid height differences with respect to the EIGEN-GL04C model for solution C, E, F and G. Again, no regularization was applied. It is clearly visible that solution E, which is based on kinematic

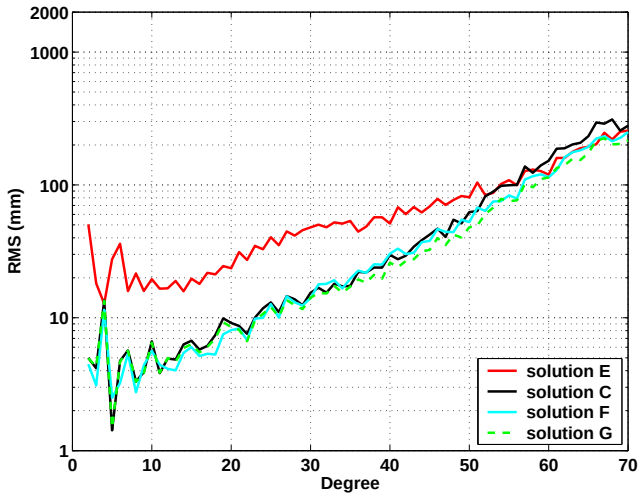

Fig. 4.4. Degree geoid height differences with respect to the EIGEN-GL04C model computed for: (i) solution E (red), (ii) solution C (black), (iii) solution F (light blue) and (iv) solution G (dashed green). Regularization is not applied

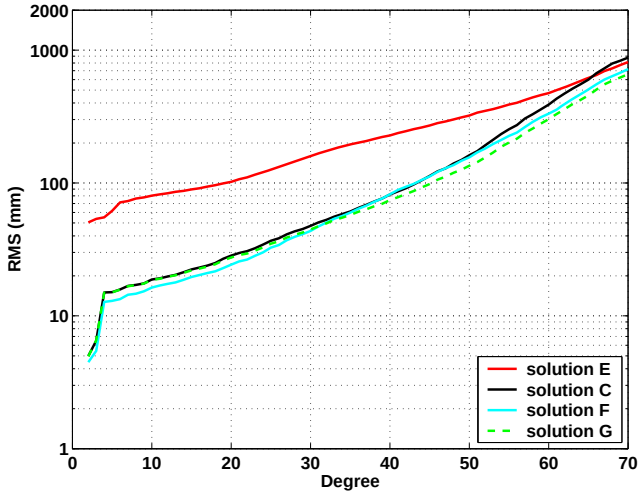

Fig. 4.5. Cumulative geoid height differences with respect to the EIGEN-GL04C model computed for: (i) solution E (red), (ii) solution C (black), (iii) solution F (light blue) and (iv) solution G (dashed green). Regularization is not applied

baselines, contains relatively large errors at the low and mid degrees. Starting from about degree 55, however, this solution shows higher accuracy than solution C, which is based on kinematic orbits of the two GRACE satellites. The overall cumulative error of solution E is slightly lower than that of solution C. The higher overall accuracy of solution E is probably due to a lower noise level in the computed baseline relative to that in the orbits. Therefore, baselines may be preferred for the high-resolution determination of the gravity field. The low accuracy of solution E at the low and mid degrees can be explained by two reasons. One is that a majority of the gravity signal at the low degrees is the same for both satellites. At the same time, the accuracy of the ISAs derived from the kinematic baselines does not significantly increase when compared to the accelerations derived from a single satellite. Therefore, the differentiation operation between the two satellites makes the large part of signals 'non-visible' in the ISAs – smaller than even noise in the domain of frequencies. Furthermore, the differences measured in baselines at two points are located at the same meridian. Such kind of measurements are not sensitive to the East-West signal. The other reason is that the geographical locations of the two satellites used to compute the partial elements of the design matrix are relatively close to each other, and the differentiation operation between the individual design matrices could make the whole design matrix more ill-posed (see equation 4.10).

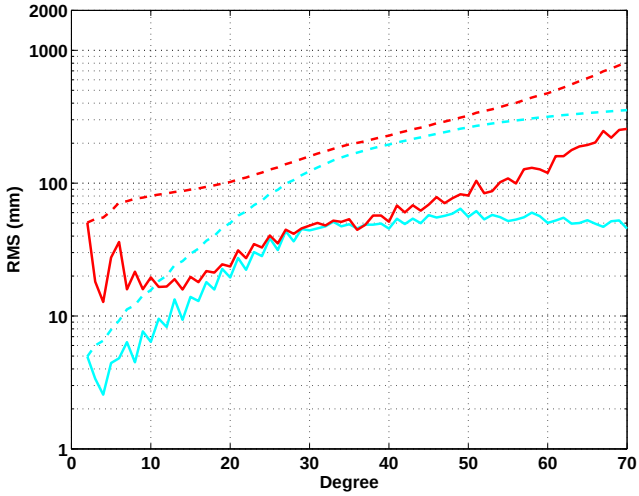

Fig. 4.6. The geoid height differences with respect to the EIGEN-GL04C model. Solid lines present the geoid height difference per degree and the dashed lines the cumulative geoid height differences. The models were produced from GRACE kinematic baselines with regularization (blue line) and without regularization (red line). The regularization matrix used was the full covariance matrix of EGM96 model up to degree and order 70.

Improving the accuracy at the low degrees could be achieved using the following means: (1) combining baseline data with kinematic positions. (2) regularization of the solution (3) increasing the accuracy of the baselines. The last idea will be discussed in the next chapter in the context case of using more precise KBR data. In this section, we consider the first two ideas. From figures 4.4 and 4.5, it can be clearly seen that solutions F and G improve the quality of the gravity field when compared to solution E, particularly at the low degrees. The quality of the combined solution, however, does not exceed that of the solution based on the kinematic orbits. Only at the high degrees was the accuracy of the combined solution slightly higher. The overall cumulative error (at degree 70) is improved in the case of the combined solution by 15% - 25%. This fact confirms that the GPS measurements of satellite A (or B) are implicitly employed twice in this case, the baselines do contain additional information that is absent in the orbits.

Figure 4.6 shows the comparison of regularized solutions based on the kinematic baselines. It is clear that the regularization significantly improves the quality of the gravity field model at the low and high frequencies. One reason for this is that the regularized solution contains information from an *a priori* model, i.e. EGM96, which has relatively high accuracies at the low and high degrees thanks to the incorporation of many years worth of satellite orbit and altimetry data. Another reason is that the regularization stabilizes the normal matrix, and decreases the oscillation of the solution.

4.4 Summary and Remarks

In this chapter, we extended our gravity field modeling methodology to GRACE hl-SST data. Both kinematic positions and baselines of the GRACE satellites were processed, both individually and jointly. We found that, in general, the kinematic baselines themselves are not favored for the purposes of deriving gravity field models, due to a limited accuracy of the kinematic baselines (even though it is higher than that of kinematic orbits). This problem can be solved using high-precision KBR measurements of GRACE mission (see next chapter). On the other hand, the GRACE mission has a limitation of life period. Currently, there are a few existing and proposed formation flying missions not supplied with the KBR system. Therefore, it might be still valuable to make use of these missions for gravity field modeling. The kinematic baselines might still be useful, since they can somehow improve the quality of gravity field model, particularly at high frequencies, if used jointly with the kinematic orbits.

Chapter 5

Gravity field modeling from GRACE ll-SST data

5.1 Introduction

This chapter discusses in detail the procedure of gravity field modeling from ll-SST data provided by the GRACE satellite mission. Making use of ll-SST data does not mean that the hl-SST data can be fully ignored. The hl-SST data are still needed to compute the precise orbits, which are indispensable for high-quality gravity field modeling. However, the hl-SST data are not used as observations and do not provide any additional contribution to the normal equations.

We will describe three approaches of processing GRACE ll-SST data that make use of range-acceleration, range-rate and range measurements, respectively. These three approaches are referred to as the classic acceleration approach, the 3-point Range-Rate Combination (3RRC) approach and the 3-point Range Combination (3RC) approach. The first one was proposed by Rummel [1979], while the latter two are innovative approaches proposed in the frame of this research. The common feature of these approaches is that the functional models are linear, and that the calculation of the partial derivatives through numerical solution of the variational equations, which is typically computationally expensive, can be avoided. The chapter starts with the derivation of the classical acceleration approach in section 5.2.1. The approach connects inter-satellite gravitational potential gradients with point-wise range-accelerations and the component of inter-satellite velocities orthogonal to the LOS. After a realistic sensitivity analysis we find that it is difficult to compute high-precision gravity field models using this approach since the velocity term does not match the accuracy of KBR range-acceleration. To cope with this problem, we derive the 3RRC approach and the 3RC approach in section 5.2.2 and 5.2.3, respectively. The first approach virtually makes use of range-rate measurements to determine the orthogonal component of the inter-satellite velocities. The second approach even allows the velocity term in the observation equation to be avoided by computing the gravitational potential gradients from KBR ranges rather than

from KBR range-accelerations or range-rates.

A comprehensive description of the data processing strategy, which includes the pre-processing and inversion process, is given in section 5.3. The pre-processing is described in an integrated manner for all three approaches. In order to generate residuals from the ranges, range-rates and range-accelerations, the purely dynamic orbits of the two GRACE satellites are computed in such a way that they best fit the existing reduced-dynamic orbits. By using the generated residuals, the corresponding residual quantities are formed for the final inversion. The inversion strategies of the three approaches are based on the similar procedure used for processing baselines, as described in chapter 4. The peculiar features of the inversion using ll-SST data are discussed in section 5.3.4.

The aim of section 5.4 is to compare the results obtained by the three approaches, with a focus on estimating time variable gravity fields. Two months of GRACE mission data are processed using the data processing strategy outlined. A corresponding set of hydrological models is taken as a reference for the comparison.

In section 5.5, we further refine the data processing procedure based on the 3RC approach. An iterative estimation is implemented to retrieve the gravity signal potentially absorbed by the empirical parameters introduced in the first iteration. Section 5.6 summarizes the main findings of the chapter and discusses possible ways to improve the accuracy of gravity field models derived by the classic acceleration approach and the 3RRC approach.

5.2 Functional models

5.2.1 Classical acceleration approach

Following Rummel [1979], this section derives the functional model of the classic acceleration approach. Let $\mathbf{r}_A$ and $\mathbf{r}_B$ be the positions of GRACE satellites A and B in an inertial Earth centered frame at a given epoch, respectively. The range vector between two satellites is given by

$$\mathbf{r}_{AB} = \mathbf{r}_B - \mathbf{r}_A. \tag{5.1}$$

The square of the range can be expressed as

$$\rho^2 = \mathbf{r}_{AB} \cdot \mathbf{r}_{AB}. \tag{5.2}$$

Differentiation of equation (5.2) with respect to time gives

$$2\rho\dot{\rho} = 2\mathbf{r}_{AB} \cdot \dot{\mathbf{r}}_{AB}, \tag{5.3}$$

where $\dot{\mathbf{r}}_{AB} = \dot{\mathbf{r}}_B - \dot{\mathbf{r}}_A$. Therefore, the range-rate can be expressed as

$$\dot{\rho} = \mathbf{e}_{AB} \cdot \dot{\mathbf{r}}_{AB}, \tag{5.4}$$

with the unit vector of the LOS defined as

$$\mathbf{e}_{AB} = \frac{\mathbf{r}_{AB}}{\rho}. \tag{5.5}$$

Equation (5.4) means that the inter-satellite range-rate can be interpreted by projection of the inter-satellite velocity vector $\dot{\mathbf{r}}_{AB}$ onto the LOS of the two satellites. The range-acceleration can be obtained by the differentiation of equation (5.4):

$$\ddot{\rho} = \dot{\mathbf{e}}_{AB} \cdot \dot{\mathbf{r}}_{AB} + \mathbf{e}_{AB} \cdot \ddot{\mathbf{r}}_{AB}, \tag{5.6}$$

where $\ddot{\mathbf{r}}_{AB} = \ddot{\mathbf{r}}_B - \ddot{\mathbf{r}}_A$. The time derivative of the unit vector can be obtained on the basis of equation (5.5):

$$\dot{\mathbf{e}}_{AB} = \frac{\dot{\mathbf{r}}_{AB}}{\rho} - \frac{\dot{\rho}\mathbf{r}_{AB}}{\rho^2} = \frac{\dot{\mathbf{r}}_{AB}}{\rho} - \frac{\dot{\rho}\mathbf{e}_{AB}}{\rho}. \tag{5.7}$$

Therefore, the functional model of the classical acceleration approach can be written as:

$$\mathbf{e}_{AB} \cdot \ddot{\mathbf{r}}_{AB} = \ddot{\rho} - \frac{\parallel \dot{\mathbf{r}}_{AB} \parallel^2 - \dot{\rho}^2}{\rho} = \ddot{\rho} - \frac{\parallel \dot{\mathbf{r}}_{AB}^{\perp} \parallel^2}{\rho}, \tag{5.8}$$

where $\dot{\mathbf{r}}_{AB}^{\perp}$ is the inter-satellite velocity vector projected onto the plane orthogonal to the LOS, which can be obtained through

$$\dot{\mathbf{r}}_{AB}^{\perp} = \dot{\mathbf{r}}_{AB} - (\dot{\mathbf{r}}_{AB} \cdot \mathbf{e}_{AB})\mathbf{e}_{AB}. \tag{5.9}$$

Equation (5.8) linearly connects the difference between gravitational potential gradients at the satellite locations with the inter-satellite range-acceleration compensated by a velocity term, i.e. the second term on the right-hand side [Thomas, 1999].

In order to estimate the time variable component of the gravity field, a significant parts of the known signal should firstly be removed from the KBR range-accelerations. Let us introduce a reference field and denote any quantities that are derived from it with the subscript c (the subscript AB will no longer be used for the sake of brevity), so that:

$$\mathbf{e}_c \cdot \ddot{\mathbf{r}}_c = \ddot{\rho}_c - \frac{\parallel \dot{\mathbf{r}}_c^{\perp} \parallel^2}{\rho_c}. \tag{5.10}$$

By subtracting this equation from equation (5.8), and introducing the approximation $\rho_c \cong \rho$ and $\mathbf{e}_c \cong \mathbf{e}$, we obtain

$$\mathbf{e}_c \cdot \delta\ddot{\mathbf{r}} = \delta\ddot{\rho} - \frac{\parallel \dot{\mathbf{r}}^{\perp} \parallel^2 - \parallel \dot{\mathbf{r}}_c^{\perp} \parallel^2}{\rho_c}, \tag{5.11}$$

where $\delta\ddot{\rho} := \ddot{\rho} - \ddot{\rho}_c$ is the residual inter-satellite range acceleration, and $\delta\ddot{\mathbf{r}} := \ddot{\mathbf{r}} - \ddot{\mathbf{r}}_c$ is the residual inter-satellite acceleration vector. Let us introduce the residual

orthogonal velocity vector $\delta\dot{\mathbf{r}}^{\perp} = \dot{\mathbf{r}}^{\perp} - \dot{\mathbf{r}}_c^{\perp}$. Therefore,

$$\begin{aligned} \| \delta\dot{\mathbf{r}}^{\perp} \|^2 &= (\dot{\mathbf{r}}^{\perp} - \dot{\mathbf{r}}_c^{\perp}) \cdot (\dot{\mathbf{r}}^{\perp} - \dot{\mathbf{r}}_c^{\perp}) = \| \dot{\mathbf{r}}^{\perp} \|^2 - 2\dot{\mathbf{r}}^{\perp} \cdot \dot{\mathbf{r}}_c^{\perp} + \| \dot{\mathbf{r}}_c^{\perp} \|^2 \\ &= \| \dot{\mathbf{r}}^{\perp} \|^2 - 2(\dot{\mathbf{r}}_c^{\perp} + \delta\dot{\mathbf{r}}^{\perp}) \cdot \dot{\mathbf{r}}_c^{\perp} + \| \dot{\mathbf{r}}_c^{\perp} \|^2 \\ &= \| \dot{\mathbf{r}}^{\perp} \|^2 - 2(\dot{\mathbf{r}}_c^{\perp} \cdot \delta\dot{\mathbf{r}}^{\perp}) - \| \dot{\mathbf{r}}_c^{\perp} \|^2 . \end{aligned} \tag{5.12}$$

Then, equation (5.11) can be written as:

$$\mathbf{e}_c \cdot \delta\ddot{\mathbf{r}} = \delta\ddot{\rho} - \frac{\| \delta\dot{\mathbf{r}}^{\perp} \|^2 + 2\dot{\mathbf{r}}_c^{\perp} \cdot \delta\dot{\mathbf{r}}^{\perp}}{\rho_c}. \tag{5.13}$$

We define $\delta\ddot{\rho}$ as the range-acceleration term and the rest of the right-hand side in equation (5.13) as the velocity term. A few remarks should be made here with regard to equation (5.13). Firstly, working with reference quantities, i.e. $\mathbf{e}_c$ and ρ_c, rather than with observed quantities, i.e. $\mathbf{e}$ and ρ, holds a practical advantage since latter ones can not be obtained from KBR data. Secondly, all of the reference quantities, i.e. $\mathbf{e}_c$, ρ_c, $\ddot{\rho}_c$ and $\dot{\mathbf{r}}_c$, have been computed from accurate reference orbits of two GRACE satellites. The details surrounding the computation of the reference orbit will be described later in the section on real data processing. Thirdly, the velocity term is important, which must be taken into account for the full computation of $\mathbf{e}_c \cdot \delta\ddot{\mathbf{r}}$. The observed quantity $\dot{\mathbf{r}}$ is determined by a numerical differentiation of kinematic baselines, which are defined on the basis of GPS measurements without dependence on the reference model. The velocity term is an important contributor to the error budget. The kinematic baselines have relatively large errors, and the magnitude of the vector $\dot{\mathbf{r}}_c^{\perp}$ is rather significant: about 250 m/s. Assume that noise of along-track and cross-track component of velocity differences is at the level of $\pm 0.5 \times 10^{-3}$ m/s, whereas the radial component may have 2 times higher noise than other two components [Švehla and Földváry, 2006]. Because the orthogonal component to the LOS is comprised of the cross-track and radial components, its noise could be at the level of $\pm\sqrt{5} \times 0.5 \times 10^{-3}$ m/s. Therefore, the contribution of the corresponding velocity term in equation (5.13) to the overall error budget is $\pm 2 \times 250 \times \sqrt{5} \times 0.5 \times 10^{-3}/(200 \times 10^3)\,\mathrm{m/s^2} = \pm 2.8 \times 10^{-6}\,\mathrm{m/s^2}$. This is at least one order of magnitude larger than that caused by the range-acceleration term, which is usually at the level of $\pm(0.08 \sim 0.09) \times 10^{-6}\,\mathrm{m/s^2}$ [Biancale et al., 2005]. Therefore, the velocity term is not accurate enough to match the accuracy of KBR range-accelerations for high-precision gravity field modeling. A similar conclusion was also made earlier by [Visser et al., 2002] in the context of the energy integral method. Of course, this is a very simplistic error analysis, because the dependence of noise on frequency is not taken into account. Nevertheless, even such an analysis indicates that the acceleration approach is probably not well suited for high-quality gravity field modeling. Still, in view of the long history of this approach, an attempt at processing GRACE real data with this approach has been made in this thesis.

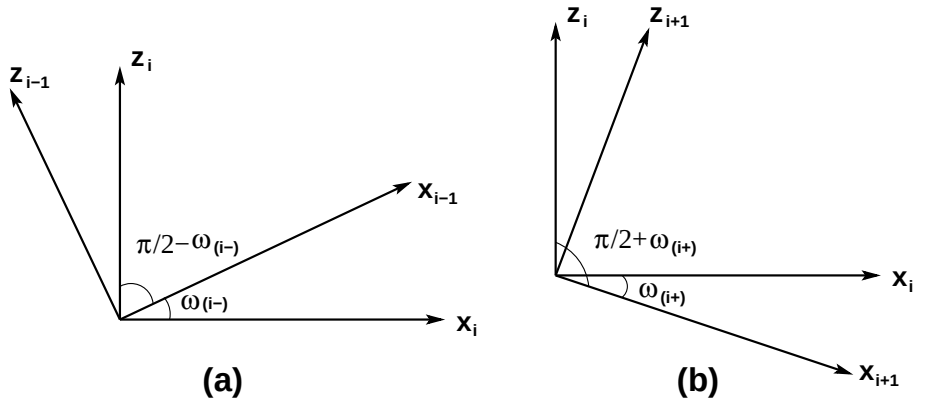

Fig. 5.1. Angle $\omega_{(i-)}$ and orientation of the frame at the epoch i relative to the axes defined for the epoch $i-1$ (a), and the angle $\omega_{(i+)}$ and orientation of the frame at the epoch $i+1$ relatively to the axes defined for the epoch i (b)

5.2.2 3-point range-rate combination approach

We have discussed in the previous section that it may be problematic to compute a high-precision gravity field model using the classic acceleration approach, because the inter-satellite velocities computed from the GPS data are not accurate enough. This section is devoted to the range-rate combination approach, which allows the determination of not only the LOS, but also the radial component of the inter-satellite velocities directly from KBR-data, thereby reducing the influence of the GPS data on the overall error budget [Ditmar and Liu, 2006b, Ditmar and Liu, 2006c, Liu et al., 2007a].

To derive the functional model of the 3-point Range-Rate Combination (3RRC) approach, we make use of the LOSRF frame defined in section 4.4.1 (see figure 4.1). Three successive epochs, denoted as $i-1$, i and $i+1$, are used to form one observation equation. For the sake of simplicity, assume that the satellite's motion is 2-dimensional (i.e. that the inter-satellite velocity vector does not have a cross-track component). Let $\omega_{(i-)}$ be the angle between $\mathbf{x}$-axes at epochs $i-1$ and i. Similarly, let $\omega_{(i+)}$ be the angle between $\mathbf{x}$-axes at epochs i and $i+1$, see figure 5.1. The angles $\omega_{(i-)}$ and $\omega_{(i+)}$ are assumed to be positive. The 3-D average inter-satellite accelerations between the epochs $i-1$ and i (i.e. $\bar{\ddot{\mathbf{r}}}_{(i-)}$) and between the epochs i and $i+1$ (i.e. $\bar{\ddot{\mathbf{r}}}_{(i+)}$) are defined as follows:

$$\bar{\ddot{\mathbf{r}}}_{(i-)} = \frac{\int_{t_i-\Delta t}^{t_i} \ddot{\mathbf{r}}(t)\,\mathrm{d}t}{\Delta t}; \quad \bar{\ddot{\mathbf{r}}}_{(i+)} = \frac{\int_{t_i}^{t_i+\Delta t} \ddot{\mathbf{r}}(t)\,\mathrm{d}t}{\Delta t},$$

where $\ddot{\mathbf{r}}(t)$ is the point-wise inter-satellite acceleration as a function of time t, and Δt is the sampling interval. From these definitions, the following equalities hold:

$$\Delta t \cdot \bar{\ddot{\mathbf{r}}}_{(i-)} = \dot{\mathbf{r}}_i - \dot{\mathbf{r}}_{i-1}, \tag{5.14}$$

$$\Delta t \cdot \ddot{\bar{\mathbf{r}}}_{(i+)} = \dot{\mathbf{r}}_{i+1} - \dot{\mathbf{r}}_i, \tag{5.15}$$

where $\dot{\mathbf{r}}_k \quad (k = i-1, i, i+1)$ are inter-satellite velocities at three successive epochs. Consider the projections of equations (5.14) and (5.15) onto the $\mathbf{z}_i$ axis:

$$\Delta t \cdot \ddot{\bar{r}}^{\perp}_{(i-)} = \dot{r}^{\perp}_i - \dot{r}^{\perp}_{i-1}, \tag{5.16}$$

$$\Delta t \cdot \ddot{\bar{r}}^{\perp}_{(i+)} = \dot{r}^{\perp}_{i+1} - \dot{r}^{\perp}_i, \tag{5.17}$$

where $\dot{r}^{\perp}_k$, $\ddot{\bar{r}}^{\perp}_{(i-)}$ and $\ddot{\bar{r}}^{\perp}_{(i+)}$ are the projections of vectors $\dot{\mathbf{r}}_k$, $\ddot{\bar{\mathbf{r}}}_{(i-)}$ and $\ddot{\bar{\mathbf{r}}}_{(i+)}$ onto the $\mathbf{z}_i$ axis, respectively, (thus, $\dot{r}^z_i = \dot{r}^{\perp}_i$). By adding equations (5.16) and (5.17) together, we have:

$$\Delta t \cdot \left(\ddot{\bar{r}}^{\perp}_{(i-)} + \ddot{\bar{r}}^{\perp}_{(i+)} \right) = \dot{r}^{\perp}_{i+1} - \dot{r}^{\perp}_{i-1}. \tag{5.18}$$

Furthermore, $\dot{r}^{\perp}_{i-1}$ can be represented as a linear combination of "locally defined" **x**- and **z**-components of the vector $\dot{\mathbf{r}}_{i-1}$, i.e. $\dot{r}^x_{i-1}$ and $\dot{r}^z_{i-1}$ (with this notation, we imply that the axes **x** and **z** correspond to the epoch of the vector under consideration, i.e. $i-1$):

$$\dot{r}^{\perp}_{i-1} = \dot{r}^x_{i-1} \cdot \cos\left(\frac{\pi}{2} - \omega_{(i-)}\right) + \dot{r}^z_{i-1} \cdot \cos\omega_{(i-)} = \dot{\rho}_{i-1} \cdot \sin\omega_{(i-)} + \dot{r}^z_{i-1} \cdot \cos\omega_{(i-)}, \tag{5.19}$$

where $\dot{\rho}_k$ is the range-rate at the epoch k. Similarly, $\dot{r}^{\perp}_{i+1}$ can be represented as a linear combination of $\dot{\rho}_{i+1}$ and $\dot{r}^z_{i+1}$:

$$\dot{r}^{\perp}_{i+1} \quad = \quad -\dot{\rho}_{i+1} \cdot \sin\omega_{(i+)} + \dot{r}^z_{i+1} \cdot \cos\omega_{(i+)}. \tag{5.20}$$

Substitution of equations (5.19) and (5.20) into (5.18) yields:

$$\Delta t \cdot \left(\ddot{\bar{r}}^{\perp}_{(i-)} + \ddot{\bar{r}}^{\perp}_{(i+)} \right) = -\dot{\rho}_{i-1} \cdot \sin\omega_{(i-)} - \dot{\rho}_{i+1} \cdot \sin\omega_{(i+)} - \dot{r}^z_{i-1} \cdot \cos\omega_{(i-)} + \dot{r}^z_{i+1} \cdot \cos\omega_{(i+)}. \tag{5.21}$$

Now, let us express $\dot{r}^z_{i-1}$ and $\dot{r}^z_{i+1}$ in terms of range-rates and average inter-satellite accelerations. To do that, we can consider the projection of equations (5.14) and (5.15) onto the $\mathbf{x}_i$ axis:

$$\Delta t \cdot \ddot{\bar{r}}^{\parallel}_{(i-)} = \dot{r}^{\parallel}_i - \dot{r}^{\parallel}_{i-1} = \dot{r}^x_i - \dot{r}^{\parallel}_{i-1} = \dot{\rho}_i - \dot{r}^{\parallel}_{i-1}; \tag{5.22}$$

$$\Delta t \cdot \ddot{\bar{r}}^{\parallel}_{(i+)} = \dot{r}^{\parallel}_{i+1} - \dot{r}^x_i = \dot{r}^{\parallel}_{i+1} - \dot{\rho}_i, \tag{5.23}$$

where $\dot{r}_k^{\parallel}$, $\bar{\bar{r}}_{(i-)}^{\parallel}$ and $\bar{\bar{r}}_{(i+)}^{\parallel}$ are projections of the vectors $\dot{\mathbf{r}}_k$, $\bar{\bar{\mathbf{r}}}_{(i-)}$ and $\bar{\bar{\mathbf{r}}}_{(i+)}$ onto the $\mathbf{x}_i$ axis, respectively. Next, $\dot{r}_{i-1}^{\parallel}$ can be represented as a linear combination of $\dot{\rho}_{i-1}$ and $\dot{r}_{i-1}^{z}$:

$$\dot{r}_{i-1}^{\parallel} = \dot{\rho}_{i-1} \cdot \cos\omega_{(i-)} - \dot{r}_{i-1}^{z} \cdot \sin\omega_{(i-)}. \tag{5.24}$$

Substitution of equation (5.24) into (5.22) yields the following expression for $\dot{r}_{i-1}^{z}$.

$$\dot{r}_{i-1}^{z} = \frac{\Delta t \cdot \bar{\bar{r}}_{(i-)}^{\parallel}}{\sin\omega_{(i-)}} - \frac{\dot{\rho}_i}{\sin\omega_{(i-)}} + \dot{\rho}_{i-1} \cdot \cot\omega_{(i-)}. \tag{5.25}$$

Similarly, $\dot{r}_{i+1}^{\parallel}$ can be represented as a linear combination of $\dot{r}_{i+1}^{x}$ and $\dot{r}_{i+1}^{z}$:

$$\dot{r}_{i+1}^{\parallel} = \dot{r}_{i+1}^{x} \cdot \cos\omega_{(i+)} + \dot{r}_{i+1}^{z} \cdot \sin\omega_{(i+)}. \tag{5.26}$$

Then, $\dot{r}_{i+1}^{z}$ can be obtained by substituting equation (5.26) into (5.23):

$$\dot{r}_{i+1}^{z} = \frac{\Delta t \cdot \bar{\bar{r}}_{(i+)}^{\parallel}}{\sin\omega_{(i+)}} + \frac{\dot{\rho}_i}{\sin\omega_{(i+)}} - \dot{\rho}_{i+1} \cdot \cot\omega_{(i+)}. \tag{5.27}$$

Now, equations (5.25) and (5.27) can be inserted into (5.21) with the inter-satellite accelerations being arranged in the left-hand side and the range-rates in the right-hand side:

$$\begin{aligned} &\Delta t \cdot \left(\bar{\bar{r}}_{(i-)}^{\parallel} \cdot \cot\omega_{(i-)} - \bar{\bar{r}}_{(i+)}^{\parallel} \cdot \cot\omega_{(i+)} + \bar{\bar{r}}_{(i-)}^{\perp} + \bar{\bar{r}}_{(i+)}^{\perp} \right) \\ &\quad = \dot{\rho}_i \left(\cot\omega_{(i+)} + \cot\omega_{(i-)} \right) - \tfrac{\dot{\rho}_{i-1}}{\sin\omega_{(i-)}} - \tfrac{\dot{\rho}_{i+1}}{\sin\omega_{(i+)}}. \end{aligned} \tag{5.28}$$

After a scaling factor has been applied, which will be explained below, equation (5.28) can be finally written as follows:

$$\begin{aligned} &\Delta t \left[(\tau_{(i+)}) \bar{\bar{r}}_{(i+)}^{\parallel} - (\tau_{(i-)}) \bar{\bar{r}}_{(i-)}^{\parallel} - \nu_i (\bar{\bar{r}}_{(i-)}^{\perp} + \bar{\bar{r}}_{(i+)}^{\perp}) \right] \\ &\quad = (\epsilon_{(i-)}) \dot{\rho}_{i-1} - (\tau_{(i-)} + \tau_{(i+)}) \dot{\rho}_i + (\epsilon_{(i+)}) \dot{\rho}_{i+1}, \end{aligned} \tag{5.29}$$

with

$$\nu_i := \frac{2}{(\Delta t)^2 \cdot (\cot\omega_{(i-)} + \cot\omega_{(i+)})}, \qquad \tau_{(i-)} := \nu_i \cdot \cot\omega_{(i-)},$$

$$\tau_{(i+)} := \nu_i \cdot \cot\omega_{(i+)}, \qquad \epsilon_{(i-)} := \frac{\nu_i}{\sin\omega_{(i-)}}, \quad \text{and} \quad \epsilon_{(i+)} := \frac{\nu_i}{\sin\omega_{(i+)}}.$$

Hereafter, the parameters ν_i, $\tau_{(i-)}$, $\tau_{(i+)}$, $\epsilon_{(i-)}$ and $\epsilon_{(i+)}$ are referred to as the navigation parameters. Equation (5.29) defines our functional model, which connects a linear combination of three successive range-rates with a linear

combination of gravitational potential gradients at the satellite locations.

Strictly speaking, equation (5.29) is only valid in the 2-D case, i.e. if all 3 line-of-sight unit vectors coincide with the orbital planes of the satellites. However, real data can be reduced to the (local) 2-D case by applying small corrections to $\dot{\rho}_{i-1}$, $\dot{\rho}_i$ and $\dot{\rho}_{i+1}$. The corrections are calculated from the **y**-components of inter-satellite velocity vectors at epochs $i-1$ and $i+1$ projected onto the **x**- or **z**-axes of the epoch i. For example, $\dot{\rho}_i$ is corrected by $-\dot{r}^y_{i-1}(\mathbf{e}^x_i \cdot \mathbf{e}^y_{i-1})$ or $-\dot{r}^y_{i+1}(\mathbf{e}^x_i \cdot \mathbf{e}^y_{i+1})$. In these corrections, we need GPS data to derive only the cross-track component of the inter-satellite velocity vectors rather than the entire set of orthogonal components (i.e., both cross-track and radial components), as is the case with the classical acceleration approach. The radial component is now derived from the KBR range-rates, see equation (5.29). The cross-track component of the inter-satellite velocity vector has the smallest value among the three components. The range of values is within $\pm 0.5\,\mathrm{m/s}$, see figure 5.2. The ranges of values for the LOS and radial components are $\pm 2.5\,\mathrm{m/s}$ and $\pm 250\,\mathrm{m/s}$, respectively. Furthermore, the **x**-axis of epoch i is almost orthogonal to the **y**-axes of neighboring epoches, since the orbit planes do not change much within a short time interval. Therefore, the values of $\mathbf{e}^x_i \cdot \mathbf{e}^y_{i-1}$ and $\mathbf{e}^x_i \cdot \mathbf{e}^y_{i+1}$ are rather small, roughly within $\pm 1.0 \times 10^{-5}$, see figure 5.2. Since these values act as scale factors applied to the cross-track velocity component, they dramatically reduce the influence of noise in this component. If it is assumed that the noise of the cross-track component derived by GPS measurements is at the level of $\pm 0.5 \times 10^{-3}\,\mathrm{m/s}$, then the noise level of these corrections should be at the level of $\pm 1.0 \times 10^{-5} \times 0.5 \times 10^{-3}\,\mathrm{m/s} = \pm 0.5 \times 10^{-8}\,\mathrm{m/s}$. Considering that the noise level of KBR range-rates is $\pm 0.2 \times 10^{-6}\,\mathrm{m/s}$, these corrections fully preserve the accuracy of KBR range-rates. Although we did not explicitly express these corrections in the functional model, i.e. equation (5.29), we do implement them in the course of real data processing shown later in section 5.3.

In the special case of circular satellite orbits, we have:

$$\omega_{(i-)} = \omega_{(i+)} = \omega_i, \qquad \nu_i = \frac{\tan\omega_i}{(\Delta t)^2},$$

$$\tau_{(i-)} = \tau_{(i+)} = \frac{1}{(\Delta t)^2}, \quad \text{and} \quad \epsilon_{(i-)} = \epsilon_{(i+)} = \frac{1}{(\Delta t)^2 \cos\omega_i}.$$

If we assume further that the orbit radius approaches infinity, $\tan\omega_i \to 0$ and $\cos\omega_i \to 1$. Then, equation (5.29) turns into:

$$\frac{\ddot{\bar{r}}^{\parallel}_{(i+)} - \ddot{\bar{r}}^{\parallel}_{(i-)}}{\Delta t} = \frac{\dot{\rho}_{i-1} - 2\dot{\rho}_i + \dot{\rho}_{i+1}}{(\Delta t)^2}. \tag{5.30}$$

Thus, the computation of range-rate combinations in this special case reduces to the double numerical differentiation of range-rates with the 3-point scheme. In other words, the range-rate combinations become approximately equal to

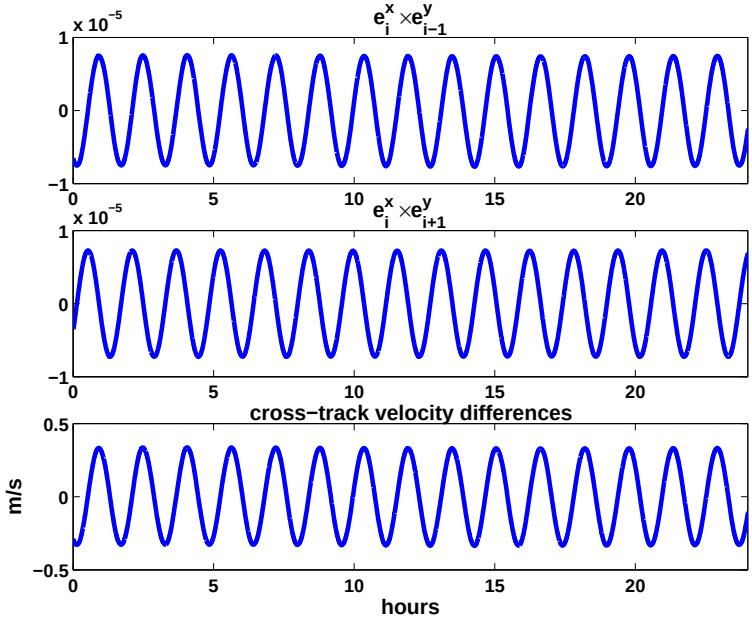

Fig. 5.2. Time series of $\mathbf{e}_i^x \cdot \mathbf{e}_{i-1}^y$, $\mathbf{e}_i^x \cdot \mathbf{e}_{i+1}^y$ and $\dot{r}^y$ for August 1, 2003

second time-derivatives of range-rates. This explains the scaling applied to equation (5.28).

The functional model shown with equation (5.29) is strictly linear, therefore, it can be re-written for residual quantities:

$$\begin{aligned}\Delta t \Big[&(\tau_{(i+),c})\delta\bar{\ddot{r}}^{\parallel}_{(i+)} - (\tau_{(i-),c})\delta\bar{\ddot{r}}^{\parallel}_{(i-)} - (\nu_{i,c})(\delta\bar{\ddot{r}}^{\perp}_{(i-)} + \delta\bar{\ddot{r}}^{\perp}_{(i+)}) \Big] \\ &= (\epsilon_{(i-),c})\delta\dot{\rho}_{i-1} - (\tau_{(i-),c} + \tau_{(i+),c})\delta\dot{\rho}_i + (\epsilon_{(i+),c})\delta\dot{\rho}_{i+1}, \end{aligned} \tag{5.31}$$

with all navigation parameters being replaced by the derived quantities, which are calculated from the reference orbits. In addition, $\delta\bar{\ddot{r}}_j^{(\parallel,\perp)} = \bar{\ddot{r}}_j^{(\parallel,\perp)} - \bar{\ddot{r}}_{j,c}^{(\parallel,\perp)}$ with $j = i-, i+$; and $\delta\dot{\rho}_k = \dot{\rho}_k - \dot{\rho}_{k,c}$ with $k = i-1, i, i+1$. The computed range-rates are also calculated from the reference orbits by numerical differentiation. The right-hand side of equation (5.31) is hereafter called the residual range-rate combination.

5.2.3 3-point range combination approach

In the previous section, we have derived a functional model that can determine the radial component of inter-satellite velocities directly from the KBR range-rates. Although the cross-track component, which is derived from GPS data, is still

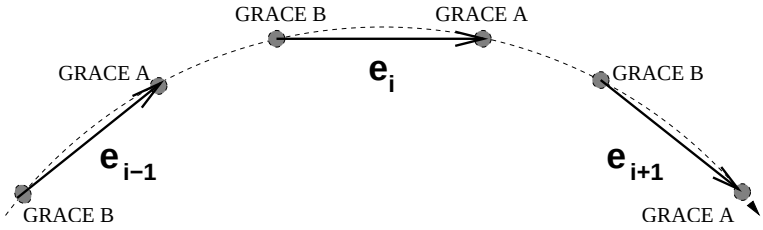

Fig. 5.3. Unit vectors of line-of-sight directions at three successive epochs

involved in correcting the range-rates, this does not cause problems since it is scaled with a factor of the order of 10^{-5}. In this section, we demonstrate that it is even possible to avoid the velocity term in an observation equation. The observation equations can directly connect the potential gradients with KBR ranges rather than with a combination of KBR range-acceleration and velocity orthogonal to the LOS [Liu et al., 2007b, Liu et al., 2007c, Liu et al., 2007d].

The 3-D average inter-satellite acceleration between epochs $i-1$ and $i+1$ can be related to the inter-satellite range vectors $\mathbf{r}_{i-1}$, $\mathbf{r}_i$ and $\mathbf{r}_{i+1}$ according to a simple three-point scheme, similarly to that given by equation (4.2).

$$\ddot{\bar{\mathbf{r}}} = \frac{\mathbf{r}_{i-1} - 2\mathbf{r}_i + \mathbf{r}_{i+1}}{(\Delta t)^2}. \tag{5.32}$$

Since $\mathbf{r}_k = \mathbf{e}_k \cdot \rho_k$ where $k = i-1, i, i+1$, and $\mathbf{e}_k$ is the unit vector of LOS at epoch k as defined before, equation (5.32) can be written as:

$$\ddot{\bar{\mathbf{r}}} = \frac{\mathbf{e}_{i-1} \cdot \rho_{i-1} - 2\mathbf{e}_i \cdot \rho_i + \mathbf{e}_{i+1} \cdot \rho_{i+1}}{(\Delta t)^2}. \tag{5.33}$$

By taking the projection of both sides of equation (5.33) onto the unit vector $\mathbf{e}_i$ at the epoch i, we obtain the following relationship:

$$\mathbf{e}_i \cdot \ddot{\bar{\mathbf{r}}} = \frac{\xi_{(i-)} \cdot \rho_{i-1} - 2\rho_i + \xi_{(i+)} \cdot \rho_{i+1}}{(\Delta t)^2}, \tag{5.34}$$

where $\xi_{(i-)} = \mathbf{e}_i \cdot \mathbf{e}_{i-1}$ and $\xi_{(i+)} = \mathbf{e}_i \cdot \mathbf{e}_{i+1}$, see figure 5.3, which are defined as the navigation parameters for this so-called 3-point Range Combination (3RC) approach. $\xi_{(i-)}$ and $\xi_{(i+)}$ are approximately equal to 1 since the radius of the satellite orbit is much larger than the distance that satellites travel during a sampling interval. Therefore, computation of the right-hand side of equation (5.34) is approximately equivalent to a 3-point double numerical differentiation based on the range measurements. The only problem is that the GRACE KBR range measurements have unknown ambiguities, which can not be restored from KBR data themselves. In order to determine the constant bias in the measured KBR ranges within one continuous segment, precise GRACE satellite baselines are needed.

The functional model given by equation (5.34), is linear and straightforward. We can write it also in the residual form:

$$\mathbf{e}_{i,c} \cdot \delta\ddot{\bar{\mathbf{r}}} = \frac{\xi_{(i-),c} \cdot \delta\rho_{i-1} - 2\delta\rho_i + \xi_{(i+),c} \cdot \delta\rho_{i+1}}{(\Delta t)^2}, \tag{5.35}$$

with $\mathbf{e}_{i,c}$, $\xi_{(i-),c}$ and $\xi_{(i+),c}$ being the reference quantities, which are calculated from the reference orbits. In addition, $\delta\ddot{\bar{\mathbf{r}}} = \ddot{\bar{\mathbf{r}}} - \ddot{\bar{\mathbf{r}}}_c$, and $\delta\rho_k = \rho_k - \rho_{k,c}$ with $k = i-1, i, i+1$. The reference ranges $\rho_{k,c}$ are also calculated from the reference orbits of the two satellites. The right-hand side of equation (5.35) is hereafter called the residual range combination.

5.3 Data processing methodology

In this section, we will describe in detail the data processing strategy for all three approaches presented above. Because many input data and processing steps are shared by all the approaches, it is logical to consider all three approaches at the same time. The reduced-dynamic orbits, which are used as input values, are discussed in section 5.3.1. The computation of purely dynamic orbits is given in section 5.3.2. In section 5.3.3, we discuss how to generate residual quantities from ranges, range-rates and range-accelerations. Section 5.3.4 is devoted to the inversion of the corresponding residuals into unknown parameters. A comparison of the results produced by the three approaches is given in section 5.3.5.

5.3.1 Preparation of orbits

The GRACE satellite orbits, as the result of high-low satellite-to-satellite tracking data processing, do not play a major role of observations. However, they are of importance for establishing accurate reference positions as well as for computing reference quantities and navigation parameters in processing KBR data. We claim that only a purely dynamic orbit can be taken as an accurate reference since neither empirical accelerations nor pseudo-stochastic parameters are introduced as takes place for reduced-dynamic orbits (to reduce the effect of an insufficiently known force model). Therefore, the reference quantities (ranges, range-rates or range-accelerations) derived from purely dynamic orbits can be directly subtracted from the corresponding observed quantities to form the residual observations.

In the classical acceleration approach, the GRACE satellite orbits are also needed to derive observed satellite velocities. In this sense, the orbit must be provided kinematically, since it does not depend on any *a priori* force model. A reduced-dynamic orbit is also not suitable in this context, since it relies on the *a priori* force model.

Of course, a reduced-dynamic orbit might be more accurate than the corresponding purely dynamic orbit from the point of view of positioning accuracy as it is less subject to errors in force models. Therefore, it can be advised, e.g. as the

input for estimation of accelerometer calibration parameters to isolate its errors [Luthcke et al., 2006]. For this reason, reduced-dynamic orbits of the GRACE satellites are used as input to compute the purely dynamic orbit and, at the same time, calibration parameters of the accelerometers. It should be mentioned that the kinematic orbits are also suitable for this purpose if they are available.

Instead of using the reduced-dynamic orbits of both GRACE satellites as input, we use one reduced-dynamic orbit in combination with a set of reduced-dynamic baselines. The reasons to use baselines are as follows. 1) Several investigations have shown that the gravity field models produced from GRACE KBR data are, as a whole, more sensitive to the relative positioning errors of the two satellites than they are to the absolute positioning errors [Jekeli, 1999] [Ditmar and Liu, 2006b]. This means that the accuracy of the baselines is more important than that of the absolute positions of individual satellites. 2) The accuracy of baselines is higher than that of the absolute positions. Furthermore, it can be somewhat improved further by using the KBR measurements. Additionally, precise GRACE satellite baselines are also needed to determine the constant bias in the measured KBR ranges within one continuous segment for the 3RC approach.

For the years 2003-2005, precise reduced-dynamic orbits of the GRACE A satellite and a set of reduced-dynamic baselines were provided by the Astrodynamics and Satellite Systems in DEOS (Delft Institute of Earth Observation and Space Systems) [Kroes et al., 2005]. It should be mentioned that baseline solutions are directly determined from GPS measurements rather than being computed from the L1B ephemerides [Case et al., 2004]. An important feature of the exploited baselines is that double difference ambiguities of GPS phase measurements are fixed with a relatively high success-rate. In addition, an extended Kalman filter, complete with a rigorous ambiguity validation, was employed to smooth the relative baseline estimates in the estimation process. As a result, the baselines of the GRACE satellites were determined with a precision of slightly less than 1 mm, as determined through a comparison with KBR measurements [Kroes et al., 2005].

The orbit data of 2006 were kindly provided by the GNSS Research Center of Wuhan University. The high-precision kinematic orbits and baselines are used instead of reduced-dynamic ones. The accuracy of the exploited baselines is 3-4 mm. The baselines were also processed in relative mode, but added to an absolute orbit, resulting in two individual kinematic orbits before they are provided to us [Zhao et al., 2007]. In this case, we directly use the provided kinematic orbits as input to compute the purely dynamic orbits.

Although the exploited baselines are of high quality, we still make an attempt to improve them using KBR range measurements. However, KBR range measurements can not be used for that purpose directly, since they are suffer from phase ambiguities, just like GPS phase measurements. To determine the KBR range bias (also needed in the 3RC approach), the GPS baselines within a continuous KBR tracking segment are used. A continuous KBR tracking segment

is a segment, in which the ambiguities do not change. The unknown constant in the KBR ranges can be computed as:

$$B_{KBR} = \frac{1}{n}\sum_{i=1}^{n}(\rho_c(t_i) - L_{KBR}(t_i)), \tag{5.36}$$

where $\rho_c(t_i)$ and $L_{KBR}(t_i)$ are the computed ranges and measured biased ranges at the epoch t_i, respectively, and n is the number of KBR range measurements within a continuous KBR tracking segment. In this way, we can restore the unknown constant in the KBR ranges:

$$\rho(t_i) = L_{KBR}(t_i) + B_{KBR}. \tag{5.37}$$

Theoretically, the precision of KBR bias-corrected ranges can reach a few microns when the length of a continuous segment is above ten thousand epochs as it follows from the the error propagation law ($1\,\mathrm{mm}/\sqrt{10000} = 10\,\mu\mathrm{m}$). In most cases, the actual segment length exceeds this number. It is important to add that range combinations derived from the bias-corrected observed ranges in the 3RC approach do not suffer from errors in the estimated biases because the latter ones are canceled out after the double differentiation.

The orbit preparation for the years 2003-2005 is outlined in the flow chart shown in figure 5.4. The input data sets include reduced-dynamic positions of satellite A, with the 30-sec sampling rate, and baseline vectors between satellite A and B, with the 10-sec sampling rate [Kroes et al., 2005]. Positions and baselines are given in an Earth-fixed Earth-centered frame and in the GPS time system. Both are transformed into the inertial frame using rotation matrices. Afterwards, an 11th order shifted Legendre interpolation scheme is applied to obtain 5-sec sampling positions and baselines. Our experiments tell us that the accuracy of the 11th shifted Legendre interpolation is sufficient. After the interpolation, both positions and baselines have the same sampling rates as the KBR measurements, i.e. 5-sec interval. The baselines are used to determine the bias in the KBR biased-ranges, and after that the bias-corrected ranges can be used to adjust (scale) the baselines. The vector summation of the corrected baselines and satellite A results in the orbit of satellite B. Finally, the orbits of the two satellites are rotated back into the Earth-fixed Earth-center frame to be used as the input for orbit fitting and for the computation of the design matrix.

5.3.2 Orbit fitting for computation of purely dynamic orbit

As discussed previously, the purely dynamic orbit must be taken as an accurate orbital reference. Ideally, the purely dynamic orbit can be computed on the basis of GPS measurements directly; however, this will dramatically increase both the computational burden and overall complexity of the problem, and is a topic considered to be beyond the scope of this thesis. Therefore, we prefer to compute dynamic orbits by fitting an existing high-precision orbit. To this end, the reduced-dynamic orbits prepared in the previous section are exploited in this

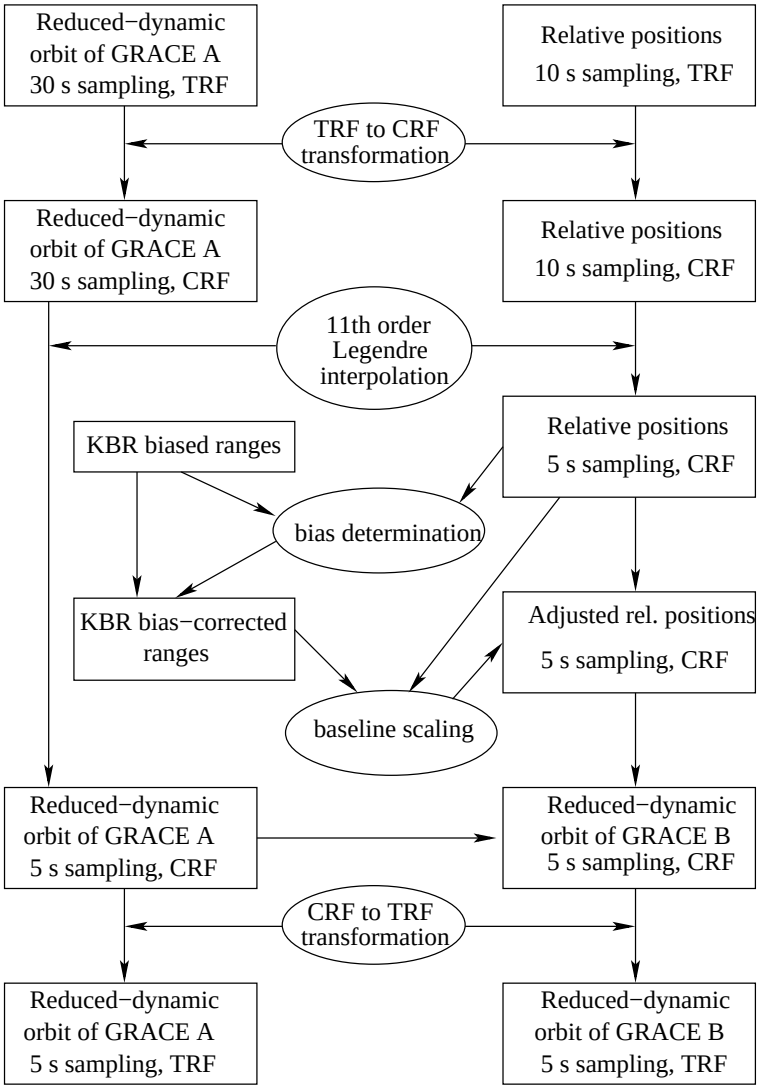

Fig. 5.4. Flow chart of orbit preparation

step as the input.

An accurate dynamic orbit can not be obtained without an improvement in the non-gravitational acceleration measurements. In other words, the accelerometer data should be calibrated simultaneously with orbit fitting. This section discusses the exploited procedure of orbit integration and orbit fitting. The procedure is based on the integration and orbit fitting module of PANDA, a

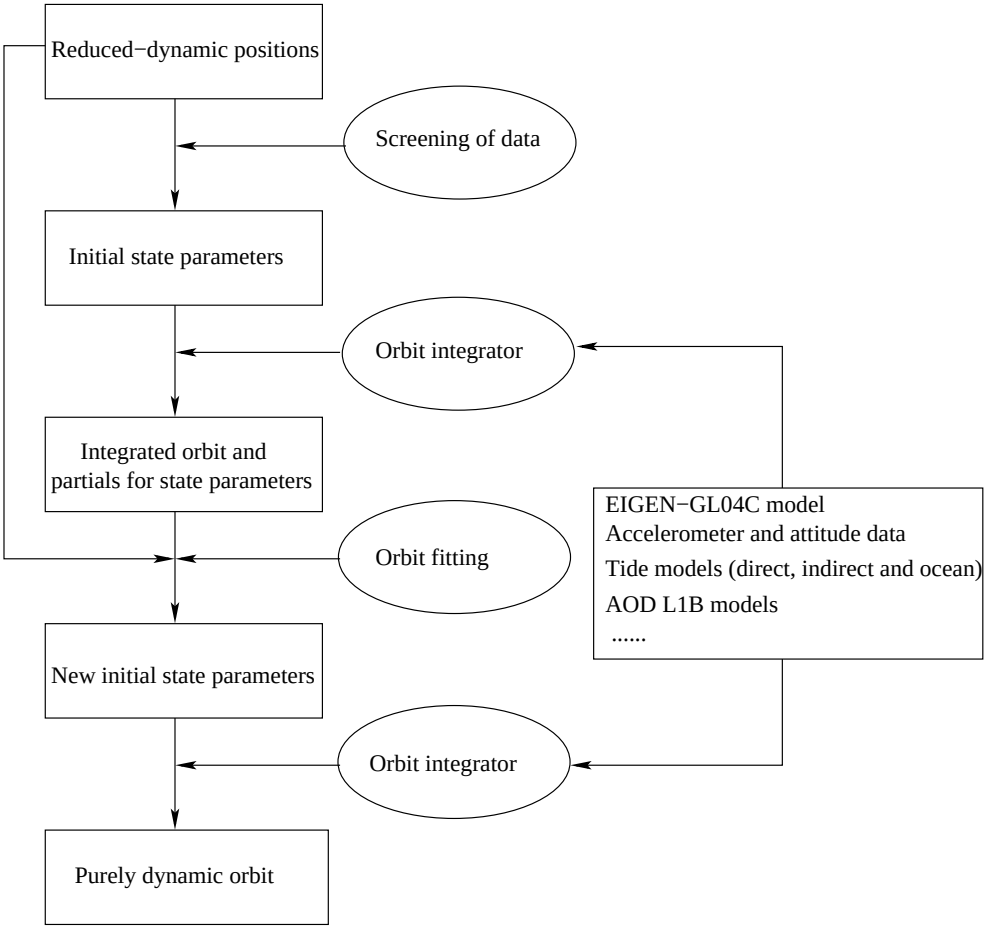

Fig. 5.5. Flow chart of orbit fitting

precise orbit determination software originally developed at the GNSS Research Center of Wuhan University [Zhao et al., 2007]. The module was updated in the context of this study by incorporation of the latest updates of force models and conventions.

The computation procedure is demonstrated in the flow chart shown in figure 5.5. In essence, the procedure is divided into three steps. The first step is the orbit integration on the basis of (i) the initial state parameters that are the initial position and velocity per orbit arc and (ii) the calibration parameters that include 3-dimensional bias and scale factor vectors for non-gravitational accelerations per arc. The *a priori* initial position and velocity are picked up from the reduced-dynamic positions at the beginning of the arc. The *a priori*

values for the biases and scale factors are set to zero. During the first integration, the partial derivatives with respect to the initial state parameters and calibrated parameters are computed, together with the positions, on the basis of known force models. The orbit fitting is carried out in the second step, during which the residuals between the reduced-dynamic orbit and the integrated one are computed. After that, corrections to the *a priori* initial state parameters and calibration parameters are estimated using the least-squares adjustment. Based on the newly obtained estimates, the purely dynamic orbit is computed in the third step by using the integrator.

The procedure is similar to that presented by [Luthcke et al., 2006]. However, we implicitly make use of bias-corrected ranges instead of range-rates during the orbit fitting, since the baseline vectors of the two satellites are adjusted using bias-corrected ranges beforehand. Additionally, we do not estimate one-cycle-per-revolution (cpr) parameters in the along-track direction for the accelerometer data calibration, but only bias and scale factors for each of three directions per arc. Furthermore, the length of the arc is 6 hours rather than one day. In this way, we can largely avoid the accumulation of resonance effects caused by errors in the initial state vector and the zonal coefficients of the background gravity field model [Visser, 2005].

The numerical integration of the equations of motion is carried out using the 11th order Adams multi-step method [Montenbruck and Gill, 2000]. The integration step-size is 1 second. The Runge-Kutta single-step method is used to compute the values at the first few points so that the Adams integrator is properly initialized. The integration is performed in the inertial frame.

The integration of the equations of motion relies on the accelerations experienced by the satellite. The accelerations are the sum of gravitational and non-gravitational perturbations. The non-gravitational accelerations are measured by the accelerometers. The known gravity signals, including those related to the static field, should be fully considered during the orbit integration. The acceleration vector caused by direct planetary perturbations can be easily evaluated using the planetary ephemerides. Other geopotential perturbations are represented by a spherical harmonic series with time-variable coefficients, to a specified maximum degree and order.

The background force models and data sets for the computation of accelerations of the satellites are given as follows. Firstly, the EIGEN-GL04C model up to degree 150 is taken as the static reference field. The secular changes of coefficients $C_{20}, C_{21}, S_{21}, C_{30}$ and C_{40} are considered according to the IERS 2003 convention [McCarthy and Petit, 2003]. The reference epoch of the secular change is the epoch 2004. These secular changes are mainly the differences between the mean figure axis and mean rotation pole averaged over the observation period of the background gravity field model. These differences would be due to long-term fluid motions in the atmosphere, oceans, or Earth's fluid core. Secondly, solid

Earth tidal contributions to the geopotential are computed as specified in chapter 7, IERS 2003 conventions. The DE-405 planetary ephemerides are used to compute the N-body perturbations. The direct perturbations due to the Sun, Moon and all the planets are also evaluated. All of the N-body accelerations acting on the satellite are computed using point-mass attraction formulas. The indirect effects due to the accelerations of the Earth caused by the planets are also computed as point-mass attractions. The frequency independent term is computed from degree 2 to degree 4, while the frequency dependent one is only considered as corrections to coefficients of degree 2. Thirdly, the ocean tides are modeled according to the FES2004 model [Lyard et al., 2006]. Nine diurnal/semi-diurnal and four long-period constituents are considered up to degree 80. Fourthly, the AOD1B RL04 product is used to take atmosphere and oceanic variability into account [Flechtner, 2007a]. The product is a combination of the ECMWF operational atmospheric fields and the barotropic ocean model OMCT driven by the atmospheric fields. The AOD1B RL04 product is provided in terms of spherical harmonics up to degree 100 and with 6-hour temporal resolution. The value of the harmonic coefficients at intermediate epochs is obtained by linear interpolation. In addition, the pole tide, caused by rotational deformation, is also computed as changes to the coefficients C_{21} and S_{21}. For the ocean pole tides, a self-consistent equilibrium Desai model [Desai, 2002] up to degree 30 is used to consider the centrifugal effect of polar motion on the oceanic mass. Furthermore, the general relativistic perturbations are computed as specified in the IERS2003 convention. Finally, the level 1B non-gravitational accelerations measured by accelerometers, and quaternions measured by the star cameras, are used to take surface forces into account [Case et al., 2004].

5.3.3 Generation of residual quantities

Once we have obtained the purely dynamic orbits for the two GRACE satellites, the reference quantities necessary for the three approaches can be computed. Figure 5.6 shows the procedure for generating the computed ranges and range-rates, which are derived easily from the position differences and velocity differences, respectively. Furthermore, the orthogonal components of velocity differences can also be computed for the classic acceleration approach. In order to form the residual quantities (also called residuals of pseudo-observation) for these three approaches, unit vectors (that define the LOSRF) and navigation parameters are calculated as well. In addition, the range-accelerations are obtained from the computed ranges by using numerical differentiation. The scheme of the double numerical differentiation has been already discussed in section 2.5.4.

The computation of residual quantities for the classical acceleration approach and the 3RRC approach must involve the velocity differences, see figure 5.7 and figure 5.8. The observed velocity differences are derived from the kinematic baselines, which were also used in section 4.4 for the GRACE hl-SST data processing. The noise level of the kinematic baselines we used is around 4 mm, according to the comparison made by [Kroes, 2006]. It is higher than that of the

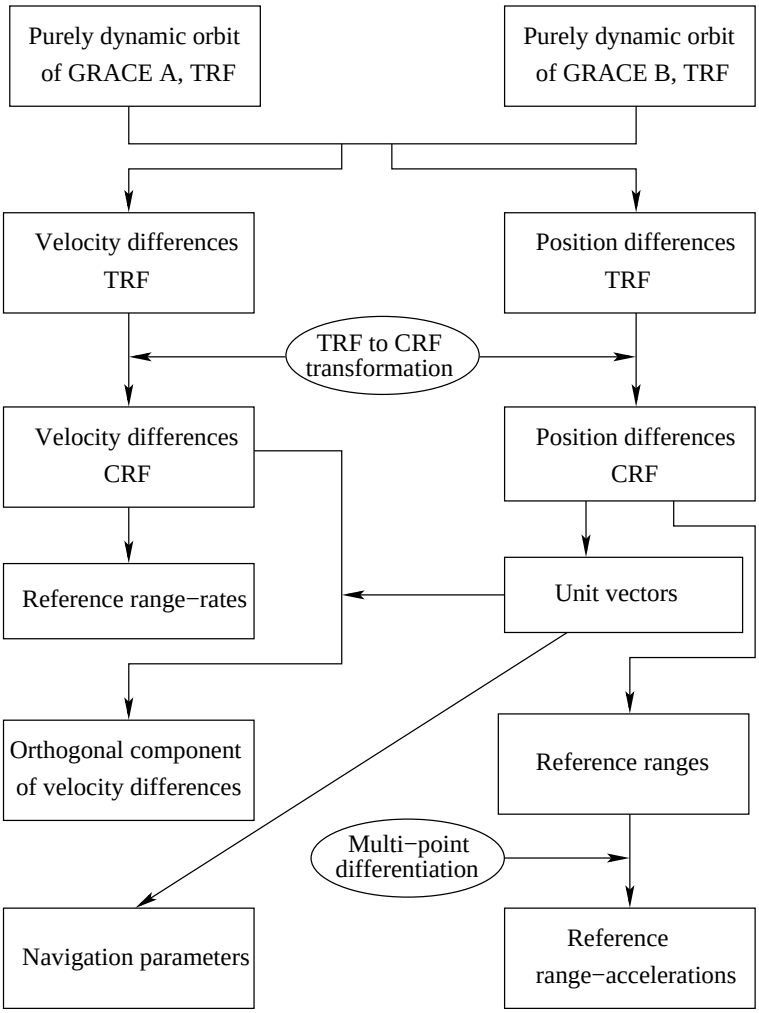

Fig. 5.6. Generation of reference ranges, range-rates and range-accelerations as well as the orthogonal component of velocity differences and navigation parameters

reduced-dynamic baselines since the kinematic baselines suffer from larger random noise. The sampling rate of the baselines is 10 sec, and the interpolation (same as before) is applied to match the sampling rate of the KBR measurements (5 sec). We found that the interpolation does not reduce the accuracy of the baselines, see figure 5.9a, which remains at the level of 4 mm. The observed velocity differences can then be derived from the kinematic baselines by means of numerical differentiation. Figure 5.9(b) demonstrates that the precision of the derived inter-satellite velocities is 0.5×10^{-3} m/s, which is three orders of magnitude larger than that of the KBR range-rates, and is consistent with the analysis of section 5.2.

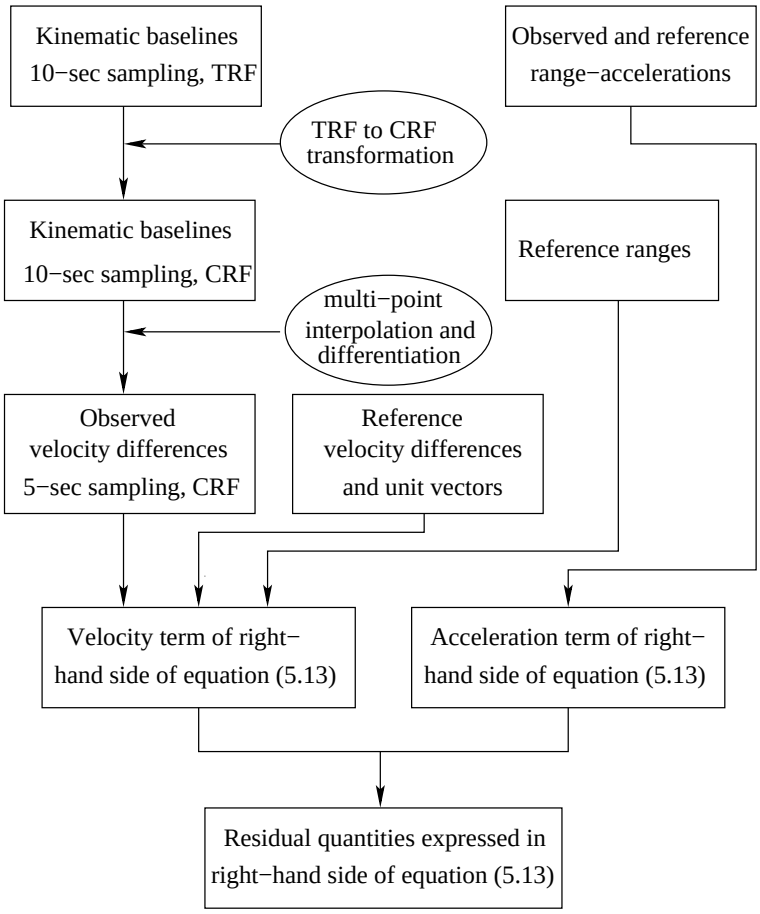

Fig. 5.7. Computation of residual quantities for the classic acceleration approach

The residual velocity and range-acceleration terms in equation (5.13) are computed, as shown in figure 5.7. In order to validate the analysis conducted in section 5.2, the daily Root-Mean-Square (RMS) values of the two terms in equation (5.13) are shown for August 2003 in figure 5.10. There is no data available for the statistics in August 24 since the purely dynamic orbit of the day is not good enough to be taken as the reference one. Regarding the other days, the RMS values of the velocity term are around $3.0\,\mu\mathrm{m/s}^2$, while less than $0.1\,\mu\mathrm{m/s}^2$ RMS values are indicated for the range-acceleration term, see figure 5.10. The velocity term is more than 30 times larger than the range-acceleration term. These statistics are similar to the analysis in section 5.2. The gravity field model estimated with the acceleration approach represented by equation (5.13) (the sum of these two terms) will be demonstrated in section 5.3.5.

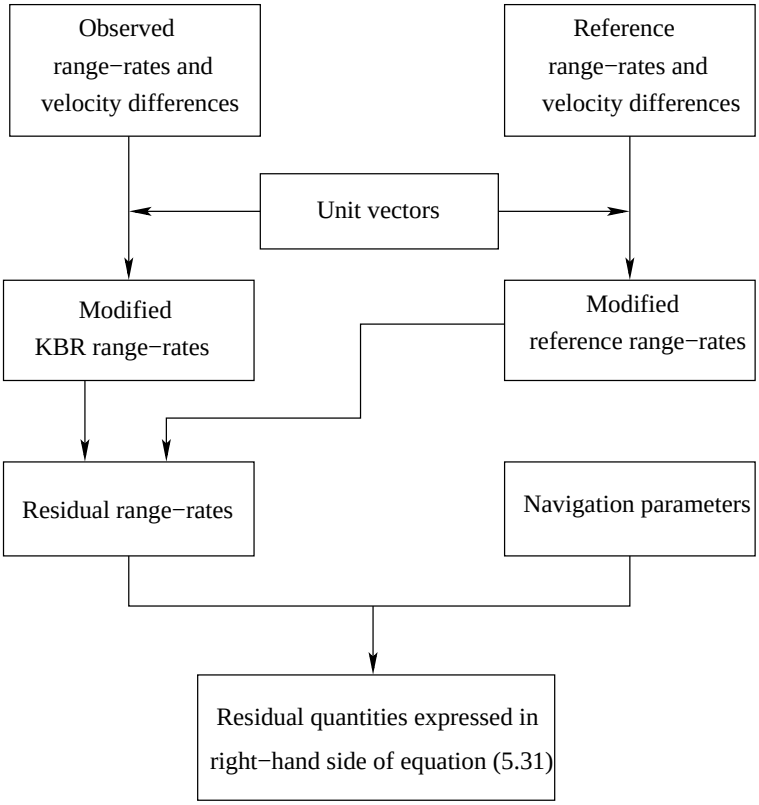

Fig. 5.8. Computation of residual quantities for the 3RRC approach

As far as the computation of residual range-rate combinations and the residual range combinations is concerned, we can refer to the procedures shown in figure 5.8 and figure 5.11. First of all, residual ranges and residual range-rates have to be computed, respectively. Figures 5.12(a) and 5.12(c) show a one day time series of residual ranges and residual range-rates, respectively. The resonance effects, shown as a low-frequency variations, are still seen in the time series, though they are largely avoided by using relatively short arcs (6 hours per arc), in the integration of purely dynamic orbits. The resonance effects are caused by the errors in the initial state vector, i.e. the initial position and velocity of the satellite, which may not be 100% correct, even though they are adjusted in the course of orbit fitting. Furthermore, even if the initial state vector is 100% correct at the beginning of the procedure, the differences between the reference gravity field model and the true one could cause errors in the positions and velocities after the integration of the first epoch. These errors will further cause large errors at the epochs afterwards. The resonance effects must be eliminated or

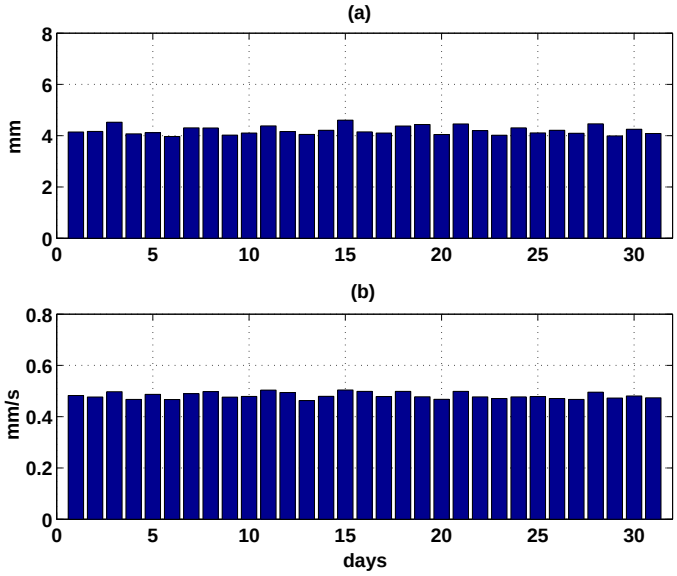

Fig. 5.9. Daily RMS values of the differences between the ranges derived from the kinematic baselines and the ones observed by the KBR system (a). Daily RMS values of the differences between the range-rates derived from the kinematic baselines and the ones observed by the KBR system (b). Shown are data of August 2003

modeled, otherwise they can be mapped onto all the coefficients of the estimated gravity field model, according to our experiments. In many cases, the influence could be larger than the signal to be estimated. As indicated by [Colombo, 1984], resonance effects result in a bow-tie pattern in orbit perturbations. Such a bow-tie pattern can be modeled with a sufficient accuracy by using empirical parameters, i.e. bias, bias trend and 1-cpr parameters every orbital revolution [Visser, 2005]. Taking the residual range-rates as an example, we can write

$$\Delta\dot{\rho} = a_1 + a_2\omega_0 t + a_3\cos\omega_0 t + a_4\sin\omega_0 t + a_5(\omega_0 t)^2 + a_6\omega_0 t\cos\omega_0 t + a_7\omega_0 t\sin\omega_0 t, \tag{5.38}$$

where ω_0 represents the orbital angular velocity of the satellite, t is time and $a_i (i = 1, 2, ..., 7)$ are constant values that can be estimated by least-squares fitting. Figures 5.12(b) and 5.12(d) demonstrate the residual ranges and range-rates after resonance effects are eliminated. It can be seen from figure 5.12 that the residuals of range-rates contain more power at high-frequencies, and much less power at low-frequencies than those of ranges. This can be explained by the fact that the numerical differentiation acts as a high-pass filter.

After the subtraction of resonance effects, the residual range-rate combinations and range combinations are obtained that are suitable for gravity field

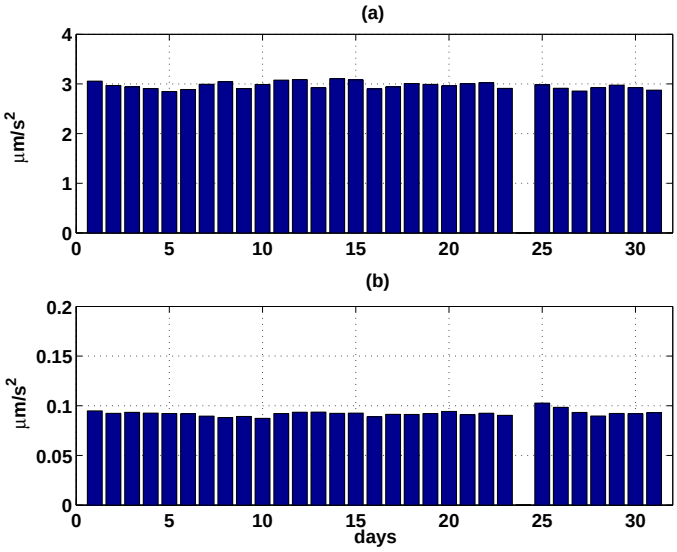

Fig. 5.10. Daily RMS values of the velocity term (a) and the range-acceleration term (b) of equation (5.13) for August 2003

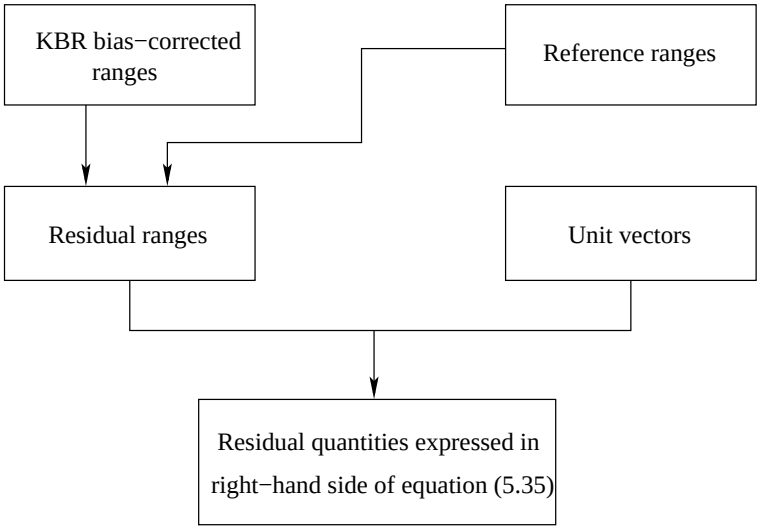

Fig. 5.11. Computation of residual quantities for the 3RC approach

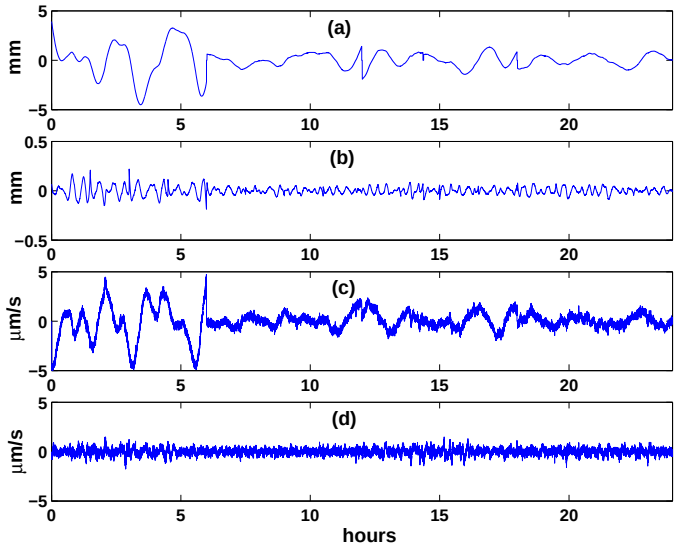

Fig. 5.12. Time series of residual ranges and residual range-rates. (a) residual ranges, (b) residual ranges after resonance effects are eliminated, (c) residual range-rates, (d) residual range rates after resonance effects are eliminated. Shown are data of August 1, 2003

modeling. According to the definition of the force model used for the computation of reference orbits, the residuals contain gravity signals only from non-modeled time-varying effects, e.g. hydrology, snow cover, ice sheets and post-glacial rebound, as well as signals caused by imperfections of the exploited temporal models used. In addition, noise from the KBR measurements, inaccurate calibration of the accelerometer data, and inaccurate orbits remain in residuals. As we know from the previous sections, the range-rate combinations are approximately equal to third-order derivatives of ranges, and the range combinations are approximately double differentiated ranges. One may argue that the differentiation amplifies high-frequency noise, which may exceed the level of temporal gravity field signals. Therefore, these residuals can not be used to achieve even a reasonable gravity field solution. This is fortunately not true. The total noise level of residuals may indeed be higher than that of signals which we expect to recover; however, noise in the residuals depends on frequency. In other words, noise can be very strong at the high frequencies (for example, roughly proportional to the frequency squared in the case of range-combination), whereas, at lower frequencies, the noise rapidly decreases so that no information is lost. To validate this statement, we plot in figure 5.13, a global distribution of residual range combinations of August 2003 at the geographical locations of the middle point of the two satellites. The original residuals are showed in figure 5.13(a), from which nothing but scattered noise can be seen. Figure 5.13(b) displays the residuals after low-pass filtering. To this end,

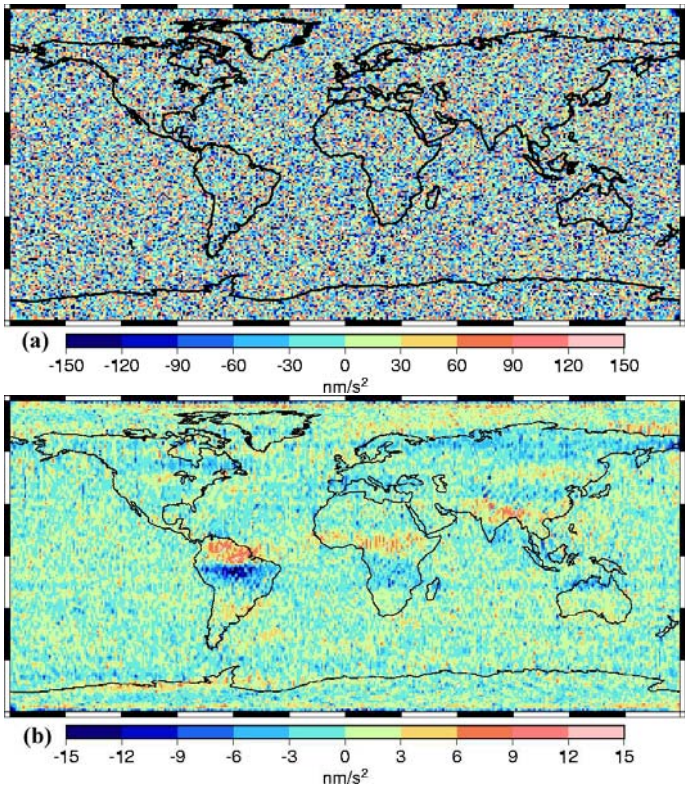

Fig. 5.13. Map of residual range combinations of August 2003 without low-pass filtering (a) and with a low-pass filtering (b); Note that the two maps have different color bars.

a wavelet decomposition and reconstructing procedure is used [Mallat, 1989]. The decomposition level is selected on a low-pass cutoff frequency which was defined to ensure the spectral representation of the gravity field up to degree 40. As can be seen from figure 5.13(b), clear signals are observed in many geographical areas, e.g. the Amazon and Orinoco river basins of South America, the Zambezi basins of Africa, the Ganges basin of the southern Asia and Siberia region. The pattern of the residuals of range-combinations is very similar to that of mass changes in terms of equivalent water height (shown later), up to a scale factor. Therefore, it can be concluded that residual range combinations still preserve temporal gravity field variations and can be used to quantify them. The same holds also for the range-rate combinations, though in that case it is more difficult to demonstrate directly the presence of signal in the residuals. A prerequisite is that the frequency-dependent data weighting is required in estimation of gravity field parameters.

5.3.4 Least-squares adjustment

In the previous section, we have discussed the computation of the residual quantities for all three approaches. In this section, the inversion of the generated residual quantities into residual gravity field parameters is described in our discussion. We focus on the differences with respect to the processing of the kinematic baselines described in chapter 4. The major difference is that an ll-SST observation is a scalar value rather than a 3-component vector as it is the case for kinematic baselines. Another difference concerns the averaging filter: the 3RC approach uses the same filter as was already introduced in the context of hl-SST data processing (see section 2.5.4.2); the classical acceleration approach does not need an averaging filter since it makes use of point-wise range-accelerations to form its functional model; and the 3RRC approach needs a new averaging filter, which is derived below. Finally, the noise models used in the three approaches also need to be adjusted.

5.3.4.1 Design matrices for the three functional models

Just like in the case of processing the hl-SST data, the conjugate gradient method is exploited for the inversion of ll-SST data into the Earth's gravity field model. In doing so, dedicated synthesis and co-synthesis procedures are applied. A general expression of the synthesis can be given as:

$$\mathbf{A} = \mathbf{R}_{\mathbf{ll}}(\mathbf{A}_{\mathbf{pw,B}} - \mathbf{A}_{\mathbf{pw,A}}), \tag{5.39}$$

where $\mathbf{A}$ is the final design matrix; and $\mathbf{A}_{\mathbf{pw,A}}$ and $\mathbf{A}_{\mathbf{pw,B}}$ are the satellite A and B related point-wise design matrices in TRF, respectively. They are the same as described by equation (4.10). $\mathbf{R}_{\mathbf{ll}}$ is the transformation matrix, which links the point-wise inter-satellite accelerations to the observations.

The explicit expression for the matrix $\mathbf{R}_{\mathbf{ll}}$ depends on the functional model. For the classic acceleration approach, $\mathbf{R}_{\mathbf{ll}}$ can be written as:

$$\mathbf{R}_{\mathbf{ll}} = \mathbf{R}^{(\mathbf{C}\rightarrow\mathbf{LF.x})}\mathbf{R}^{(\mathbf{T}\rightarrow\mathbf{C})}, \tag{5.40}$$

where $\mathbf{R}^{(\mathbf{T}\rightarrow\mathbf{C})}$ is the transformation matrix of rotation from TRF to CRF, and $\mathbf{R}^{(\mathbf{C}\rightarrow\mathbf{LF.x})}$ is the matrix that describes the projection of a 3-D vector defined in the CRF onto the $\mathbf{x}$-axis of the LOSRF. Notice that there is no need for an averaging filter.

For the 3RC approach, $\mathbf{R}_{\mathbf{ll}}$ can be written as:

$$\mathbf{R}_{\mathbf{ll}} = \mathbf{R}^{(\mathbf{C}\rightarrow\mathbf{LF.x})}\mathbf{E}\mathbf{R}^{(\mathbf{T}\rightarrow\mathbf{C})}. \tag{5.41}$$

In this case, the averaging filter is included, which is exactly the same as in processing the kinematic baselines.

For the 3RRC approach, $\mathbf{R}_{\mathbf{ll}}$ can be written as:

$$\mathbf{R}_{\mathbf{ll}} = \mathbf{D}\mathbf{R}^{(\mathbf{C}\rightarrow\mathbf{LF.xz})}\mathbf{E}_v\mathbf{R}^{(\mathbf{T}\rightarrow\mathbf{C})}. \tag{5.42}$$

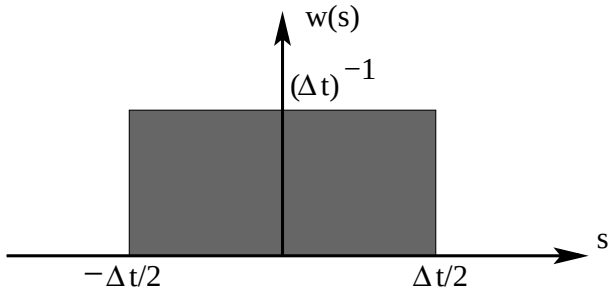

Fig. 5.14. Weight function that describes the averaging of accelerations derived from velocities by a single differentiation with a two-point scheme

The matrix $\mathbf{R_{ll}}$ includes four different operators, three of which are new. First of all, the average filter given by the matrix $\mathbf{E}_v$ is different from the one used in the 3RC approach. This is discussed in section 5.3.4.2. Secondly, $\mathbf{R}^{(\mathbf{C}\rightarrow\mathbf{LF}.\mathbf{xz})}$ describes the projection of vector defined in the CRF onto xz-plane in the LOSRF. Finally, the matrix $\mathbf{D}$ consists of the navigation parameters, such as ν_i, $\tau_{(i-)}$, $\tau_{(i+)}$, defined in equation (5.29). These parameters are computed along with the residual quantities. From the implementation point of view, the classic acceleration approach is the easiest approach, and the 3RRC approach is the most complicated one among the three.

5.3.4.2 Averaging filter for the 3RRC approach

The averaging filter for the 3RRC approach is different from that used in the range-combination approach, because average accelerations are derived here from the range-rates, i.e. velocities. It is obvious that a single differentiation based on velocities at two epochs results in exactly the average acceleration within the differentiation interval. Therefore, the weight function should be written as:

$$w(s) = \frac{1}{\Delta t}, \tag{5.43}$$

see also figure 5.14. In this case, the accelerations can be represented for a given time interval $[t - \frac{n}{2}\Delta t, t + \frac{n}{2}\Delta t]$ as follows:

$$a(t+s) = \sum_{j=0}^{2n-1} c_j s^j, \quad s \in [-\frac{n}{2}\Delta t, \frac{n}{2}\Delta t] \tag{5.44}$$

where c_j are the coefficients to be found and n being an odd number. Notice that the time range of the averaging filter is not identical to the one in equation (2.83). The coefficients c_j can be found with equation (2.74). The square matrix $\mathbf{V}$ is

defined as:

$$\mathbf{V} = \begin{pmatrix} 1 & \frac{-n}{2}\Delta t & \cdots & (\frac{-n}{2}\Delta t)^k & \cdots & (\frac{-n}{2}\Delta t)^{2n-1} \\ 1 & (\frac{-n+2}{2})\Delta t & \cdots & (\frac{-n+2}{2}\Delta t)^k & \cdots & (\frac{-n+2}{2}\Delta t)^{2n-1} \\ \vdots & \vdots & \ddots & \vdots & \ddots & \vdots \\ 1 & (\frac{-n+2k}{2})\Delta t & \cdots & (\frac{-n+2k}{2}\Delta t)^k & \cdots & (\frac{-n+2k}{2}\Delta t)^{2n-1} \\ \vdots & \vdots & \ddots & \vdots & \ddots & \vdots \\ 1 & \frac{n}{2}\Delta t & \cdots & (\frac{n}{2}\Delta t)^k & \cdots & (\frac{n}{2}\Delta t)^{2n-1} \end{pmatrix}. \quad (5.45)$$

Taking the weighting function into account, we can write the average acceleration as:

$$\bar{a}(t) = \int_{-\Delta t/2}^{\Delta t/2} w(t)a(t+s)ds = \frac{1}{\Delta t}\int_{-\Delta t/2}^{\Delta t/2} \sum_{j=0}^{2n-1} c_j s^j \mathrm{d}s$$

$$= \frac{1}{\Delta t}\sum_{j=0}^{2n-1} \frac{c_j}{j+1} s^{j+1}\Bigg|_{-\Delta t/2}^{\Delta t/2} = \frac{1}{\Delta t}\sum_{j=0}^{2n-1} \frac{c_j}{j+1}\left\{(\frac{\Delta t}{2})^{j+1} - (\frac{-\Delta t}{2})^{j+1}\right\}$$

$$:= \mathbf{w}_v^T \mathbf{c}, \quad (5.46)$$

where elements of the vector $\mathbf{w}_v$ are defined as:

$$\{\mathbf{w}_v\}_j = \begin{cases} (\frac{\Delta t}{2})^j \frac{1}{2(j+1)} & \text{for even} \quad j \\ 0 & \text{for odd} \quad j \end{cases} \quad (j = 0, 1, ..., 2n-1) \quad (5.47)$$

Similar to equation (2.87), we obtain:

$$\bar{a}(t) = \mathbf{w}_v^T \cdot \mathbf{V}^{-1}\mathbf{a} := \mathbf{e}^T\mathbf{a}, \quad (5.48)$$

where

$$\mathbf{e} = (\mathbf{V}^T)^{-1}\mathbf{w}_v. \quad (5.49)$$

Thus, the averaging filter has three differences with respect to the one given by equation (2.88): the Vandermonde-type matrix $\mathbf{V}$ is different; the degree of the polynomial to be chosen is an even integer rather than odd; the input vector $\mathbf{w}$ of the Vandermonde-type system of linear equations is also different.

5.3.4.3 Noise models used in the three approaches

Because all the three approaches make use of differentiation to derive the input data for the inversion, the noise in the input data sets is increased with frequency

in the spectral domain. Therefore, a frequency-dependent weighting should be included into the least-squares adjustment. The noise models used in the three approaches should be considered differently; however, they all can be linked to the procedure of noise estimation described in section 3.4. The major steps of the noise estimation are the computation of the PSD of the residuals, and an analytic approximation of PSD by estimation of the parameters β and τ (see equation (3.25). It should be mentioned that the scaling parameter, β, is not that important as in the case of CHAMP data processing, since there is only one data component to be processed. Therefore, the relative weighting of components is not an issue. In the absence of regularization, this parameter plays no role at all. However, it still makes sense to have a realistic estimation of β if the variance-covariance matrix of the obtained gravity field model is required.

Ideally, the *a posteriori* residuals should be used as input for the estimation of the noise model. However, we found that it did not make much of a difference when using the original residuals obtained as discussed in the previous sections, since they only contained minor additional signals compared to the posteriori residuals. These signals are mostly present at low frequencies and practically do not change the estimation of parameters β and τ.

In order to clarify the noise estimation in the three approaches further, let us consider an example. The residuals of August 2003 produced as discussed in section 5.3.3 are taken as input. The PSDs of three sets of residuals are displayed in figure 5.15 (red line). The parameters β and τ are estimated and used to build the analytical approximations, which are displayed as blue dashed lines in figure 5.15. We also introduce a trial noise model for each type of residuals to investigate whether the obtained results are sensitive to the noise models. The trial noise models are shown as a black line in figure 5.15. The estimated and trial noise models are used to process the real data of August 2003. Additionally, the processing is repeated with the frequency-dependent data weighting switched off, i.e. with identical weighting of all frequencies. The gravity field models are estimated up to degree 120, without regularization. Table 5.1 allows the models to be quantitatively compared. The cumulative geoid height differences with respect to the EIGEN-CG04C model computed for degree 40 is taken as the indication of a model quality.

From the comparison, we can see that absence of frequency-dependent data weighting gave the worst results for the 3RRC. The result can be an order of magnitude worse in that case. Therefore, it can be concluded that the frequency-dependent data weighting is essential for this approach. In addition, it is found that the results of the 3RRC approach are sensitive to the noise model. The trial noise model gave even better results than that estimated from the residuals. This may demonstrate that the noise estimation procedure may not very suitable for the approach. Further research here is needed. In the classic acceleration approach, we can see that the total error is dominated by noise in the velocity term. This noise does not vary significantly in the frequency

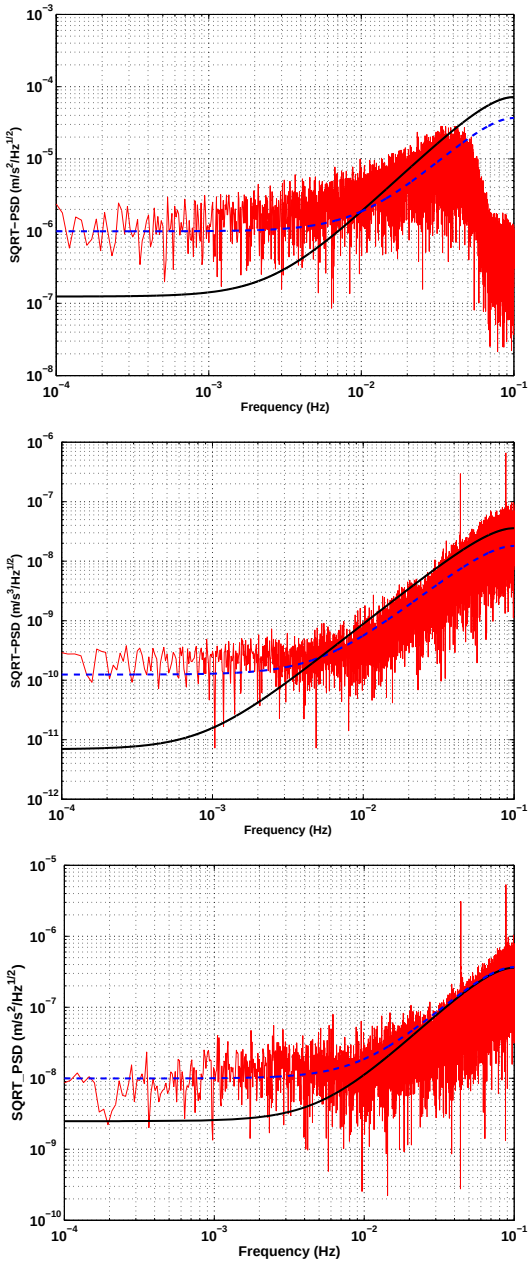

Fig. 5.15. Noise models for the classical acceleration approach (top), the 3RRC approach (middle), and the 3RC approach (bottom). The residuals of real data are displayed in red, their analytical noise models in dashed blue, and the corresponding trial noise models in black

Table 5.1. Cumulative geoid height differences with respect to EIGEN-GL04C computed for degree 40. The trial noise model and the noise model from real residuals indicate that frequency-dependent data weighting is used

approach	identical data weighting	trial noise model	noise model from real residuals
acceleration	127.0 mm	136.0 mm	126.0 mm
3RRC	63.0 mm	2.7 mm	3.9 mm
3RC	1.1 mm	1.1 mm	1.1 mm

range under consideration. The results obtained with the trial noise model give slightly worse results, mainly due to the fact that unrealistically high weights are given to the low frequencies. As far as the 3RC approach is concerned, the frequency-dependent data weighting does not make any difference at the low degrees. Therefore, the noise model and uniform weighting results with the same accuracy. At the higher degrees, it is found that the frequency-dependent data weighting gives slightly better results than those produced without frequency data weighting (around 5% at degree 110 - 120, not shown here). The same behavior is observed for other months. We consider this to be an advantage of the 3RC approach. From the comparison, we also find that the 3RC approach produced better results than the other two. More details of the comparison of three approaches will be given in next section.

5.4 Comparison of results

Using the procedures of data processing described in previous sections, we carried out gravity field modeling on the basis of real data. In this section we will compare the results obtained with the three approaches for two months: August 2003 and October 2003. In order to investigate the quality of the results, the GLDAS hydrological model is used for a comparison.

GLDAS stands for the NASA's Global Land Data Assimilation System [Rodell et al., 2004], which is jointly developed by the NASA Goddard Space Flight Center (GSFC) and the NOAA National Center for Environmental Prediction. GLDAS is an advanced modeling system, parameterizing and constraining multiple land surface models with ground- and satellite- based measurements, with the aim of estimating the water and energy cycle states and fluxes. GLDAS can be used, in particular, to estimate water storage variations in a given region. The change in total water storage has many components, such as changes in soil moisture, snow water, ground water and open water. The total storage ΔS is

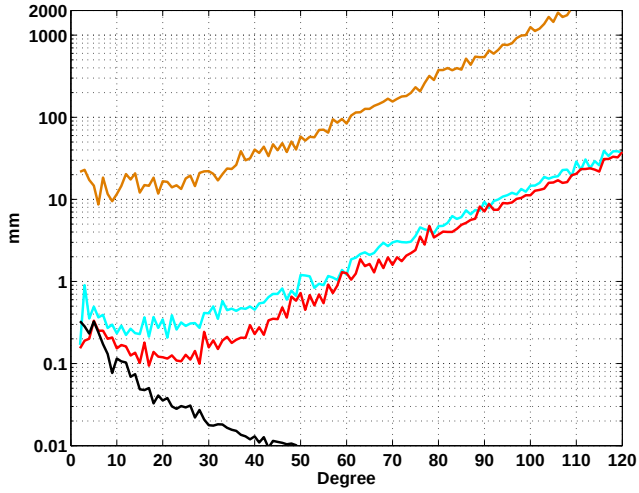

Fig. 5.16. Degree amplitude of the recovered gravity field variations in August 2003 in terms of geoid heights. The models are obtained with the classical acceleration approach (orange), the 3RRC approach (light blue), and the 3RC approach (red). The GLADS hydrological model (black) is shown for a comparison

described by the water balance equation:

$$\Delta S = P - E - R, \tag{5.50}$$

where P is the precipitation, E is the evapotranspiration, and R is the run-off in open water body and/or discharge through underground flows. The precipitation and evapotranspiration are estimated with a relatively high accuracy by assimilating the latest surface observations and remote sensing data in the GLDAS system. However, the run-off is still not trivial to measure with the same level of accuracy. Consequently, GLDAS does not monitor all components of the water storage; it reflects only soil moisture and snow water equivalent [Rodell et al., 2006]. Furthermore, Greenland and Antarctica are excluded in the GLDAS models because the ice sheet flow and ice mass balance are not modelled due to that they are not represented by the Noah land surface model [Ek et al, 2003] applied for deriving the version of GLDAS hydrological models. Nevertheless, the GLDAS hydrological models are used in the thesis, because better alternatives do not exist at the global scale. The GLDAS terrestrial water storage changes are converted into a series of fully normalized surface spherical harmonics up to degree and order 100. Finally, the mean model of two years (2003 and 2004) is subtracted from each monthly model. This is consistent with the processing applied to the time-variable GRACE gravity field models.

The comparison of the results starts with August 2003. Figure 5.16 shows the signal RMS per degree in terms of geoid heights. The GRACE models produced

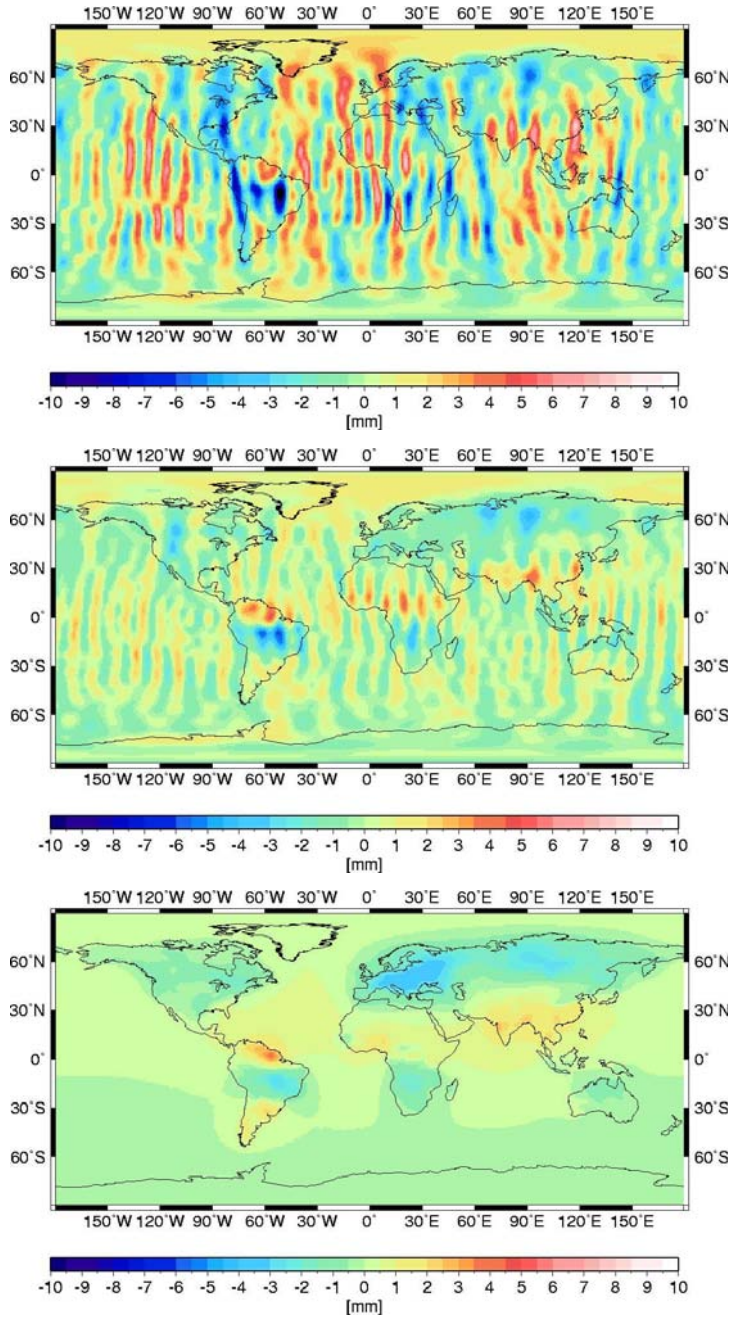

Fig. 5.17. Maps of geoid height variations in August 2003 on the basis of the models obtained with the 3RRC approach (top) and the 3RC approach (middle). The GLDAS hydrological model (bottom) is shown for a reference. All the models are truncated at degree and order 40

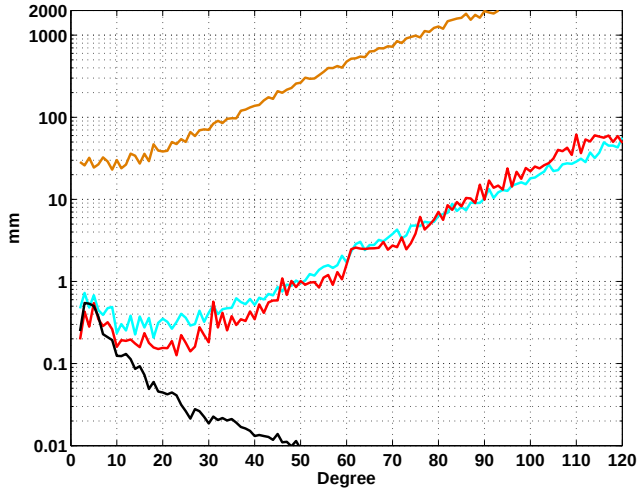

Fig. 5.18. Degree amplitude of the recovered gravity field variations in October 2003 in terms of geoid heights. The models are obtained with the classical acceleration approach (orange), the 3RRC approach (light blue), and the 3RC approach (red). The GLADS hydrological model (black) is shown for a comparison

with the three approaches are computed with respect to the background model, i.e. EIGEN-GL04C up to degree and order 120. Therefore, the values shown mainly contain the temporal gravity signal and model errors. The temporal gravity signal is itself limited to the mean value for the month under consideration. As can be seen in figure 5.16, the degree RMS of the solution obtained by the classic acceleration approach is more than one order of magnitude larger than that of the other two GRACE solutions. The gravity signal of monthly variation can not be that large (see the curve of the hydrological model in the figure), therefore, the shown values must be mostly due to model errors. In fact, this is consistent with the error analysis of section 5.3.3. The model errors are probably caused by noise in the velocity term along the orbit. It can be concluded that the classic acceleration approach must not be used if the accuracy of velocities is not improved.

The other two GRACE solutions show a much smaller magnitude of the recovered signal. Furthermore, the model computed with the 3RC approach demonstrates a factor two smaller magnitude at the intermediate degrees when compared to the model obtained with the 3RRC approach. At the high degrees (above degree 50), the differences are rather close. It is remarkable that at the very low degrees (lower than 10), the 3RC solution shows magnitudes closer to the GLDAS hydrological model than to the RRC solution. On the other hand, a significant difference between the hydrological model and the GRACE models is observed at higher degrees. The signal RMS per degree of GRACE solutions

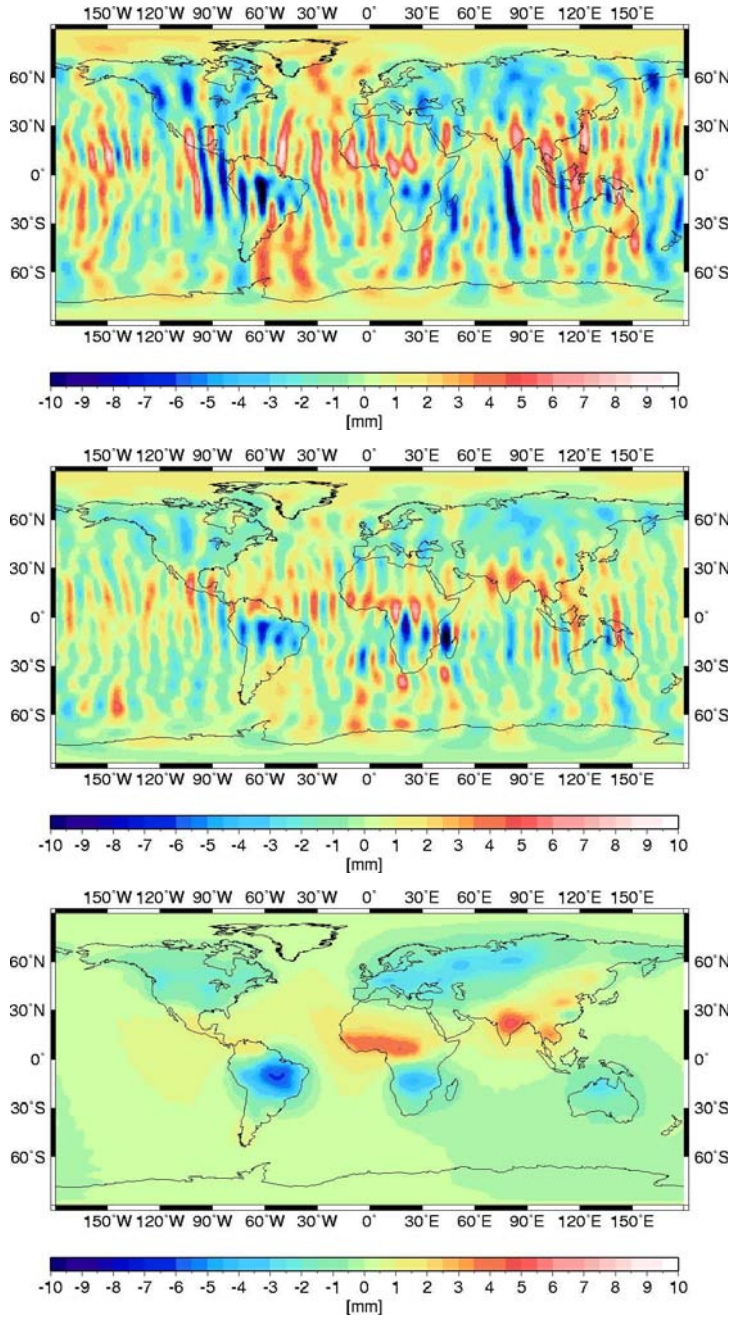

Fig. 5.19. Maps of geoid height variations in October 2003 on the basis of the models obtained with the 3RRC approach (top) and the 3RC approach (middle). The GLDAS hydrological model (bottom) is shown for a reference. All the models are truncated at degree and order 40

quickly increases with degree, which can be explained by noise due to GRACE measurement errors as well as other errors. On the contrary, hydrological models are free from such errors, and consequently show a signal that decreases with increasing degree.

In order to further compare the GRACE solutions obtained with the 3RC and 3RRC approach, they are shown as maps of geoid height variations in figure 5.17, together with the similar variations computed from the GLDAS hydrological model. The cumulative geoid height differences are only computed up to degree 40 in order to avoid the noise at high frequencies. The maps provide information of the spatial distribution of gravity signal contaminated by model errors. The comparison in the spatial domain firstly shows that the GRACE solutions have distinct North-South stripes which mainly coincide with the ground tracks of the GRACE satellites. These stripes are definitely caused by model errors. This anisotropic pattern of errors may be considered as an intrinsic feature of GRACE KBR measurements, which are not sensitive to the gravity variations in the cross-track direction. The second observation is that both GRACE-based solutions show gravity signals in the Amazon river basin and in the Europe-Asia continent. On the other hand, the 3RRC solution demonstrates a less smoothed pattern than the 3RC solution, although the signal can be still seen. We can not exclude that it might be possible to enhance the signal in the 3RRC solutions by designing a dedicated post-processing filter. However, this is a challenging task, and is beyond the scope of this research.

From the comparison of results of August 2003, it is tentatively concluded that the 3RC approach produces the best gravity field model among the three approaches. In order to validate this conclusion, similar comparisons were also made for other months. Here, we show results for only one more month: October 2003. Figure 5.18 shows the RMS signal per degree and figure 5.19 demonstrates the maps of geoid height variations. It can be seen that the major phenomena observed and the conclusions made for August 2003 are confirmed. The only exception is that the 3RRC solution is closer to the 3RC solution in the degree domain. In particular, the 3RRC solution shows a higher quality than the 3RC solution at the high frequencies. However, the 3RRC solution still displays much stronger stripes than the 3RC solution. Therefore, the focus of the rest of thesis will be only on the 3RC approach, even though we still consider the 3RRC approach as a promising method, which deserves further studies.

5.5 Iterative improvement of the gravity field model

This section will focus on the necessity and benefits of making several iterations in the course of producing the gravity field models. Firstly, an investigation is conducted to see whether there are some signals remaining in the data after the least-squares adjustment after subtracting the adjusted observations from the original ones. Then, an iterative estimation procedure is proposed in order to improve

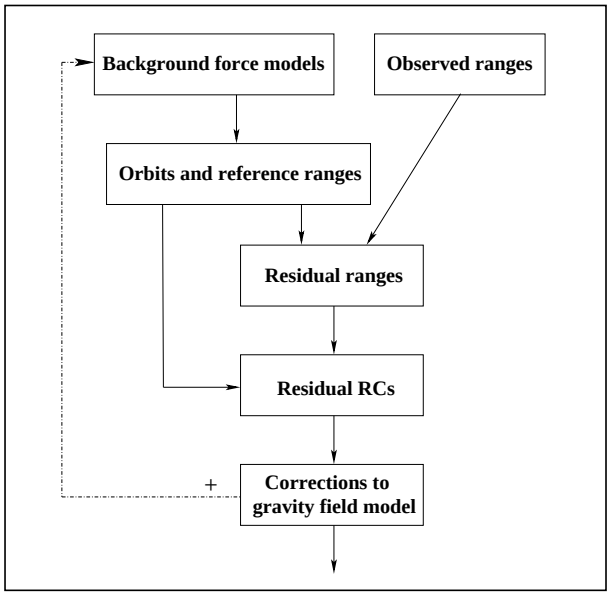

Fig. 5.20. Flow chart of iterative gravity field modeling

the accuracy of gravity field models.

As soon as a gravity field model is obtained, it is important to be sure that the gravity signal contained in the measurements is sufficiently recovered. The point of concern is the fact that empirical parameters are introduced in the data processing. The empirical parameters are a double-edged sword. On the one hand, they are essential for accurate GRACE data processing since they can efficiently absorb some unwanted signals (e.g. bias, scale factor of non-gravitational accelerations, and 1 cpr resonance effects), see also [Reigber et al., 2005b, Tapley et al., 2005, Han et al., 2006a]. On the other hand, the empirical parameters are correlated with the gravity field parameters. They may absorb part of the gravity signal, particularly when the latter one is relatively large. If this is indeed a problem, it can be solved by modeling the gravity field iteratively. The corrections of gravity field model estimated in the first iteration are added to the background force models. Then, the purely dynamic orbits and the 3RC residuals are computed again. The total model of temporal gravity field variations is a sum of models obtained after each iteration. Figure 5.20 shows the flow chart of the proposed iterative procedure.

Figure 5.21 demonstrates maps of the 3RC residuals and the obtained models after three iterations. The models are presented in terms of equivalent water height smoothed by the Gaussian filtering with 600 km radius (see Appendix B). The 3RC

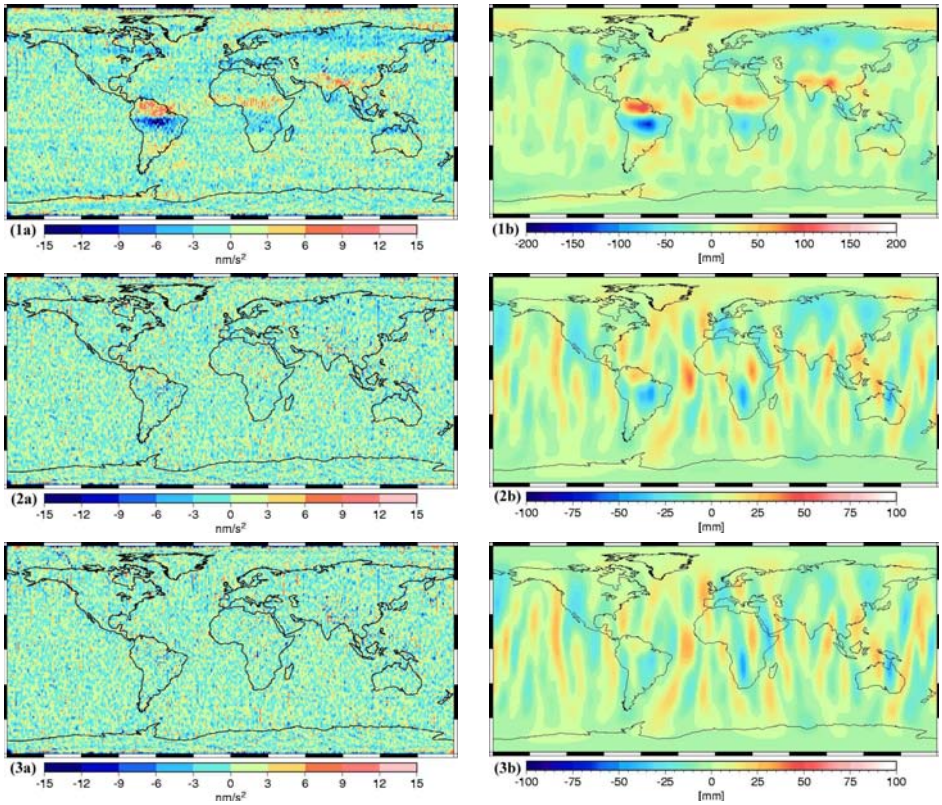

Fig. 5.21. Iterative estimation with the 3RC approach for August 2003. Residuals generated for the first iteration (1a), the model obtained after the first iteration (1b). Residuals generated for the second iteration (2a), the model obtained after the second iteration (2b). Residuals generated for the third iteration (3a), the model obtained after the third iteration (3b). Residuals are shown after a low-pass filtering that was also used to produce figure (5.13). The models are shown as maps of water storage changes in terms of equivalent water height after 600 km Gaussian smoothing. Notice that (1b) has different color bars than (2b) and (3b)

residuals before the first iteration clearly show spatial variations, and the gravity field model obtained after the first iteration demonstrates a similar pattern as the residuals. The residuals generated for the second inversion do not display a very clear gravity signal, but some tiny signals can be seen in Amazon and Zambezi river basins – two of the areas with large water storage changes. The model obtained after the second iteration indeed shows spatial variations in the two above mentioned river basins. At the same time, some stripes are present in the model, even though the Gaussian filtering is applied. From the results of the second iteration, it can be concluded that (1) there is indeed a remaining gravity signal not recovered after the first iteration, which is particularly visible in the areas with large gravity variations; (2) the remaining signals are rather small compared with

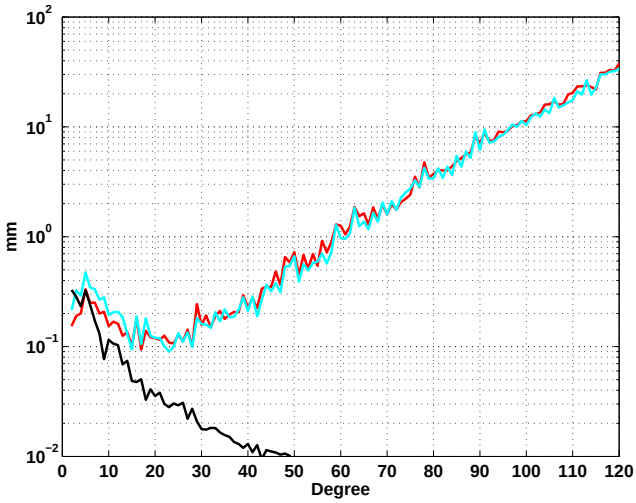

Fig. 5.22. Signal degree RMS for August 2003 in terms of geoid heights. Red line shows the model obtained after the first iteration, light blue line presents the model obtained after two iterations, and black line is the GLDAS model

the signal recovered in the first iteration. As far as the third iteration is concerned, it is even more difficult to find any signal in the residuals, and little signal can be seen in the map of water storage changes.

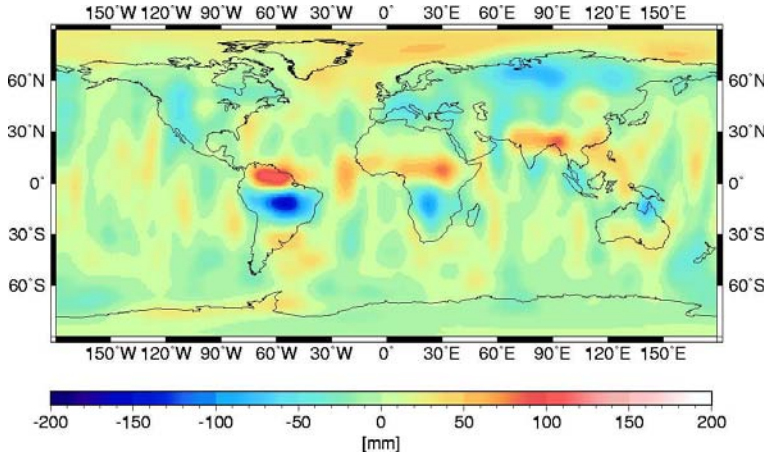

Fig. 5.23. Water storage changes in terms of equivalent water heights for August 2003. The model is the sum of the second iteration model and the first iteration model truncated at degree 13

From this case study, it can be concluded that two iterations are sufficient to extract all the signal from the data. More iterations make no sense because they only increase the estimation errors. The same holds for other months, such as October 2003, according to our experience. Of course, the second iteration also introduces model errors. In order to reduce the noise in the total model obtained after the second iteration, we propose to suppress high-frequency noise in the model after the first iteration, which is added up to the background force models. There are two ways to do that: 1) the model truncated at a certain degree, or 2) the model is smoothed. We have chosen the first way: the model is truncated at degree 13. Our motivation is as follows. Firstly, it is easy to implement this operation because no further operator like filtering is needed. Secondly, the model errors at the degrees below 13 are much lower than those at degrees above 13 [Luthcke et al., 2006]. Thirdly, the absorbed signal is mainly concentrated at the low frequencies. Thus, the total model of temporal gravity field variations is the sum of the second iteration model and the first iteration model taken only up to degree 13. Figure 5.22 shows the total model in terms of geoid height per degree. It can be seen that the total model up to degree 13 is larger than that after the first iteration. Above degree 13, the signal RMS per degree of the two models is extremely close. This can be considered as evidence that the model errors do not increase after the second iteration. In addition, figure 5.23 demonstrates the map of the total model in terms of equivalent water height. A comparison with the map shown in figure 5.21(1b) tells that the spatial variations in many areas, e.g. Amazon, Zambezi and Gangs river basins as well as in Siberia increase by at least 10%-15%. The same effect can also be seen in figure 5.24, which shows similar results for October 2003.

By using the methodology presented above (the 3RC approach with two iterations), we have processed 4 years of GRACE data (February 2003 to December 2006), resulting in 46 monthly solutions (June 2003 is skipped due to a lack of data). These solutions will be presented and analyzed in the next chapter.

5.6 Summary and remarks

In this chapter we present two innovative methodologies of gravity field modeling from GRACE ll-SST data. They are compared with the classic acceleration approach. The functional models exploited in all three approaches are discussed in detail. Their advantages and disadvantages are considered in the context of realistic assumptions about data noise. In the classical acceleration approach, knowledge is needed about the components of inter-satellite velocities orthogonal to the LOS. Since these components are derived from GPS measurements, they are not known with a sufficient accuracy. The idea of the 3RRC approach is to determine the radial component of inter-satellite velocities directly from the KBR data and therefore, reduce the influence of GPS data on the overall error budget. The 3RC approach totally avoids the velocity term in the observation equation, and directly connects the potential gradients with KBR ranges.

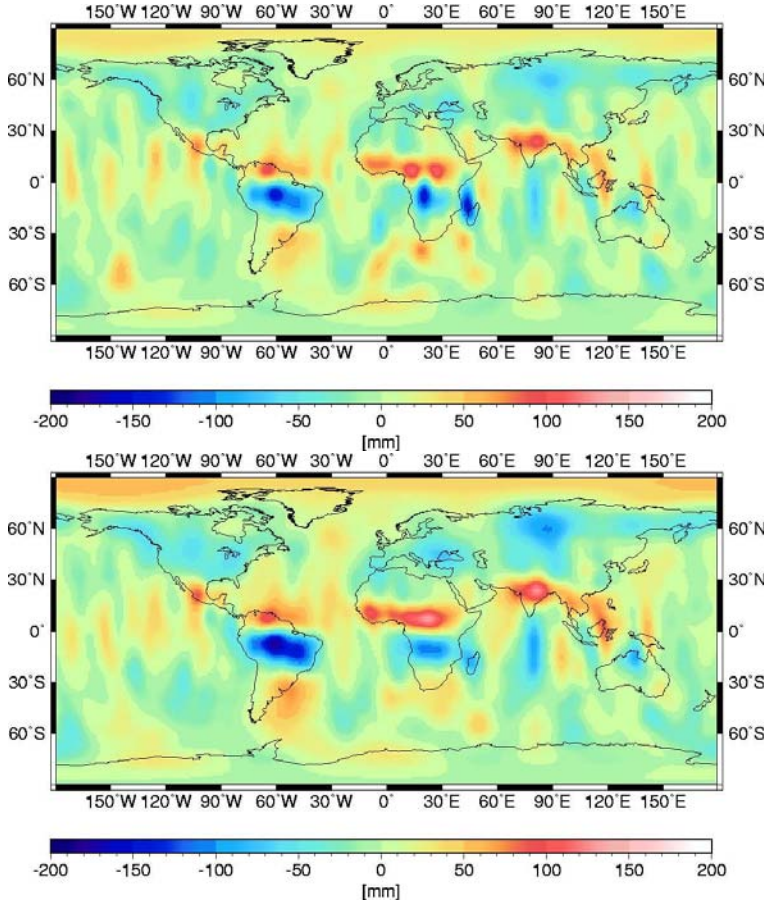

Fig. 5.24. Water storage changes in terms of equivalent water heights of October 2003 for the model (top) of the first iteration, and the model (bottom) obtained from the sum of the second iteration model and the first iteration model truncated at degree 13)

In order to process real GRACE data, a comprehensive data processing strategy is developed for all three approaches. The strategy comprises the data pre-processing and inversion. The key point of the data pre-processing is to compute purely dynamic orbits of GRACE satellites as reference ones. The orbits are integrated on the basis of state-of-the-art force models, and meanwhile fit the provided high-precision kinematic or reduced-dynamic orbits. The reference orbits are used to derive the computed KBR observations (ranges, range-rates or range accelerations) and ultimately the corresponding residual quantities. The inversion procedure used in all three approaches is developed on the basis of that used for the processing of kinematic baselines as described in chapter 4. Furthermore, we have

investigated the sensitivity of the three approaches to the accuracy of the noise model and corresponding data weighting. It is found that frequency-dependent data weighting is a must for the 3RRC approach. The classic acceleration approach and the 3RC approach are less sensitive to the noise model, particularly at the low degrees, though frequency-dependent data weighting still improves results.

The chapter presents a comparison of the three approaches based on processing the real data for August 2003 and October 2003. The corresponding GLDAS hydrological models are used for a comparison. The classic acceleration approach produces the worst results among three. The 3RRC and 3RC approach produce gravity field models of a much higher quality. The models obtained with the 3RC approach are particularly accurate as they contain less noise in the form of along-track stripes than those based on the 3RRC approach.

Finally, the 3RC approach is refined further. An iterative estimation is adopted in order to retrieve gravity signal absorbed by the empirical parameters estimated in the data pre-processing. It is found that two iterations are sufficient. The results show that an increase of the signal by at least 10%-15% at the areas with large gravity variations can be achieved by the iterative estimation.

One more issue is worth further discussion. From the functional model of the classic acceleration approach, it seems to be impossible to increase the accuracy of result without improving the the velocity term. However, it is not trivial to significantly increase the accuracy of kinematic baselines, which are used to derive the velocity term. There may be another way to improve the results of the classic acceleration approach, i.e. ignoring the contribution of velocity term entirely by only considering the contribution of point-wise accelerations. This way may not be totally strict in the physical sense, but it could, in practice, produce quite reasonable results. In a very late stage of this PhD research project, such an attempt has been made. Indeed, the accuracy of gravity field modeling has increased dramatically. However, this idea still needs more investigation in the future.

Chapter 6

Analysis of results obtained from the 3RC approach

6.1 Introduction

We have developed two methodologies to process GRACE ll-SST data to estimate time variation of the Earth's gravity field: the 3RC approach and the 3RRC approach. The 3RC approach was shown in chapter 5 to produce better results than the 3RRC approach. Therefore, the 3RC approach is used for routine computations of monthly GRACE solutions at Delft institute of Earth Observation and Space System (DEOS). These solutions are referred to as "DEOS solutions". We have so far processed 4-year of GRACE data, spanning the interval from February 2003 to December 2006 except for the month of June 2003, resulting in 46 monthly solutions. The measurements of June 2003 are not good enough to produce a reasonable result. The monthly gravity estimates are obtained as corrections (or variations) with respect to the high-quality EIGEN-GL04C model which is used as the *a priori* static field. The time series of these DEOS solutions will be presented in section 6.2, mainly for the purpose of demonstrating spatio-temporal gravity variation. As gravity is an integral of mass, spatio-temporal gravity variations represent (horizontal) mass redistributions. On a large variety of time scales, mass redistribution mainly occurs inside the surface fluid envelopes, i.e. oceans, atmosphere, ice caps and continental water reservoirs. Furthermore, there are variations that reflect processes in the solid Earth. Some geophysical variations are corrected for during pre-processing, e.g. solid Earth and oceanic tides, selected low-degree secular variations, pole-tide effects and a combination of atmospheric pressure variations with the response of a baro-tropical ocean. The final GRACE gravity field estimates therefore contain mostly mass variability due to: change in continent water storage, polar ice mass accumulation and ablation, Post Glacial Rebound (PGR) and effects of co-seismic and post-seismic deformation. We will analyze the global secular and seasonal variations in the Earth's gravity field in section 6.3.

Section 6.4 focuses on scientific applications of the DEOS solutions. Firstly

we will estimate the possible mass loss of Greenland ice sheets. Secondly, it will be demonstrated that Antarctic seasonal mass variations can be detected from DEOS solutions. Thirdly, the DEOS solutions are used to investigate the effects of co-seismic and post-seismic deformation caused by the Sumatra-Andaman earthquake.

In section 6.5, we will compare the DEOS GRACE solutions with those produced by the Center of Space Research (CSR) at University of Austin, GeoForschungsZentrum (GFZ) in Potsdam, Jet Propulsion Laboratory (JPL) in Pasadena and the Centre National d'Etudes Spatiales (CNES) in Paris as well as the GLDAS hydrological models, mentioned in chapter 5. We will perform comparisons of spherical harmonic coefficients and estimations of the water storage variations in large river basins.

6.2 Time series of DEOS monthly solutions

The DEOS solutions are a series of monthly estimates of the Earth's gravity field variation with respect to the static EIGEN-GL04C model. Some gravitational variations were subtracted in the course of data processing: the secular changes of the $C_{20}, C_{21}, S_{21}, C_{30}$ and C_{40} coefficients; direct and indirect Earth tides [McCarthy and Petit, 2003]; FES2004 ocean tides [Lyard et al., 2006]; Atmospheric and oceanic variability (AOD1B RL04 products) [Flechtner, 2007a] ocean pole tides (Desai model); and general relativistic perturbations. The DEOS solutions therefore only estimate deviations from the static gravity field caused by un-modeled effects: hydrology, snow cover, ice sheets, baro-clinic oceanic signals, post-glacial rebound and tectonics events. The errors in the DEOS models reflects measurement errors, numerical errors in the processing, and any errors in the inprecise ocean/load tidal models and AOD1B model products. Furthermore, a lack of spatial coverage takes place for some months, which amplifies the errors additionally.

The DEOS solutions are obtained without any regularization, and they are output as normalized spherical harmonic coefficients from degree 2 to a certain maximum degree. The maximum degree varies from 50 to 120 depending of the measurement ground coverage. The data density distribution across the Earth's surface is dramatically reduced when the satellite orbit is characterized by a short repeat period, and when the KBR data contain large gaps. Figure 6.1 shows examples of the ground coverage for three months: August 2003, January 2004 and July 2004. The common feature of the three maps is a dense distribution of measurements at the two poles compared to the equators, which occurs due to the convergence of the satellite tracks at the poles. It is found that much sparser measurements were acquired in July and January 2004, compared with the coverage achieved in August 2003. This is due to a repeat orbit (about every 4 days) during July 2004 and the collection of only 13 days of KBR data during January 2004. In these two cases, recovering of a gravity field model to

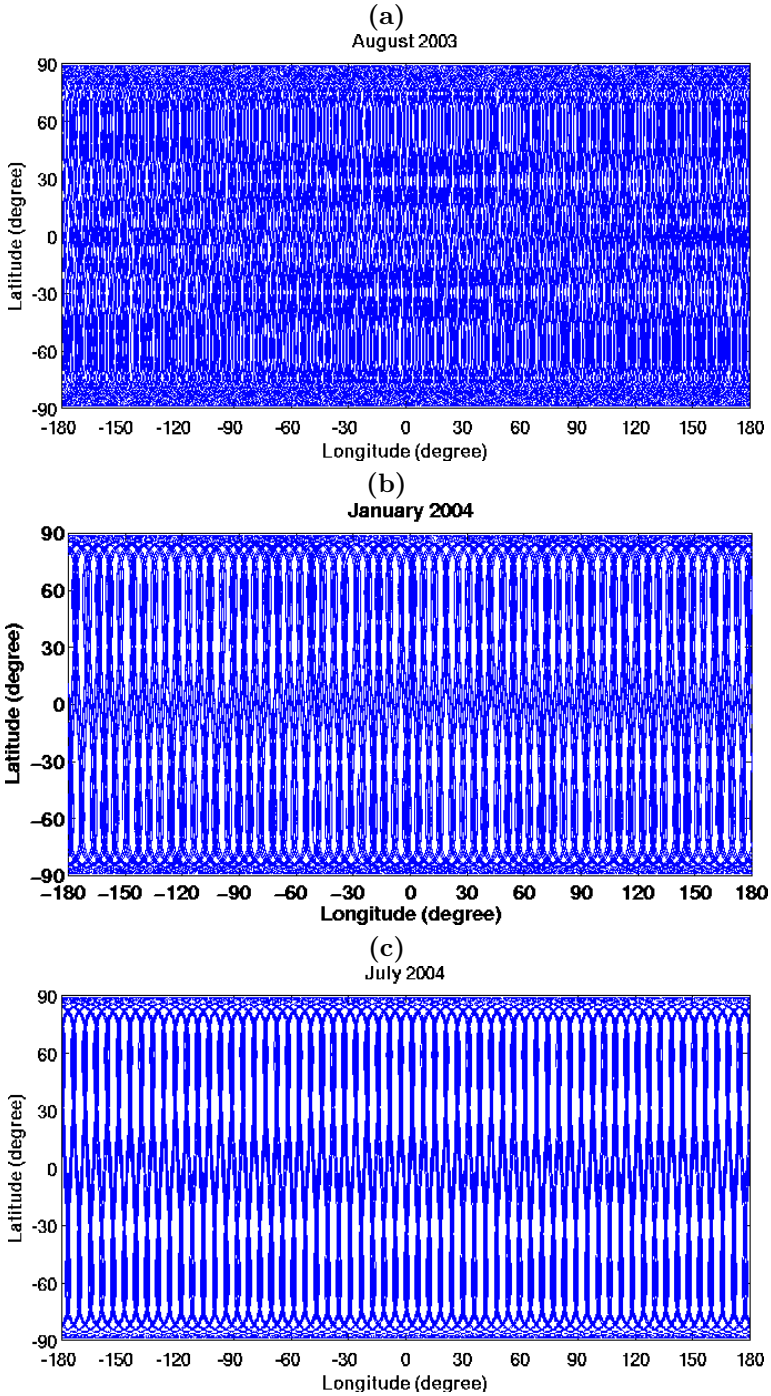

Fig. 6.1. Geographical location of middle points of two GRACE satellites during the periods of August 2003 (a), January 2004 (b) and July 2004 (c)

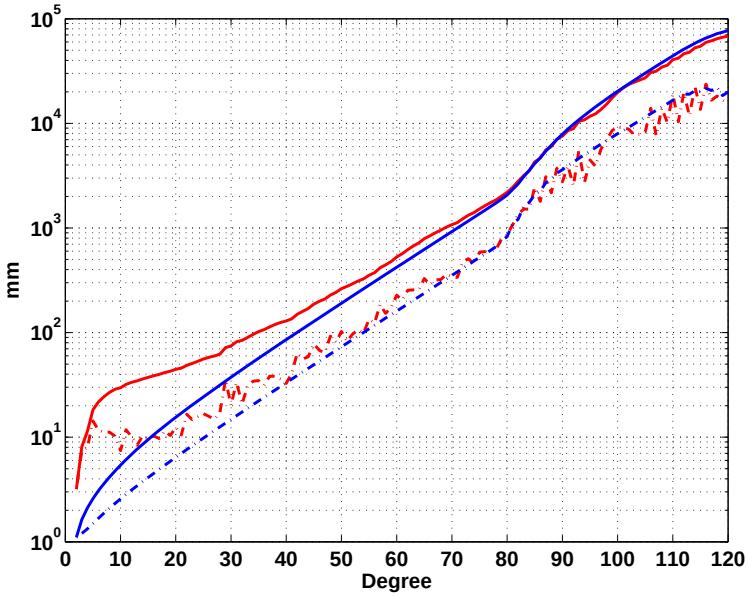

Fig. 6.2. Signal (in red) and error (in blue) estimates of the DEOS solutions (September 2003), computed per degree (dashed lines) and cumulatively (solid lines) in terms of equivalent water height

a high degree (e.g. higher than 70) may not be reasonable. Fortunately, it was possible to compute all the solutions up to at least degree 50 with a corresponding variance-covariance matrix for each estimate.

The signal to be estimated from the GRACE measurements is rather weak. Above degree 30-40 the errors of the monthly solutions are typically larger than the likely geophysical signal. Figure 6.2 displays the estimated DEOS gravity spectrum (red curves) alongside the calibrated formal error spectrum obtained from the covariance matrix (blue curves), in terms of equivalent water height for September 2003. Figure 6.2 shows that the gravity signal between degrees 2 and 30-35 is clearly greater than the noise. The overall accumulated error of the DEOS solutions is less than 6 mm equivalent water height at degree 10 (2000 km resolution), 1.5 cm at degree 20 (1000 km resolution) and 3.7 cm at degree 30 (666 km resolution). Above degree 35, the red and blue curves get closer and closer, which means that noise dominates at high degrees. The cumulative error is about 20 cm at degree 50 and about 200 cm at degree 80. At degrees higher than 80, it is not easy to distinguish the two curves. This means that the signal is totally embedded into the noise, and is no longer visible.

To highlight geophysical signals, a filter is required that suppresses the high-

frequency noise. In our study a Gaussian filter is employed for this purpose [Jekeli, 1981]. Figures 6.3(a) and 6.3(b) demonstrate the geographical distribution of the calibrated formal error of a DEOS solution after the Gaussian filtering with 400 km radius and 600 km radius, respectively. The corresponding solution after Gaussian filtering is shown in figures 6.4(a) and 6.4(b), respectively. The geographical error distribution is calculated according to the propagation law of variances.

$$\mathbf{Q_{geog}} = \mathbf{A}\mathbf{Q_{sol}}\mathbf{A}^T, \tag{6.1}$$

where $\mathbf{Q_{sol}}$ is the variance matrix of our monthly solution containing diagonal elements $\sigma^2_{lm,C}$ and $\sigma^2_{lm,S}$ (covariances are not considered since their effects in the spatial domain are minor [Swenson and Wahr, 2002]), $\mathbf{A}$ is the propagation matrix, which is a combination of the spherical harmonic synthesis and Gaussian filtering. Figure 6.3 shows the square roots of the diagonal elements of $\mathbf{Q_{geog}}$. The geographical distribution of the formal error depends only on latitude, with a maximum at the equator and a minimum at the two poles. This is likely due to the increased observation density at the poles. For the case of 600 km Gaussian filtering, the total error is not larger than 12.5 mm at the equator and around 2.0 mm at the poles. In the case of 400 km Gaussian filtering, the geographic error is around 5.0 mm at the poles and 35.0 mm near the equator. The average error ratio between the latitude of the Amazon River basin of South America and the north part of Greenland is about 3-4 for both cases.

Significant North-South stripes are present in the results when insufficient filtering is applied, see figure 6.4(a). These stripes are classified as errors, the huge amplitude of meridional water transport derived from these stripes is not observed in independent estimates [Swenson and Wahr, 2006]. When the radius of the filter is increased, the amplitude of the stripes decreases, see figure 6.4(b). However, choosing the radius of the Gaussian filter is a trade-off process. On the one hand, some artifacts may still appear even if the filter is relatively wide (for example, over the Caribbean Sea and at the southern coast of North America). On the other hand, the filtering also reduces the amplitude of the real signal. Thus, the aim is to reduce the stripes as much as possible, while preserving the signal.

In a recent investigation of the CSR GRACE solutions (see section 6.5.1.1 for details), Swenson and Wahr [2006] found that the observed stripes are associated with correlations among certain groups of spherical harmonic coefficients. The coefficients of a particular degree show no obvious correlations as a function of order. However, the coefficients of a particular order starting approximately from a certain order e.g. $m = 8$, reveal clear correlations if grouped as a function of either even or odd degree (even and odd degree coefficients do not appear to be correlated with one another). The stripes appearing in the GRACE solutions are attributed to these systematic correlations. [Swenson and Wahr, 2006] proposed a de-striping technique to remove systematic errors; [Chambers, 2006] developed this concept further. The basic idea behind the de-striping technique is to fit a

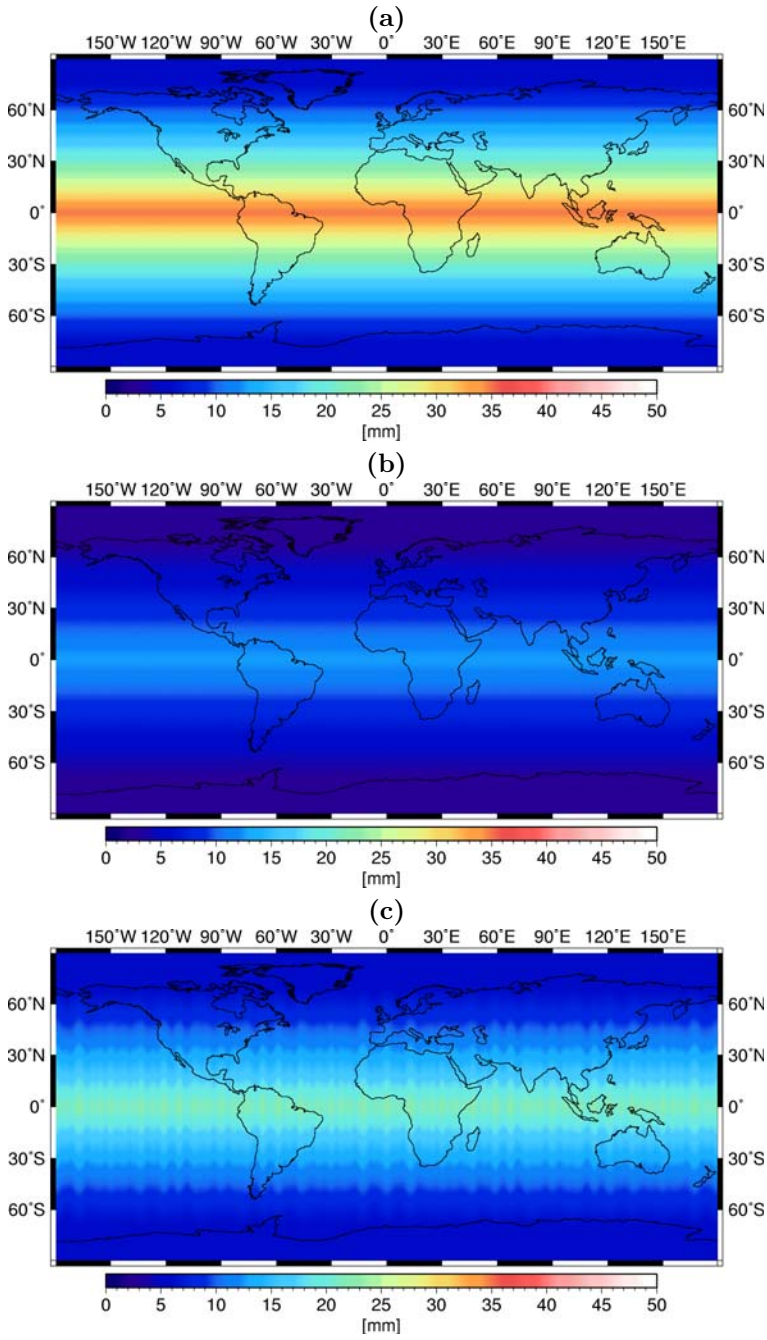

Fig. 6.3. Geographical distribution of the calibrated formal errors of the monthly solution (September 2003) in terms of equivalent water height: the 400 km Gaussian filtering is applied (a), the 600 km Gaussian filtering is applied (b), and the P3M8 de-striping and 400 km Gaussian filtering are applied (c)

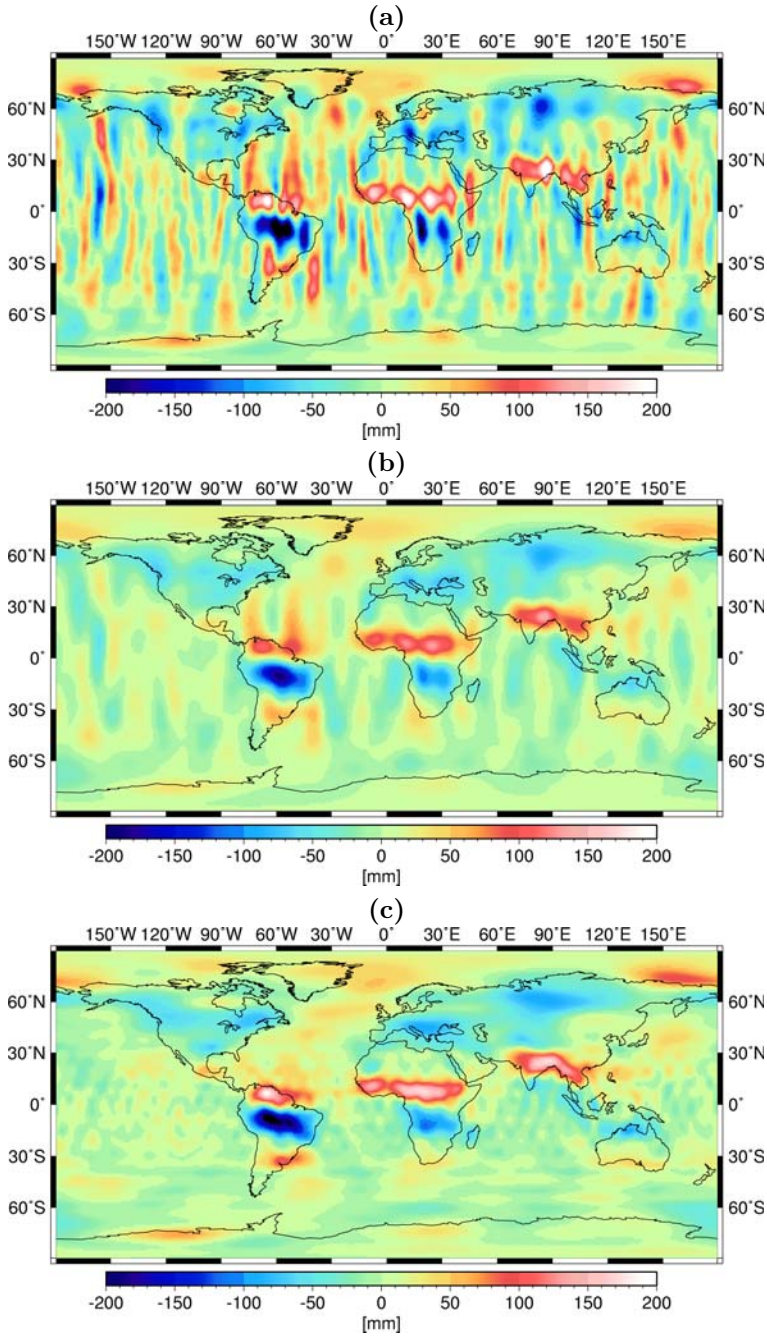

Fig. 6.4. Monthly solution (September 2003) in terms of equivalent water height: the 400 km Gaussian filtering is applied (a), the 600 km Gaussian filtering is applied (b), and the P3M8 de-striping and 400 km Gaussian filtering are applied (c)

high-order polynomial as a function of degree to coefficients of order higher than e.g. $m = 8$ in a moving window while ensuring the coefficients of low degree and order (e.g. $m = 8$) remain unaltered. The polynomial fit is separately applied to odd and even degrees. The de-striped coefficients are calculated by subtracting the polynomial fit from the original coefficients. By applying a de-striping procedure we do risk removing real signals if we choose too low a starting order. However, to study the pole areas, the starting order may be chosen higher than for a study at or near the equator. In practice, the starting order is chosen from a trade-off between significant stripe removal and maximum signal retention.

The DEOS solutions have similar inter-coefficient correlations as the CSR GRACE solutions. For this reason we applied the de-striping technique to the DEOS solutions as well. After some experimentation, the polynomial order and the half width of the moving window were fixed to 3. The de-striping starts for the coefficients of order 8. The de-striping procedure is therefore referred to as P3M8, the same notation is used by [Chen et al., 2007]. After de-striping, 400 km Gaussian filtering was applied. The results are shown in figure 6.4(c). Comparing figure 6.4(c) with the previous result after 400 km Gaussian filtering (figure 6.4(a)), one can see that the dominant stripes over the oceans are mostly removed. The remaining signal (or noise) in the oceans is isotropic, it even looks much smoother than in the previous 600 km Gaussian filtered results. Some of nonphysical features, e.g. the two positive "tails" over the Caribbean Sea and at the southern coast of North America, disappear after de-striping. On the other hand, the expected geophysical signals are more clearly visible.

One issue that needs addressing is how to update the formal errors after the de-striping. To this end, a relatively simple approach is followed, which is based on just re-scaling. Taking the C-coefficients as an example:

$$\sigma^{ds}_{lm,C} = k_m \cdot \sigma_{lm,C}, \tag{6.2}$$

where $\sigma^{ds}_{lm,C}$ is the standard deviation of the coefficients after de-striping, and k_m is the scale factor which is order-dependent and is different from 1 only for the coefficients that were subject to de-striping. The scale factor is computed separately for even and odd degrees as the ratio of power of the coefficients before and after the de-striping. Taking the even degree as an example:

$$k_m = \sqrt{\frac{\sum_{l=8}^{\max} (C^{ds}_{lm})^2}{\sum_{l=8}^{\max} (C_{lm})^2}}, \tag{6.3}$$

where C^{ds}_{lm} are the coefficients of even degree after de-striping. The same holds for the S-coefficients. In this way, four scale factors have to be computed for each order (for even and odd degrees; for C-coefficients and S-coefficients). The geographical error distribution corresponding to the solution of figure 6.4(c) is

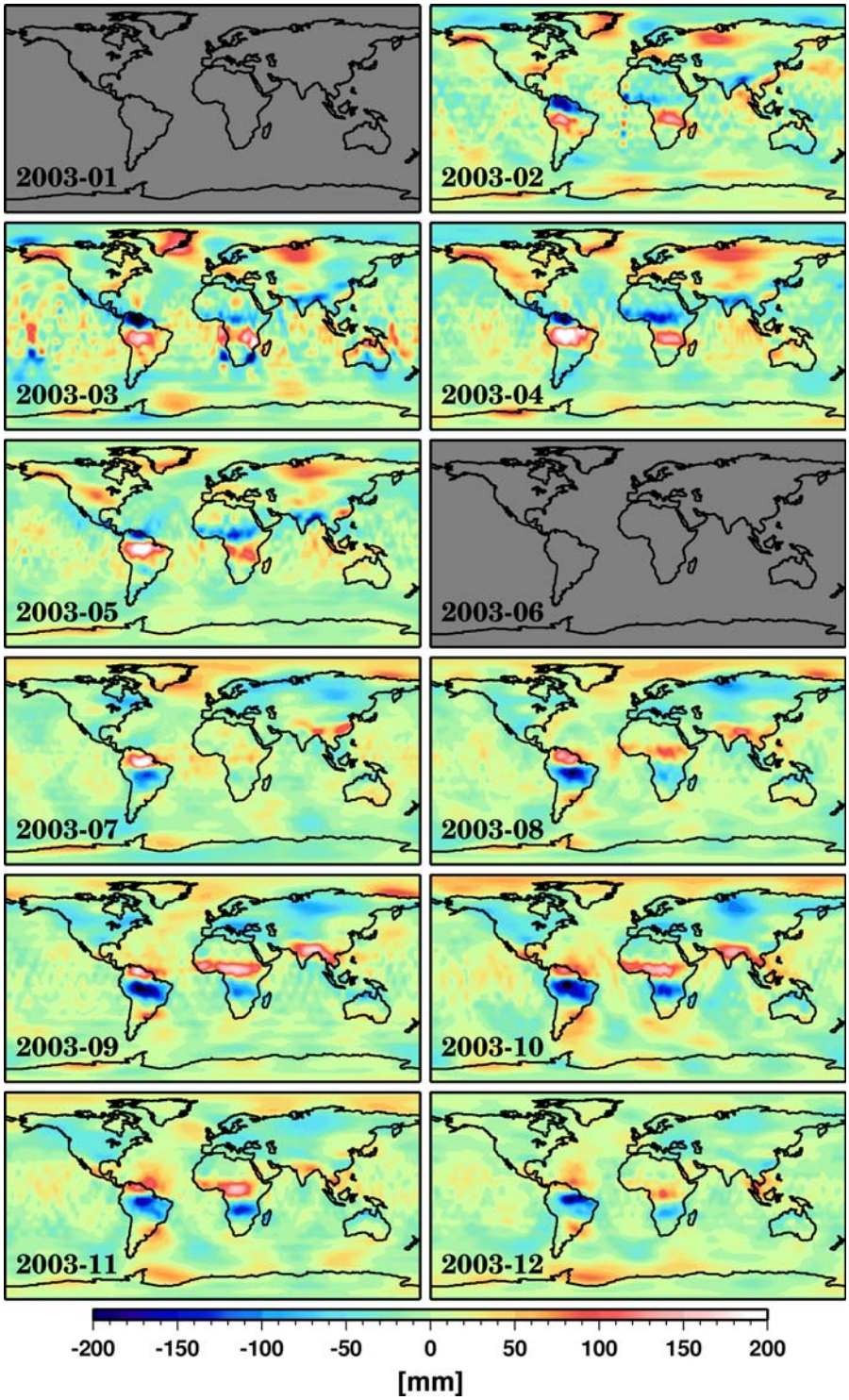

Fig. 6.5. Maps of DEOS solutions from January 2003 to December 2003

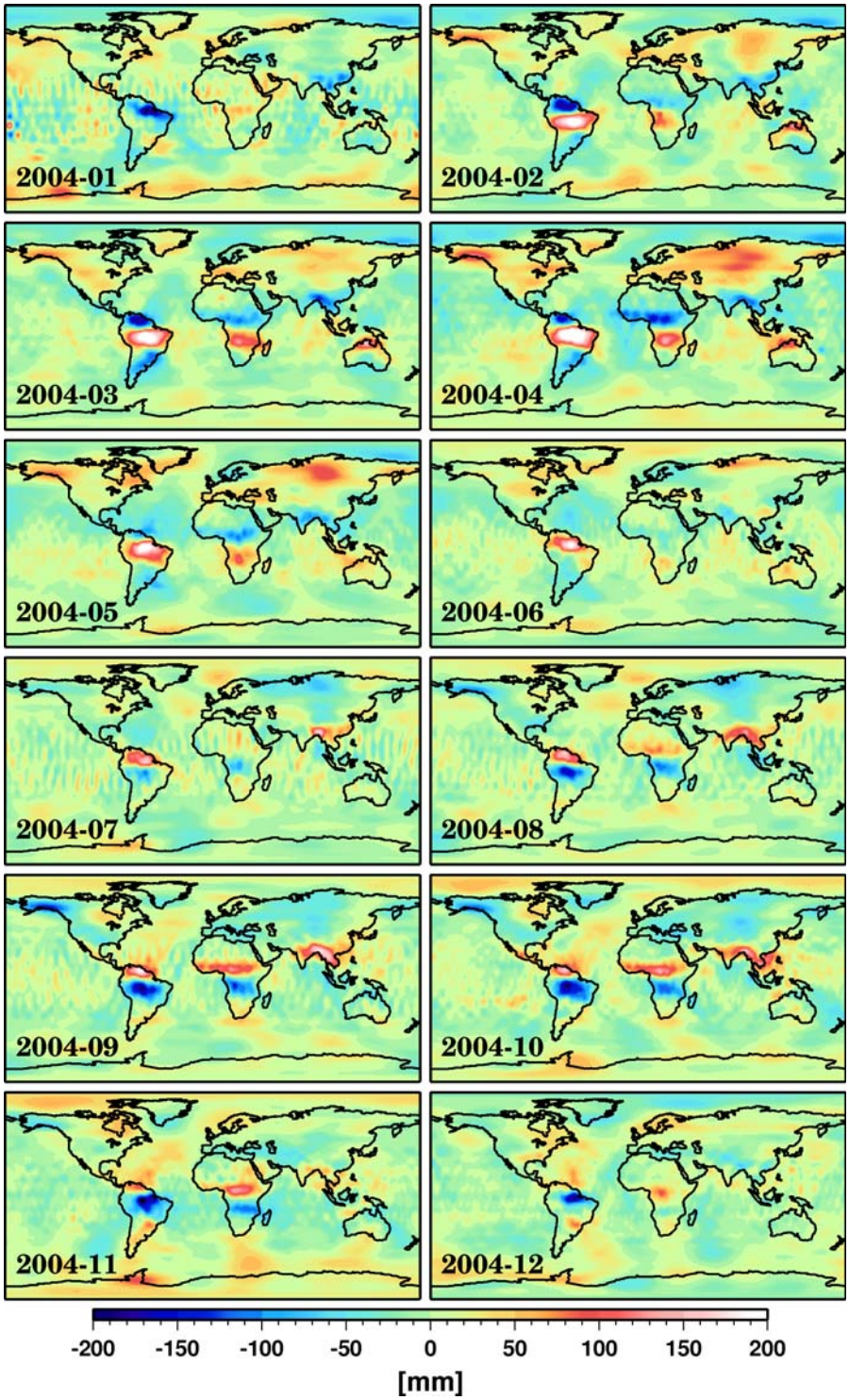

Fig. 6.6. Maps of DEOS solutions from January 2004 to December 2004

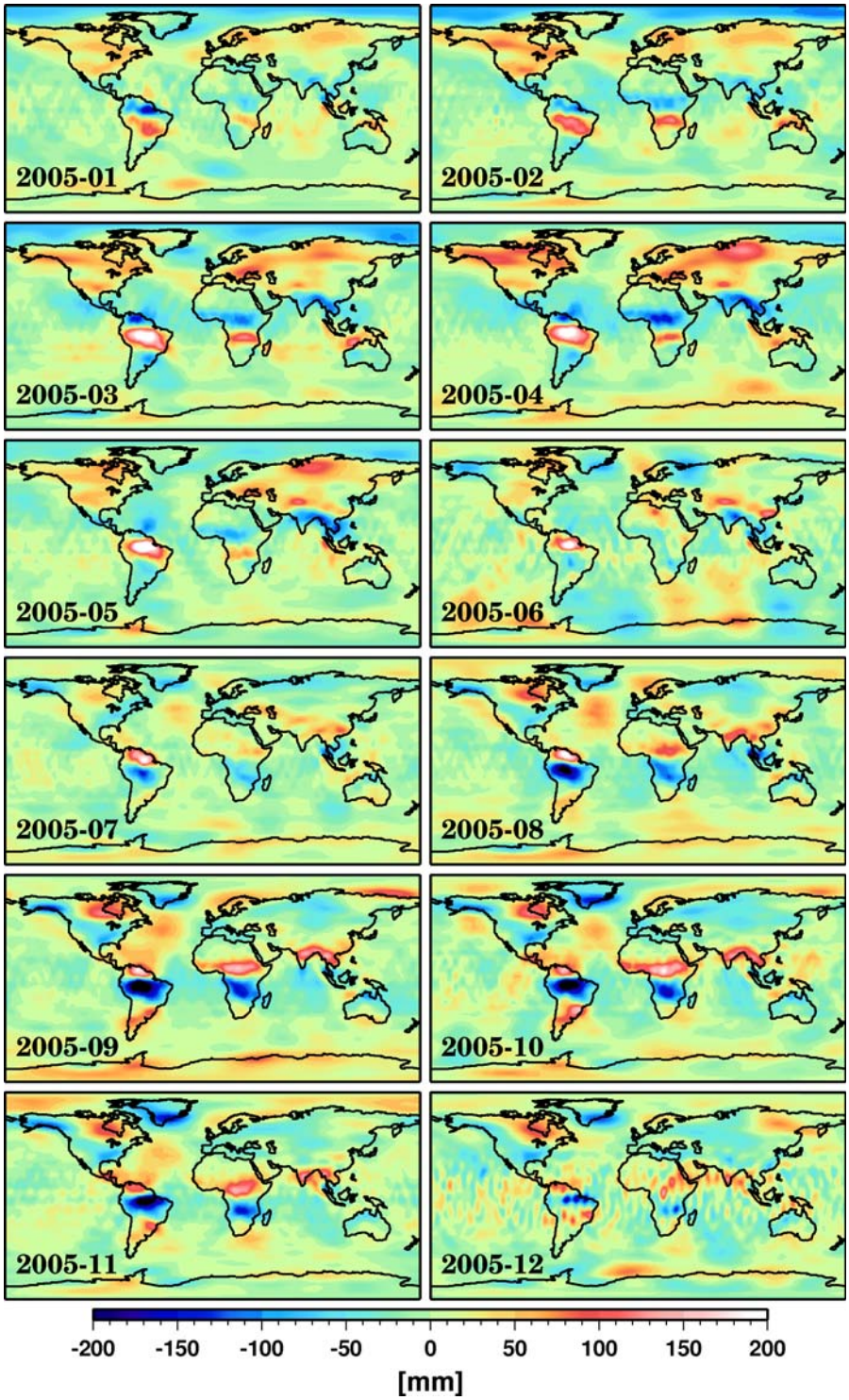

Fig. 6.7. Maps of DEOS solutions from January 2005 to December 2005

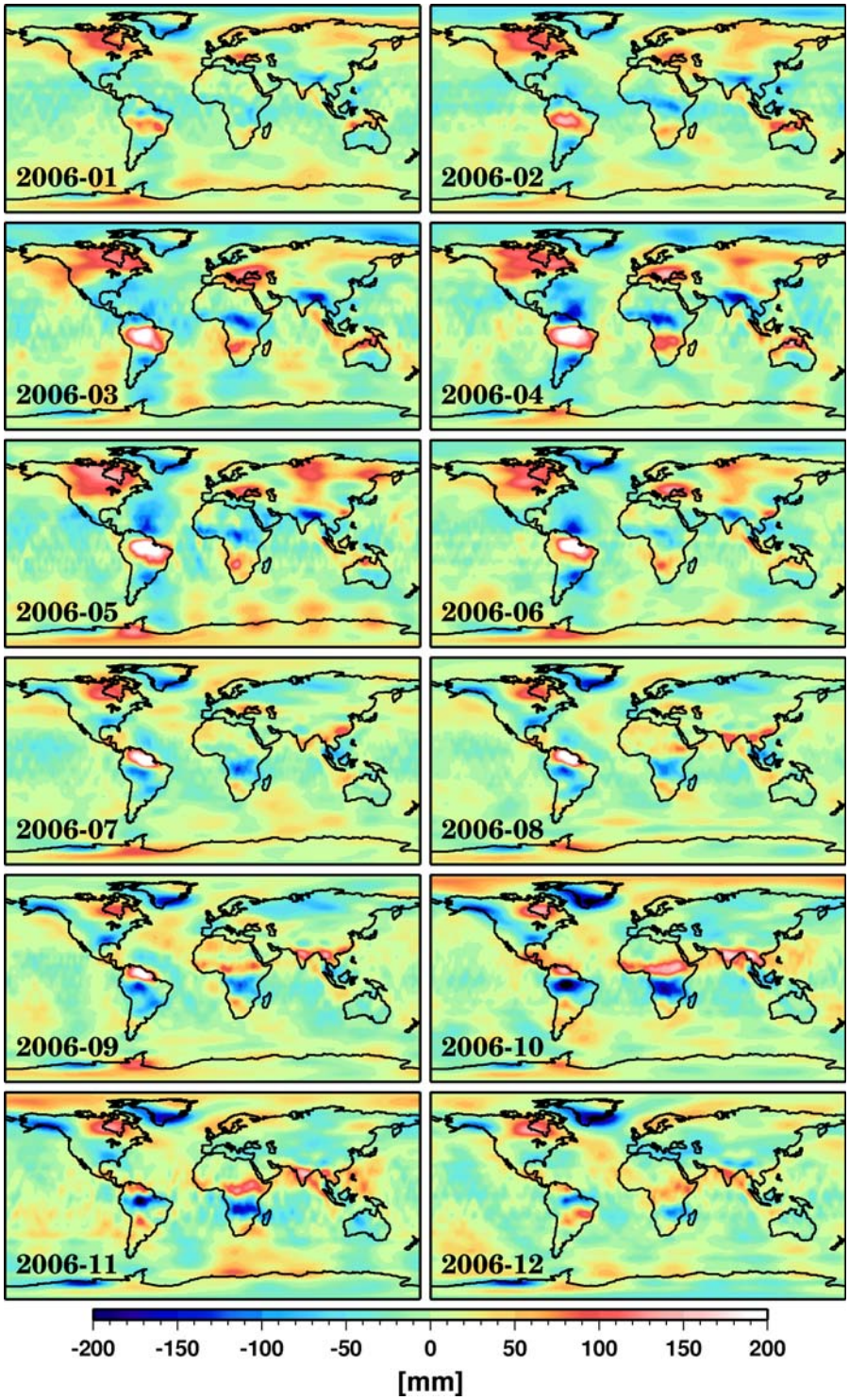

Fig. 6.8. Maps of DEOS solutions from January 2006 to December 2006

shown in figure 6.3(c). The errors are still only dependent on latitude. Compared with the error distribution shown in figure 6.3(a), the errors at the equator are significantly reduced, from 35.0 mm to 22.0 mm. On the other hand, little is changed at the poles. In general, the error distribution after the scaling due to the de-striping is close to that shown in figure 6.3(b) for the case of 600 km Gaussian filter without de-striping.

The observed signal (or noise) over the oceans in the post-processed gravity field models is almost at the same level in two cases: 600 km Gaussian filtering (see figure 6.4(b)) and P3M8 de-striping plus 400 km Gaussian filtering (see figure 6.4(c)).

Figure 6.5-6.8 shows the time series of DEOS monthly solutions in terms of equivalent water heights after P3M8 de-striping and 400 km Gaussian filtering. Not all monthly solutions are of the same quality, some of them have relatively large errors over the oceans. For example, solutions for February and March 2003; January and July of 2004; December 2005 and November 2006 still show nonphysical patterns, which might be caused by lack of measurements or an orbit with a short repeat period. Nevertheless, the hydrological signals in the continental areas do appear clearly, even in the solutions of a relatively poor quality. Furthermore, a clear seasonal variation of water storage can be seen in several large tropical river basins: the signal is well above the error level. The largest observed variation is observed in the Amazon River basin. Starting from July of each year the dry season begins and the water storage gradually reaches a minimum in October. After the end of dry season the river basin starts to accumulate water with the maximum storage usually occurring in April of each year. Another remarkable example is the West Siberian Plain. The observed water storage variations in the area show a clear seasonal periodicity. The maximum variation is observed in spring (April), whereas the minimum is reached at the beginning of the autumn (September to October). Importantly, this pattern is consistently repeated from year to year. The mass variation is likely due to the effects of snow accumulation and melting. A more quantitative analysis of the GRACE observed hydrological signals is given in the following sections. In particular, we found that during the four-year period of measurements there is a significant decline of mass in Greenland which is very likely the consequence of ice sheet melting.

6.3 Derivation of secular and seasonal gravity changes

Observations of secular gravity field change are particularly relevant to the investigation of climate change and global warming. Observations of seasonal variations in the Earth's gravity field impose important constraints on models of global mass variability and mass exchange among the land, ocean and atmosphere [Tapley et al., 2004]. We have already mentioned the observed seasonal and secular mass changes in the previous section. In this section, a quantitative analysis

of secular and seasonal gravity field changes is conducted.
The inter-annual and seasonal gravity field changes are estimated from the DEOS GRACE monthly gravity fields and associated covariance matrices in a least-squares process. Since some of our solutions are only computed up to degree and order 50, all the monthly solutions are first truncated at degree 50 in this computation. This is justified by the fact that noise at degrees above 50 dominates. The spherical harmonic coefficients of the gravity fields are approximated in the time domain with 6-parameter curves:

$$\mathbf{y}(t_i) = \mathbf{a}_0 + \mathbf{a}_1 t_i + \mathbf{a}_2 \cos\omega t_i + \mathbf{a}_3 \sin\omega t_i + \mathbf{a}_4 \cos 2\omega t_i + \mathbf{a}_5 \sin 2\omega t_i \qquad (6.4)$$

where $\mathbf{y}(t_i)$ is the vector of spherical harmonic coefficients at the month t_i, with $i = 1, 2, ..., 46$ standing for 46 monthly solutions; $\omega = \frac{2\pi}{T}$ with T being one year; and $\mathbf{a}_j, j = 0, 1, ..., 5$ are unknown vectors to be solved for: $\mathbf{a}_0$ is a mean model of corrections; $\mathbf{a}_1$ is a linear trend; $\mathbf{a}_2$ and $\mathbf{a}_3$ are the amplitudes of seasonal cosine and sine terms; $\mathbf{a}_4$ and $\mathbf{a}_5$ are the amplitudes of semi-annual cosine and sine terms. It should be noted that a joint estimation of trend and annual signal is needed to avoid possible leakage between the two signals since the data used are not regularly distributed in time or space [Andersen and Hinderer, 2005]. The full variance-covariance matrices $\mathbf{Q}_{\mathbf{y}_{(t_i)}}$ of the monthly solutions are used, to yield a statistically optimal estimation. The normal matrix $\mathbf{N}$ and the right-hand side vector $\mathbf{b}$ are computed block by block as follows:

$$\mathbf{N} = \begin{pmatrix} \sum_{i=1}^{n} \mathbf{Q}_{\mathbf{y}_{(t_i)}}^{-1} & \sum_{i=1}^{n} t_i \mathbf{Q}_{\mathbf{y}_{(t_i)}}^{-1} & \cdots & \sum_{i=1}^{n} \sin 2\omega t_i \mathbf{Q}_{\mathbf{y}_{(t_i)}}^{-1} \\ & \sum_{i=1}^{n} t_i^2 \mathbf{Q}_{\mathbf{y}_{(t_i)}}^{-1} & \cdots & \sum_{i=1}^{n} t_i \sin 2\omega t_i \mathbf{Q}_{\mathbf{y}_{(t_i)}}^{-1} \\ & & \cdots & \vdots \\ symm & & & \sum_{i=1}^{n} (\sin 2\omega t_i)^2 \mathbf{Q}_{\mathbf{y}_{(t_i)}}^{-1} \end{pmatrix}, \qquad (6.5)$$

$$\mathbf{b} = \begin{pmatrix} \sum_{i=1}^{n} \mathbf{Q}_{\mathbf{y}_{(t_i)}}^{-1} \mathbf{y}(t_i) \\ \sum_{i=1}^{n} t_i \mathbf{Q}_{\mathbf{y}_{(t_i)}}^{-1} \mathbf{y}(t_i) \\ \vdots \\ \sum_{i=1}^{n} \sin 2\omega t_i \mathbf{Q}_{\mathbf{y}_{(t_i)}}^{-1} \mathbf{y}(t_i) \end{pmatrix}, \qquad (6.6)$$

with $n = 46$. The least-squares solution is obtained by $\mathbf{x} = \mathbf{N}^{-1}\mathbf{b}$, and the variance-covariance matrix of the solution is $\mathbf{Q}_{\mathbf{x}} = \mathbf{N}^{-1}$. After the secular and seasonal variations are derived, the P3M8 de-striping and 400 km Gaussian filtering are implemented as described in section 6.2. The variances of the derived solutions are also scaled to account for the de-striping and Gaussian filtering

procedures. Error propagation is applied to compute the error estimates on global grids alongside the equivalent water heights from the estimated secular and seasonal models, as indicated in equation (6.1).

For comparison, secular trends, annual and semi-annual cycles are estimated from the GLDAS hydrological models in the same way as the DEOS GRACE solutions. The GLDAS hydrological models used span a period from February 2003 to December 2006. Variance-covariance matrices are not available for the GLDAS hydrological models, therefore, they are treated as unit matrices in the least-squares inversion. For consistency de-striping and 400 km Gaussian filtering are applied to the GLDAS fields.

6.3.1 Global secular water mass variations

The secular mass changes observed from the DEOS GRACE solutions and the GLDAS hydrological models are shown in figure 6.9a and 6.9b, respectively. Some remarkable similarities can be observed between the models. For instance, the areas of decreasing mass include southeastern Alaska, Southwestern United States, the La Plata River basin, middle Africa and southern Asia. Examples of regions consistently showing an increase in mass are the northern part of South America, southern Africa, central Europe and the Eastern Siberian Plain. Aside from these similarities, there are some large signals in the GRACE estimates which are not observed in the GLDAS hydrological models: significant mass decline in Greenland, mass loss in the Amundsen Sea Embayment (West Antarctica), and significant positive rates in Hudson Bay and Scandinavia. Some of these discrepancies, e.g. the positive rate in the Hudson Bay and Scandinavia, can be attributed to Post Glacial Rebound (PGR). The PGR signal is caused by a redistribution of lithospheric mass, as a consequence of glacial loading during the last ice age. These signals appear as secular trends in the Earth's gravity field. The PGR signals show up in the trend analysis of the DEOS solutions since no attempt has been made to remove the signals at the GRACE data pre-processing stage. In order to derive the secular change due to the water storage, the PGR signal has to be removed.

The PGR model used in the thesis was computed from using the de-glaciation models ICE-5G [Peltier, 2004] and IJ05 [Ivins and James, 2005]. The IJ05 model is only available for the Antarctic, therefore, outside of the Antarctic area it is combined with the global ICE-5G model. The computation was based on the assumption of an incompressible, self-gravitating Earth. The mantle viscosity model was a 4-layered approximation to Peltier's model [Peltier, 2004]. The viscosity profiles were based on a lithospheric thickness of 90 km, upper mantle viscosity of 9.0×22 Pa-sec, lower mantle viscosity of 3.6×21 Pa-sec, and upper mantle/lower mantle boundary radius of 1170 km. The set of PGR Stokes coefficients is truncated at degree and order 50 and is smoothed using the P3M8 de-striping and the 400 km Gaussian filtering. Degree-one terms are omitted, because they are not included in the DEOS GRACE solutions. The results are

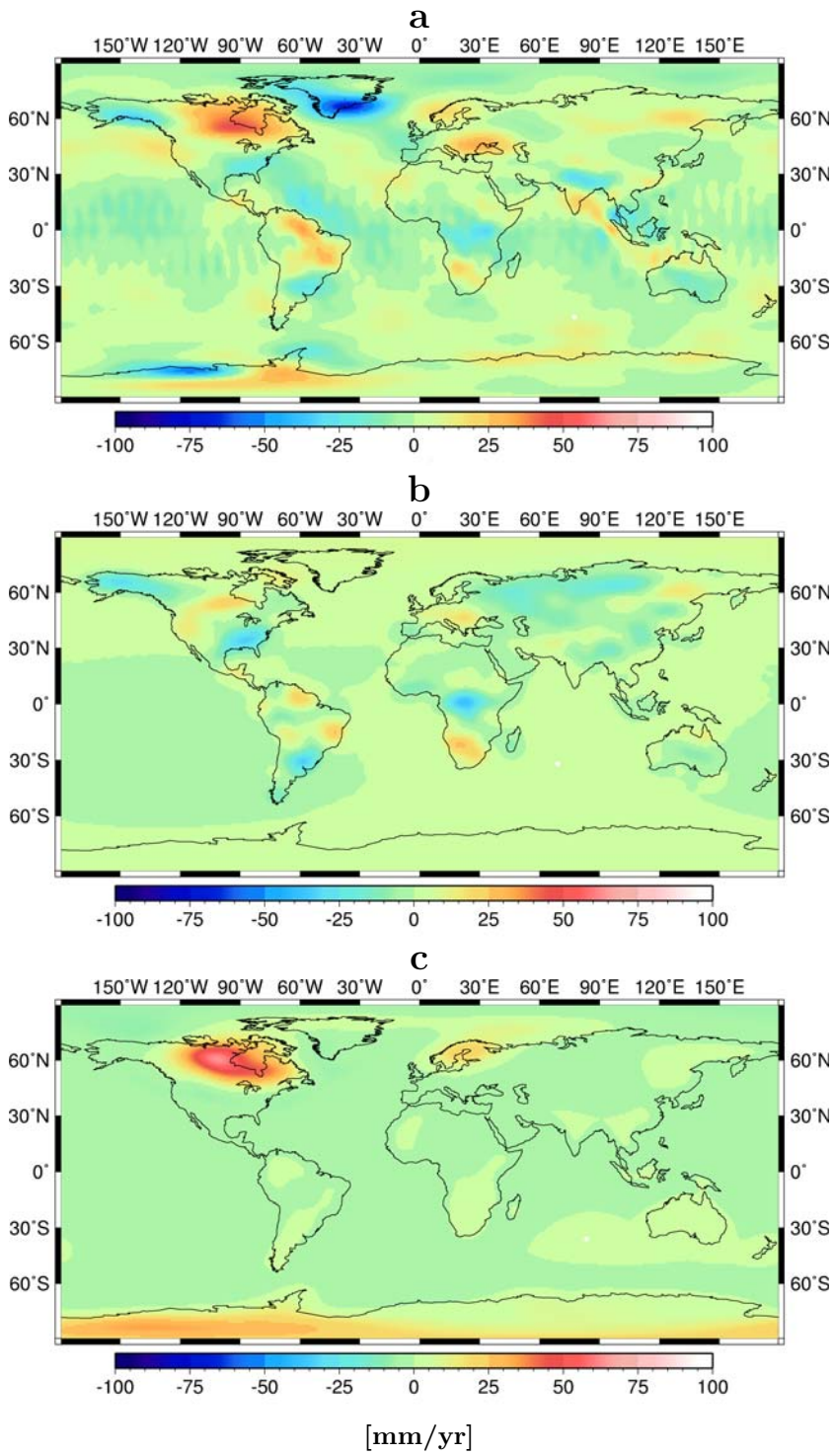

Fig. 6.9. Estimated secular mass changes from DEOS GRACE solutions (a), from GLDAS hydrological models (b), and the mass change signal (c) provided by the PGR model of [Peltier, 2004, Ivins and James, 2005]

shown in figure 6.9c. After that, the PGR model is mapped to grid values, representing the rate of surface mass change, expressed in terms of equivalent water height. The results are shown in figure 6.9c. As can be seen from the figure, the PGR signal is located in the Hudson Bay, Antarctic and Scandinavia regions, which agrees very well with the DEOS GRACE-based secular signal. Figure 6.10a shows the secular change of the water storage obtained by removing the PGR signal (i.e. figure 6.9a minus figure 6.9c). It should be mentioned that the estimated secular changes include the errors of the PGR model; nevertheless, the dominant positive signals in the Hudson Bay, Antarctic and Scandinavia areas almost disappear. The resulting map is definitely more similar to that derived from the GLDAS hydrological model (figure 6.9b) than the original GRACE solution.

The GRACE derived secular trend (figure 6.10) has the following major features (excluding the Greenland and Antarctic areas):

1) One of the largest positive signals is a more than 30 mm/yr water mass increase in central Europe. This increase is likely caused by ground water discharge associated with a record-breaking heat-wave in 2003 followed by water storage restoration [Andersen and Hinderer, 2005].

2) The peak estimated trend for the Tocantins and Orinoco River basins within the South American continent exceeds 30 mm/yr. The neighboring river basin, La Plata, shows a peak of 25-30 mm/yr of water mass loss.

3) Within the continent of North America, the water storage in southeastern Alaska is decreasing with a peak value of 30 mm/yr, which is close to other estimates [Chen et al., 2006a]. In addition, the western part of Hudson Bay shows a negative mass change rate of 30 mm/yr, which is probably due to snow mass variation and uncertainty in the subtracted PGR signal.

4) Within the continent of Africa, a peak of more than 40 mm/yr of water storage decrease is detected in the Congo River basin (central Africa), and an increase of about 20 mm/yr can be seen in South Africa.

5) In Asia, a positive trend is observed in southern India and in the Eastern Siberian Plain, the latter could be due to the snow accumulation. A negative mass change rate of more than 25 mm/yr can be observed over northern India. We see a pair of negative and positive trends within the Indonesia, Malaysia and Andaman Sea regions. This is very likely due to mass changes caused by the Sumatra-Andaman earthquake and will be discussed later in section 6.4.3.

The calibrated formal error estimates for the secular trends are shown in figure 6.10b. The error estimate has a mean of 1.2 mm/yr in terms of equivalent water height, ranging from 0.7 mm/yr near the poles to 1.7 mm/yr around the equator. The stochastic estimates could be too optimistic, since the PGR model

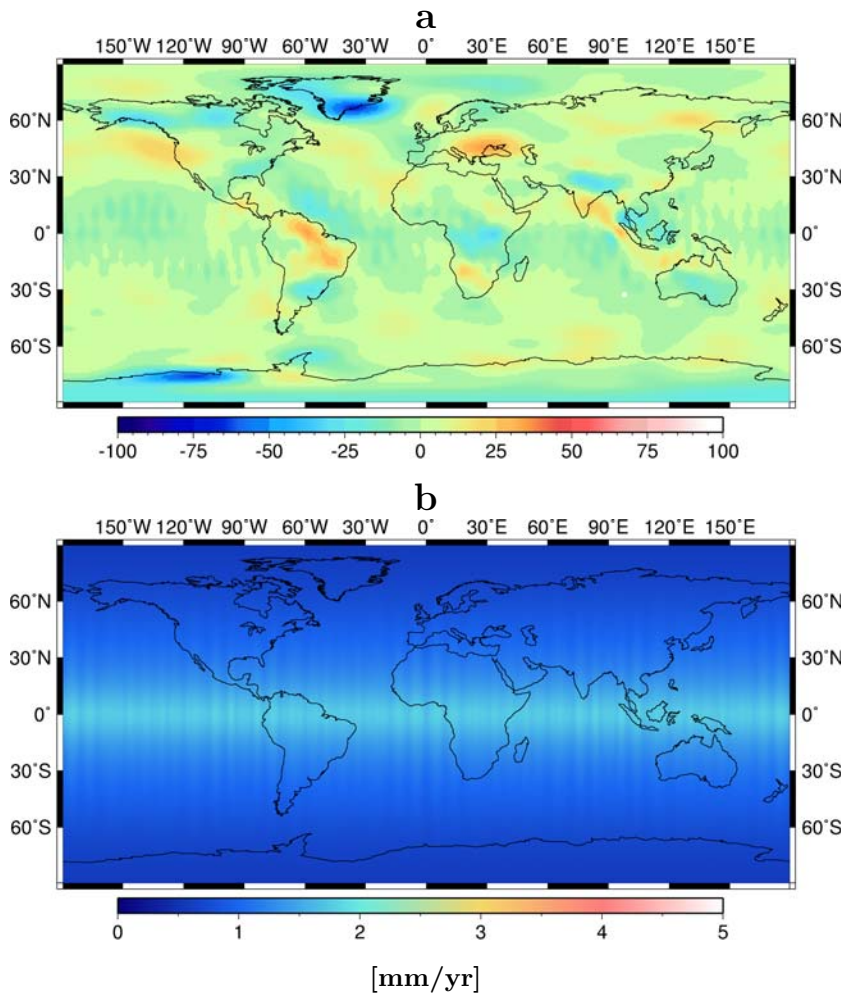

Fig. 6.10. Estimated secular water mass changes after removing the post-glacial rebound signal (a), and formal errors of secular water mass changes (b)

could introduce errors. A more realistic error estimate can be obtained by computing the Root Mean Square (RMS) signal over the ocean where the noise should be significantly smaller than on land [Andersen and Hinderer, 2005]. With possible leakage of the land signal (due to the Gaussian filtering) and the existing ocean secular signal (e.g. bottom pressure signal), a value of 3 mm/yr is estimated. With this empirical estimate of precision (here called "empirical error"), we can conclude that our estimates of global secular signals are reliable. The estimated secular signals provide very valuable information for future hydrological modeling, and could also offer reasonable constraints on the PGR modeling.

6.3.2 Global seasonal water mass variations

This section is devoted to the analysis of seasonal mass changes observed from the DEOS GRACE solutions. The annual sine terms derived from the DEOS GRACE solutions and the GLDAS hydrological models are shown in figures 6.11a and 6.11b, respectively. In addition, the formal error of the GRACE DEOS estimate is shown in figure 6.11c. The maps of annual sine terms are remarkably similar. The sine term from GRACE models ranges from -166.0 mm (at Orinoco River basin) to +214.0 mm (at Amazon River basin) with a global empirical error RMS of 5.0 mm (formal error is 2.0 mm). The sine term from the GLDAS hydrological models ranges from -140.0 mm (in the Ganges River basin) to +193.0 mm (in Amazon River basin) with a global error RMS of 2.0 mm. A positive value indicates a variation that has a maximum in Spring, a negative value indicates a variation that is opposite in phase, i.e. reaching the maximum in Fall. The annual cosine term from the DEOS and hydrological models are shown in figure 6.12a and 6.12b together with the formal error of the DEOS estimates (figure 6.12c). The GRACE cosine term ranges from -236.0 mm (at Orinoco River basin) to +70.0 mm (at the southern border of the Amazon River basin) with a global RMS of 8.0 mm (formal error is 2.0 mm). The cosine term from the GLDAS hydrological models ranges from -142.0 mm (the Congo River basin) to +34.0 mm (at the Ganges River basin) with a global RMS of 2.0 mm. A positive cosine term is a variation that reaches maximum in Winter.

The amplitude and phase of the seasonal signal can be calculated from the sine and cosine components as follows:

$$\mathbf{A}_{am} = \sqrt{\mathbf{a}_2^2 + \mathbf{a}_3^2} \qquad \phi = \arctan\left(\frac{\mathbf{a}_2}{\mathbf{a}_3}\right), \tag{6.7}$$

where $\mathbf{a}_2$ and $\mathbf{a}_3$ represent the computed equivalent water heights at each grid point derived from the sine and cosine components; $\mathbf{A}_{am}$ and ϕ are the amplitude and phase at the given grid point, respectively. The amplitude and phase maps are plotted in figure 6.13. One can clearly see regions with relatively large water mass variations, including the Amazon, Orinoco and Tocantins River basins in South America; the Zambezi and Congo river basins in Africa; and the Ganges and Siberia river basins in Asia. Some areas have smaller water mass variations, for example: central Europe, Southern Australia, Alaska and the Mississippi River basins in North America, the La Plata River basin in South America. There are also minor variations in some areas, e.g. central America, Madagascar island, southern China and Greenland. A clear separation in phase of water mass changes can be observed from figure 6.13b. Almost all areas in the northern hemisphere (above latitude 30^oN) have maximum water storage in Spring or Summer (positive values). The areas between latitude 0 and 30^oN mostly have maximum water storage in Fall or Winter. In southern hemisphere, the areas between latitude 0^o and 30^oS have positive phase values, which indicates that water storage occurs in Spring or Summer. The areas below latitude 30^oS (except for eastern Antarctic) have negative phases, which means that a minimum water

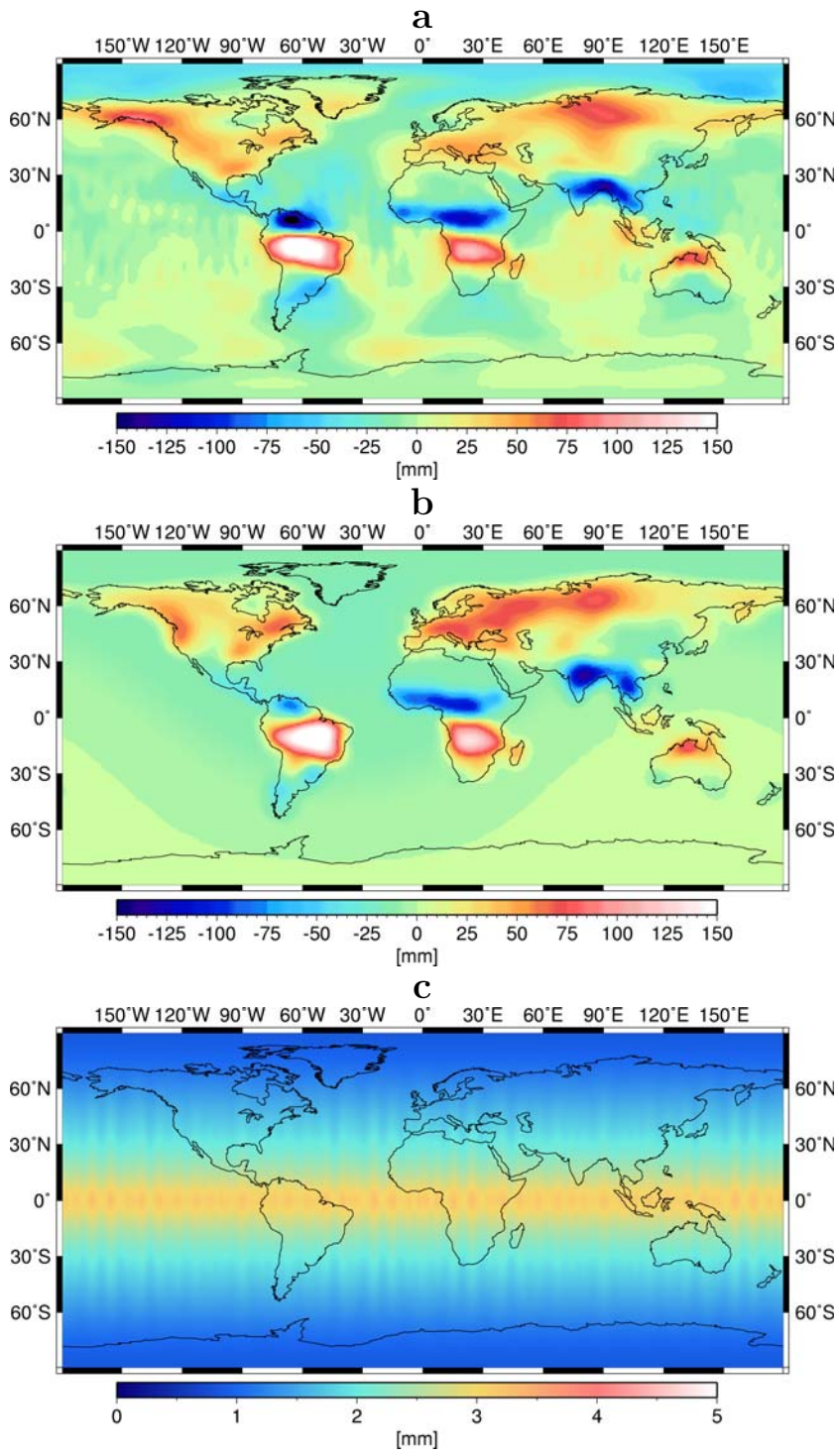

Fig. 6.11. Estimated sine term of annual water mass variations between February 2003 and February 2006 from DEOS GRACE solutions (a), from GLDAS hydrological models (b), and formal errors of the DEOS estimate. Positive values in (a) and (b) indicate an increase in Spring

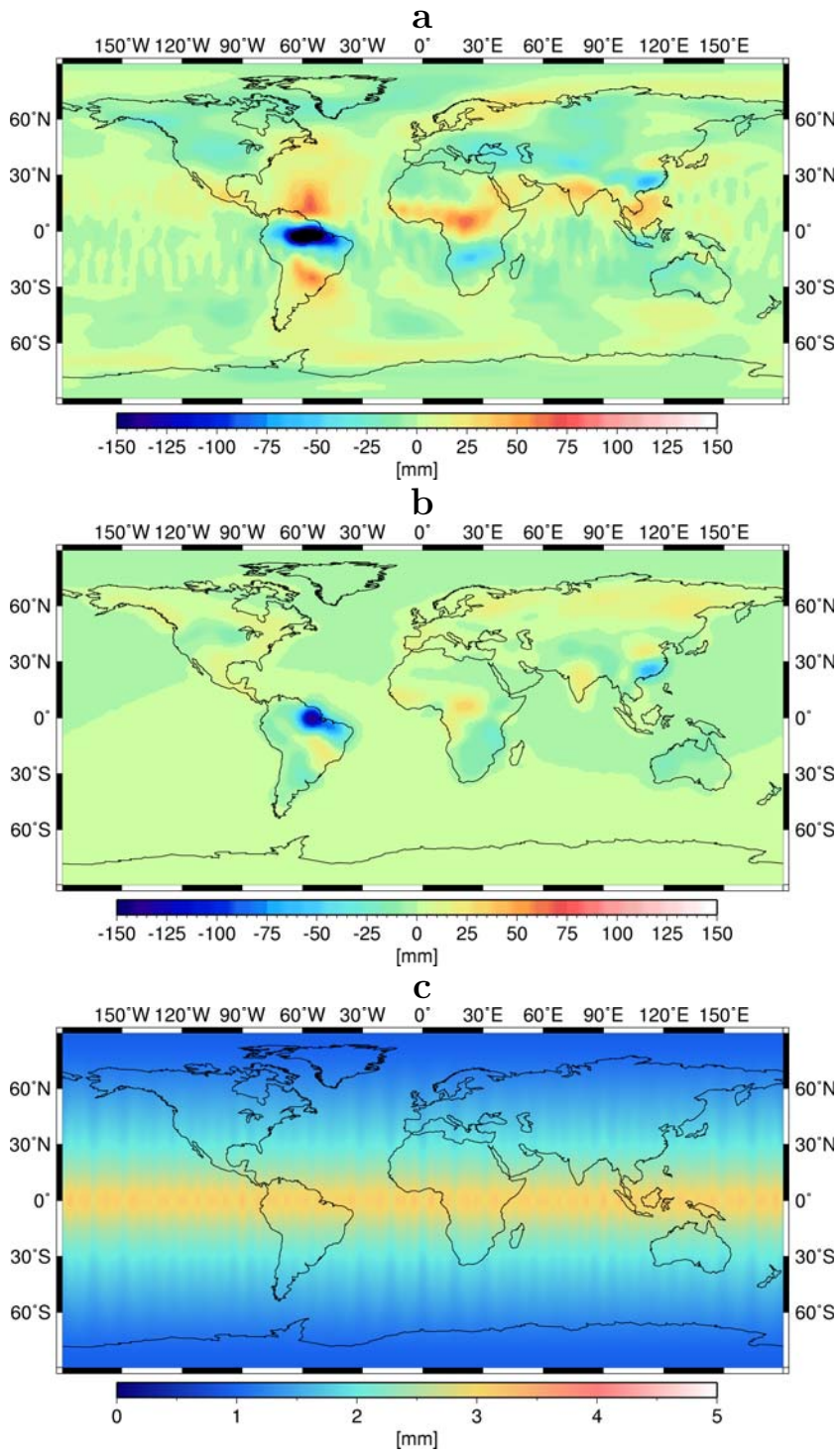

Fig. 6.12. Estimated cosine term of annual water mass variations between February 2003 and December 2006 from DEOS GRACE solutions (a), from GLDAS hydrological models (b), and formal errors of the DEOS estimate (c). Positive values in (a) and (b) indicate an increase in Winter

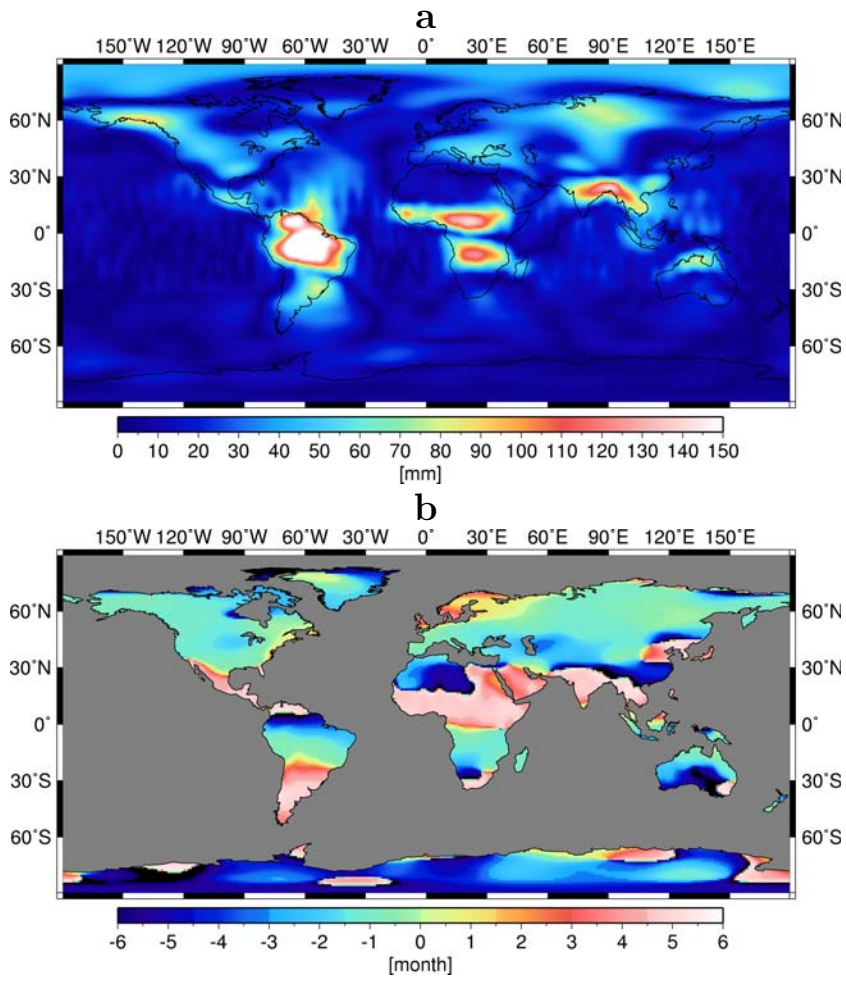

Fig. 6.13. Estimated signal amplitude and phase of water mass variations between February 2003 and December 2006 from DEOS GRACE solutions: amplitude of annual term (a), phase of annual term (b). Positive values in (b) indicate the interval from January to June, and negative ones display the interval from July to December

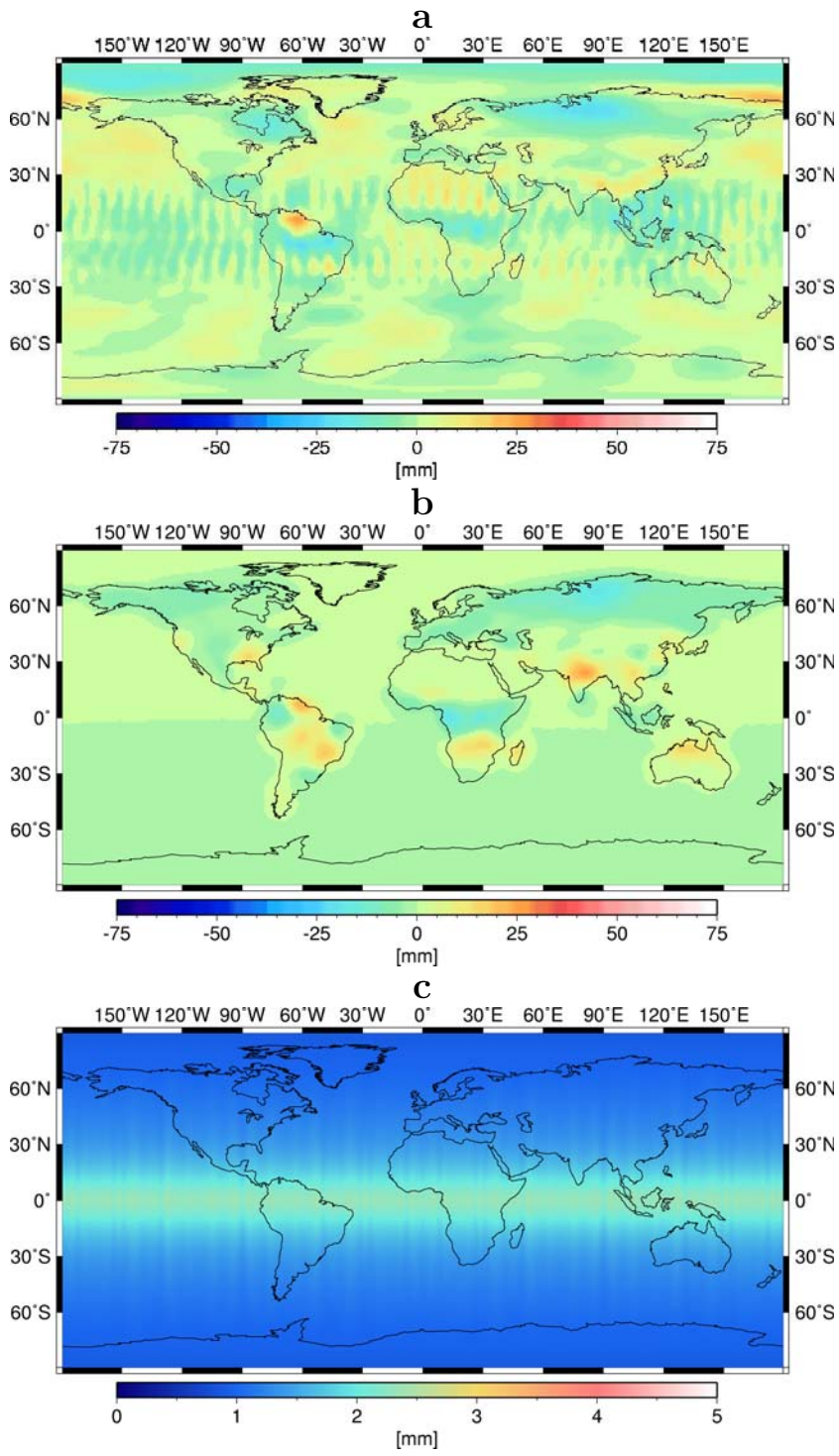

Fig. 6.14. Estimated sine term of semi-annual water mass variations between February 2003 and February 2006 from DEOS GRACE solutions (a), from GLDAS hydrological models (b), and formal errors of the DEOS estimates

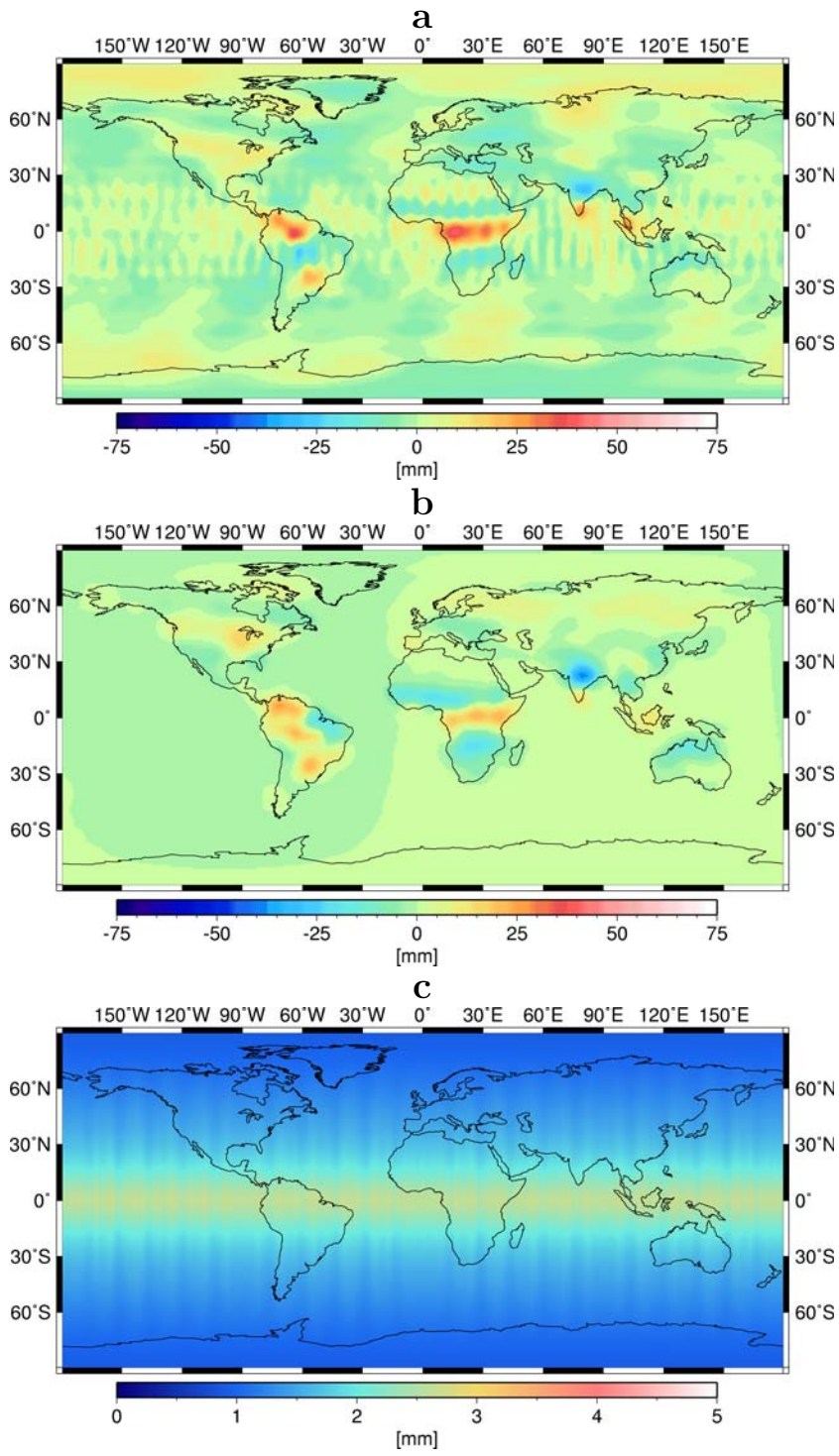

Fig. 6.15. Estimated cosine term of semi-annual water mass variations between February 2003 and December 2006 from DEOS GRACE solutions (a), from GLDAS hydrological models (b), and formal errors of the DEOS estimate (c)

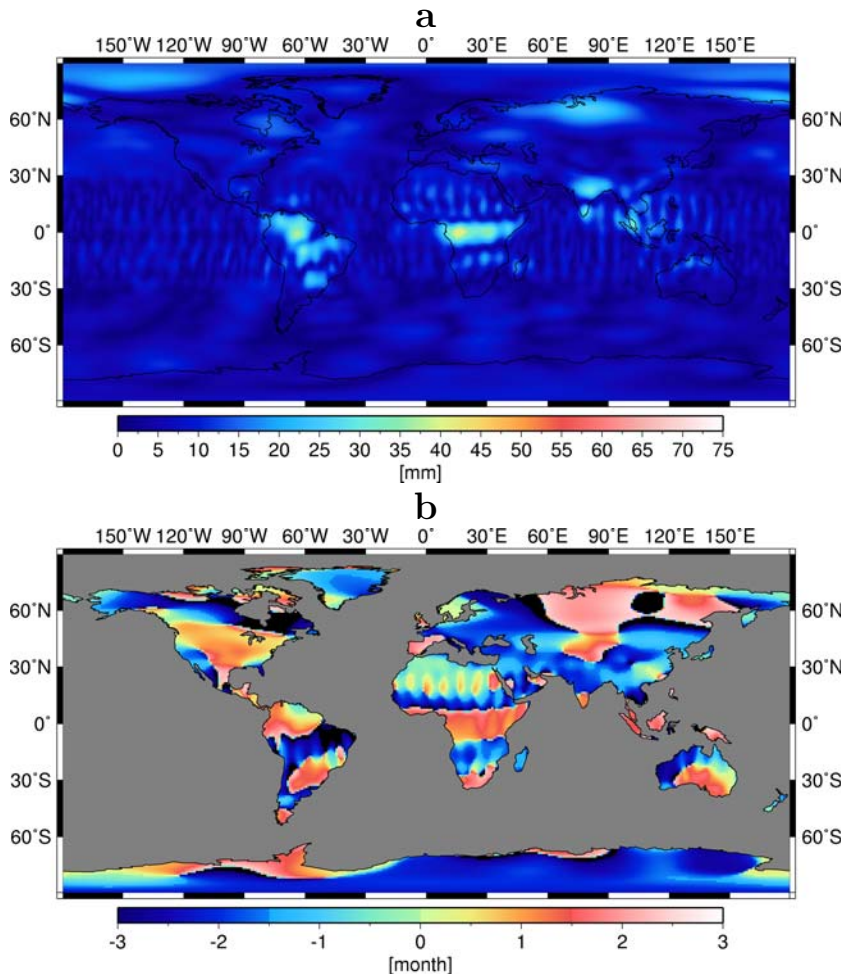

Fig. 6.16. Estimated signal semi-amplitude and phase water mass variations between February 2003 and December 2006 from DEOS GRACE solutions: amplitude of semi-annual term (a), phase of semi-annual term (b)

storage takes place in spring or summer.

The semi-annual sine and cosine terms derived from the DEOS GRACE solutions and the GLDAS hydrological models are shown in figure 6.14 and 6.15, respectively (alongside their formal errors). Compared with the annual terms, the semi-annual terms are much smaller. Still, the maps produced from the GRACE estimates and GLDAS hydrological models show some similarities. The sine term from GRACE ranges from -24.0 mm (in the Amazon River basin) to +27.0 mm (in the Orinoco River basin) with a global RMS of 4.0 mm (the formal error is 1.5 mm). The sine term from the GLDAS hydrological models ranges from -19.0 mm (in the Ob River basin) to +27.0 mm (in the Orinoco River basin) with a global RMS of 1.0 mm. The annual cosine terms from the DEOS GRACE solutions and the hydrological models are shown in figure 6.15a and 6.15b together with the formal error of the DEOS estimate, which is shown in figure 6.15c. The cosine term from GRACE ranges from -29.4 mm (in southern India) to +40.0 mm (in the Congo River basin) with a global RMS of 4.0 mm (formal error is 1.8 mm). The cosine term from the GLDAS hydrological models ranges from -39.0 mm (in southern India) to 25.0 mm (in the Orinoco River basin) with a global RMS of 1.0 mm.

The amplitude and phase of the semi-seasonal variations derived from the DEOS models are shown in figure 6.16. Compared to the amplitude of the one-year cycle, the half-year amplitude is rather small. The signal is mostly concentrated in the Orinoco, Amazon and La Plata River basins in South America; central Africa; India; and the Ob River basin in Russia. This behavior is interpreted as an evidence that seasonal mass variations in these regions have maximum deviations from the sinusoidal behavior. In the Ob river basin, for example, this can be explained by a slow accumulation of snow during Fall and Winter, and fast snow melting in Spring.

6.4 Applications of DEOS monthly solutions

6.4.1 Greenland ice sheet

In the previous section, we have presented a global model of secular mass changes. This section will concentrate on Greenland and the surrounding regions.

Greenland is the world's largest island and the second largest ice cap on Earth after Antarctica. Its total area measures 2166 086 km^2, of which the ice sheet covers 1755 637 km^2. The volume of the ice sheet is of 2.5 million km^3, about 10% of the total global ice mass on Earth. If the Greenland ice sheet completely melted away, sea level would rise by 6.5 m to 7.0 m. The addition of such a large quantity of fresh water to the oceans would disrupt normal ocean currents, which could have disastrous effects for weather systems. Monitoring the ice melt and accumulation within the Greenland region is of utmost importance for the study of sea level rise and climate change.

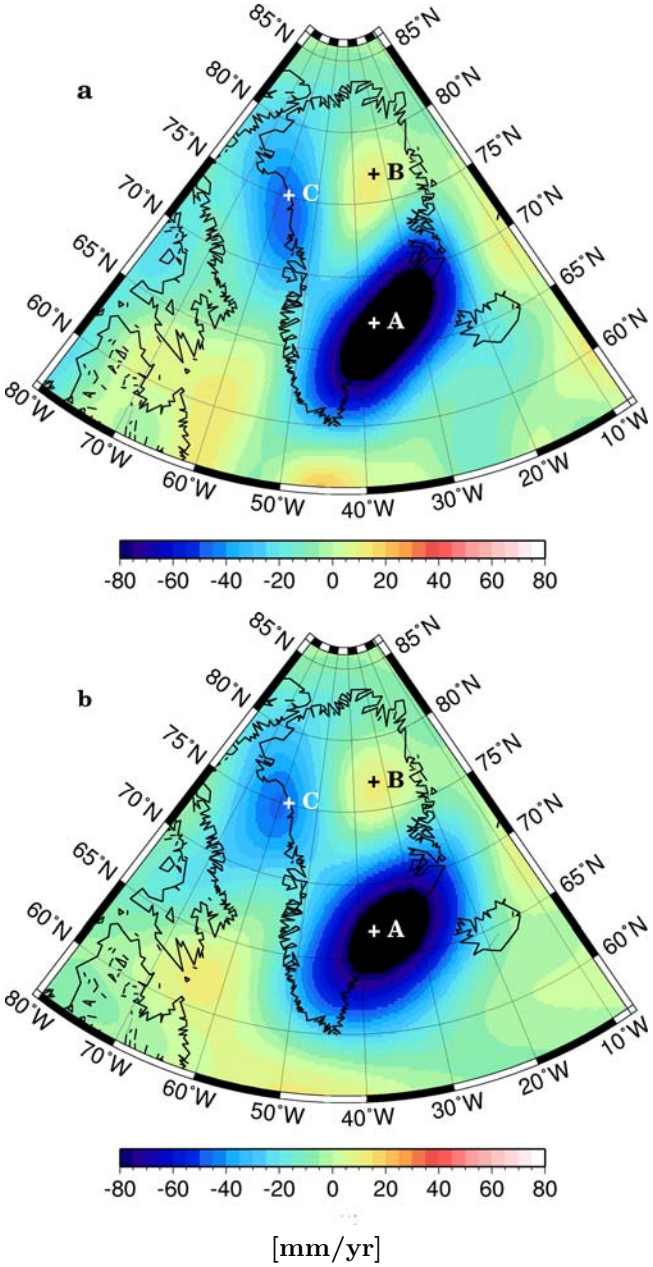

Fig. 6.17. Estimated secular mass change rates over Greenland from DEOS GRACE solutions after 300 km Gaussian filtering (a) and the P3M12 de-striping plus 300 km Gaussian filtering (b). The PGR signal has been removed. Time series of variations for the points A, B and C are shown in figure 6.18.

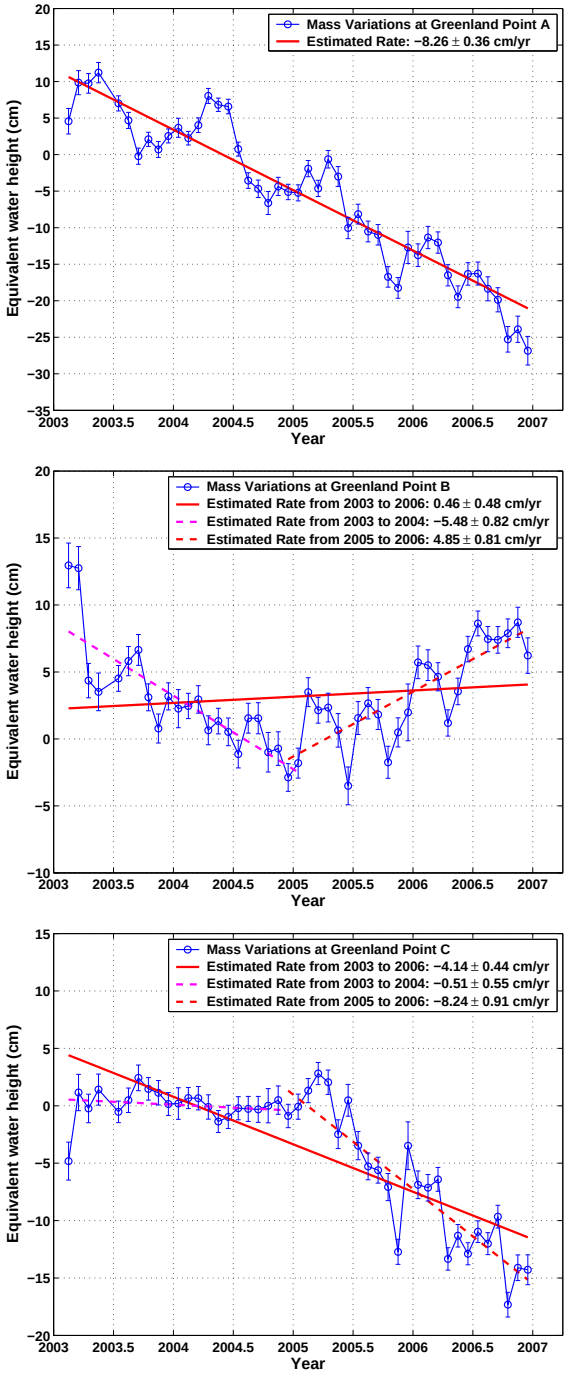

Fig. 6.18. Mass variations obtained from DEOS GRACE solutions at three selected points shown in figure 6.17: A (top), B (middle) and C (bottom). The straight lines are linear trends estimated by a weighted least-squares. The monthly values are equivalent water heights after P3M12 de-striping and 300 km Gaussian filtering are applied. The PGR signal has been removed

Prior to the GRACE mission, various techniques were applied to measure the ice mass balance in Greenland, for example, repeat-pass airborne laser altimetry and satellite interferometry, see [Krabill et al., 2004, Rignot and Kanagaratnam, 2006]. Both techniques indicated that the Greenland ice sheet is, as a whole, melting, although the estimated rates of melting were significantly different. One explanation for this difference is that the periods of measurements differ.

The satellite gravity measurements provided by GRACE mission can also be used to measure the ice mass balance in Greenland. Two recent investigations of ice melting in Greenland were conducted by [Velicogna and Wahr, 2005] and [Chen et al., 2006c] on the basis of CSR GRACE solutions. The periods of measurements for their research were 2 years and 3.5 years, respectively. [Luthcke et al., 2006] used 2 years of GRACE mascon solutions. The common result from these earlier studies is that the ice sheet in the southeast coast of Greenland is rapidly melting. Here we conduct a similar investigation using 4-years of DEOS monthly solutions.

Figure 6.17 shows the estimated mass change rates in Greenland and surrounding regions after subtraction of the PGR signal. Its magnitude in Greenland is much smaller than the GRACE estimated rate (figure 6.9a and 6.9c). A 300 km Gaussian filter is applied to the total GRACE-based estimates after subtraction of the PGR signal. It is found that the 300 km Gaussian filtering is sufficient to suppress the noise over the region of Greenland for the *trend estimates* and that de-striping of the model is unnecessary. We suggest three reasons why de-striping is not necessary: 1) Greenland is located at high latitudes and the GRACE measurements there are much denser than near the equator. 2) The satellite ground-tracks intersect each other at larger angles than near the equators, so that East-West variations of gravity field are sensed better. 3) The secular mass change signal is rather large. The estimated secular rates are shown in figure 6.17a. Unfortunately, the 300 km Gaussian filtering is not sufficient for obtaining *individual* monthly solutions for the Greenland region, de-striping is still needed. We applied de-striping to the individual monthly solutions, starting at order 12, this value is higher than previously used to estimate continental water change rates since the stripes in the Greenland region are of a smaller amplitude than at the lower latitudes. For consistency, we also plot the rates after applying the P3M12 de-striping and 300 km Gaussian filtering, in figure 6.17b. The de-striping does not appear to change the magnitude of the signal in the Greenland region.

As can be seen from figure 6.17, there are two prominent negative signals centered at the southeast and northwest coast of Greenland (marked as A and C), and a slight positive trend in the interior highland (marked as B). Our estimation confirms that the largest mass loss takes place at the southeast coast, where active glaciers, ice flows and corresponding ice losses are also observed by remote

sensing techniques and satellite radar altimetry. This is also consistent with the earlier estimate from CSR GRACE solutions, see [Velicogna and Wahr, 2005] and [Chen et al., 2006c]. In order to see the temporal variations at these centers, the monthly grid values at points A, B and C are computed, and the time series are plotted in figure 6.18. A trend and seasonal terms are estimated from a least squares fit to the time series at points A, B and C. The least-squares procedure is similar to that described in section 6.3, but the input data are the grid values instead of spherical harmonic coefficients. The uncertainty of the estimates is also computed in the least-squares fit using the GRACE monthly error and the model error of the PGR model. The PGR model error is assumed to be 100% of the model value at each grid point. The obtained trend at Point A is -8.26 ± 0.36 cm/yr over the observation period, which implies a rather large melting speed. The other center of mass loss at the northwest coast (C), was not observed in CSR GRACE solutions by earlier studies [Chen et al., 2006c]. The time series at Point C (see figure 6.18) shows that the trend during the first two years was slightly negative and the ice/snow storage looks stable (-0.51 ± 0.55 cm/yr) whereas during the second two years the trend was strongly negative (-8.24 ± 0.91 cm/yr), causing the overall trend during the four years to be -4.14 ± 0.44 cm/yr. Earlier studies did not use the 2006 data, and this likely explains why mass loss at point C was not previously detected. There is a slight mass accumulation in the interior highland at point B, which can be decomposed into mass loss in the first two years (-5.48 ± 0.82 cm/yr) and mass gain in the last two years ($+4.85 \pm 0.81$ cm/yr). Our conclusion is that glaciers along the southeast and northwest coast of Greenland are, in general, melting, whereas the ice sheets in the Greenland's interior are getting slightly thicker over the four years from 2003 to 2006.

6.4.2 Antarctic ice sheet

In this section, the mass loss of Antarctic ice sheet is investigated. Antarctica is the Earth's southernmost continent with an area of approximately 14.4 million km^2. The continent is divided into two parts by the Transantarctic Mountains, close to the neck between the Ross Sea and the Weddell Sea. The portion west of the Weddell Sea and east of the Ross Sea is called Western Antarctica and the remainder Eastern Antarctica. Some 98% of Antarctica is covered by ice sheet, which averages at least 1.6 km in thickness. The continent stores about 90% of the world's ice, equivalent of about 70% of the world's fresh water. If all ice in Antarctic melted, sea level would rise about 60 meters. Quantifying Antarctic ice sheet mass balance is a vital part of understanding the global hydrological cycle, predicting sea level rise and assessing climate change, and has obvious social and economic impacts.

The stability of Western Antarctic glaciers along the coast of the Amundsen Sea Embayment have been of recent concern because of the real possibility of collapse. If the ice sheet in only this area breaks down, the ocean level would rise by several meters. Thomas et al. [2004] revealed a significant ice melting

along the coast of the Amundsen Sea Embayment using satellite altimetry, InSAR (Interferometric Synthetic Aperture Radar), and GPS data. The Antarctic Peninsula is similar to the subpolar glacial systems along coastal Greenland and Alaska [Chen et al., 2008], and is more sensitive to atmospheric warming than the rest of the Antarctic continent [Vaughan, 2006]. Collapses of the peninsula glaciers have been frequently observed by InSAR and other remote sensing techniques [Rignot et al., 2005, Rignot and Kanagaratnam, 2006]. However, it is difficult to measure the mass variability of Antarctica by remote sensing techniques because of the ice sheet's size, complex geography and steep slopes. The GRACE mission is able to provide monthly variation of Earth's gravity, which can directly be related to mass variability. Several other investigations have estimated the mass balance of the Antarctic continent from CSR GRACE solutions, see [Chen et al., 2006b], [Velicogna and Wahr, 2006] and [Chen et al., 2008] and CNES GRACE solutions, e.g. [Ramillien et al. 2006], [Llubes et al., 2007]. In our study, we focus on Antarctica: the Antarctic Peninsula, the Amundsen Sea Embayment, Southern Ronne Ice Shelf, Enderby Land and East Antarctica. The data analysis is similar to that used in the previous section.

Figure 6.19 shows the estimated mass change rates within Antarctica and the surrounding regions. Figure 6.19a presents the mass rates after applying only 300 km Gaussian filtering. Although the polar areas have dense coverage with GRACE ground tracks, the stripes, particularly over oceans near Western Antarctica (Amundsen Sea, Southern Ocean and Ross Sea) are still present. In order to suppress these stripes, de-striping is applied with a polynomial of order 3 that removes correlations between spherical harmonics of order 10 and above. Figure 6.19b shows the map after applying the P3M10 de-striping and 300 km Gaussian filtering. As can be seen, the stripes are significantly suppressed, whereas the signal is retained. The biggest negative rates occur at the coast of the Amundsen Sea Embayment (marked as Point A in figure 6.19) and in the northern Antarctic Peninsula (Graham Land, marked as Point B). A smaller negative rate can be seen in the region of New Schwabenland (Point E). Two points with large positive rates are found in Ellsworth Land extending into the Ronne Ice Shelf (Point C), and Marie Byrd Land in West Antarctica (Point F). A relatively large positive rate can be found in Enderby Land in East Antarctica (Point D). The positive mass rates in West Antarctica are very likely PGR effects. The PGR model is represented by spherical harmonics and the same P3M10 de-striping and Gaussian filter are applied. The obtained PGR signal is shown in figure 6.19c. Notice that the color scale differs by a factor of 2 from figure 6.19a. The PGR effects are mostly concentrated in West Antarctica. As can be seen from figure 6.19b, the PGR signal is also visible in the GRACE measurements in the region of points C and F. After removing the PGR signals the estimated ice mass change rates are estimated (see figure 6.19d). Remarkably, the positive mass changes signals are removed to large extent. The results are consistent with those obtained from CSR GRACE solutions by [Chen et al., 2008], except that the mass rates in Enderby land (D) and in the region of New Schwabenland (E) are not as large as the estimates of [Chen et al., 2008].

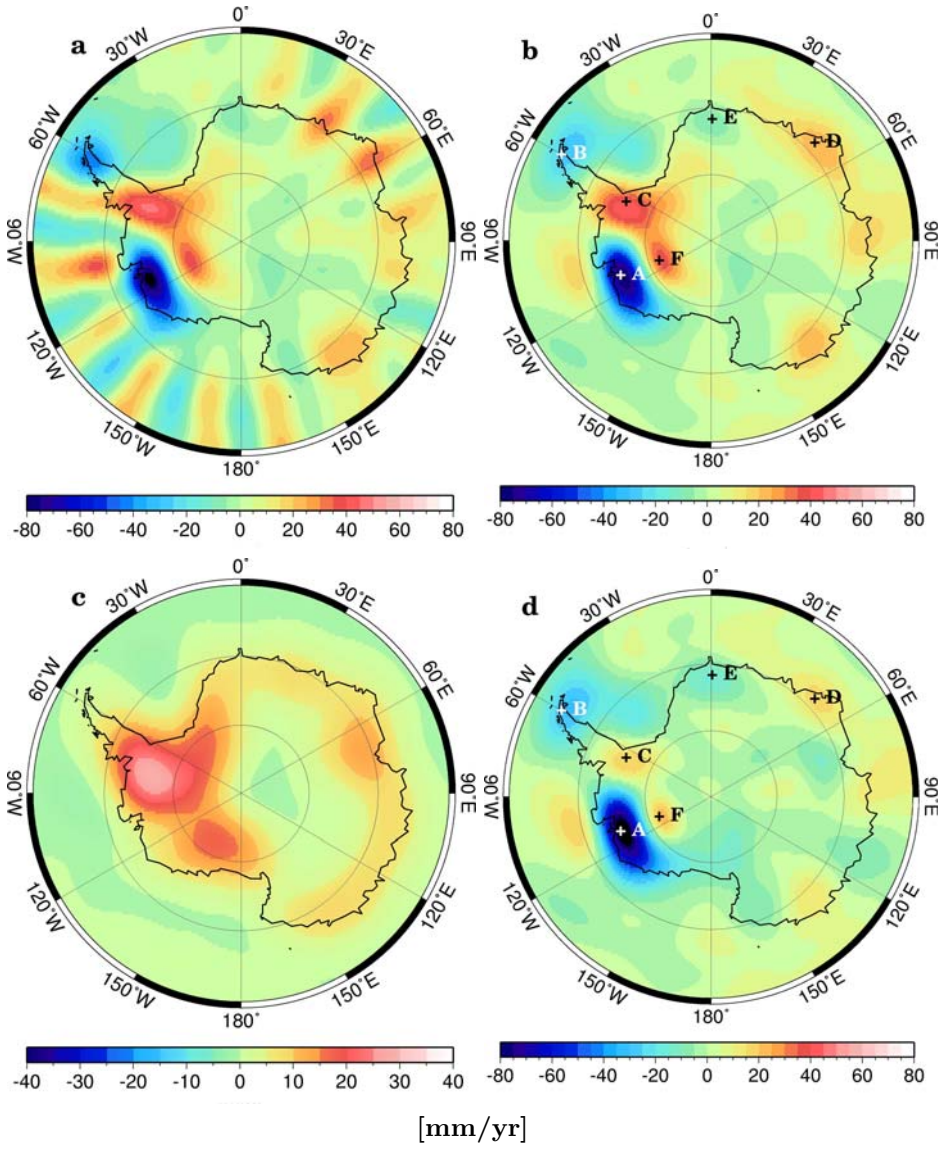

Fig. 6.19. GRACE secular mass change rates over Antarctica in terms of equivalent water heights, estimated from the DEOS monthly solutions after 300 km Gaussian filtering (a) and P3M10 de-striping plus 300 km Gaussian filtering (b). The PGR signal after P3M10 de-striping and 300 km Gaussian filtering is plotted in (c). The GRACE secular mass change rates after removing the PGR signal is plotted in (d). Time series of variations for six selected points are shown in later figures. Note that a different scale is used in (c)

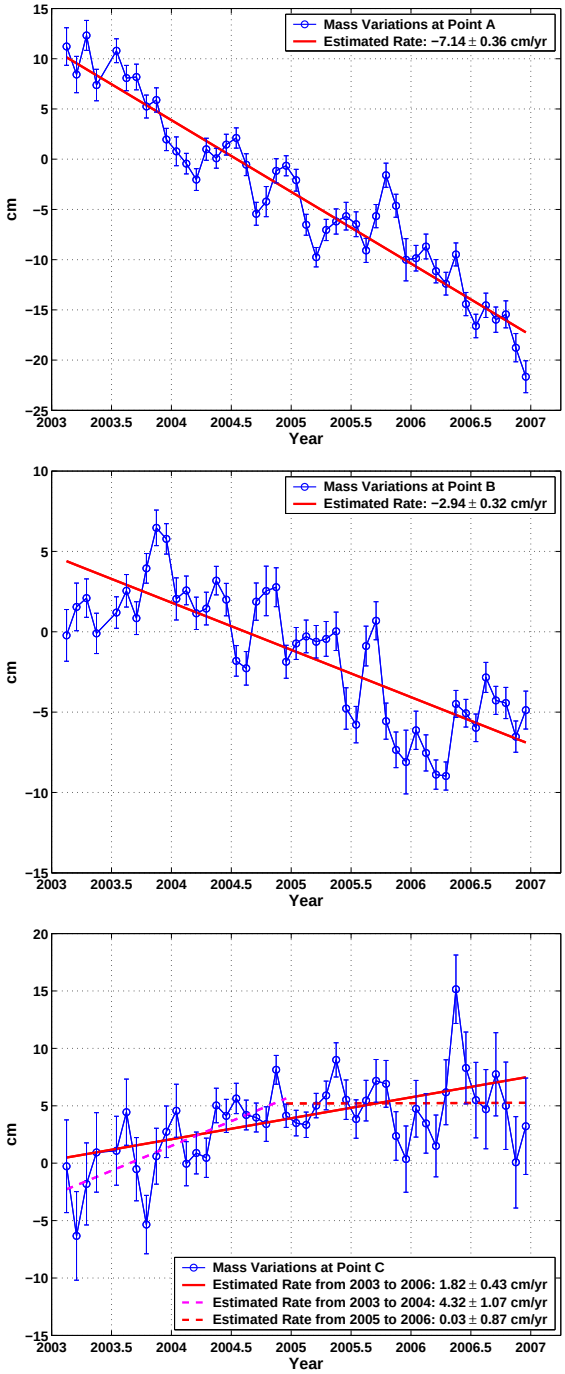

Fig. 6.20. Mass variations obtained from DEOS GRACE solutions at point A (top), B (middle) and C (bottom), marked on figure 6.19. The straight lines are linear trends estimated from a weighted least-squares fit. The monthly values are equivalent water heights after the P3M10 de-striping and 300 km Gaussian filtering. The PGR signal has been removed

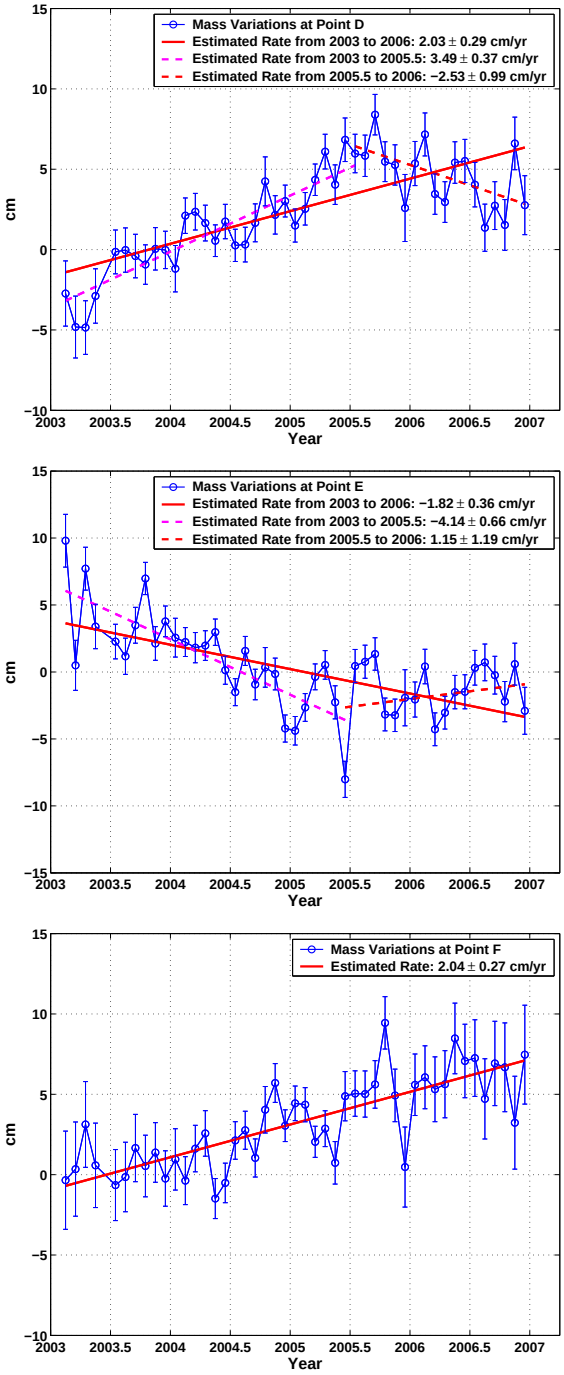

Fig. 6.21. Mass variations obtained from DEOS GRACE solutions at point D (top), E (middle) and F (bottom), marked on figure 6.19. The straight lines are linear trends estimated from a weighted least-squares fit. The monthly values are equivalent water heights after the P3M10 de-striping and 300 km Gaussian filtering. The PGR signal has been removed

To analyze the temporal mass variations further, the time series of mass changes at 6 grid points are plotted in figures 6.20 and 6.21. The corresponding error bars are computed using the GRACE monthly error and the model errors of the PGR model. The PGR model errors are again assumed to be 100% of model values at the grid points. The mass variations at the melting center on the coast of the Amundsen Sea Embayment (A) show a trend of -7.14 ± 0.36 cm/yr, the total mass decline is more than 30 cm during the 4-year observation period. At the ice melt center on the Antarctic Peninsula (B), the mass change rate is -2.94 ± 0.32 cm/yr, an acceleration of ice melting is observed around the beginning of 2006. These two estimates are close to those made by [Chen et al., 2008] and dominate the ice mass rate over the whole Antarctic continent. At Point C, the rate in the first two years is positive (1.82 ± 0.43 cm/yr) and in the second two years is close to zero (0.03 ± 0.87 cm/yr). The overall rate at Point D is positive (2.03 ± 0.29 cm/yr), but is dominated by the period from 2003 to August of 2005. After August 2005, the rate is negative, which reduces the overall estimated rate. For this reason the positive rate at Point D is not as large as the estimate made by [Chen et al., 2008], which did not include GRACE solutions for the second half of 2006. Another discrepancy with one made by [Chen et al., 2008] is observed at Point E. The overall rate at Point E is -1.82 ± 0.36 cm/yr). During the first two and half years, the mass decreases (-4.14 ± 0.66 cm/yr), whereas a slight increase (1.15 ± 1.19 cm/yr) is observed during the last one and a half years. At Point F, a positive rate is observed. The main increase took place during 2003 and 2004, and the mass seems rather stable since then.

We conclude from 4-year DEOS solutions that the mass of the whole Antarctic continent is not in balance. The ice sheet or glaciers in the West Antarctic (mainly the Amundsen Sea Embayment and Peninsula) show a large mass loss, whereas a small mass accumulation is observed in the interiors of West and East Antarctica.

6.4.3 Sumatra-Andaman earthquake

The 2004 Indian Ocean Sumatra-Andaman earthquake occurred at 00:58:53 UTC on December 26, 2004, with the hypocenter beneath the sea floor (3.3°N, 95.9°E) off the northwest coast of Sumatra, Indonesia. The magnitude of the earthquake was between 9.1 and 9.3, the second largest earthquake ever recorded in the history of seismograph. The earthquake lasted between 8.3 and 10 minutes, the longest duration of faulting ever observed. The raptures expanded at a speed of about 2.5 km per second toward the north and northwest, extending 1200 - 1300 km along the Andaman trough. Peak displacements reached 15 meters along a 600 km segment of the plate boundary offshore of northwestern Sumatra and southern Nicobar islands, see [Ammon et al., 2005] and [Lay et al. 2005]. The earthquake triggered a series of devastating tsunamis along the coasts of most landmasses bordering the Indian Ocean, killing more than 225 000 people in eleven countries, and inundating coastal communities with waves up to 30

meters. It was one of the deadliest natural disasters in history. Indonesia, Sri Lanka, India, and Thailand were hardest hit. Apart from the Sumatra-Andaman earthquake, a relatively small earthquake, namely Nias, occured in the region on March 28, 2005 with less disastrous consequences. The hypocenter was located at 2.1°N, 97.9°E. The magnitude of the earthquake was about 8.7.

The Sumatra-Andaman earthquake was associated with megathrust events in subduction zones where the India Plate (part of the great Indo-Australian Plate) slides under the Burma Plate (portion of the great Eurasian Plate). The corresponding seismic stress was accumulated with the Indian Plate slipping deeper and deeper beneath the Burma Plate. Eventually, the earthquake released the seismic stress and permanently changed the mass distribution in Sumatra-Andaman region. Measurements from GPS static stations have revealed significant permanent deformations both horizontally and vertically associated with the earthquake [Hashimoto et al., 2006] and [Banerjee et al, 2007]. The mass re-distribution caused by the earthquake perturbed the motion of the GRACE low-orbit satellites to an extent that can be sensed by the inter-satellite range measurements. After the Sumatra-Andaman earthquake, the GRACE science community immediately started to investigate the possibility of using GRACE measurements to detect these gravity changes caused by the earthquake. [Han et al., 2006b] was the first to successfully detect the gravity changes associated with the subduction and uplift from GRACE L1B range-rates. [Ogawa et al., 2007] demonstrated that both the coseismic and post seismic changes due to the Sumatra-Andaman earthquake can be detected using the GRACE L2 Release 01 products provided by CSR. Later, [Chen et al., 2007] showed that the new release of L2 products of CSR is comparable to the estimates from the L1B data, provided that an improved filtering is applied. In this section, we make use of the DEOS solutions to conduct a similar investigation of the Sumatra-Andaman earthquake as published by [Chen et al., 2007].

Firstly, we compute four yearly mean models (as the same way as the monthly solutions) on the basis of GRACE range combinations in order to suppress seasonal variations. These four models are for the years 2003, 2004, 2005 and 2006, respectively. GRACE data from December 26 to December 31 are excluded in the computation of the 2004 mean model. In addition, two 2-year mean models, i.e. the mean of 2003 and 2004 (before the earthquake), and the mean of 2005 and 2006 (after the earthquake), are computed for this investigation. Secondly, the differences between the successive yearly mean models are derived, as well as the difference between the mean of 2003 and 2004 and the mean of 2005 and 2006. Thirdly, P3M10 de-striping and a 300 km Gaussian filter are applied to the differences between the mean models, in order to suppress the high degree and order noise. Caution is taken in de-striping since the orientation of the Sumatra-Andaman rupture is approximately north-south. Therefore, the starting order of de-striping is chosen to be 10. Figure 6.22 shows the mass changes within the region of the Sumatra-Andaman earthquake from these mean model differences. There are no significant mass changes between 2003 and 2004,

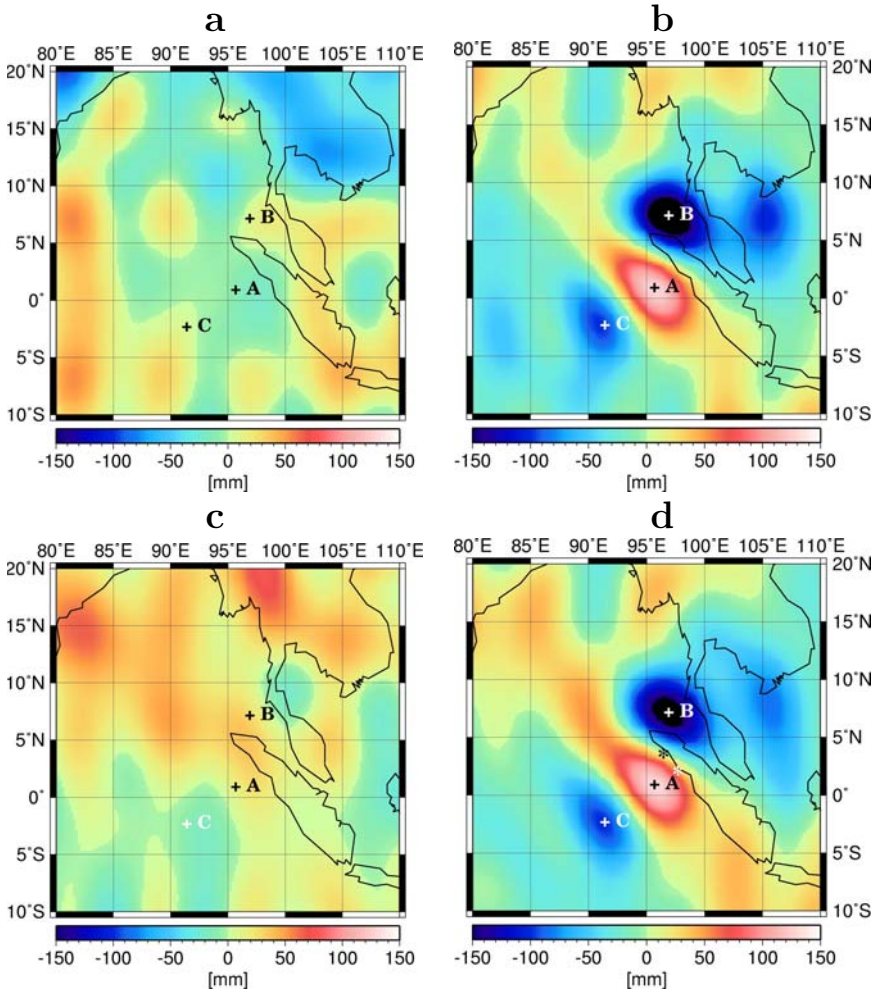

Fig. 6.22. Mass changes in the region of the Sumatra-Andaman earthquake obtained from DEOS yearly mean models. (a) mass changes between models of 2004 and 2003, (b) mass changes between the models of 2005 and 2004, (c) mass changes between models of 2006 and 2005, (d) mass changes between the mean of 2005 and 2004 and the mean of 2003 and 2004. P3M10 de-striping and a 300 km Gaussian filtering were applied. The epicenters of the Sumatra-Andaman and Nias earthquakes are marked as black and white stars, respectively in (d). Three grid points, A ($0.75°$N, $95.75°$E), B ($6.75°$N, $96.75°$E) and C ($2.25°$S, $91.25°$E), marked as crosses, are the centers of gravity change, which are used to display time series for a further analysis

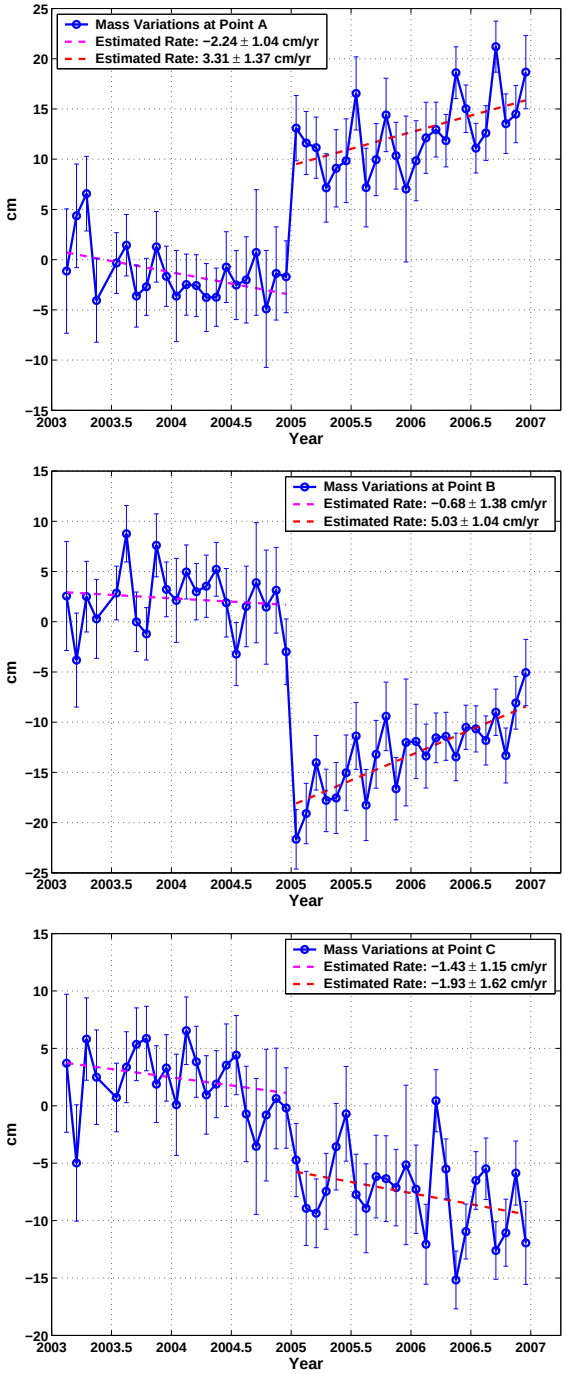

Fig. 6.23. Mass changes at three selected grid points A (top), B(middle) and C (bottom) after seasonal and semi-seasonal signals are removed. The seasonal terms are estimated separately for the pre-earthquake period (2003 and 2004) and the after-earthquake period (2005 and 2006)

and 2005 and 2006. However, clear signatures can be observed in figure 6.22b and 6.22d, which show gravitational changes in the rupture zone. The negative and positive changes are well separated, these changes correspond to subduction and uplift zones respectively. The gravitational signature is very similar to that predicted on the basis of seismic measurements (Figure 2 of [Han et al., 2006b]) and the CSR estimate (Figure 2 in [Chen et al., 2007]). The difference of the 2-year mean models (figure 6.22d) does not seem to differ significantly to the difference of the 1-year mean models (figure 6.22b). In addition to the two large centers of gravitational change (marked as Points A and B), we find a relatively smaller negative change (marked as Point C), which was not clearly observed by [Han et al., 2006b] and [Chen et al., 2007].

The time series of mass change during the 4-year period at the three selected points (marked in figure 6.22 as A, B and C) are derived from the DEOS four-year gravity solutions after the same post-processing as before (P3M10 de-striping and 300 km Gaussian filtering). The corresponding error bars are calculated according to the error propagation law. In order to analyze the pre-seismic, coseismic and post-seismic deformation, we remove seasonal variations, including annual and semiannual sine and cosine terms. These seasonal variations are estimated from each time series for the two separate periods, i.e. 2003-2004 and 2005-2006. The resulting time series are shown in figure 6.23. Significant jumps occur at the moment of the Sumatra-Andaman earthquake in the areas with both positive and negative mass change. The magnitude of change at Point A (14 cm of equivalent water height) is smaller than that at Point B (20 cm of equivalent water height). This is similar to the estimate of [Han et al., 2006b] and [Chen et al., 2007]. At the Point C (much further away from the epicenters than Points A and B), the change at the moment of the earthquake is not present as an abrupt change but a general trend is visible. The major decline took place during the period of 2004 and 2005. This signal is unlikely to be a model error, but might be related to the earthquake. However, the physics of this signal requires further investigation. It should be mentioned that a mass change due to the rupture of companion Nias earthquake is not clearly visible in the time series.

As far as the pre- and post-seismic variations are concerned, we can see from figure 6.23 that the mass change rates at all chosen points are negative prior to the earthquake, particularly at Point A. After the earthquake, the post-seismic mass changes at Points A and B are positive with relatively large rates (3.31 ± 1.37 cm/yr and 5.03 ± 1.04 cm/yr, respectively). These changes are also detected by [Chen et al., 2007] and [Ogawa et al., 2007] from CSR GRACE solutions. The mechanism behind this trend could be a slow positive surface displacement caused by viscous relaxation of the mantle and/or by pore fluid diffusion. Another mechanism suggested by [Ogawa et al., 2007] is that the positive rates were caused by infiltration of supercritical water that abundantly exists in subduction zones after the stress release of the earthquake. Certainly, this issue requires further analysis.

6.5 Comparison with other GRACE solutions

This section aims at a comparison of the DEOS solutions with other published solutions (CSR, GFZ, JPL, CNES) with emphasis on the spectrum assessment and analysis of water storage changes in several large river basins. In order to provide an independent comparison, the GLDAS hydrological models are also used in this section. It should be mentioned that the JPL solutions were validated as the best among others (CNES not involved) on the basis of comparisons with independent observations from satellite altimetry and a numerical ocean model [Dobslaw and Thomas, 2007]. Therefore, we pay a special attention to the comparison with the JPL solutions.

6.5.1 Description of other GRACE solutions

6.5.1.1 CSR RL04 solutions

The monthly solutions issued by CSR have three versions: Release 01 (RL01), Release 02 (RL02) and Release 04 (RL04) versions. The CSR Release 03 does not exist. The RL04 products are used in this thesis for comparison and analysis. The monthly solutions contain fully normalized spherical harmonic coefficients up to degree and order 60. The gravity field coefficients were estimated using one-step variational equations approach. The 5 sec KBR range-rates and 30 sec GPS double differences (formed by one GRACE satellite, one ground station and 2 GPS satellites) are used to form the normal equations. The solution is obtained as an optimally weighted combination of GPS and KBR data using one-day dynamic arcs for the month under consideration. The numerical integration used for the computation of dynamic arcs is the predictor-corrector formulation by Krogh-Shampine-Gordon (5-second step size and 7th order). The background static model was the gravity field model GIFF22a, compiled from the previous 22-month RL02 product (up to degree 120) combined with the GGM02C model (degree 121 to 200) and EGM96 model (degree 201 to 360). The Solid Earth tidal contributions to the geo-potential coefficients are computed as specified in IERS 2003 Conventions. The FES2004 ocean tide model was used to compute the effects of diurnal and semidiurnal tides. The solid Earth pole tide model was defined based on IERS 2003 conventions. Ocean pole tide effects were modeled using a self-consistent equilibrium model based on satellite altimetry data. The atmospheric and oceanic effects were largely removed by using the AOD1B Release 04 products. Non-gravitational accelerations are taken into account using the GRACE accelerometer data. The bias and scale factor of non-gravitational accelerations were the estimated parameters (but the length of estimation period was not made public). Apart from this, empirical satellite accelerations were estimated and removed as a sinusoidal along-track and cross-track variation with an orbital period (1 cpr). More details of the RL04 model computation processing can be found in [Bettadpur, 2007].

6.5.1.2 GFZ RL04 Solutions

The GFZ has distributed several versions of the GRACE monthly solutions (RL01-RL04). The RL04 products are used for the following comparison and analysis. Basically, the GFZ GRACE data processing starts from the adjustment of the GPS satellites orbit and clock parameters from ground-based tracking data with an improved ambiguity fixing method (Step 1). The resulting improved GPS satellite positions and clocks are therefore fixed in Step 2 of data processing. GRACE undifferenced high-low GPS code and phase measurements are used together with KBR range-rates. They all form the observation equations. The background mean model used is the EIGEN-CG03C model truncated at degree and order 150. The time-dependent background models are not significantly different from these used to produce the CSR solutions. More details about the GFZ RL04 models and data processing can be found in [Flechtner, 2007b].

6.5.1.3 JPL validation solutions

The monthly solutions issued by JPL are validation solutions, which contain fully normalized spherical harmonic coefficients complete to degree 120. The methodology and background models used are generally the same as those of CSR except that no empirical accelerations were estimated and only 6-minute GPS measurements rather than 30-second ones were used. More details of the JPL data processing can be obtained from [Watkins and Yuan, 2007].

6.5.1.4 CNES solutions

The Centre National d'Etudes Spatiales at Toulouse (CNES) provides gravity field models expressed in normalized spherical harmonic coefficients from degree 2 to degree 50 at 10 day intervals. The models are based on the running average of three 10-day data periods with weights 0.5/1.0/0.5. The methodology of data processing follows the traditional one-step variation approach. The models are estimated from GRACE GPS and K-band range-rate data and from LAGEOS-1/2 SLR data (LAGEOS data provide over 90% of the information on the degree 2 of the gravity field, whereas GRACE data provide nearly 100% of the information on all the other spherical harmonic coefficients). According to [Biancale et al., 2007], gravitational variations associated with Earth tides (IERS Convention 2003), ocean tides (FES2004 model), ECMWF 3D-atmospheric pressure fields every 6 hours and OBP variations (MOG2D barotropic ocean model) have been used in the processing of the data. A model of the static gravity field named EIGEN-GL04S (GRGS/GFZ), complete to degree and order 150, is taken as the static background model. This model was based on a subset of 73 10-day periods, covering exactly two years (February 24, 2003 to February 23, 2005) in order to avoid the aliasing of seasonal processes into the mean field. It should be mentioned that a constraint towards the mean field is applied for high degree coefficients above degree 30 in order to stabilize them. More details of the CNES GRACE solutions can be found in [Biancale et al., 2007].

6.5.1.5 Deriving monthly variations for all solutions

The solutions of CSR, GFZ and JPL are downloaded from the NASA-JPL PO.DAAC (Physical Oceanography Distributed Active Archive Center), which is responsible for archiving and distributing data relevant to the physical state of the ocean. The solutions cover the period from February 2003 to December 2006. All three processing centers do not provide a solution for June 2003. Additionally, GFZ has no solutions available for December 2003 and January 2004. In order to analyze the variations between gravity field models, we compute an individual mean gravity field over the period of January 2004 to December 2005 separately for solutions of each processing center. For GFZ solutions, we use January 2006 instead of January 2004. The monthly gravity variations used in this section are obtained by subtracting the monthly solutions from the individual mean models.

The CNES GRACE solutions can be downloaded from the CNES web pages. The mean model used for CNES solutions is the EIGEN-GL04S model, with which the monthly variations are derived as suggested by [Biancale et al., 2007].

6.5.2 Spectral assessment

In order to compare the solutions, we compute geoid height variations per degree for each of the models. They are plotted separately for each processing center in figures 6.24 and 6.25. The mean geoid height variations per degree are also shown in these figures. We assume that the low-degree (below degree 20-30) geoid contains most of the gravity signal, while the high-degree (above degree 30-40) part mainly reflects the noise. Between the signal and noise parts, there is a part where signal and noise are mixed. In our study, we model the signal using the following function, similarly to [Slobbe, 2007]:

$$\delta g_l = \frac{x_1}{l^{x_2}}, \tag{6.8}$$

where δg_l is an analytic approximation of geoid height variations per degree; l is degree; x_1 and x_2 are parameters to be estimated. The parameter x_1 indicates the signal amplitude and x_2 indicates the rate of signal amplitude decreasing. The noise part is modeled by a linear function in a logarithmic scale:

$$\log \delta g_l = x_3 + x_4(l - l_0), \tag{6.9}$$

Again, x_3 and x_4 are parameters to be estimated. The parameter x_3 represents the noise amplitude at the starting degree l_0(e.g. degree 30), and x_4 represents the rate of noise amplitude increasing.

From figures 6.24 and 6.25, and table 6.1, we can see that, in terms of geoid heights, the DEOS solutions have a very similar pattern to the JPL solutions, whereas the GFZ solutions and CSR solutions are also rather similar. In addition, the signal part of the DEOS and JPL solutions are very close to the GLDAS hydrological solutions. Notice that the signal amplitude at the starting degree for GFZ and CSR solutions is nearly two times larger than

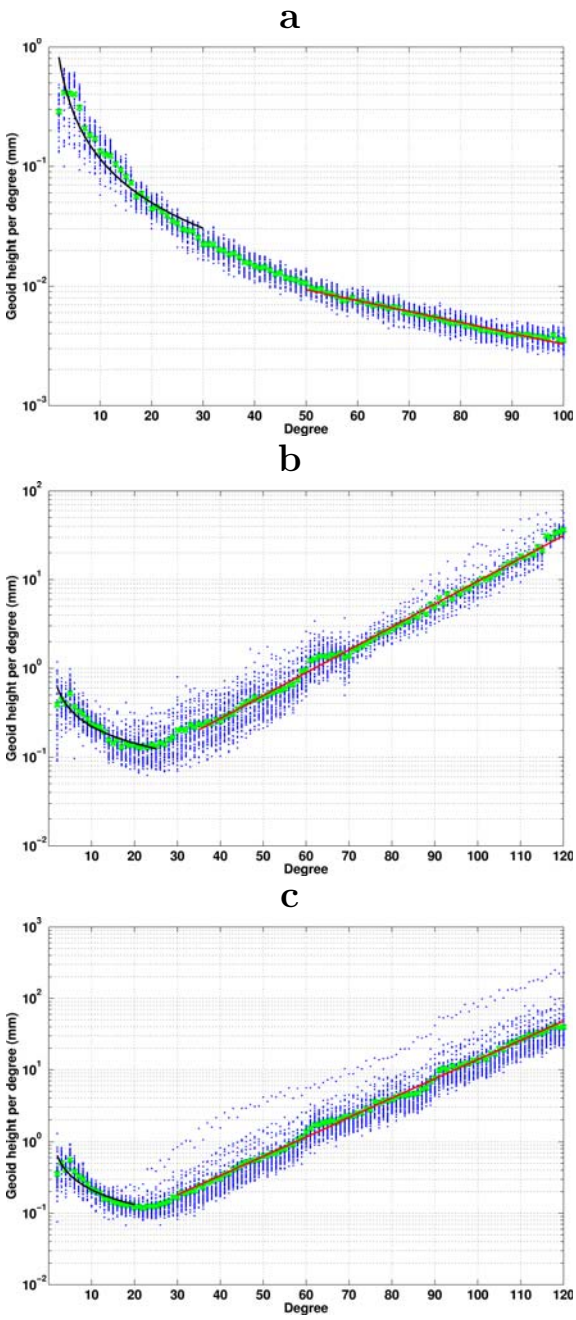

Fig. 6.24. Geoid height differences per degree of monthly solutions with respect to the corresponding mean models. (a) GLDAS hydrological models, (b) DEOS GRACE models, (c) JPL GRACE models. The blue dots represent the degree differences for all monthly solutions. The green crosses are the averages per degree based on all monthly degree differences. The black and red solid lines are the analytical approximation of the signal part and the noise part (except for the GLDAS), respectively

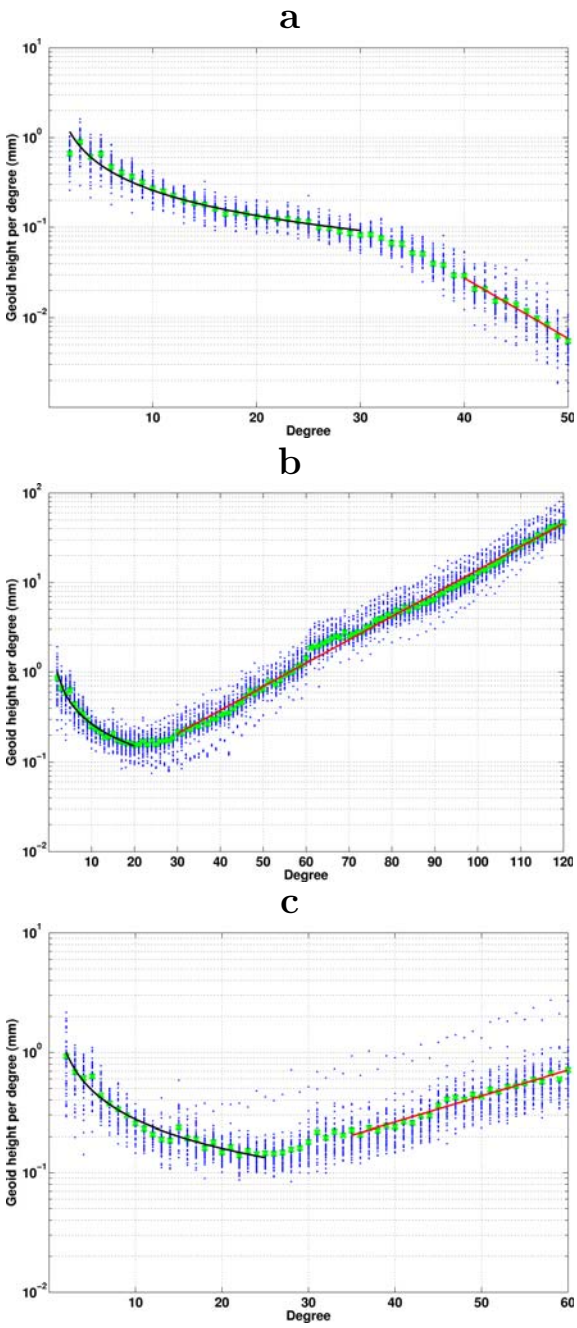

Fig. 6.25. Geoid height differences per degree of monthly solutions with respect to the corresponding mean models. (a) CNES GRACE models, (b) GFZ GRACE models, (c) CSR GRACE models. The blue dots represent the degree differences for all monthly solutions. The green crosses are the averages per degree based on all monthly degree differences. The black and red solid lines are the analytic approximation of the signal part and the noise part, respectively.

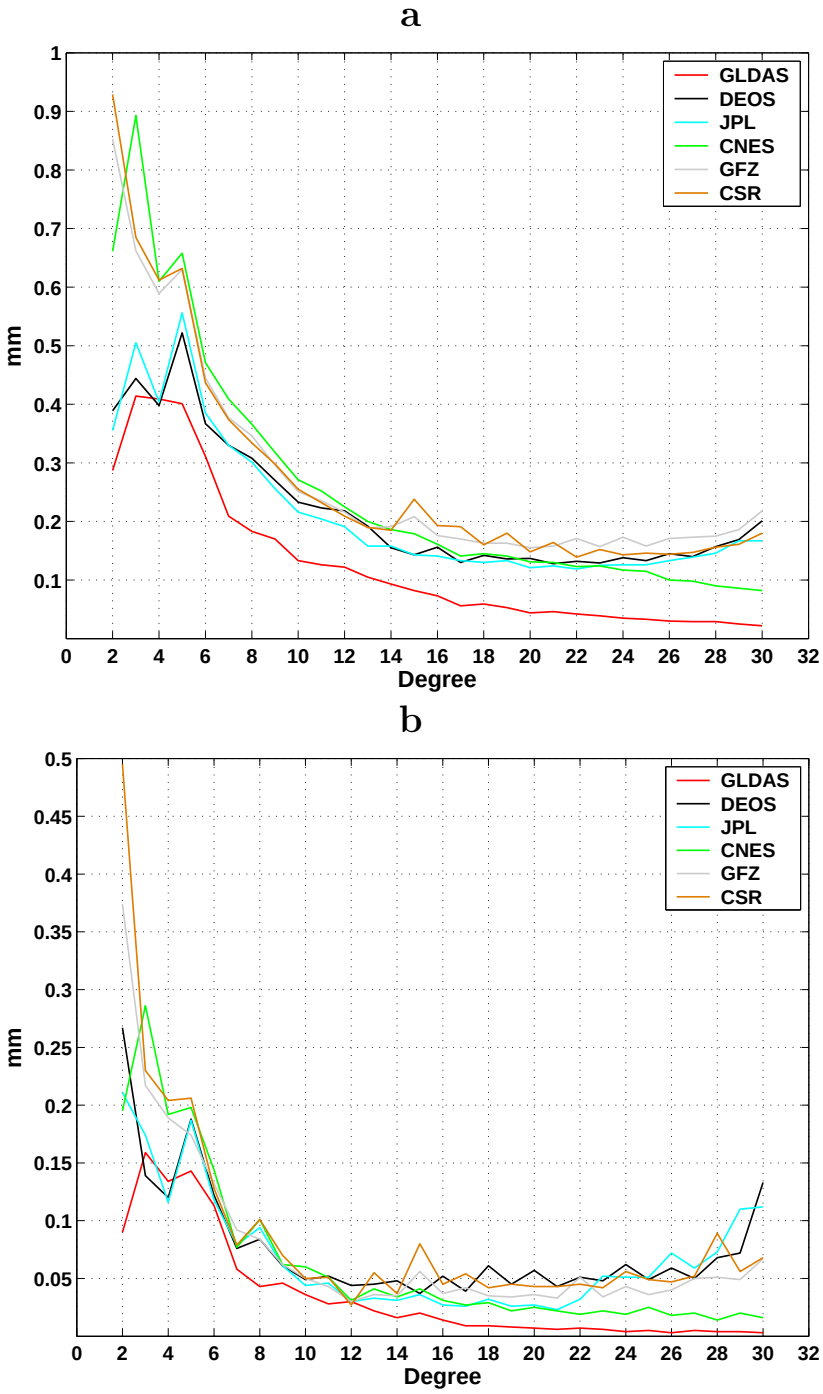

Fig. 6.26. Signal amplitude in terms of geoid height for all GRACE solutions as well as the GLDAS hydrological models. (a) mean of signal amplitude, (b) RMS of signal amplitude.

Table 6.1. Estimated parameters of the analytic functions (see equations (6.8) and (6.9)), which are used to model the corresponding signal and noise in gravity field solutions

Solutions	x_1	x_2	x_3	x_4
GLDAS	1.032	0.865	-1.382	-0.012
DEOS	0.954	0.638	-1.595	+0.026
JPL	1.040	0.688	-1.550	+0.027
CNES	2.050	0.892	+0.856	-0.061
GFZ	1.768	0.820	-1.462	+0.026
CSR	1.809	0.820	-1.365	+0.020

that of the DEOS and JPL solutions. In addition, the signal in the GFZ and CSR solutions decreases faster than that in the DEOS and JPL solutions. Furthermore, it can be seen that the CNES solutions have the largest signal amplitude and the fastest rate of signal decrease. The noise part of the CNES solutions decreases with the degree due to the regularization used in data processing.

In order to further compare these solutions, the mean values per degree up to degree 30 are shown at larger scale in figure 6.26a. Apart from the discrepancies already observed in previous figures and table, the main differences in mean values per degree between the DEOS and JPL and the GFZ and CSR solutions are in the range from degree 2 to 5, whereas the mean values at other degrees are rather close. Notice that the CNES solutions have a smaller mean value at degree 2 than the GFZ and CSR solutions, but the largest value at degree 3 among all solutions. We compute the signal variabilities (i.e. root mean square) of each solution of each processing center with respect to the corresponding mean. The signal variabilities are shown in figure 6.26b in terms of RMS values per degree. The DEOS and JPL solutions display smaller signal variability than the GFZ and CSR solutions at degree 2 to 4. The CSR solutions have the largest signal variability at degree 2 (up to 0.5 mm), while the CNES solutions show the smallest RMS value among all GRACE solution. It should be noticed that degree 2 coefficients in the CNES solutions are jointly estimated from LAGEOS SLR data and GRACE data. The reason for the discrepancies between different types of solutions could be due to the differences in GRACE data processing schemes. This issue certainly needs more investigation in the future.

6.5.3 Water storage changes in large river basins

In order to make a further inter-comparison of different GRACE solutions and the GLDAS hydrological models we derived the water storage changes in sixteen large river basins. The locations and areas of these selected river basins can be seen in figure 6.27 and table 6.2, respectively. These basins are characterized by various sizes and climate environments. To evaluate water storage changes in these basins,

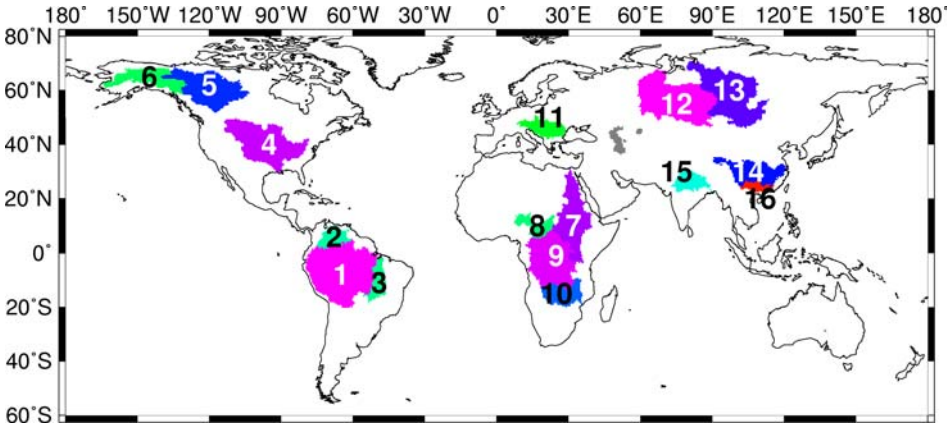

Fig. 6.27. Locations of selected sixteen river basins, their areas are listed in table 6.2

we truncate all available solutions at degree and order 50, and apply P3M8 destriping combined with 400 km Gaussian filtering. Subsequently, equivalent water height variations for the period February 2003 to December 2006 are computed on a global grid ($0.5^\circ \times 0.5^\circ$) as for the DEOS solutions. The mean equivalent water height variations for each river basin at a certain month t is computed for each set of solutions as follows:

$$\bar{q}(t) = \frac{\sum_{j \in S} q(\theta_j, \lambda_j, t) \sin\theta_j}{\sum_{j \in S} \sin\theta_j}, \tag{6.10}$$

where $q(\theta_j, \lambda_j, t)$ are equivalent water height variations computed at grid nodes; θ_j, λ_j are respectively the colatitude and longitude of a grid node. S represents the region associated with the selected river basin. The contour of each basin is based on masks of 0.5° resolution from [Oki and Su, 1998]. We analyze and compare the water storage variations derived from GRACE solutions, as well as from the GLDAS hydrological model, which is taken as an independent reference. It should be mentioned that all the geographical descriptions of the selected river basins are taken from [Wikipedia, 2008].

Two issues are worth mentioning here. Firstly, the GLDAS-derived water storage variations only contain soil moisture and snow water equivalent. For some regions where the ground water storage is rather stable, these two components may be sufficient to represent the total water storage variations. For others, ground water variations may play a significant role in entire storage changes. Then, relatively differences between the GRACE-derived variations and the GLDAS-derived ones may be expected. Secondly, the application of Gaussian filtering to GRACE based models may cause bias in estimation of mean storage changes in a given region [Klees et al., 2007]. In principle, it is possible to make use of a hydrological model

Table 6.2. Area of selected sixteen river basins [Nakaegawa, 2006]

Map Number	River Basin	Area (10^3 km^2)
1	Amazon (South America)	6150
2	Orinoco (South America)	944
3	Tocantins (South America)	900
4	Mississippi (North America)	3248
5	Mackenzie (North America)	1668
6	Yukon (North America)	900
7	Nile (Africa)	3007
8	Chari (Africa)	880
9	Congo (Africa)	3690
10	Zambeze (Africa)	1330
11	Danube (Europe)	817
12	Ob (North Asia)	2978
13	Yenisey (North Asia)	2592
14	Changjiang (South Asia)	1809
15	Ganges (South Asia)	1100
16	Pearl (South Asia)	437

(as *a priori* information) to estimate this bias. This is beyond the scope of the thesis, but can be definitely advised as the subject of further researches. In the current study we eliminated the problem of such a bias by applying the same de-striping and spatial filtering to all models used.

6.5.3.1 South America

In South America, water storage variations are estimated in three selected river basins, Amazon, Orinoco and Tocantins River basins. The river of Amazon is the largest river in the world by volume, accounting for approximately 1/5 of the world's total river flow. The total river flow of Amazon is greater than the sum of flows of the next ten largest rivers. The Amazon basin is also the largest drainage basin in the world, covering the area of some 6150 000 km^2. In an average dry season, 110 000 km^2 of land are water-covered, while in the wet season the flooded area in the Amazon basin rises to 350 000 km^2. The Orinoco is one of the longest rivers in South America reaching the length of 2410 km. Its drainage basin covers 944 000 km^2. In the rainy season the Orinoco could swell to a breadth of 22 km and a depth of 100 m. The rain season of the Orinoco River basin is opposite to that of the Amazon river basin. The Tocantins river is popularly regarded as a tributary of the Amazon, but it is technically a separate system, with a drainage basin of 900 000 km^2. All the three river basins are located in tropical areas.

From figures 6.28 and 6.29, we can see that seasonal water height variation

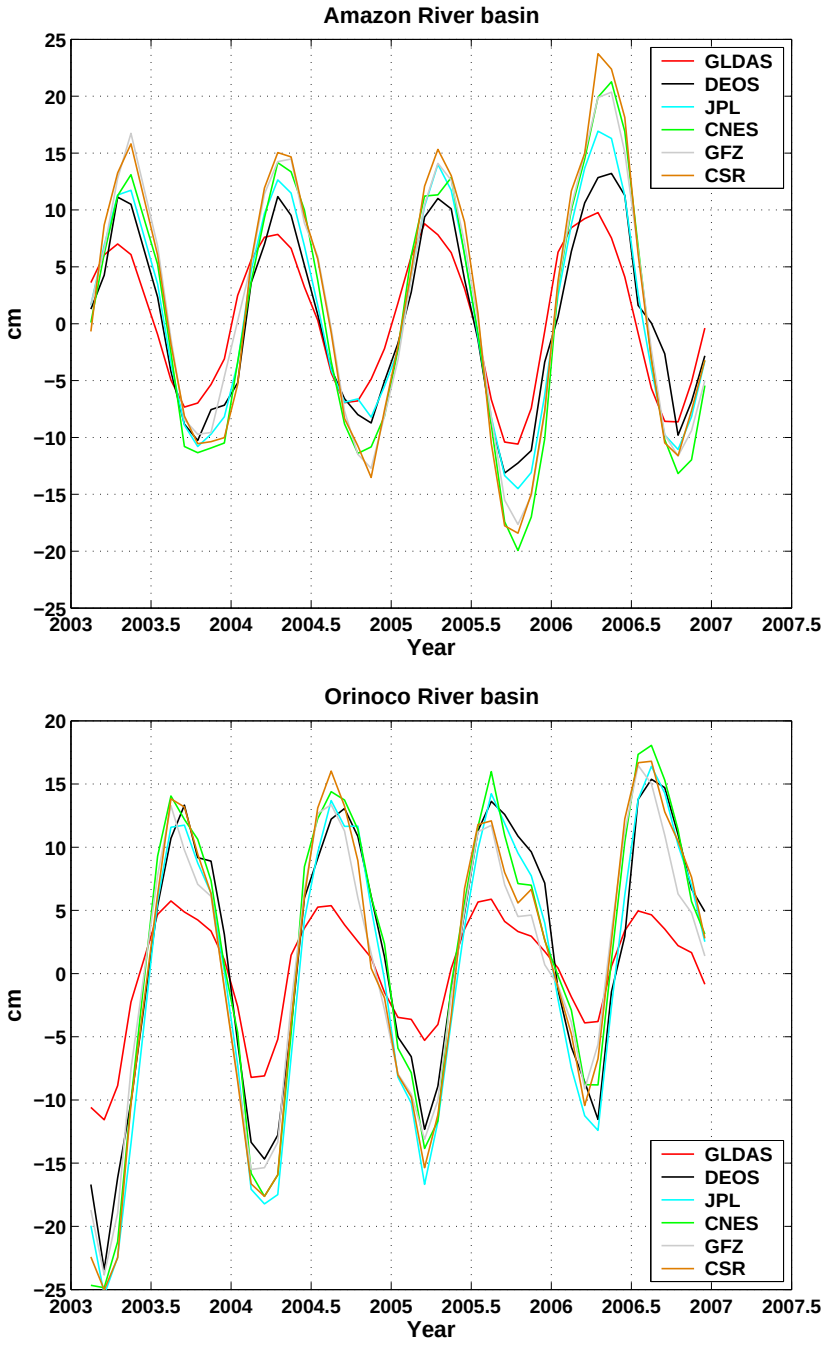

Fig. 6.28. Mean water storage variations over Amazon River basin (top) and Orinoco River basin (bottom) from DEOS, JPL, CNES, GFZ and CSR GRACE solutions as well as from the GLDAS hydrological models. Units are cm of equivalent water heights

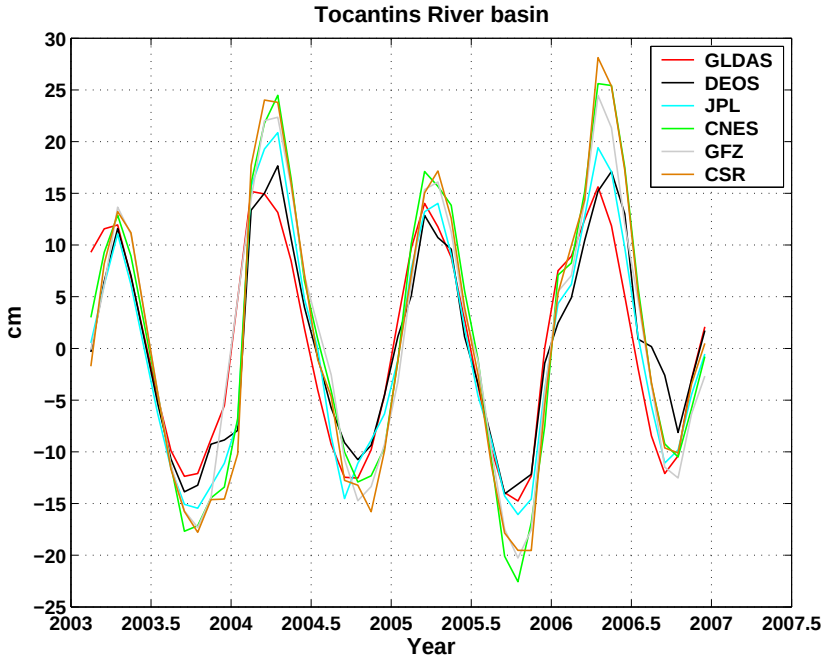

Fig. 6.29. Mean water storage variations over Tocantins River from DEOS, JPL, CNES, GFZ and CSR GRACE solutions as well as from the GLDAS hydrological models. Units are cm of equivalent water heights

derived from different GRACE solutions are in a good agreement with each other for these three river basins. The Amazon and Tocantins River basins have the same seasonal cycle: a positive peak in April, and a negative peak in September-October. The Orinoco River basin has nearly the opposite seasonal variation with respect to the Amazon and Tocantins river basins: negative peak in March, and positive peak in August-September. We observe that the amplitudes of GRACE-derived water variations are larger than computed from the GLDAS hydrological model, particularly at the Orinoco River basin, where the GRACE-derived water variations are more than two times larger. A possible explanation is that the GLDAS solution underestimates the water storage variations because it models mostly the soil moisture in the region. Thus, the stock variations associated with ground water and open water bodies are ignored.

In order to see the differences of these solutions, we compute the RMS values of the differences between the individual GRACE monthly solutions and (i) the corresponding monthly mean of all GRACE solutions, (ii) GLDAS monthly values and JPL monthly values. The reason to choose the JPL solutions as a reference is that the JPL solutions were validated as the best GRACE solutions on the basis of a comparison with satellite altimetry data and a numerical ocean model [Dobslaw and Thomas, 2007]. From the RMS values shown in table 6.3, we find that the DEOS solutions differ from the mean of all GRACE solutions more than

Table 6.3. Analysis of mean water storage variations in selected river basins in South America. Values shown here are standard deviations of the differences between individual GRACE monthly solutions and (i) corresponding mean values of all GRACE solutions, (ii) mean monthly values from the GLDAS hydrological models, and (iii) JPL GRACE monthly solutions. Units are cm of equivalent water heights

River Basin	Reference	DEOS	JPL	CNES	GFZ	CSR
Amazon	mean	2.57	1.32	1.43	1.13	1.68
	GLDAS	3.34	3.95	5.94	5.64	6.32
	JPL	2.04	--	2.50	2.27	2.77
Orinoco	mean	1.94	1.35	1.25	1.88	1.41
	GLDAS	6.22	7.41	7.40	5.90	7.26
	JPL	1.81	--	1.82	3.16	2.33
Tocantins	mean	2.97	1.70	1.85	1.39	1.95
	GLDAS	3.99	3.66	5.74	4.94	6.13
	JPL	2.58	--	3.28	2.66	3.36

Table 6.4. Fit of a yearly sinusoidal through the time series from February 2003 till December 2006 for Amazon, Orinoco and Tocantins. $\hat{\sigma}$ is the a posteriori standard deviation and $R^2 = 1 - \frac{\hat{\sigma}^2}{\sigma^2}$, where σ^2 is the signal variance around the 4-year mean

River Basin	Models	Amplitude [cm]	Phase [months]	$\hat{\sigma}$	R^2
Amazon	GLDAS	8.5±0.6	-0.07±0.13	1.3	0.96
	DEOS	10.6±1.0	-0.72±0.15	2.2	0.93
	JPL	12.5±1.5	-0.69±0.15	2.3	0.94
	CNES	14.8±1.3	-0.85±0.18	3.2	0.92
	GFZ	14.7±1.5	-0.88±0.18	3.0	0.93
	CSR	15.3±1.5	-0.85±0.18	3.5	0.91
Orinoco	GLDAS	5.6±0.7	-4.96±0.31	2.1	0.82
	DEOS	13.1±1.1	-5.43±0.17	2.8	0.93
	JPL	14.7±1.5	-5.35±0.17	3.0	0.94
	CNES	14.8±1.6	-5.18±0.22	3.9	0.90
	GFZ	12.6±1.1	-4.86±0.24	3.6	0.89
	CSR	14.1±1.5	-5.06±0.22	3.8	0.90
Tocantins	GLDAS	13.6±1.8	0.12±0.11	1.8	0.97
	DEOS	12.5±1.4	-0.37±0.21	3.4	0.88
	JPL	14.8±1.4	-0.30±0.19	3.4	0.93
	CNES	18.0±1.7	-0.49±0.19	4.1	0.90
	GFZ	16.9±1.6	-0.49±0.20	3.8	0.92
	CSR	17.4±1.9	-0.51±0.20	4.5	0.90

other solutions do (for Orinoco though the RMS of the DEOS solutions is very close to that of GFZ solutions). The reason for this is that the CNES, CSR and GFZ solutions have, in most cases, larger amplitudes, which dominate the mean value. On the other hand, the DEOS solutions are, in general, closer to the JPL solutions and the GLDAS hydrological model. This can be further seen from table 6.4, which shows parameters of a yearly sinusoidal computed through the time series of all GRACE solutions and hydrological models for these river basins. The list of presented parameters includes the amplitudes and phases as well as the corresponding posteriori standard deviations $\hat{\sigma}$ and the values of parameter R^2 defined as $R^2 = 1 - \frac{\hat{\sigma}^2}{\sigma^2}$, where σ^2 is the signal variance around the 4-year mean. The value of R^2 indicates how significant is the one-year cycle signal in the data records. Obviously, the yearly cycle signal dominates in the water mass variations for all three river basins. In the meanwhile, it is found that the estimated parameters of DEOS solutions shown in table 6.4 are very close to others except for the amplitudes.

6.5.3.2 North America

In North America, we selected the following three river basins: Mississippi, Mackenzie and Yukon. The Mississippi River Basin is the largest watershed in North America, draining 41% of the continental United States and discharging into the Northern Gulf of Mexico at an average rate of 17 330 m^3/s. The Mississippi flows 3763 km from the Lake of Itasca in northern Minnesota to its delta in southern Louisiana. The Mackenzie River is the longest river in Canada reaching the length of 1738 km. It originates in Great Slave Lake, in the Northwest Territories, and flows north into the Arctic Ocean. The Mackenzie and its tributaries drain 1805 200 km^2. Its mean discharge is 9700 m^3/s. The Yukon River is a major watercourse of northwestern North America. The river is 3700 km long and empties into the Bering Sea at the Yukon-Kuskokwim Delta. The average flow is 6430 m^3/s. The total drainage area is 832 700 km^2, of which 323 800 km^2 is in Canada.

The mean water storage variations in Mississippi and Mackenzie River basins are shown in figure 6.30 and in Yukon River basin in figure 6.31. The RMS values of all GRACE solutions are listed in table 6.5. The fit of the yearly sinusoidal is shown in table 6.6.

The three North American river basins show similar seasonal cycle: a positive peak around April, and a negative peak around October. The differences of phases between the GRACE solutions are less than 0.3 month for the Mackenzie and Yukon River basins, but almost 0.5 month for the Mississippi River Basin. Notice that the GLDAS hydrological models show significant phase differences with GRACE-based solutions, particularly in Mackenzie and Yukon River basins.

Compared to the tropical river basins (Amazon, Orinoco and Tocantins), the water variations in North America are much smaller with the largest seasonal

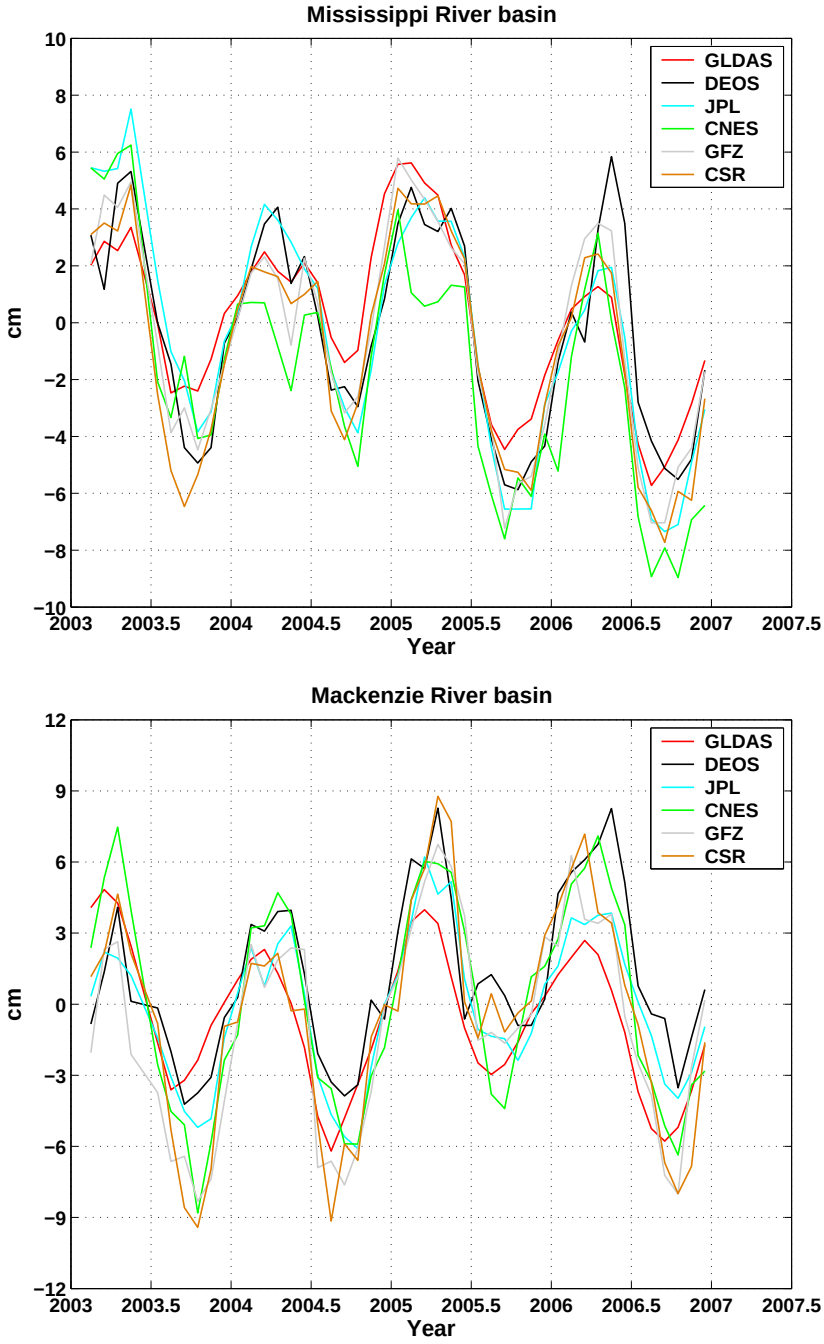

Fig. 6.30. Mean water storage variations over Mississippi River basin (top) and Mackenzie River basin (bottom) from DEOS, JPL, CNES, GFZ and CSR GRACE solutions as well as from the GLDAS hydrological models. Units are cm of equivalent water heights

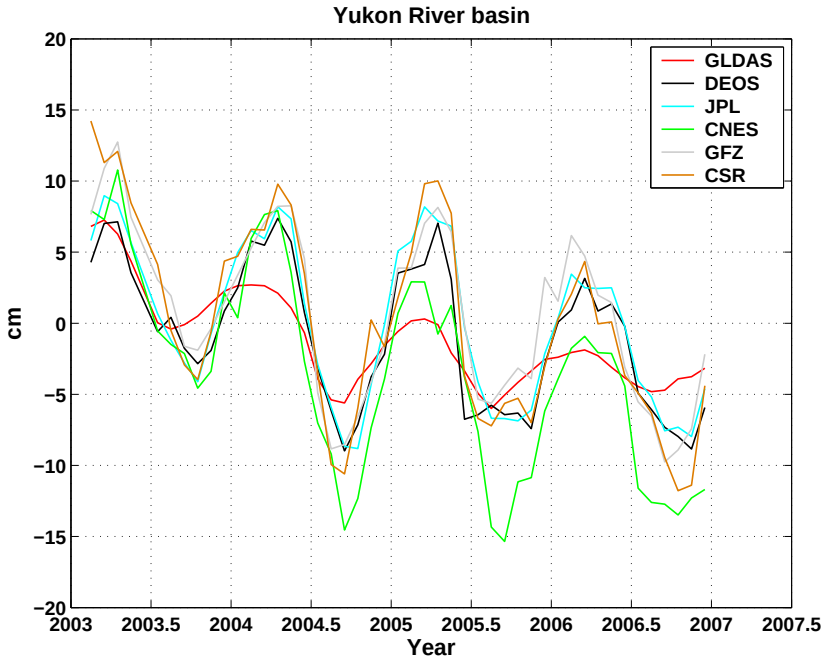

Fig. 6.31. Mean water storage variations over Yukon from DEOS, JPL, CNES, GFZ and CSR GRACE solutions as well as from the GLDAS hydrological models. Units are cm of equivalent water heights

Table 6.5. Analysis of mean water storage variations in selected river basins in North America. Values shown here are standard deviations of the differences between individual GRACE monthly solutions and (i) corresponding mean values of all GRACE solutions, (ii) mean monthly values from the GLDAS hydrological models, and (iii) JPL GRACE monthly solutions. Units are cm of equivalent water heights

River Basin	Reference	DEOS	JPL	CNES	GFZ	CSR
Mississippi	mean	1.22	0.90	1.33	0.78	0.94
	GLDAS	2.22	2.39	2.71	2.31	2.92
	JPL	1.57	--	1.59	1.51	1.57
Mackenzie	mean	1.38	1.01	1.38	1.23	1.39
	GLDAS	2.55	1.99	2.51	2.80	2.80
	JPL	1.40	--	1.90	1.82	2.14
Yukon	mean	1.50	1.20	2.00	1.41	1.69
	GLDAS	3.08	3.57	4.39	3.76	4.42
	JPL	1.50	--	2.69	1.99	2.53

Table 6.6. Fit of a yearly sinusoidal through the time series from February 2003 till December 2006 for Mississippi, Mackenzie and Yukon. $\hat{\sigma}$ is the a posteriori standard deviation and $R^2 = 1 - \frac{\hat{\sigma}^2}{\sigma^2}$, where σ^2 is the signal variance around the 4-year mean

River Basin	Models	Amplitude [cm]	Phase [months]	$\hat{\sigma}$	R^2
Mississippi	GLDAS	2.9±0.7	0.51±0.49	1.7	0.68
	DEOS	4.2±0.7	-0.34±0.32	1.6	0.80
	JPL	4.3±0.5	-0.18±0.24	1.2	0.91
	CNES	3.6±0.8	0.10±0.45	2.0	0.77
	GFZ	4.1±0.8	0.23±0.38	1.9	0.77
	CSR	4.3±0.7	0.18±0.34	1.8	0.79
Mackenzie	GLDAS	3.7±0.4	0.79±0.22	1.1	0.89
	DEOS	4.2±0.6	-0.06±0.29	1.5	0.82
	JPL	4.1±0.5	-0.01±0.22	1.1	0.88
	CNES	5.8±0.6	-0.04±0.22	1.5	0.89
	GFZ	5.2±1.0	0.23±0.36	2.2	0.77
	CSR	5.5±1.0	0.17±0.36	2.5	0.73
Yukon	GLDAS	2.5±0.5	1.03±0.43	1.3	0.85
	DEOS	5.5±0.8	0.23±0.27	1.8	0.88
	JPL	6.8±0.8	0.19±0.19	1.5	0.93
	CNES	7.1±0.8	0.30±0.23	2.0	0.92
	GFZ	6.5±0.9	0.36±0.28	2.2	0.87
	CSR	7.2±1.0	0.29±0.27	2.4	0.89

variations being less than 20 cm (peak-to-peak) in terms of mean equivalent water height. The largest amplitude is 7.2 cm observed by the CSR solutions for the Yukon River basin (see table 6.6). The Mackenzie river basin shows a secular water accumulation, whereas the Yukon river basin, conversely, is characterized by a secular water loss, probably due to glacial melting [Chen et al., 2006a]. We find that the amplitudes of GLDAS-derived signal are still smaller than those derived from the GRACE solutions, particularly for the Yukon river basin. The DEOS solutions for these three river basins are not significantly smaller than the other GRACE solutions. Compared to the mean of all GRACE solutions, the DEOS solutions are not the most outstanding ones; the CNES solutions show the largest discrepancies in two cases out of three. Compared with the GLDAS model, the DEOS solutions are closer than the other GRACE solutions over the Mississippi and Yukon River basins. In the Mackenzie River basin, the JPL solutions are the closest to the GLDAS model. When compared with the JPL solutions, the DEOS solutions are in the closest agreement in the Mackenzie and Yukon river basins, while in the Mississippi River basin, all the GRACE solutions are almost equally close.

6.5.3.3 Africa

In Africa, we consider four river basins: Nile, Chari, Congo and Zambezi. The Nile River is the major north-flowing river in Africa and the second longest river in the world. The drainage basin of the Nile River covers more than 3 million km^2, about 10% of the area of Africa. Most of the Nile's water comes from the Blue Nile, one of its two major tributaries. The northern section of the Nile river flows almost entirely through desert, from Sudan into Egypt. The Nile ends in a large delta and empties into the Mediterranean Sea. The Chari or Shari River is a 949 km-long river in central Africa. It flows from the Central African Republic through Chad into the Chad Lake, following the Cameroon border from N'Djamena. The area of river watershed covers 880 000 km^2. The Congo River is the second longest river in Africa (next to the Nile) with an overall length of 4700 km. The river and its tributaries flow through the second largest rain forest area in the world (second only to the Amazon Rainforest). The river also has the second-largest flow in the world behind the Amazon. Because large sections of the river basin lie above and below the equator, its flow is stable. The Congo river has the second-largest watershed in the world (about 3690 000 km^2), which is slightly larger than that of the Mississippi river, and much smaller than that of Amazon river. The Zambezi River is the fourth longest river in Africa, and the largest one flowing into the Indian Ocean from Africa. The area of its basin is 1,330,000 km^2, nearly half that of the Nile. The 2574 km-long river has its source in Zambia and flows through Angola, along the borders of Namibia, Botswana, Zambia, and Zimbabwe, to Mozambique, where it empties into the Indian Ocean.

The water storage variations in the Nile and Chari River basins are shown in figure 6.32 and variations in the Congo and Zambezi river basins are shown in figure 6.33. The RMS values of all GRACE solutions are listed in table 6.7. The fit to the yearly sinusoidal is shown in table 6.8.

Firstly, let us look at the Nile and Chari River basins. From figure 6.32, we can see that the two river basins have the same seasonal cycle: positive peak at around October and negative peak at around April. The absolute variation in the Nile River basin is around 15 cm and around 25 cm in the Chari River basin. Additionally, it is found that in the Nile River basin the JPL and DEOS solutions differ significantly from the other GRACE solutions in the Fall season of 2004 and 2005. Except for the Fall of 2004 and 2005, all GRACE solutions are in a good agreement with each other in these two river basins. From table 6.8, the GLDAS models show more than half month phase difference with the GRACE solutions. The estimated amplitude of seasonal variations is about 5.2 cm in Nile River basin and 10.5 cm in Chari River basin (mean for all kinds of solutions). The DEOS estimates of amplitude and phase of seasonal signal are very close with other GRACE solutions. Secondly, let us analyze the Congo river. Although it has the largest watershed, the spatially averaged water storage variations there do not seem to be larger than in the other selected African river basins. A negative long-term trend and seasonal variation in the Congo River basin are clearly observed by all

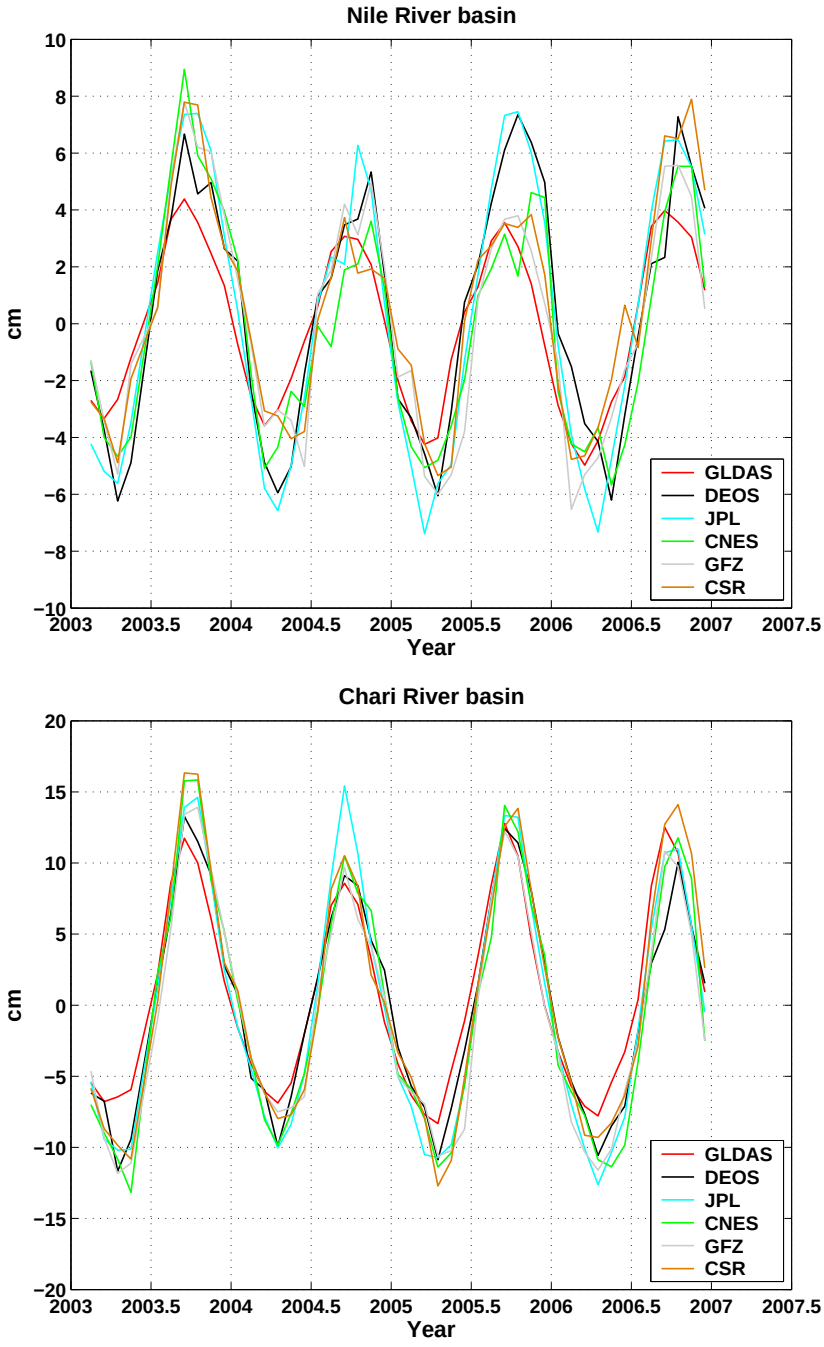

Fig. 6.32. Mean water storage variations over Nile River basin (top) and Chari river basin (bottom) from DEOS, JPL, CNES, GFZ and CSR GRACE solutions as well as from the GLDAS hydrological models. Units are cm of equivalent water heights

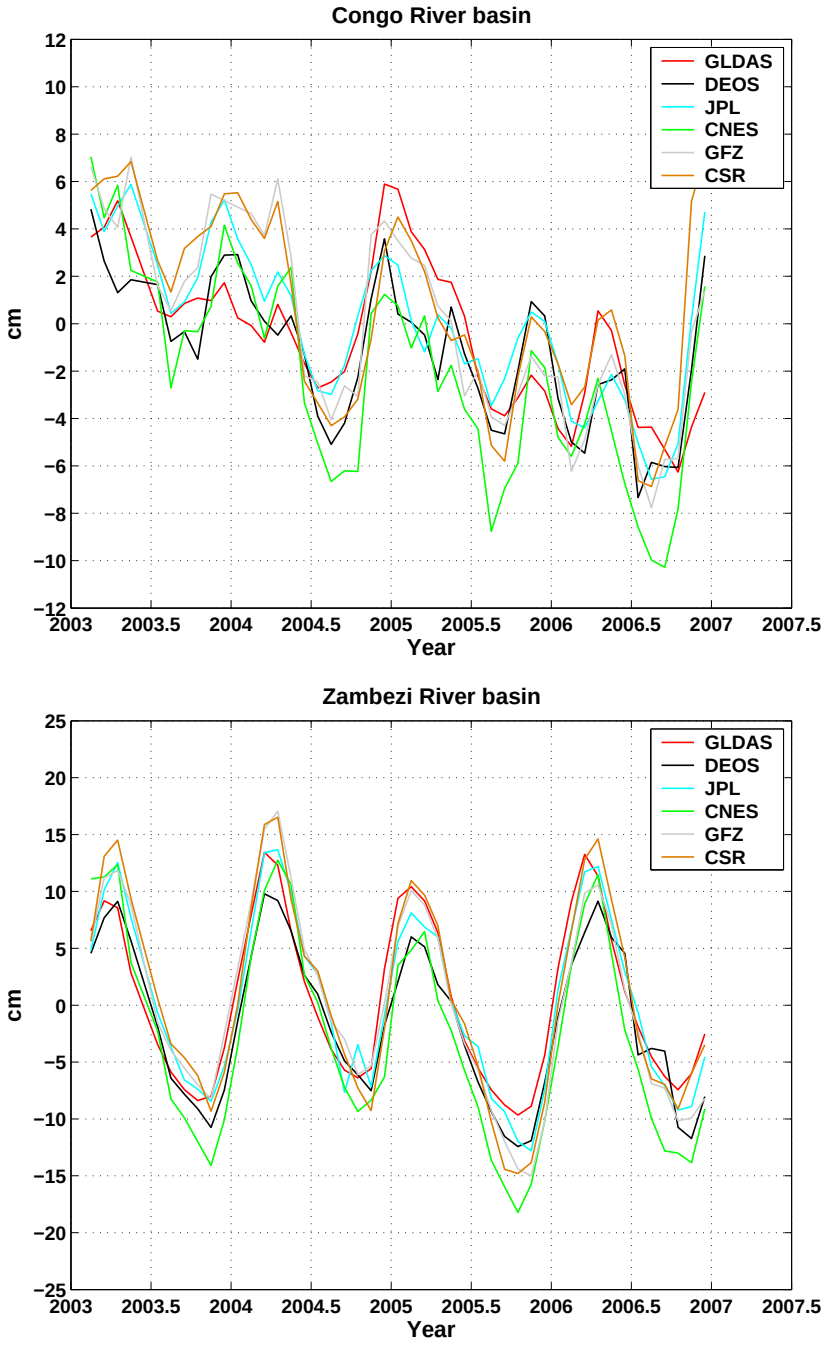

Fig. 6.33. Mean water storage variations over Congo River basin (top) and Zambezi river basin (bottom) from DEOS, JPL, CNES, GFZ and CSR GRACE solutions as well as from the GLDAS hydrological models. Units are cm of equivalent water heights

Table 6.7. Analysis of mean water storage variations in selected river basins in Africa. Values shown here are standard deviations of the differences between individual GRACE monthly solutions and (i) corresponding mean values of all GRACE solutions, (ii) mean monthly values from the GLDAS hydrological models, and (iii) JPL GRACE monthly solutions. Units are cm of equivalent water heights

River Basin	Reference	DEOS	JPL	CNES	GFZ	CSR
Nile	mean	1.20	1.26	1.02	1.11	1.13
	GLDAS	2.28	2.43	2.04	1.86	1.84
	JPL	1.55	--	1.99	2.00	2.04
Chari	mean	1.41	1.16	1.12	1.12	1.20
	GLDAS	2.34	2.66	3.14	2.46	2.81
	JPL	2.08	--	1.81	1.78	1.80
Congo	mean	1.22	0.97	1.18	1.14	1.25
	GLDAS	2.22	2.39	2.71	2.31	2.92
	JPL	1.29	--	1.85	1.67	1.89
Zambezi	mean	1.76	1.07	1.69	1.20	1.33
	GLDAS	2.60	2.29	3.46	3.03	3.05
	JPL	1.81	--	2.42	1.84	1.89

GRACE measurements. A seasonal positive peak is not observed during March 2006, instead a negative peak is present. The R^2 values of the Congo River basin display that the seasonal signal is below 0.70 on average, less than for the other selected river basins in the region. The DEOS and (particular) JPL solutions show more than half month phase difference with other GRACE solutions. As far as the Zambezi River basin is concerned, a regular pattern of seasonal variations can be seen from all the GRACE solutions as well as from the GLDAS models. However, the amplitude of variations derived from different GRACE solutions does differ, with the DEOS solutions showing the smallest positive peaks.

Analysis of the RMS values listed in table 6.7 tells us that the DEOS solutions are comparable with the others. In the Nile River basin, DEOS solutions show the second largest RMS values (after JPL solutions) with respect to the mean of all the GRACE solutions and the GLDAS models. In the Chari and Congo River basins, the DEOS solutions show the largest difference from the mean of GRACE solutions, but are the closest to the GLDAS models. In the Zambezi River basin, the DEOS solutions show the largest deviations from the mean of GRACE solutions, but are the second closest models to GLDAS (after JPL solutions).

6.5.3.4 Europe and North Asia

In Europe and North Asia, we analyzed water variations in three river basins: Danube, Ob and Yenisey.

Table 6.8. Fit of a yearly sinusoidal through the time series from February 2003 till December 2006 for Nile, Chari, Congo and Zambezi. $\hat{\sigma}$ is the a posteriori standard deviation and $R^2 = 1 - \frac{\hat{\sigma}^2}{\sigma^2}$, where σ^2 is the signal variance around the 4-year mean

River Basin	Models	Amplitude [cm]	Phase [months]	$\hat{\sigma}$	R^2
Nile	GLDAS	3.9±0.3	6.30±0.14	0.6	0.95
	DEOS	5.5±0.6	5.53±0.21	1.4	0.90
	JPL	6.5±0.5	5.80±0.14	1.1	0.95
	CNES	5.0±0.7	5.55±0.26	1.6	0.84
	GFZ	5.2±0.6	5.70±0.22	1.3	0.89
	CSR	4.8±0.7	5.70±0.45	1.7	0.82
Chari	GLDAS	8.9±0.8	6.19±0.20	1.6	0.94
	DEOS	9.8±0.7	5.75±0.14	1.8	0.95
	JPL	11.6±0.8	5.87±0.14	2.0	0.95
	CNES	11.3±1.1	5.67±0.18	2.5	0.92
	GFZ	10.4±1.0	5.76±0.20	2.3	0.92
	CSR	11.2±1.1	5.71±0.18	2.6	0.91
Congo	GLDAS	1.6±0.9	1.01±1.03	2.1	0.59
	DEOS	2.0±0.8	2.23±0.80	2.0	0.59
	JPL	2.0±0.8	2.60±0.73	1.9	0.69
	CNES	3.2±0.9	1.69±0.55	2.2	0.76
	GFZ	2.5±1.0	1.87±0.70	2.2	0.72
	CSR	3.1±1.1	1.84±0.69	2.6	0.60
Zambezi	GLDAS	9.3±1.1	0.25±0.22	2.5	0.88
	DEOS	8.4±1.1	-0.33±0.27	2.8	0.85
	JPL	9.5±1.5	-0.25±0.25	2.9	0.87
	CNES	10.8±1.5	-0.20±0.27	3.5	0.85
	GFZ	9.7±1.5	-0.17±0.30	3.5	0.85
	CSR	10.7±1.5	-0.21±0.27	3.5	0.85

The Danube is the longest river in the European Union, originating in the Black Forest in Germany, flowing eastwards for a distance of some 2850 km, and passing through several Central and Eastern European capitals (Vienna of Austria, Bratislava of Slovakia, Budapest of Hungary and Belgrade of Serbia), before emptying into the Black Sea via the Danube Delta in Romania and Ukraine. Crossing through ten countries and draining some 817 000 km^2 and the territory of 18 countries, the Danube is the most international river in the world and the most important non-oceanic body of water in Europe. The Ob River originates from the Altai Mountains in central Asia, flowing across western Siberia northwestward. It goes through the Gulf of Ob into the Kara Sea of the Arctic Ocean. The river is about 3650 km long from the head of the Katun River or about 5410 km long from the head of the Irtysh River. Its middle course

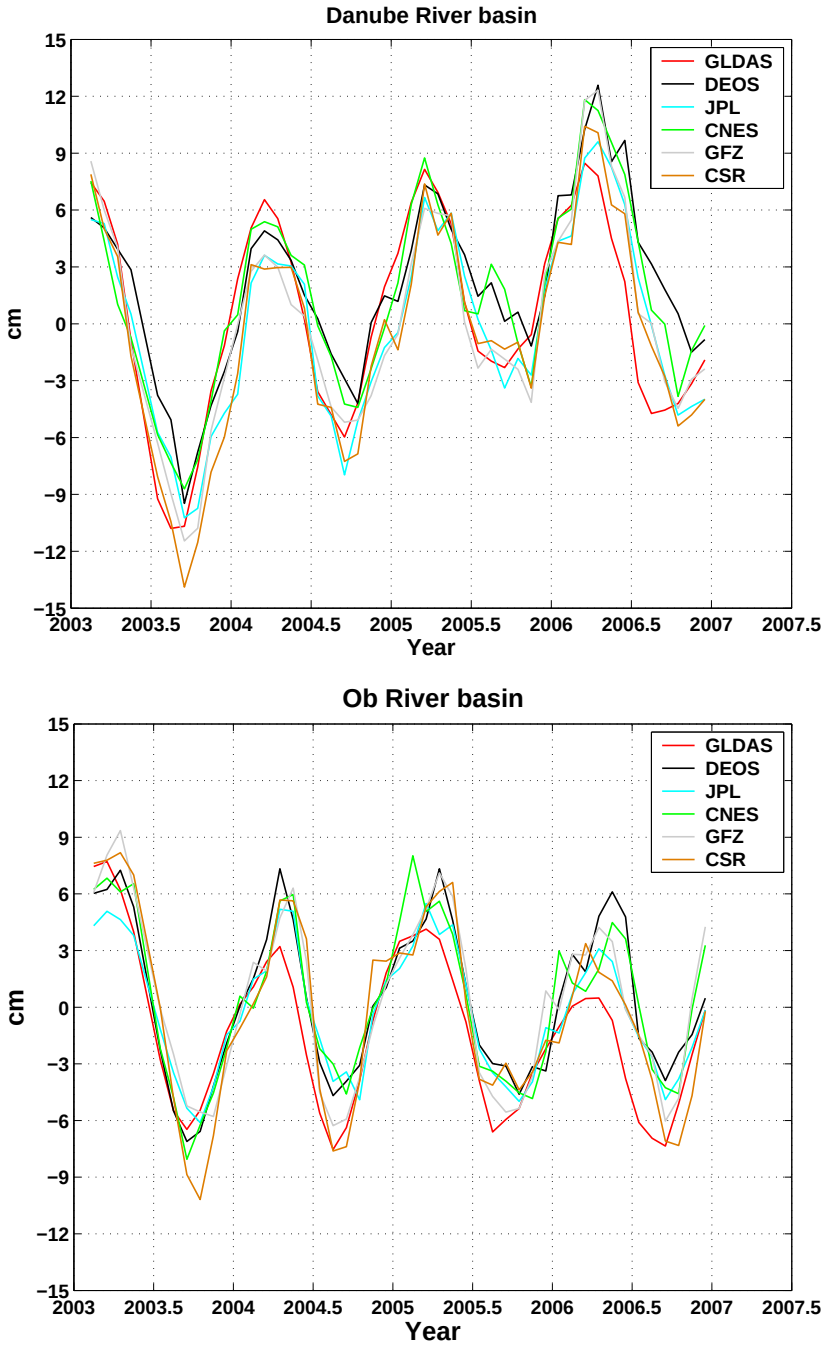

Fig. 6.34. Mean water storage variations over Danube River basin (top) and Ob river basin (bottom) from DEOS, JPL, CNES, GFZ and CSR GRACE solutions as well as from the GLDAS hydrological models. Units are cm of equivalent water heights

Table 6.9. Analysis of mean water storage variations in selected river basins in Europe and North Asia. Values shown here are standard deviations of the differences between individual GRACE monthly solutions and (i) corresponding mean values of all GRACE solutions, (ii) mean monthly values from the GLDAS hydrological models, and (iii) JPL GRACE monthly solutions. Units are cm of equivalent water heights

River Basin	Reference	DEOS	JPL	CNES	GFZ	CSR
Danube	mean	1.08	0.88	1.12	0.92	0.96
	GLDAS	2.87	2.52	2.51	1.35	2.28
	JPL	1.43	--	1.72	1.42	1.32
Ob	mean	1.01	1.02	1.14	1.13	1.39
	GLDAS	2.16	1.87	2.13	1.89	2.27
	JPL	1.44	--	1.67	1.67	2.03
Yenisey	mean	1.23	0.90	1.30	1.51	1.27
	GLDAS	2.48	1.88	2.13	2.53	2.34
	JPL	1.42	--	1.66	2.10	1.65

Table 6.10. Fit of a yearly sinusoidal through the time series from February 2003 till December 2006 for Danube, Ob and Yenisey. $\hat{\sigma}$ is the a posteriori standard deviation and $R^2 = 1 - \frac{\hat{\sigma}^2}{\sigma^2}$, where σ^2 is the signal variance around the 4-year mean

River Basin	Models	Amplitude [cm]	Phase [months]	$\hat{\sigma}$	R^2
Danube	GLDAS	6.9±0.8	0.62±0.21	1.9	0.88
	DEOS	5.4±0.8	-0.22±0.28	1.8	0.85
	JPL	6.3±0.8	0.02±0.25	1.9	0.87
	CNES	5.8±0.9	0.00±0.31	2.2	0.82
	GFZ	6.7±1.0	0.06±0.31	2.3	0.83
	CSR	6.8±1.1	-0.01±0.31	2.6	0.81
Ob	GLDAS	5.0±0.7	0.78±0.26	1.6	0.86
	DEOS	5.2±0.7	-0.01±0.27	1.7	0.84
	JPL	4.3±0.6	0.01±0.24	1.3	0.87
	CNES	5.0±0.9	0.17±0.36	2.2	0.75
	GFZ	5.5±1.0	0.23±0.32	2.0	0.81
	CSR	5.7±1.0	0.03±0.36	2.6	0.75
Yenisey	GLDAS	3.6±0.5	1.05±0.23	1.0	0.89
	DEOS	5.0±0.7	0.15±0.28	1.7	0.82
	JPL	4.4±0.5	0.26±0.20	1.1	0.89
	CNES	4.0±0.7	0.44±0.42	1.7	0.75
	GFZ	4.1±0.9	0.56±0.42	2.1	0.70
	CSR	4.4±0.9	0.29±0.37	2.0	0.72

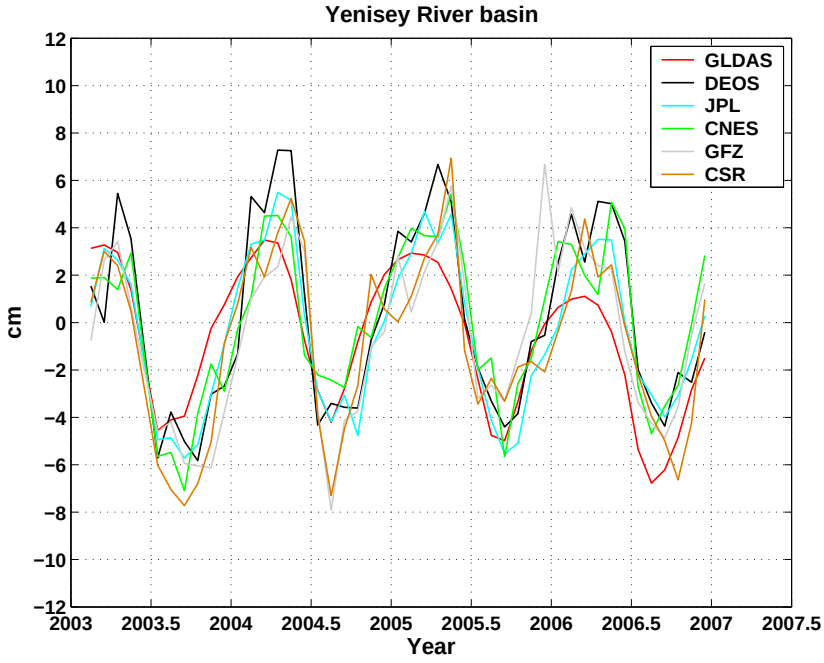

Fig. 6.35. Mean water storage variations over Yenisey River basin from DEOS, JPL, CNES, GFZ and CSR GRACE solutions as well as from the GLDAS hydrological models. Units are cm of equivalent water heights

is through taiga, swampy coniferous forest with expanses of marshland. In the north it crosses vast stretches of icy, treeless tundra. The Ob River basin is ice-bound at southern Barnaul from early November to near the end of April, and at northern Salekhard, 160 km above its mouth, from the end of October to the beginning of June. The Ob is an important source of hydroelectric power and one of Siberia's major transportation routes during the six months of the year when it is not frozen. The Yenisey River is the fifth longest river in the world (5539 km long), rising from Darkhad Valley in Mongolia. It follows a northerly course to the Yenisei Gulf in the Kara Sea with an average discharge of 19 600 m^3/s. The draining area is about 2580 000 km^2, a large part of central Siberia, and most of this area is at a height of between 487 m to 700 m above sea level. Most of the Yenisey River is icebound for more than half of the year.

The water storage variations in the Danube and Ob River basins are shown in figure 6.34 and in the Yenisey River basin in figure 6.35. The RMS values of all GRACE solutions are listed in table 6.9. The fit of the yearly sinusoidal is shown in table 6.10.

The linear trends and seasonal variations observed by all the GRACE solutions seem to be consistent with each other. These three river basins have almost the same seasonal cycle: a positive peak around March-April and a negative peak

around September-October. The absolute variation of the seasonal variations are less than 20 cm. The Danube River basin has a secular water mass accumulation during the period between 2003 and 2006, while the Ob River basin shows an obvious mass decline in this period as previously observed in section 6.3. It can also be noticed that a rapid loss of mass takes place in Ob and Yenisey river basins in April-June. This can be explained by intensive melting of snow accumulated during the Fall and Winter.

From the RMS values listed in table 6.9, we can see that the DEOS solutions are relatively close to the mean of all GRACE solutions (particularly in the Ob River basin). Referring to the GLDAS models, the DEOS solutions show the largest discrepancy in the Danube River basin, but not in the Ob and Yenisey River basins. Noteworthy, all the GRACE solutions show approximately the same agreement with GLDAS models except for GFZ, which is particularly close to GLDAS in the Danube river basin, and JPL, which is rather close to GLDAS in the Yenisey river basin.

6.5.3.5 South-East Asia

In Asia, we analyze water storage in three river basins: Changjiang, Pearl and Ganges.

The Changjiang (or Yangtze River) is the longest river in Asia and the third longest river in the world, after Amazon and Nile. The river is about 6300 km long and spreading over 1800 000 km^2 of basin area. It originates in Qinghai Province, flowing eastwards into the East China Sea at Shanghai. The river is a major transportation waterway for China, connecting the interior with the coast. Flooding along the river has been a major problem. The rainy season is May and June in the southern part of river basin, and July and August in the northern part. The huge river system receives water from both southern and northern flanks, which causes its flood season to extend from May to August. Meanwhile, a relatively dense population and rich cities along the river make the floods more deadly and costly. The Pearl River (or Zhujiang) is the China's third longest river (2200 km, after the Changjiang and the Yellow River), and the second largest by volume (after the Yangtze). Located in the south, it flows into the South China Sea between Hong Kong and Macau. Its lower reach forms the Pearl River Delta. The river flows through the majority of Guangdong, Guangxi, Yunnan, and Guizhou Provinces, and parts of Hunan and Jiangxi, forming one of the leading economic regions and a major manufacturing center of mainland China. The Ganges is a major river in the Indian subcontinent, which is about 2510 km long. It starts from the Gangotri Glacier in the Indian state of Uttarakhand, in the central Himalayas, flows east through the plains of northern India into Bangladesh, and drains into the Bay of Bengal through its vast delta in the Sunderbans. The Ganges and its tributaries drain an area about one million square kilometers and a fertile basin that supports one of the world's highest-density human populations.

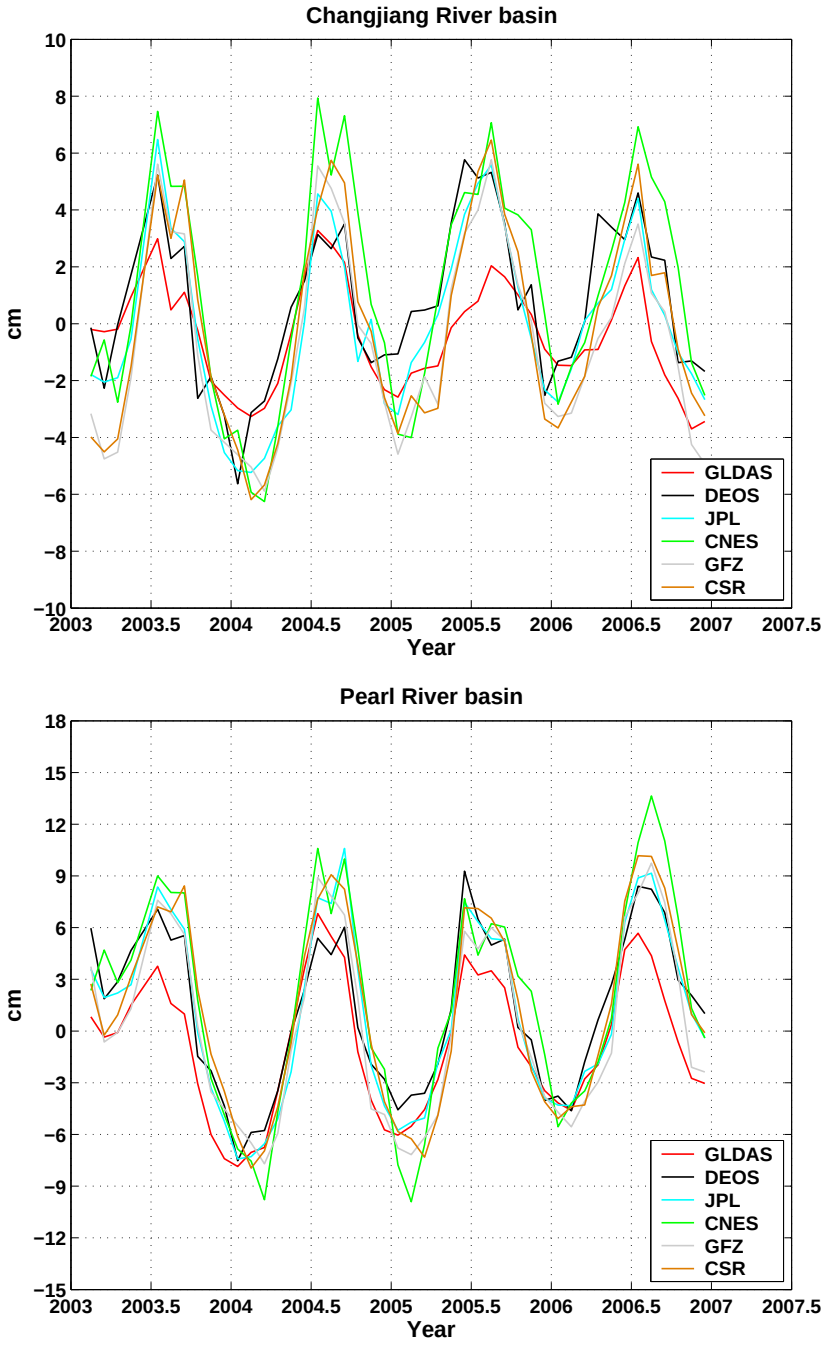

Fig. 6.36. Mean water storage variations over Changjiang River basin (top) and Pearl River basin (bottom) from DEOS, JPL, CNES, GFZ and CSR GRACE solutions as well as from the GLDAS hydrological models. Units are cm of equivalent water heights

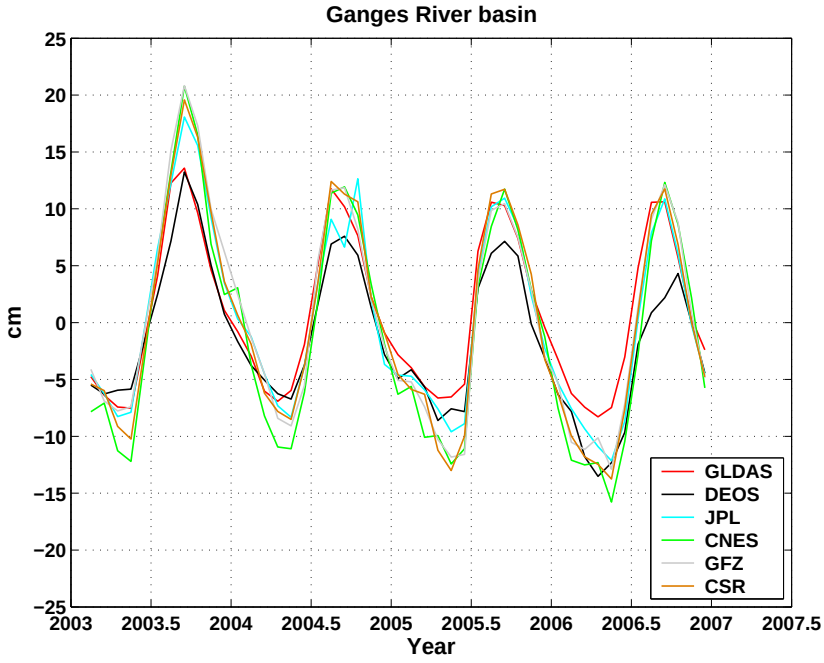

Fig. 6.37. Mean water storage variations over the Ganges River basin (bottom) from DEOS, JPL, CNES, GFZ and CSR GRACE solutions as well as from the GLDAS hydrological models. Units are cm of equivalent water heights

Table 6.11. Analysis of mean water storage variations in selected river basins in South-East Asia. Values shown here are standard deviations of the differences between individual GRACE monthly solutions and (i) corresponding mean values of all GRACE solutions, (ii) mean monthly values from the GLDAS hydrological models, and (iii) JPL GRACE monthly solutions. Units are cm of equivalent water heights

River Basin	Reference	DEOS	JPL	CNES	GFZ	CSR
Changjiang	mean	1.37	0.75	1.19	0.60	0.85
	GLDAS	1.78	1.81	2.56	2.04	2.32
	JPL	1.32	--	1.71	1.09	1.39
Pearl	mean	1.48	0.74	1.47	0.84	0.96
	GLDAS	1.72	2.02	3.02	2.18	2.50
	JPL	1.57	--	1.87	1.20	1.35
Ganges	mean	2.45	1.02	1.63	1.13	1.03
	GLDAS	2.50	2.50	3.57	3.01	2.91
	JPL	2.50	--	2.30	1.79	1.62

Table 6.12. Fit of a yearly sinusoidal through the time series from February 2003 till December 2006 for Changjiang, Ganges and Pearl. $\hat{\sigma}$ is the a posteriori standard deviation and $R^2 = 1 - \frac{\hat{\sigma}^2}{\sigma^2}$, where σ^2 is the signal variance around the 4-year mean

River Basin	Models	Amplitude [cm]	Phase [months]	$\hat{\sigma}$	R^2
Changjiang	GLDAS	2.1±0.5	-3.67±0.44	1.1	0.65
	DEOS	3.2±0.6	-3.25±0.38	1.4	0.73
	JPL	3.6±0.7	-3.76±0.38	1.7	0.72
	CNES	4.8±0.8	-4.21±0.28	1.7	0.82
	GFZ	4.2±0.7	-4.08±0.33	1.7	0.78
	CSR	4.6±0.6	-4.20±0.25	1.5	0.85
Ganges	GLDAS	9.0±1.0	-5.62±0.21	2.3	0.89
	DEOS	8.2±0.8	-5.92±0.21	2.1	0.90
	JPL	10.3±1.3	-5.90±0.25	3.1	0.86
	CNES	12.5±1.4	-5.99±0.22	3.3	0.89
	GFZ	11.5±1.4	-5.88±0.26	3.4	0.87
	CSR	11.8±1.3	-5.91±0.30	3.2	0.89
Pearls	GLDAS	5.1±0.8	-3.58±0.29	1.8	0.80
	DEOS	5.2±1.1	-3.82±0.40	2.6	0.69
	JPL	6.3±1.1	-4.11±0.34	2.6	0.76
	CNES	7.4±1.3	-4.25±0.31	3.1	0.76
	GFZ	6.6±1.1	-4.19±0.32	2.5	0.78
	CSR	7.0±1.0	-4.27±0.26	2.3	0.84

The water storage variations in the Changjiang and Pearl River basins are shown in figure 6.36 and the Ganges River basin in figure 6.37. The RMS values of all GRACE solutions are listed in table 6.11. The fit of the yearly sinusoidal is shown in table 6.12.

In general, the Changjiang and Pearl River basins show positive peaks in June-July and negative peaks in January-February. The seasonal peaks in the Ganges River basin have a delay of one or two months, see table 6.12. From the RMS values listed in table 6.11, we can also see that the DEOS solutions show the biggest differences with respect to the mean of all GRACE solutions in these three river basins. This can be explained by the fact that the DEOS solutions show much smaller signals than the other GRACE solutions, see table 6.12. At the same time, the DEOS solutions have the best consistency with the GLDAS models.

6.6 Summary and Remarks

In this chapter, we made a comprehensive analysis of the DEOS solutions, spanning the interval from February 2003 to December 2006. In order to suppress

North-South artifacts, the de-striping technique was applied in combination with 400 km Gaussian filtering. On the basis of the DEOS gravity field solutions with their associated full covariance matrices, we estimated global secular trends, seasonal and semi-seasonal variations of the Earth's gravity field. In a similar way, we also computed the secular changes and seasonal variations from the GLDAS hydrological models. We found many similarities between the secular trends derived from the DEOS solutions and GLDAS models. Apart from these similarities, there are some signals that are not observed in the GLDAS models, but clearly present in the DEOS GRACE solutions, e.g. due to ice mass loss in some polar areas and PGR signals in Hudson Bay and Scandinavia. The seasonal variations derived from both DEOS solutions and GLDAS models demonstrate close similarities. In particular, the largest water mass variations according to models of both types always happen in the areas between 30°S and 30°N. In addition, the phase of the annual cycle is very clearly separated along the latitudes of 30°S and 30°N. Compared with the amplitude of the annual cycle, the semi-annual amplitude is rather small, and the phase does not show a clear separation according to the latitude.

We have applied the DEOS solutions to the analysis of the Greenland ice melting and Antarctic mass loss. In Greenland, we found two ice melting centers: one is at the south-east coast, and the other is at the north-west coast. The maximum mass loss rate at the south-east ice-melting center is approximately -8 cm/yr in terms of water height. This is two times larger than at the north-west ice-melting center. On the other hand, the ice sheets in Greenland's interior slightly accumulate mass over the whole 4-year period (with mass loss in the first two years and mass gain in the latter two years). In Antarctica, we found a mass loss in several regions. After removal of the PGR signals, the major loss of mass can be seen in the costal Amundsen Sea Embayment and western Antarctic Peninsula. Meanwhile, a total accumulation can be observed in the interior of West Antarctica and East Antarctica. Importantly, the total loss of mass in Antarctica is much larger than the mass accumulation.

We have also demonstrated that the DEOS solutions clearly detect mass redistribution caused by the Sumatra-Andamam earthquake. The differences between two yearly mean gravity field models show the anomalies associated with both mass gain and mass loss. In addition, a negative mass change rate is found prior to the earthquake and a strong positive rate is observed after the earthquake at the points with the maximum signal.

A comparison with other GRACE solutions was another goal of this chapter. The published GRACE solutions produced at CSR, GFZ, JPL and CNES, as well as the GLDAS hydrological models were used for this comparison. The analysis in the domain of spherical harmonic degrees shows that the DEOS solutions are relatively close to the JPL solutions, and less close to the GFZ and CSR solutions, which are consistent with each other. The main differences between the group of DEOS and JPL solutions and the group of GFZ and CSR

solutions is concentrated between degree 2 and degree 5. The causes of these discrepancies should be investigated in the future. We have also computed the mean values of water storage variations in sixteen large river basins from all solutions. The selected basins represent various sizes and climate environments. The comparison was conducted basin by basin with emphasis on the differences with respect to the mean of all the GRACE solutions, the JPL solutions and the GLDAS models. We found that in general the DEOS solutions have a reasonable agreement with other GRACE solutions, and are particularly close to the JPL solutions. We observe that the GRACE-derived water storage variations seem to be consistent with each other in some river basins, e.g. the Amazon, Orinoco, Chari and Zambezi River basins (at least in terms of phase). However, it is also observed that differences between the GRACE solutions are still rather large in some other basins, e.g. the Nile, Congo, Yenisey and Changjiang river basins. It should be mentioned that the DEOS solutions have a smaller signal amplitude when compared with other GRACE solutions in some river basins (e.g. the Ganges River basin), but, at the same time, are relatively close to the GLDAS models.

Chapter 7
Summary, conclusions and recommendations

7.1 Summary and conclusions

The primary goals of this research were: 1) to develop efficient techniques for computing the Earth's static gravity field represented by spherical harmonics, from satellite accelerations derived from hl- and ll-SST data. 2) to extend this technique in order to compute temporal variations of the gravity field and apply it to real data; and 3) to analyze the estimated gravity field models and validate them using existing gravity field models provided by other research institutions. All these goals have been fully met on the basis of the preceding chapters.

The conducted research can be divided into three major parts. In the first part, we refined a pre-existing CHAMP hl-SST data processing methodology (chapter 3). Secondly, we further developed that methodology to process GRACE hl-SST data (chapter 4). Thirdly, we developed two new GRACE ll-SST data processing methodologies (chapter 5). Finally, we conducted a comprehensive analysis of the estimated GRACE solutions. The main results and conclusions can be summarized as follows.

1) We have implemented two refinements of a pre-existing CHAMP data processing technique. The purpose of these refinements was to compute an optimal gravity field model independently from any CHAMP- or GRACE-based a priori information. The first refinement was the development of a procedure for smoothing a kinematic orbit by means of a regularized least-squares adjustment on the basis of B-splines. In this way, we could avoid using a reduced-dynamic orbit to compute the reference accelerations, and consequently, exclude an implicit usage of CHAMP- or GRACE-based a priori information in gravity field modeling. A real data processing demonstrated that smoothed kinematic orbits can indeed replace reduced-dynamic orbit in the data processing procedure since they result in virtually the same accuracy. The second refinement was the implementation of a procedure for estimation of data noise as a function of frequency from *posterior*

residuals. The estimated noise model is used to apply a proper frequency-dependent data weighting and, consequently obtain a statistically optimal gravity field solution. These two refinements were used to compute both regularized (DEOS_CHAMP-02C_70) and an un-regularized (DEOS_CHAMP-02S_70) gravity field models from nearly one-year of CHAMP accelerations. The DEOS_CHAMP-02C_70 model proved to be better than the regularized ITG-CHAMP01E model, and slightly more accurate than the older DEOS_CHAMP-01C_70 model. The DEOS_CHAMP-02S_70 solution was compared to several other non-regularised CHAMP-only models. The comparison showed that our solution is much better than the TUM-2S model and somewhat outperforms the EIGEN-CHAMP03S and the ITG-CHAMP01S models particularly at high degrees. Compared with the AIUB-CHAMP01S model, the DEOS_CHAMP-02S_70 model demonstrated a remarkably small difference in quality, despite being produced two years earlier than the AIUB-CHAMP01S model.

2) The methodology of processing CHAMP hl-SST data was extended to deal with the GRACE hl-SST data, including the GRACE satellite baselines. The kinematic positions and baselines are processed both individually and jointly. It is found that the kinematic baselines themselves are, in general, not favorable for the derivation of gravity field models. We explain this, first of all, by a poor sensitivity of the baseline data to East-West variations of the gravity field. Nevertheless, kinematic baselines slightly improve the quality of gravity field modeling if added to a set of kinematic positions. Additionally, this research bridged the investigation of processing hl-SST data with the ll-SST data.

3) Two innovative methodologies of gravity field modeling from GRACE ll-SST data (the so-called 3RRC approach and 3RC approach) were developed as extensions of the classic acceleration approach. The corresponding functional models were derived. Furthermore, a comprehensive data processing strategy for processing real GRACE data was developed for both new approaches as well as for the classic acceleration approach. The data processing consists of two major parts: pre-processing and inversion. The main elements of data pre-processing is the computation of purely dynamic orbits as reference ones and on the basis of state-of-the-art background models of static and rapidly changing gravity fields. The reference orbits together with the observed KBR data were used to form the KBR residuals and the residual quantities associated with the three functional models. The inversion strategies for the three approaches were developed on the basis of the procedure for inversion of kinematic baselines. The sensitivity of the result to the accuracy of the data noise model in the three approaches was investigated. It was found that the frequency-dependent data weighting was a must in the 3RRC approach, while the classic acceleration approach and the 3RC approach are not very sensitive to the noise models, particularly at the low frequency degrees. More importantly, the approaches were compared with each other using real GRACE data from both August 2003 and October

2003. The corresponding GLDAS hydrological models are used as a reference in the comparison. It was shown that the classic acceleration approach produced the worst results. The 3RC approach resulted in the highest accuracy of gravity field modeling and, consequently, was chosen as the primary one. In the course of further refinement, an iterative estimation was adopted in order to retrieve the gravity signal absorbed by the empirical parameters estimated in the data pre-processing. It was found that a signal increase of at least 10%-15% can be achieved in this way. Furthermore, it was shown that two iterations are sufficient to reach convergence.

4) The 3RC approach was applied to routinely process real GRACE data. A 4-year GRACE data set, spanning the period from February 2003 to December 2006, was processed on a monthly basis. The solutions were supplied with full variance-covariance matrices. Each solution represents a set of spherical harmonic coefficients, which describes the average gravity field within the month under consideration. The estimated solutions were subject to P3M8 de-striping and 400 km Gaussian filtering to generate a definitive time series of DEOS filtered solutions. The models with their associated full covariance matrices were used to estimate global secular trends as well as seasonal and semi-seasonal variations of the Earth's gravity field. In a similar way, we computed the secular, seasonal and semi-seasonal variations from the GLDAS hydrological models. There are many remarkable similarities found between the secular changes derived from the DEOS solutions and GLDAS models, e.g. a mass decrease in south-eastern Alaska, in the south-western part of United States, in La Plata river basin, as well as a mass increase in the north part of South America, in southern Africa, in central Europe and so on. Apart from these similarities, there are some signals that are not observed in the GLDAS models, but are clearly present in the DEOS GRACE solutions, e.g. ice mass loss in some polar areas and PGR signals in Hudson Bay and Scandinavia. The seasonal variations derived from both DEOS solutions and GLDAS models are even more similar. In particular, the largest water variations are always in the area between 30°S and 30°N. In addition, the phase of the annual cycle changes clearly along the latitudes 30°S and 30°N. The semi-annual cycle is rather small, compared with the annual cycle, and its phase does not show a clear dependence on latitude.

5) A further analysis of the obtained gravity field solutions allowed ice melting in Greenland and Antarctica as well as the Sumatra-Andaman earthquake to be observed and quantified. In Greenland, we found two ice mass loss centers: one at the south-east coast, and the other at the north-west coast. The mass loss rate in the south-east center is about -8 cm/yr. This is two times faster than at the north-west center. On the other hand, the ice mass in Greenland's interior is getting slightly larger over the whole 4-year period (with mass loss in the first two years and mass accumulation in the last two years). In the Antarctic, we reveal a mass loss in several regions. After removal of the PGR signal, the major loss of mass occurs in the coastal Amundsen Sea Embayment and the western Antarctic Peninsula. On the other hand, a to-

tal mass accumulation can be observed in the interior of West Antarctic and East Antarctic. In Antarctica the loss of mass is much larger than the mass accumulation. We have also demonstrated that the DEOS solutions clearly detect the mass redistribution caused by the Sumatra-Andaman earthquake. The differences between two yearly mean gravity field models show anomalies associated with both mass gain and mass loss. In addition, a negative rate of mass changes is found prior to the earthquake and a strong positive rate is observed after the earthquake at the center of both mass gain and mass loss.

6) A comparison was made between our GRACE solutions and those produced at CSR, GFZ, JPL and CNES, as well as GLDAS hydrological models. Our analysis showed that the DEOS solutions are relatively close to the JPL solutions, and less close to the GFZ and CSR solutions, which are in turn relatively close to each other. The main differences between the group of DEOS and JPL solutions and the group of GFZ and CSR solutions are concentrated between degree 2 and 5. We also computed the mean values of water storage changes in sixteen large river basins from all solutions. The selected basins represent various sizes and climatic environments. The comparison was conducted basin by basin with an emphasis on the differences between a given solution and (i) the mean of all GRACE solutions, (ii) the JPL solutions and (iii) the GLDAS models. We found that in general the DEOS solutions had a reasonable agreement with other GRACE solutions, and were particularly close to the JPL solutions. Furthermore, we observed that all the GRACE-derived water storage changes seemed to be consistent with each other in some river basins, e.g. the Amazon, Orinoco, Chari and Zambezi river basins. In some other basins, however, the differences between the GRACE solutions were still quite large, e.g. in the Nile, Congo, Yenisey and Changjiang river basins. It should be mentioned that the DEOS solutions showed smaller signal amplitude compared to the other GRACE solutions in some river basins (e.g. the Ganges river basin), but, at the same time, are relatively close to the GLDAS hydrological models.

7.2 Recommendations for future work

1) The classical acceleration approach to gravity field modeling from GRACE data should be investigated further. From the functional model of the classic acceleration approach, the results seem impossible to improve upon if the accuracy of the velocity term is not improved. However, it is not trivial to significantly improve the accuracy of the kinematic baselines, which are used to derive the velocity term. There may be another way to improve the results of the classic acceleration approach, i.e. ignoring the contribution of velocity term entirely by only considering the contribution of point-wise accelerations. This way may not be totally strict in the physical sense, but it could, in practice, produce quite reasonable results. In the very late stages of this PhD research project, an attempt has been made to do just this.

Indeed, very reasonable results were obtained; however, this still needs more investigation in the future.

2) Real GRACE ll-SST data processing showed that both the 3RRC and 3RC approach produced gravity field models of high quality. Nevertheless, the models obtained with the 3RC approach are less noisy than those based on the 3RRC approach. For this reason the 3RC approach was selected to routinely produce the DEOS monthly GRACE solutions. However, the 3RRC approach is also very promising. We believe that the quality of gravity field models can be further improved if a dedicated filtering at the post-processing stage is applied. In this way, the ultimate performance of the 3RRC approach can be made closer to that of the 3RC approach. This should also be the subject of the future work.

3) The current GRACE data processing strategy may not be optimal, in spite of considerable efforts we put into its development. There is still some space to refine the strategy further and, consequently to improve the quality of the gravity field models. For example, background models and calibration of non-gravitational accelerations could be updated. Additionally, a comprehensive simulation of the GRACE data processing is recommended in order to tune different processing steps.

4) After comparison of our GRACE models with the solutions produced by other institutions, we found that the DEOS solutions frequently show a relatively small signal amplitude (though they remain close to the JPL solutions), e.g. in the Ganges river basin. At the same time, the DEOS solutions show agreement with the GLDAS model in many river basins. Therefore, further analysis and validation of the GRACE solutions obtained with the proposed methodology is recommended.

5) Future research should also attempt to improve the monthly models of mass variations by combining GRACE data with hydrological data and models. The errors in hydrological models and in GRACE models show a substantially different behavior, both in the time and the spatial domain. The accuracy of hydrological models is mainly dependent on the availability of in situ data. Therefore, it is not homogeneous over the globe; some areas and river basins have been investigated much more exhaustively than others. Furthermore, it is also problematic to quantify all the relevant hydrological processes equally well. On the other hand, the accuracy of GRACE solutions is limited by the setup of the mission, precision of measurements, inaccuracies of background models and data processing errors. These issues limit the spatial resolution of the GRACE solutions and reduce performance when mapping spatial variations in the west-east direction. Therefore, we believe that that these two types of data have an enormous potential for synergy and must be processed jointly. The development of corresponding techniques is also the subject of future researches.

Bibliography

[Ammon et al., 2005] Ammon, C., C. Ji, H.-K. Thio, D. Robinson, S. Ni, V. Hjorleifsdottir, H. Kanamori, T. Lay, S. Das, D. Helmberger, G. Ichinose, J. Polet, and D. Wald (2005). Rupture Process of the 2004 Sumatra-Andaman Earthquake. *Science* Vol. 308, No. 5725, pp. 1133-1139, doi:10.1126/science.1112260

[Andersen and Hinderer, 2005] Andersen, O. B., and J. Hinderer (2005). Global inter-annual gravity changes from GRACE: Early results. *Geophysical Research Letters*, Vol. 32, L01402, doi:10.1029/2004GL020948.

[Banerjee et al, 2007] Banerjee, P., F. Pollitz, B. Nagarajan, and R. Bürgmann (2007). Coseismic slip distributions of the 26 December 2004 Sumatra-Andaman and 28 March 25 Nias earthquake from GPS static offsets. *Bulletin of the Seismological Society of America*, Vol. 97, No, 1A, pp. S86-S102, January 2007, doi:10.1785/0120050609

[Berbery and Barros, 2002] Berbery, E. H., and V. R. Barros (2002). The Hydrologic cycle of the La Plata Basin in South America. *Journal Hydrometeorology*, 3, 630-645.

[Bettadpur, 2007] Bettadpur, S. V. (2007). UTCSR level-2 processing standards document for Level-2 product release 0004, Center for Space Research, University of Texes at Austin.

[Beutler et al, 1994] Beutler, G., E. Brockmann, W. Gurtner, U. Hugentobler, L. Mervart, M. Rothacher, and A. Verdum (1994). Extended orbit modeling techniques at the CODE processing center of the international GPS service for geodynamics (IGS): theory and initial results. *Manuscripta geodaetica*, 19:367-386.

[Beutler, 2005] Beutler, G. (2005). *Methods of celestial mechanics*. Springer, Berlin, Heidelberg, New York.

[Beutler, 2006] Beutler, G., A. Jäggi, U. Hugentobler, and L. Mervart (2006). Efficient satellite orbit modelling using pseudo-stochastic parameters. *Journal of Geodesy*, 80:353-372, doi:10.1007/s00190-006-0072-6

[Biancale et al., 2005] Biancale, R, G. Balmino, S. Bruinsma, J. M. Lemoine, S. Loyer, and F. Perosanz (2005). GRACE data processing in CNES/GRGS: results and discussion. In J. Ries and S. Bettadpur, editors, *Presentation Proceeding of the GRACE Science Team Meeting at Center for Space Research, The University of Texes at Austin, October 13-14, 2005*, pages 203–220. 2005.

[Biancale et al., 2007] Biancale, R., J-M Lemoine, G Balmino, S Bruinsma, F Perosanz, and J-C Marty (2007). 5 years of gravity variations from GRACE and LAGEOS data at 10-day intervals over the period from July 29th 2002 to June 22nd 2007. available at http://bgi.cnes.fr:8110/geoid-variations/README.html

[Case et al., 2004] Case, K., G. Kruizinga, and S. C. Wu (2004). *GRACE level 1B data product user handbook JPL D-22027 GRACE 327-733.*

[Chambers, 2006] Chambers, D. (2006). Evaluation of new GRACE time-variable gravity data over the ocean. *Geophysical Research Letters*, Vol. 33, L17603, doi:10.1029/2006GL027296

[Chen et al., 2006a] Chen, J. L., B. D. Tapley, and C. R. Wilson (2006). Alaskan mountain glacial melting observed by satellite gravimetry. *Earth Planet Science Letters*, 248, 368-378

[Chen et al., 2006b] Chen, J. L., C. R. Wilson, D. D. Blankenship, and B. D. Tapley (2006). Antarctic mass rates from GRACE. *Geophysical Research Letters*, 33, L11502, doi:10.1029/2006GL026369

[Chen et al., 2006c] Chen, J. L., C. R. Wilson, and B. D. Tapley (2006). Satellite Gravity Measurements confirm accelerated melting of Greenland ice sheet. *Science*, 313, 1958, doi:10.1126/science.1129007

[Chen et al., 2007] Chen, J. L., C. R. Wilson, B. D. Tapley, and S. Grand (2007). GRACE detects coseismic and postseismic deformation from the Sumatra-Andaman earthquake. *Geophysical Research Letters*, Vol. 34, L13302, doi:10.1029/2007GL030356

[Chen et al., 2008] Chen, J. L., C. R. Wilson, B. D. Tapley, D. D. Blankenship, and D. Young (2006). Antarctic regional loss rates from GRACE. *Earth and Planetary Letters*, 266 140-148

[Colombo, 1984] Colombo, OL (1984). *The global mapping of gravity with two satellites.* Netherlands Geodetic Commission, Publications on Geodesy, New Series vol 7, no. 3.

[Davis, 1979] Davis, P. J. (1979). *Circulant matrices.* John Wiley, New York.

[de Boor, 2001] de Boor, C. (2001). *A practical guide to splines – Rev. ed.*, Applied Mathematical Sciences, vol.27. Springer, New York.

[Desai, 2002] Desai, S. (2002). Observing the pole tide with satellite altimetry. *Journal Geophysical Research*, 107, NO. C11, 3186, doi:10.1029/2001JC001224

[Dierckx, 1993] Dierckx, P. (1993). *Curve and Surface Fitting with Splines*, Monographs on Numerical Analysis, Oxford Science Publications, New York.

[Ditmar et al., 2003] Ditmar, P., J. Kusche, and R. Klees (2003). Computation of spherical harmonic coeffcients from gravity gradimetry data to be acquired by the GOCE satellite: regularization issues. *Journal of Geodesy*, 77:465-477.

[Ditmar and van Eck van der Sluijs, 2004] Ditmar, P., and A. A. van Eck van der Sluijs (2004). A technique for Earth's gravity field modeling on the basis of satellite accelerations. *Journal of Geodesy*, **78**: 12-33, doi:10.1007/s001900-003-0362-1

[Ditmar et al., 2004a] Ditmar, P., A. A. van Eck van der Sluijs, and Kuznetsov V. (2004). Modeling the Earth's gravity field from precise satellite orbit data: the acceleration approach works! (available as http://earth.esa.int/workshops/goce04/participants/81/paper_accelerations.pdf), in: *Proceedings of the 2nd International GOCE user workshop, Frascati (Italy), March 8-10, 2004*. European Space Agency.

[Ditmar et al., 2004b] Ditmar, P., R. Klees, V. Kuznetsov, A. A. van Eck van Sluijs, E.J.O. Schrama, and X. Liu (2004). Gravity field analysis with the acceleration approach on the basis of data from the CHAMP satellite mission. *The proceedings of the IAG International Symposium "Gravity, Geoid and Space Missions - GGSM2004", Porto, Portugal, Aug. 30 - Sep. 3 2004, CDROM.*

[Ditmar et al., 2006] Ditmar, P., V. Kuznetsov, A. A. van Eck van Sluijs, E.J.O. Schrama, and R. Klees (2006). 'DEOS_CHAMP-01C_70': a model of the Earth's gravity field computed from accelerations of the CHAMP satellite. *Journal of Geodesy*, 79:586-601, doi:10-1007/500190-005-008-6

[Ditmar and Liu, 2006a] Ditmar, P., and X. Liu (2006). Dependence of the Earth's gravity model derived from satellite accelerations on a priori information. *Jounal of Geodynamics*, 43:89-99, doi:10.1016/j.jog.2006.09.009

[Ditmar and Liu, 2006b] Ditmar, P., and X. Liu (2006). Gravity field modeling on the basis of GRACE range-rate combinations. *The Proceedings of the "VI Hotine-Marussi Symposium of Theoretical and Computational Geodesy: Challenge and Role of Modern Geodesy"*. May 29 - June 2, 2006, Wuhan, China, accepted.

[Ditmar and Liu, 2006c] Ditmar, P., and X. Liu (2006). Gravity field modeling on the basis of GRACE range-rate combinations: current results and challenge. *The proceeding of the '1st international symposium of the international gravity field service (IGFS): Gravity Field of the Earth'.* Aug 28 - Sept 1, 2006, Istanbul, Turkey.

[Ditmar et al., 2007] Ditmar, P., R. Klees, and X. Liu (2007). Frequency-dependent data weighting in global gravity field modeling from satellite data contaminated by non-stationary noise. *Journal of Geodesy*, 81:81–96, doi:10.1007/s00190-006-0074-4

[Ditmar, 2007] Ditmar, P. (2007). *Satellite Gravity and the Geosphere*. Lecture notes of Aerospace Engineering faculty of Delft University of Technology.

[Dobslaw and Thomas, 2007] Dobslaw, H., and M. Thomas (2007). Time-depending variation of ocean mass anomalies from GRACE by means of satellite altimetry and numerical models. Oral presentation at the GRACE Science Meeting and the German national special priority program "Mass Transport and Mass Distribution in the Earth System", Oct. 15-17, 2007, Postdam, Germany.

[Ek et al, 2003] Ek, M. B., K. E. Mitchell, Y. Lin, E. Rogers, P. Grunmann, V. Koren, G. Gayno and J.D. Tarpley (2003). Implementation of Noah land surface model advances in the National Centers for Environmental Prediction operational mesoscale Eta model. *Journal of Geophysics Research*, *108*, (D22), 8851, doi:10.1029/2002JD003296

[Farrell, 1972] Farrell, W. E. (1972). Deformation of the Earth by surface loading. *Reviews of Geophysics*, *10*, 761-797

[Fengler et al, 2007] Fengler, M. J., W. Freeden, K. Kohlhaas, V. Michel, and T. Peters (2007). Wavelet modeling of regional and temporal variations of the Earth's gravitational potential observed by GRACE, *Journal of Geodesy*, *81*, 5-15

[Flechtner, 2007a] Flechtner, F. (2007). GRACE 327-750: AOD1B product description document for product reslease 01 to 04. GeoForschungsZentrum Potsdam, Germany.

[Flechtner, 2007b] Flechtner, F. (2007). GRACE 327-743: GFZ Level-2 Processing Standards Document for Level-2 Product Release 0004. GeoForschungsZentrum Potsdam, Germany.

[Förste et al., 2005] Förste, C., F. Flechtner, R. Schmidt, U. Meyer, R. Stubenvoll, F. Barthelmes, R. Knig, K.H. Neumayer, M. Rothacher, Ch. Reigber, R. Biancale, S. Bruinsma, J.-M. Lemoine, and J.C. Raimondo (2005). A New High Resolution Global Gravity Field Model Derived From Combination of GRACE and CHAMP Mission and Altimetry/Gravimetry Surface Gravity Data. Poster presented at EGU General Assembly 2005, Vienna, Austria, 24-29, April.

[Förste et al., 2006] Förste, C., F. Flechtner, R. Schmidt, R. König, U. Meyer, R. Stubenvoll, M. Rothacher, F. Barthelmes, H. Neumayer, R. Biancale, S. Bruinsma, J.-M. Lemoine, and S. Loyer (2006), A mean global gravity field

model from the combination of satellite mission and altimetry/gravimetry surface data - EIGEN-GL04C. Poster presented at European Geoscience Union, General Assembly 2006, Vienna, Austria, 02-07 April.

[Förste et al., 2007] Förste, C., R. Schmidt, R. Stubenvoll, F. Flechtner, U. Meyer, R. König, H. Neumayer, R. Biancale, J. Lemoine, S. Bruinsma, S. Loyer, F. Barthelmes and S. Esselborn (2007). The GeoForschungsZentrum Potsdam/Groupe de Recherche de Godsie Spatiale satellite-only and combined gravity field models: EIGEN-GL04S1 and EIGEN-GL04C. *Journal of Geodesy*, online, doi:10.1007/s00190-007-0183-8

[Gerlach et al., 2003] Gerlach, Ch., L. Földvary, D. Švehla, Th. Gruber, M. Wermuth, N. Sneeuw, B. Frommknecht, H. Oberndorfer, Th. Peters, M. Rothacher, R. Rummel, and P. Steigenberger (2003). A CHAMP-only gravity field model from kinematic orbits using the energy integral. *Geophysical Research Letters*, vol. 30(20), 2037, doi:10.1029/2003GL018025

[Götzelmann et al., 2006] Götzelmann M., W. Keller, and T. Reubelt (2006). Gross error compensation for gravity field analysis based on kinematic orbit data. *Journal of Geodesy*, 80(4):184-198, doi:10.1007/s00190-006-0061-9

[Han et al., 2003] Han, S.-C., C. Jekeli, and C. Shum (2002). Efficient Gravity Field Recovery Using in situ Disturbing Potential Observables from CHAMP. *Geophysical Research Letters*, 29, doi:10.1029/2002GL015180

[Han, 2003] Han, S.-C. (2003). Efficient global gravity determination from Satellite-to-Satellite Tracking (SST) PhD dissertation, Department of Civil and Environmental Engineering and Geodetic Science, The Ohio State University.

[Han et al., 2005] Han, S.-C., C. K. Shum, C. Jekeli, and D. Alsdorf (2005). Improved estimation of terrestrial water storage changes from GRACE. *Geophysical Research Letters*, 32, L07302, doi:10.1029/2005GL022382

[Han et al., 2006a] Han, S.-C., C. Shum, C. Jekeli (2006). Precise estimation of in situ geopotential difference from GRACE low-low satellite-to-satellite tracking and accelerometry data. *Journal of Geophysical Research*, 111, B04411, doi:10.1029/2005JB003719

[Han et al., 2006b] Han, S.-C., C. Shum, M. Bevis, C. Ji (2006). Crustal dilatation observed by GRACE after the 2004 Sumatra-Andaman earthquake. *Science*, 313, 658-662, doi:10.1126/science.1128661

[Hansen, 1992] Hansen, P. C. (1992). Regularization tools - a Matlab package for analysis and solution of discrete ill-posed problems, available at http://www.imm.dtu.dk/p̃ch/Regutools/index.html

[Hashimoto et al., 2006] Hashimoto, M., N. Chhoosakul, M. Hashizume, S. Takemoto, H. Takiguchi, Y. Fukada, and K. Fujimori (2006). Crustal deformations associated with the great Sumatra-Andaman earthquake deduced from continuous GPS observation. *Earth Planets Space*, 58, 127-139.

[Heiskanen and Moritz, 1984] Heiskanen, W. A., and H. Moritz (1984). *Physical Geodesy*. Institute of Physical Geodesy, Technical University Graz, Austria.

[Ivins and James, 2005] Ivins, E.R., and T.S. James (2005). Antarctic glacial isostatic adjustment: a new assessment. *A*ntarctic Science, 17(4), 2005

[Gerlach et al., 2003] Gerlach, Ch., L. Földvary, D. Švehla, Th. Gruber, M. Wermuth, N. Sneeuw, B. Frommknecht, H. Oberndorfer, Th. Peters, M. Rothacher, R. Rummel, and P. Steigenberger (2003). A CHAMP-only gravity field model from kinematic orbits using the energy integral, *Geophysical Research Letters*, 30(20),2037 doi: 10.1029/2003GL018025

[Girard, 1989] Girard, D. A. (1989). A fast 'Monte-Carlo Cross-Validation' procedure for large least-square probems with noisy data. *Numerical Mathematics* 56, 1-23.

[Jäggi et al., 2006] Jäggi, A., U. Hugentobler, and G. Beutler (2006). Pseudo-stochastic orbit modeling techniques for low-Earth orbiters. *Journal of Geodesy*, 80:47-60, doi:10.1007/s00190-006-0029-9

[Jekeli, 1981] Jekeli, C. (1981). Alternative methods to smooth the Earth's gravity field. Report No.327, Department of Civil and Environmental Engineering and Geodetic Science, The Ohio State University.

[Jekeli, 1999] Jekeli, C. (1999). The determination of gravitational potential differences from satellite-to-satellite tracking. *Celestial Mechanics and Dynamical Astromomy*, **75**:85-101, 1999.

[Kaula, 1966] Kaula66, W. M. (1966). *Theory of satellite geodesy*. Blaisdell Publishing Company, Waltham, USA.

[Klees and Broersen, 2002] Klees, R. and P. Broersen, (2002). *How to handle colored noise in large least-squares problems. Building the optimal filter*. Delft University Press, Delft.

[Klees and Ditmar, 2003] Klees, R. and P. Ditmar, (2003). How to handle colored noise in large least-squares problems in the presence of data gaps? In *Proceedings of the Hotine-Marussi workshop*, Matera, Italy, 17-21 June 2002, accepted for publication, 2003.

[Klees et al., 2007] Klees, R., E. A. Zapreeva, H. C. Winsemius, and H. H. G. Savenije (2007). The bias in GRACE estimates of continental water storage variations. *Hydrology and Earth System Sciences*, 11, 1227-1241.

[Klees et al., 2008] Klees, R., R. Tenzer, I. Prutkin, and T. Wittwer (2008). A data-driven approach to local gravity field modelling using spherical radial basis functions. *Journal of Geodesy*, 82:457-471, doi:10.1007/s00190-007-0196-3

[Koch, 1999] Koch, K.-R. (1999). Parameter estimation and hypothesis testing in linear models. 2nd ed. Springer, Berlin, Heidelberg, New York.

[Koch and Kusche, 2002] Koch, K.-R. and Kusche J. (2002). Regularization of Geopotential Determination from Satellite Data by Variance Components. *Journal of Geodesy*, Vol. 76: 259-268, doi:10.1007/s00190-002-0245-x

[Krabill et al., 2004] Krabill, W., E. Hanna, P. Huybrechts, W. Abdalati, J. Cappelen, B. Csatho, E. Frederick, S. Manizade, C. Martin, J. Sonntag, R. Swift, R. Thomas, and J. Yungel (2004). Greenland ice sheet: increased coastal thining. *Geophysical Research Letters*, Vol. 31, L24402, doi:10.1029/2004GL021533

[Kroes, 2006] Kroes, R., (2006). Precise relative positioning of formation flying spacecraft using GPS. PhD dissertation, Delft Institute of Earth Observation and Space Systems (DEOS), Delft University of Technology.

[Kroes et al., 2005] Kroes, R., O. Montenbruck, W. Bertiger, and P. Visser (2005). Precise GRACE baseline determination using GPS. *GPS Solution*, 9, 21–31, doi:10.1007/s10291-004-0123-5

[Kusche and Klees, 2002] Kusche, J. and Klees R. (2002). Regularization of gravity field estimation from gravity gradimetry data. *Journal of Geodesy*, 76: 359-368.

[Lay et al. 2005] Lay, T., H. Kanamori, C. J. Ammon, M. Nettles, S. N. Ward, R. C. Aster, S. L. Beck, S. L. Bilek, M. R. Brudzinski, R. Butler, H. R. DeShon, G. Ekström, K. Satake, and S. Sipkin (2005). The Great Sumatra-Andaman Earthquake of 26 December 2004. *Science*, Vol. 308, No. 5725, pp. 1127-1133, doi: 10.1126/science.1112250

[Lemoine et al., 1998] Lemoine, F.G., S.C. Kenyon, J.K. Factor, R.G. Trimmer, N.K. Pavlis, D.S. Chinn, C.M. Cox, S.M. Klosko, S.B. Luthcke, M.H. Torrence, Y.M. Wang, R.G. Williamson, E.C. Pavlis, R.H. Rapp, and T.R. Olson (1998). NASA Goddard Space Flight Center, Greenbelt, Maryland, 20771 USA, July 1998. The Development of the Joint NASA GSFC and NIMA Geopotential Model EGM96.

[Liu et al., 2005] Liu, X., P. Ditmar, and R. Klees (2006). Estimation of data noise in global gravity field modeling. In: Proceedings of the "Dynamic Planet - 2005" scientific meeting (CD-ROM), Cairns, Australia, 22-26 August, 2005

[Liu and Ditmar, 2006] Liu, X., and Ditmar P. (2006). Smoothing a satellite orbit on the basis of B-splines and regularization. *Chinese Journal of Geophysics*, Chinese Eds. 49(1), 99-105, English Eds. 49(1):86-94.

[Liu et al., 2007a] Liu, X., P. Ditmar, and Q. Zhao (2007). Recovery of temporal gravity field variations from GRACE data with the range-rate combination approach. Poster presentation at the general assembly of EGU 2007, Vienna 15-20 April.

[Liu et al., 2007b] Liu, X., P. Ditmar, and Q. Zhao (2007). A new variant of the acceleration approach for gravity field modeling from GRACE range measurements. Poster presentation at the general assembly of EGU 2007, 15-20, April, Vienna, Austria.

[Liu et al., 2007c] Liu, X., P. Ditmar, and Q. Zhao (2007). Recovery of temporal gravity field variations from GRACE data with the range-combination approach. Oral presentation at the general assembly of IUGG 2007, 2-15 July, Perugia, Italy.

[Liu et al., 2007d] Liu, X., P. Ditmar, Q. Zhao, and O. Erna (2007). A 3-year series of Earth's gravity field variations derived from GRACE range measurements. Oral presentation at the GRACE Science Meeting, Oct. 15-17, 2007, Postdam, Germany.

[Llubes et al., 2007] Llubes, M., J.-M. Lemoine, F. Remy (2007). Antarctica seasonal mass variations detected by GRACE. *Earth and Planetary Science Letters*, 260, 127-136.

[Luthcke et al., 2006] Luthcke, S. B., D. D. Rowlands, F. G. Lemoine, S. M. Klosko, D. S. Chinn, and J.J. McCarthy (2006). Monthly spherical harmonic gravity field solutions determined from GRACE inter-satellite range-rate data alone. *Geophysical Research Letters*, 33, L02402, doi: 10.1029/2005GL024846

[Luthcke et al., 2006] Luthcke, S. B., H. J. Zwally, W. Abdalati, D. D. Rowlands, R. D. Ray, R. S. Nerem, F. G. Lemoine, J.J. McCarthy and D. S. Chinn (2006). Recent Greenland ice loss by Drainage system from satellite gravity observations. *Science*, 314, 1286, doi: 10.1126/science.1130776

[Lyard et al., 2006] Lyard, F., F. Lefevre, T. Letellier, and O. Francis (2006). Modelling the global ocean tides: Insights from FES2004. *Ocean Dynamics*, 56, 394-415.

[Mallat, 1989] Mallat, S. G. (1989). A theory for multiresolution signal decomposition: the wavelet representation. *IEEE Transactions Pattern Analysis and Machine Intelligence*, vol. PAMI-11, pp. 674-693.

[Mayer-Gürr et al., 2005] Mayer-Gürr, T., K. H. Ilk, A. Eicker, M. Feuchtinger (2005). ITG-CHAMP01: A CHAMP Gravitiy Field Model from Short Kinematical Arcs of a One-Year Observation Period. *Journal of Geodesy*, 78, 462 - 480.

[Mayer-Gürr, 2006] Mayer-Gürr, T. (2006). Gravitationsfeldbestimmung aus der Analyse Kurzer Bahnbögen am Beispiel der Satellitenmissionen CHAMP und GRACE. Dr.-ing Dissertation, University of Bonn.

[Mayer-Gürr et al., 2006] Mayer-Gürr, T., A. Eicker, K.H. Ilk (2006). ITG-GRACE02s: A GRACE gravity field derived from short arcs of the satellite's orbit. *The Proceedings of the "1st international symposium of the international gravity field service (IGFS): Gravity Field of the Earth"*. Aug 28 - Sept 1, 2006, Istanbul, Turkey.

[Montenbruck and Gill, 2000] Montenbruck, O., and E. Gill (2000). *Satellite orbits: models, methods and applications*. Springer Verlag, Heidelberg.

[McCarthy and Petit, 2003] McCarthy, D. D., and G. Petit (Eds.) (2003). *IRES Conventions (2003), IERS Tech. Note*. vol. 32, Bundesamts für Kartogr. und Geod., Frankfurt, Germany.

[Nakaegawa, 2006] Nakaegawa, T. (2006). Dectectability assessment of interannual variations in terrestrial water storage from satellite gravimetry using an offline land surface model simulation. *Hydrological Processes*, 20, 1347-1364, doi:10.1002/hyp.6096

[Nerem et al, 1994] Nerem, R. S., et al. (1994). Gravity model development for TOPEX/POSEIDON: Joint gravity models 1 and 2. *Journal of Geophysical Research*, 99(C12), 24421-24448

[Nerem, 1995] Nerem, R.S. (1995). *Terrestrial and planetary gravity fields, U.S. National Report to IUGG, 1991-1994*, compiled by the NASA/Goddard Space Flight Center. *Reviews of Geophysics* Vol. 33 Suppl., 1995 American Geophysical Union.

[Oberndorfer and Mueller, 2002] Oberndorfer, H., and J. Mueller. (2002). GOCE closed-loop simulation. *Journal of Geodynamics*, 33:53-63, doi:10.1016/S0264-3707(01)00054-0

[Ogawa et al., 2007] Ogawa, R., and K. Heki (2007). Slow postseismic recovery of geoid depression formed by the 2004 Sumatra-Andaman Earthquake by mantle water diffusion. *Geophysical Research Letters*, 34, L06313, doi:10.1029/2007GL029340

[Oki and Su, 1998] Oki, T., and Y.C. Su, (1998). Design of Total Runoff Integrating Pathways (TRIP) – a global river channel network. *Earth Interactions* 2(1) (1998) 1-37.

[Peltier, 2004] Peltier, R. (2004). Global glacial isostasy and the surface of the ice-age Earth: the ICE-5G (VM2) model and GRACE. *Annual Review of Earth Planetary Sciences*, 32, 111-149.

[Prange et al. 2007] Prange, L., A. Jäggi, G. Beutler, L. Mervart, and R. Dach (2007). Gravity Field Determination at the AIUB - the Celestial Mechanics Approach. Poster presentation at the IUGG XXIV General Assembly, July 2-13 2007, Perugia, Italy.

[Press et al., 1992] Press, W. H., S. Flannery, S.A. Teukolsky, and W.T. Vetterling (1992). *Numerical Recipes in Fortran: The art of scientific computing*. Camberidge University Press.

[Ramillien et al. 2006] Ramillien, G., A. Lombard, A. Cazenave, E.R. Ivins, M. Llubes, F. Remy, R. Biancale (2006). Interannual variations of the mass balance of the Antarctica and Greenland ice sheets from GRACE. *Global Planet Change* 53(3), 198-208.

[Rangelova et al. 2007] Rangelova, E., W. van der Wal, A. Braun, M. G. Sideris, and P. Wu (2007). Analysis of Gravity Recovery and Climate Experiment time-variable mass distribution signals over North America by means of principal component analysis. *Journal of Geophysical Research*, Vol. 112, F03002, doi:10.1029/2006JF000615

[Rapp et al, 1991] Rapp, R.H., Y.M. Wang, and N.K. Pavlis (1991). *The Ohio State 1991 Geopotential and Sea Surface Topography Harmonic Coefficient Models*. The Ohio State University, Department of Geodetic Science, Report No. 410, Columbus/Ohio.

[Reigber, 1989] Reigber, Ch. (1989). Gravity field recovery from satellite tracking data. In F. Sansò and R. Rummel eds. *Theory of satellite geodesy and gravity field determination*. Lecture notes in Earth Sciences, Vol. 25, 197-234, Springer-Verlag, Berlin Heidelberg New York.

[Reigber et al., 2002] Reigber, Ch., G. Balmino, P. Schwintzer, R. Biancale, A., Bode, J.-M. Lemoine, R. König, S. Loyer, K.-H., Neumayer, J.-C. Marty, F. Barthelmes, F. Perosanz, and S.Y. Zhu (2002). A high-quality global gravity field model from CHAMP GPS tracking data and accelerometry (EIGEN-1S). *Geophysical Research Letters*, vol. 29, 10.1029/2002GL015064

[Reigber et al., 2003] Reigber, Ch., G. Balmino, P. Schwintzer, R. Biancale, A., Bode, J.-M. Lemoine, R. König, S. Loyer, K.-H. Neumayer, J.-C. Marty, F. Barthelmes, F. Perosanz, and S.Y. Zhu (2003). New global gravity field models from selected CHAMP data sets. In Reigber, Lühr and Schwintzer (Eds.), *First CHAMP mission results for gravity, magnetic, and atmospheric studies*, p120-127, Springer-Verlag, Berlin Heidelberg New York.

[Reigber et al., 2004] Reigber, Ch., H. Jochmann, H. Wnsch, J. Petrovic, S. Schwintzer, P. Barthelmes, F. Neumayer, K.-H. Knig, R. Frste, Ch. Balmino, G. Biancale, R. Lemoine, J.-M. Loyer, and S. Perosanz (2004). Earth Gravity Field and Seasonal Variability from CHAMP. In: Reigber, Ch., Lhr, H., Schwintzer, P., Wickert, J. (eds.), *Earth Observation with CHAMP - Results from Three Years in Orbit*, Springer, Berlin, 25-30, 2004.

[Reigber et al., 2005a] Reigber, Ch., H. Jochmann, J. Wünsch, S. Petrovic, P. Schwintzer, F. Barthelmes, K.-H., Neumayer, R. König, C. Förste, G. Balmino, R. Biancale, J.-M. Lemoine, S. Loyer, and F. Perosanz, (2005). Earth gravity field and seasonal variability from CHAMP. In Reigber, Lühr, Schwintzer and Wickert (Eds.), *Earth Observation with CHAMP: Results from Three Years in Orbit*, P25-30., Springer-Verlag, Berlin Heidelberg New York.

[Reigber et al., 2005b] Reigber, C., R. Schmidt, F. Flechtner, R. König, U. Meyer, K.-H. Neumayer, P. Schwintzer, and S. Y. Zhu (2005). An Earth gravity field model complete to degree and order 150 from GRACE: EIGEN-GRACE02S. *Journal Geodynamics, 39*, 1–10, doi:10.1016/j.jog.2004.07.00

[Reubelt et al., 2003] Reubelt, T., G. Austen, and E. W. Grafarend (2003). Harmonic analysis of the Earth's gravitational field by means of semi-continuous ephemerides of a low Earth orbiting GPS-tracked satellite, Case study: CHAMP. *Journal of Geodesy*, 77, 257-278, doi 10.1007/s00190-003-0322-9.

[Reubelt et al., 2006] Reubelt, T., M. Götzelmann, and E. W. Grafarend (2006). Harmonic analysis of the Earth's gravitational field from kinematic CHAMP orbits based on numerically derived satellite accelerations. In J. Flury, R. Rummel, C. Reigber, M. Rothacher, G. Boedecker and U. Schreiber (Eds) *Observation of the Earth System from Space*, Springer Berlin Heidelberg.

[Rignot et al., 2005] Rignot, E., G. Casassa, S. Gogineni, P. Kanagaratnam, W. Krabill, H. Pritchard, A. Rivera, R. Thomas, J. Turner, and D. Vaughan (2005). Recent ice loss from the Fleming and other glaciers, Wordie Bay, West Antarctic Peninsula. *Geophysical Research Letters* 32, L07502, doi:10.1029/2004GL021947

[Rignot and Kanagaratnam, 2006] Rignot, E. and P. Kanagaratnam (2006). Changes in the velocity structure of the Greenland ice sheet. *Science* 311, 986(2006); doi:10.1126/science.1121381

[Rodell et al., 2004] Rodell, M., P. R. Houser, U. Jambor, J. Gottschalck, K. Mitchell, C.-J. Meng, K. Arsenault, B. Cosgrove, J. Radakovich, M. Bosilovich, J.K. Entin, J.P.Walker, D. Lohmann, and D. Toll (2004). The global land data assimilation system. *Bulletin American Meteorological Society, 85(3)*, 381-394,

[Rodell et al., 2006] Rodell, M., J. Chen, H. Kato, J. Famiglietti, J. Nigro, and C. Wilson (2006). Estimating ground water storage changes in the Mississippi River basin using GRACE. *Hydrogeology Journal*, doi:10.1007/s10040-006-0103-7

[Rowlands et al., 2005] Rowlands, D. D., Luthcke S. B., S. M. Klosko, F. G. Lemoine, D. S. Chinn, J.J. McCarthy, C. M. Cox, and O. B. Anderson (2005). Resolving mass flux at high spatial and temporal resolution using GRACE intersatellite measurements. *Geophysics Research Letters*, 32, L04310, doi: 10.1029/2004GL021908

[Rummel, 1979] Rummel, R. (1979). Determination of short-wavelength components of the gravity field from satellite-to-satellite tracking or satellite gradiometry - an attempt to an identification of problem areas. *Manuscripta Geodaetica* 4(2), 107-148.

[Rummel, 2002] Rummel, R., G. Balmino, J. Johannessen, P. Visser, and P. Woodworth (2002). Dedicated gravity field missions - principles and aims. *Journal of Geodynamics*, 33: 3-20.

[Seeber, 2003] Seeber, G. (2003). Satellite Geodesy: Foundations, Methods and Applications, 2nd completely revised and extended edition, Walter de Gruyter, Berlin, New York.

[Schönauer, 2000] Schönauer, W. (2000). Architecture and use of shared and distributed memory parallel computers, Self-Edition by Willi Schönauer.

[Schwintzer et al., 2002] Schwintzer, P., H. Lühr, C. Reigber, L. Grunwaldt, and C. Förste (2002). *CHAMP reference systems, transformations and standards, CH-GFZ-RS-002*

[Schrama, 2001] Schrama, E. (2001). *DINGO user manual*. The internal report. Faculty of Geodetic Engineering/FMR, Delft University of Technology.

[Schuh, 2003] Schuh, W.D. (2003). The processing of band-limited measurements: Filtering techniques in the least squares context and in the presence of data gaps. *Space Science Review* 108:67-78

[Slobbe, 2007] Slobbe, C. (2007). Towards a combined estimation of Greenland's ice sheet mass balance using GRACE and ICESat data. MSc thesis, Department of Earth Observation and Space Systems (DEOS), Faculty of Aerospace Engineering, Delft University of Technology.

[Sneeuw, 1994] Sneeuw, N. (1994). Global spherical harmonic anslysis by least-squares and numerical quadrature methods in historical perspective. *Geophysical Journal International* 118:707-716.

[Švehla and Rothacher, 2002] Švehla, D. and M. Rothacher (2002). Kinematic and reduced-dynamic precise orbit determination of low earth orbters. *Advances in Geosciences* **1**: 1-10.

[Švehla and Földváry, 2006] Švehla, D. and L. Földváry (2006). From Kinematic Orbit Determination to Derivation of Satellite Velocity and Gravity Field. In: J. Flury, R. Rummel, C. Reigber, M. Rothacher, G. Boedeker and U. Schreiber (eds). *Observation of the Earth System from Space*. Springer, Berlin Heidelberg New York.

[Swenson and Wahr, 2002] Swenson, S., and J. Wahr (2002). Methods of inferring regional surface mass anomalies from Gravity Recovery and Climate Experiment (GRACE) measurements of time-variable gravity. *Journal of Geophysical Research*, 107(B9), 2193, doi:10.1029/2004GL019920

[Swenson and Wahr, 2006] Swenson, S., and J. Wahr (2006). Post-processing removal of correlated errors in GRACE data. *Geophysical Research Letters*, Vol. 33, L08402, doi:10.1029/2005GL025285

[Tapley et al., 1996] Tapley, B.D., M.M. Watkins, J.C. Ries, G.W. Davis, R.J. Eanes, S.R. Poole, H.J. Rim, B.E. Schutz, C.K. Shum, R.S. Nerem, F.J. Lerch, J.A. Marshall, S.M. Klosko, N.K. Pavlis, and R.G. Williamson (1996). The Joint Gravity Model-3, *Journal of Geophysical Research*, 101(B12), 28029-28049.

[Tapley et al., 2004] Tapley, B., S. Bettadpur, J. Ries, P. Thompson, and M., Watkins (2004). GRACE measurements of mass variability in the Erath sytem. *Science, 305*, 503-505.

[Tapley et al., 2005] Tapley, B., J. Ries, S. Bettadpur, D. Chambers, M. Cheng, F. Condi, B. Gunter, Z. Kang, P. Nagel, R. Pastor, T. Pekker, S. Poole, and F. Wang (2005). GGM02 - An improved Earth gravity field model from GRACE. *Journal of Geodesy*, 79:467-478, doi 10.1007/s00190-005-0480-z.

[Thomas, 1999] Thomas, J. B. (1999). *An analysis of gravity field estimation based on intersatellit dual-1-way biased ranging*, Jet Propulsion Lab., California Institute of Technology, JPL Publ. 98-15, Passadena, CA, May 1999.

[Thomas et al. 2004] Thomas, R., E. Rignot, G. Casassa, P. Kanagaratnam, C. Acua, T. Akins, H. Brecher, E. Frederick, P. Gogineni, W. Krabill, S. Manizade, H. Ramamoorthy, A. Rivera, R. Russell, J. Sonntag, R. Swift, J. Yungel, and J. Zwally (2004). Accelerated Sea-Level Rise from West Antarctica. *Science* 306, 255 (2004), doi:10.1126/science.1099650

[Uteras, 1981] Uteras, F. (1981). Optimal smoothing of noisy data using spline functions. *SIAM Journal on Scientific Computing* 2, 349-362.

[van Eck van der Sluijs, 2003] van Eck van der Sluijs, S. (2003). *Inversion of satellite accelerations into the Earth's gravity field model*. MSc thesis at the Physical Space Geodesy, Faculty of Aerospace Engineering, Delft University of Technology.

[Vaughan, 2006] Vaughan, D.G. (2006). Recent trends in melting conditions on the Antarctic Peninsula and their implications for ice-sheet mass balance and see level. *Arctic Antarctic and Alpine Research* 38(1), 147-152.

[Velicogna and Wahr, 2005] Velicogna, I., and J. Wahr (2005). Greenland mass balance from GRACE. *Geophysical Research Letters*, 32. L18505, doi:10.1029/2005GL023955

[Velicogna and Wahr, 2006] Velicogna, I., and J. Wahr (2006). Measurements of time-variable gravity show mass loss in Antarctica. *Science, 311*(5768), 1754-1756, doi:10.1126/science.1123785

[Voltring, 1986] Voltring, H.J. (1986). A Fortran package for generalized, cross-validatory spline smoothing and differentiation. *Advances in Engineering Software*, Vol. 8, No.2:104-107.

[Visser et al., 2002] Visser, P., N. Sneeuw, and C. Gerlach (2002). Energy integral method for gravity field determination from satellite orbit coordinates. *Journal of Geodesy*, 77: 207-216, 2003. doi:10.1007/s00190-003-0315-8

[Visser, 2005] Visser, P. (2005). Low-low satellite-to-satellite tracking: a comparison between analytical linear orbit perturbation theory and numerical integration. *Journal of Geodesy*,**79**, 160-166, doi: 10.1007/s00190-005-0455-0.

[Visser and van den IJsel, 2000] Visser, P. and J. van den IJsel (2000). GPS-based precise orbit determination of the very low Earth-orbiting gravity mission GOCE. *Journal of Geodesy* **74**, 590-602.

[Wahr et al., 1998] Wahr, J., M. Molenaar and F. Bryan (1998). Time variability of the Earth's gravity field: Hydrological and oceanic effects and their possible detection using GRACE. *Journal of Geophysical Research* 103, B12, 30,205-30,229.

[Watkins and Yuan, 2007] Watkins, M. M. and D. Yuan (2007). JPL Level-2 processing standards document for Level-2 product release 0004. Jet Propulsion Laboratory.

[Weigelt, 2007] Weigelt, M.L. (2007). Global and local gravity field recovery from Satellite-to-Satellite Tracking. PhD disseration, Department of Geomatics Engineering, University of Calgary.

[Wermuth et al., 2004] Wermuth, M., D. Svehla, L. Földvary, C. Gerlach, T. Gruber, B. Frommknecht, T. Peters, M. Rothacher, R. Rummeal, and P. Streigenberger, (2004). A gravity field model from two years of CHAMP kinematic orbits using the energy balance approach. EGU 1st General Assmbly, April 25-30, 2004, Nice, France.

[Wikipedia, 2008] Geographical description of the selected river basins, available at http://en.wikipedia.org/wiki/

[Xu and Rummel, 1994] Xu, P. and R. Rummel (1994). Generalized ridge regression with applications in determination of potential fields. Manuscripta Geodaetica 20(1): 8-20.

[Zhao, 2004] Zhao, Q. (2004). Research on precise orbit determination theory and software of both GPS navigation constellation and LEO satellites. PhD dissertation, School of Geodesy and Geomatics, Wuhan University.

[Zhao et al., 2007] Zhao, Q., P. Ditmar, X. Liu, and R. Klees (2007). Determination of precise kinematic orbits of CHAMP and GRACE satellites for gravity field modeling, in preparation.

[Zhu et al., 2004] Zhu, S., Ch. Reigber, and R. König (2004). Integrated adjustment of CHAMP, GRACE, and GPS data. *Journal of Geodesy* **78**, 103-108, doi 10.1007/s00190-004-0379-0

[Zlotnicki, 2007] Zlotnicki (2007). Post Glacial Rebound Discussion at GRACE Tellus project, available at http://gracetellus.jpl.nasa.gov/pgr_discussion.html

Appendix A

Autocorrelation

Autocorrelation is a statistical tool to study the cross-correlation of a random process with itself. In this way, it is possible to find repeating patterns in a random process, for example, the presence of a periodic signal, which may be buried under noise invisible in time series. It is also used to identify the fundamental frequency of a signal. Two terms are described here: autocovariance and autocorrelation coefficient.

Autocovariance represents the correlation between a random process at different points in time. Let x_t be the value of the process at epoch t, with $\overline{x}$ being the mean of the process and N the length of the process. The definition of autocovariance is:

$$C_k = \frac{1}{N-k} \sum_{t=0}^{N-k} (x_t - \overline{x})(x_{t+k} - \overline{x}), \tag{A.1}$$

where k is the lag time. When the autocovariance is normalized by variance (i.e. autocovariance when the lag time is zero), it is referred to as a set of the autocorrelation coefficients:

$$r_k = \frac{C_k}{C_0}. \tag{A.2}$$

In this thesis, autocorrelation is used to investigate noise in GRACE orbits by taking the difference between inter-satellite ranges derived from the orbits and measured by the KBR system.

Appendix B
Gaussian Filtering

Equation (2.9) is used to recover changes in surface mass density. ΔC_{lm} and ΔS_{lm} are the coefficients estimated from GRACE data with respect to a long-term mean. The accuracy of coefficients reduces rapidly with the increase of degree l. It is not difficult to see that the errors in the GRACE estimates can largely influence estimates of surface mass density variations. In order to reduce the effect of noise in high-degree coefficients, a spatial averaging (filtering) function is introduced. According to [Wahr et al., 1998], the spatial averages of the surface mass density is considered,

$$\Delta\overline{\sigma}(\vartheta,\lambda) = \int \Delta\sigma(\vartheta,\lambda)W(\gamma)\sin\vartheta' d\vartheta' d\lambda, \tag{B.1}$$

where $W(\gamma)$ is an averaging function, depending on γ, the central angle between the points (ϑ,λ) and (ϑ',λ') ($\cos\gamma = \cos\vartheta\cos\vartheta' + sin\vartheta\sin\vartheta' cos(\lambda-\lambda')$). Inserting equation (2.9) into equation (B.1) with some manipulation [Wahr et al., 1998], we obtain:

$$\Delta\overline{\sigma}(\vartheta,\lambda) = 2\pi \sum_{l=L_{\min}}^{L_{\max}} \sum_{m=0}^{l} K_l W_l \left(\Delta C_{lm}\cos m\lambda + \Delta S_{lm}\sin m\lambda\right)\bar{P}_{lm}(\cos\vartheta), \tag{B.2}$$

where

$$W_l = \int_0^{\pi} W(\gamma)P_l(\cos\gamma)\sin(\gamma)d\gamma, \tag{B.3}$$

with P_l being the Legendre polynomials, and its value $P_l = \bar{P}_{lm,m=0}/\sqrt{2l+1}$. Using Jekeli's Gaussian averaging (filtering) function [Jekeli, 1981], $W(\gamma)$ in equation (B.3) can be written as:

$$W(\gamma) = \frac{b}{2\pi}\frac{e^{-b(1-\cos\gamma)}}{1-e^{-2b}}, \tag{B.4}$$

where

$$b = \frac{ln(2)}{1-\cos(r_w/R)}, \tag{B.5}$$

and where r_w is the averaging radius, which can be freely chosen. The value can be understood as the distance on the Earth's surface at which $W(\gamma)$ is reduced to $1/2$ of its value at $\gamma = 0$. The coefficients W_l can be recursively computed:

$$\begin{aligned} W_0 &= \frac{1}{2\pi}, \\ W_l &= \frac{1}{2\pi}\left(\frac{1+e^{-2b}}{1-e^{-2b}} - \frac{1}{b}\right), \\ W_{l+1} &= -\frac{2l+1}{b}W_l + W_{l-1}. \end{aligned} \tag{B.6}$$